
Mapping of the Electrical Activity of Human Atria

Multiscale Modelling and Simulations

Laura Martínez Mateu

PhD Thesis

Supervisors:

Dr. Francisco Javier Saiz Rodríguez

Dra. Lucía Romero Pérez

Valencia, May 2018

Ph.D. thesis submitted to the Department of Electronic Engineering in fulfillment of the requirements for the degree of Doctor of Philosophy at the Universitat Politècnica de València, Valencia, Spain



UNIVERSITAT
POLITÈCNICA
DE VALÈNCIA

Supervisors:

Dr. Francisco Javier Saiz Rodríguez
Universitat Politècnica de València, Spain

Dra. Lucía Romero Pérez
Universitat Politècnica de València, Spain

External Evaluators:

Dr. Pablo Laguna Lasaosa
Universidad de Zaragoza

Dr. Blas Echebarria Domínguez
Universitat Politècnica de Catalunya

Dr. David Filgueiras Rama
Centro Nacional de Investigaciones Cardiovasculares Carlos III

Reading Committee:

Dr. Manuel Doblaré Castellano
Universidad de Zaragoza

Dr. José Luis Rojo Álvarez
Universidad Rey Juan Carlos

Dr. David Filgueiras Rama
Centro Nacional de Investigaciones Cardiovasculares Carlos III

This work was carried out in the *Centro de Investigación e Innovación en Bioingeniería* (Ci2B), Universitat Politècnica de València, Valencia, Spain.



To my family...

*"Everything should be made as simple as possible, but
not simpler." Albert Einstein*

Acknowledgements

I would like to express my gratitude to all the people who have supported me during the course of this PhD thesis. Without their support and encouragement I would not have been able to overcome the hardest moments and finish this project.

First, I would like to thank my supervisors, Javier Saiz and Lucía Romero, for their excellent scientific supervision, guidance, dedication and passion for science and research. It has been a pleasure for me to be their PhD student for the last years. Special thanks to Javier, who gave me the opportunity to find out this fantastic field of research some years ago. He motivated me with his tireless optimism, sometimes almost unrealistic, and convinced me to start this adventure, full of obstacles but very rewarding. His knowledge in the field of computational models and simulations, as well as in cardiac electrophysiology, has been very important to me, but not as much as his human quality. In the most complicated moments during the thesis process, mainly over the last year, he has behaved more like a father than a supervisor. I will always be grateful for his advice and talks in both, academic and personal stuff.

Second, I would like to express my gratitude to all the people who collaborated with me in these years. Their help, comments and suggestions notably improved my work. Thanks to Rafael Sebastián for transferring me his knowledge about 3D modelling and helping me with the methodology, but most important, for being a friend; to José Félix Rodríguez for his warm support and wisdom regarding mathematics and numerical methods applied to cardiac modelling; to José Jalife for bringing his immense knowledge in cardiac electrophysiology to my work and providing clarity in the dissemination of my results. And finally, special thanks to Omer Berenfeld for his invaluable collaboration. In part, this PhD thesis has been developed thanks to his incessant ideas and suggestions about mapping the electrical activity of the heart. I deeply thank him his dedication, effort and fast response, as well as for everything I have learnt from him.

Third, I have to thank my colleagues from the research group Ci2B for their

unconditional support. We shared sorrows and joys lived during the course of the thesis. I really appreciate their empathy (not everyone can understand the emotional situation of a PhD student) and above all, our times together in the lab, especially the scientific conversations, and not so scientific, during our eternal lunch times. Also our ravings and laughs on Fridays in the late afternoon, when we were obfuscated and stuck in our research. From this I have learned the best lesson in life: everything looks much better after a beer in good company. Special thanks to Ana, Alejandro, Víctor, Eduardo, Juanfran, Bea and Karen. They were colleagues and became friends.

I also would like to thank my friends for helping me to overcome the hard moments and being an important part of my life. Oliver, Nacho, Sara, Laura, Marta, Isa, Santi, Jon (the best English teacher ever)... thanks for listening to my complaints and exaggerations about the horrifying life of a PhD student. Thanks for suffering my speeches on models and electrophysiology. Thanks for the relaxing and leisure times so necessary to keep me from going crazy. Also thanks to my colleagues from Nuubo for being interested in the progress of my thesis and encouraging me.

Finally, the greatest gratitude is for my family (my parents, my sister and her partner, Luis) for their unconditional support and love throughout my life. I have become the person I am thanks to them. This PhD thesis is also theirs. To my parents, for being always there for me, emphasizing the importance of studying and offering me everything they did not have. Thanks for always respecting and supporting my decisions. To my sister, sometimes almost a second mother. We are so similar and so different... I thank her for sharing with me her artistic and bohemian vision of the world and teaching me that there is a life beyond mathematics and engineering.

Abstract

Atrial fibrillation is one of the most common cardiac arrhythmias seen in clinical practice. Therefore, it is of vital importance to develop new technologies aimed at diagnosing and terminating this kind of arrhythmia, to improve the quality of life of patients and to reduce costs to national health systems.

In the last years, new atrial mapping techniques based on multi-electrode systems are increasingly being used to map the atrial electrical activity in humans and localise and target atrial fibrillation drivers in the form of focal sources or rotors. However, significant concerns remain about their accuracy and experimental approaches to analyse them are limited due to their invasive character. Therefore, computer simulations are a helpful tool to overcome these limitations since they can reproduce with fidelity experimental observations, permit to split the problem to treat into more simple sub-studies, and allow the possibility of performing preliminary investigations impossible to carry out in the clinical practice.

This PhD thesis is focused on the analysis for accuracy of the multi-electrode mapping systems through computational models and simulations. For this purpose, we developed realistic multiscale models in order to simulate atrial electrical reentrant activity, first in a sheet of atrial tissue and, then, in the whole atria. Then, we analysed the effects of the multi-electrode geometrical configurations on the accuracy of localizing rotors, by using multi-electrode arrays with equidistant inter-electrode distances, as well as multi-electrode basket catheters with non-equidistant inter-electrode distances. After computing the intracavitary unipolar electrograms, we performed phase maps, phase singularity detections to track rotors, and dominant frequency maps. We finally found out that the accuracy of multi-electrode mapping systems depends on their position inside the atrial cavity, the electrode-to-tissue distance, the inter-electrode distance, and the contribution of far field sources. Furthermore, as a consequence of these factors, false rotors might appear and could contribute to failure of atrial fibrillation ablation procedures.

Resumen

La fibrilación auricular es una de las arritmias cardíacas más comunes observadas en la práctica clínica. Por lo tanto, es de vital importancia desarrollar nuevas tecnologías destinadas a diagnosticar y acabar con este tipo de arritmia, para mejorar la calidad de vida de los pacientes y reducir los costes de los sistemas nacionales de salud.

En los últimos años ha aumentado el uso de las nuevas técnicas de mapeo auricular, basadas en sistemas multielectrodo para mapear la actividad eléctrica en humanos. Dichas técnicas permiten localizar y ablacionar los impulsores de la fibrilación auricular, como son las fuentes focales o los rotores. Sin embargo, todavía existe incertidumbre sobre su precisión y los procedimientos experimentales para su análisis están limitados debido a su carácter invasivo. Por lo tanto, las simulaciones computacionales son una herramienta muy útil para superar estas limitaciones, al permitir reproducir con fidelidad las observaciones experimentales, dividir el problema bajo estudio en subestudios más simples, y realizar investigaciones preliminares imposibles de llevar a cabo en el práctica clínica.

Esta tesis doctoral se centra en el análisis de la precisión de los sistemas de mapeo multielectrodo a través de modelos y simulaciones computacionales. Para ello, desarrollamos modelos realistas multiescala con el objetivo de simular actividad eléctrica auricular reentrante, en primer lugar en una lámina de tejido auricular, y en segundo lugar en las aurículas completas. Posteriormente, analizamos los efectos de las configuraciones geométricas multielectrodo en la precisión de la localización de los rotores, mediante el uso de agrupaciones multielectrodo con distancias interelectrodo equidistantes, así como a través de catéteres de tipo *basket* con distancias interelectrodo no equidistantes. Después de calcular los electrogramas unipolares intracavitarios, realizamos mapas de fase, detecciones de singularidad de fase para rastrear los rotores, y mapas de frecuencia dominantes. Finalmente, descubrimos que la precisión de los sistemas de mapeo multielectrodo depende de su posición dentro de la cavidad auricular, de la distancia entre los electrodos y el tejido,

de la distancia interelectrodo, y de la contribución de las fuentes de campo lejano. Además, como consecuencia de estos factores que pueden afectar a la precisión de los sistemas de mapeo multielectrodo, observamos la aparición de rotores falsos que podrían contribuir al fracaso de los procesos de ablación de la fibrilación auricular.

Resum

La fibril·lació auricular és una de les arítmies cardíques més comunes observades en la pràctica clínica. Per tant, és de vital importància desenvolupar noves tecnologies destinades a diagnosticar i acabar amb aquest tipus d'arítmia, per tal de millorar la qualitat de vida dels pacients i reduir els costos dels sistemes nacionals de salut.

En els últims anys, ha augmentat l'ús de les noves tècniques de mapeig auricular, basades en sistemes multielèctrode per a mapejar l'activitat elèctrica auricular en humans. Aquestes tècniques permeten localitzar i ablacionar els impulsors de la fibril·lació auricular, com són les fonts focals o els rotors. No obstant això, encara hi ha incertesa sobre la seua precisió i els procediments experimentals per al seu anàlisi estan limitats a causa del seu caràcter invasiu. Per tant, les simulacions computacionals són una eina molt útil per a superar aquestes limitacions, en permetre reproduir amb fidelitat les observacions experimentals, dividir el problema sota estudi en subestudis més simples, i realitzar investigacions preliminars impossibles de dur a terme en la pràctica clínica.

Aquesta tesi doctoral se centra en l'anàlisi de la precisió del sistema de mapeig multielèctrode mitjançant els models i les simulacions computacionals. Per a això, desenvoluparem models realistes multiescala per tal de simular activitat elèctrica auricular reentrant, en primer lloc en una làmina de teixit auricular, i en segon lloc a les aurícules completes. Posteriorment, analitzarem els efectes de les configuracions geomètriques multielèctrode en la precisió de la localització dels rotors, mitjançant l'ús d'agrupacions multielèctrode amb distàncies interelèctrode equidistants, així com catèters de tipus *basket* amb distàncies interelèctrode no equidistants. Després de calcular els electrogrames unipolars intracavitaris, vam realitzar mapes de fase, deteccions de singularitat de fase per a rastrejar els rotors, i mapes de freqüència dominants. Finalment, vam descobrir que la precisió dels sistemes de mapeig multielèctrode depèn de la seua posició dins de la cavitat auricular, de la distància entre els elèctrodes i el teixit, de la distància interelèctrode, i de la contribució de les fonts de camp

llunyà. A més, com a conseqüència d'aquests factors, es va observar l'aparició de rotors falsos que podrien contribuir al fracàs de l'ablació de la fibril·lació auricular.

Contents

Acknowledgements	v
Abstract	vii
Resumen	ix
Resum	xi
List of Figures	xix
List of Tables	xxv
Acronyms	xxvii
1 Introduction	1
1.1 Motivation	2
1.2 Objectives	3
1.3 Structure of the Thesis	4
2 State of the Art	7
2.1 The Heart	8
2.1.1 Structure of the Heart	8
2.1.1.1 Atrial Anatomy	9
2.1.1.2 Position of the Heart in the Torso	11
2.1.2 Electrophysiology of the Heart	12

2.1.2.1	Electrical Conduction System	12
2.1.2.2	Action Potential	14
2.1.2.3	Electrocardiogram and Electrogram	16
2.1.2.3.1	Electrocardiographic Leads	17
2.1.2.3.2	Intracavitary Recordings and Mapping Systems	19
2.2	Cardiac Arrhythmias	22
2.2.1	Premature Atrial Contractions	22
2.2.2	Focal Atrial Tachycardia	23
2.2.3	Atrial Fibrillation	24
2.2.3.1	Paroxysmal Atrial Fibrillation	27
2.2.3.2	Chronic Atrial Fibrillation	27
2.3	Modelling the Heart Electrical Activity	29
2.3.1	Cellular Atrial Models	31
2.3.1.1	CRN Model	33
2.3.2	3D Atria and Torso Models	35
2.3.2.1	3D Atrial Models	36
2.3.2.2	3D Torso Models	38
2.3.3	Numerical and Computational Methods	40
2.3.3.1	Bidomain Formalism	40
2.3.3.2	Monodomain Formalism	42
2.4	Phase Analysis	43
2.4.1	Phase Maps	44
2.5	Frequency Analysis	44
3	Three-Dimensional Multiscale Atria-Torso Model	47
3.1	Introduction	48
3.2	Methods	48
3.2.1	Unicellular Models	48
3.2.1.1	Stabilization of the Ionic Model	48
3.2.1.2	Atrial Heterogeneity	51

3.2.2	3D Atrial Model	52
3.2.2.1	Block of Atrial Tissue	52
3.2.2.1.1	Adjustment of the Stimulation	53
3.2.2.1.2	Adjustment of Conduction Velocity	53
3.2.2.2	Atrial Geometrical Mesh	57
3.2.2.3	Numerical/Computational Methods and Stimulation Protocol	58
3.2.3	Computation of Intracavitary EGMs	59
3.2.3.1	Numerical and Computational Methods	60
3.2.3.2	3D Atria-Blood Model	61
3.2.3.2.1	Generation of the Atria-Blood Geometrical Mesh	62
3.2.3.3	3D Torso Model	64
3.2.3.3.1	Generation of the Torso Geometrical Mesh	64
3.2.3.4	Clustering of the EGMs on the Endocardial Surface	65
3.3	Results	66
3.3.1	Simulation of the Electrical Propagation in the Human Atria Under Physiological Conditions	66
3.3.2	Simulation of the Intracavitary EGMs	66
3.3.2.1	EGMs in the Atria-Blood Model	67
3.3.2.2	EGMs in the Atria-Torso Model	69
3.3.3	Simulation of the Electrical Propagation on the Torso Surface	72
3.4	Discussion	75
3.4.1	Unicellular Models	76
3.4.2	3D Atrial Model	76
3.4.3	Intracavitary EGMs	77
3.4.3.1	Atria-Blood Model and Atria-Torso Model	77
3.4.3.2	Influence of the Torso in the Computation of Intracavitary EGMs	78

4 Mapping Reentries in a Sheet of Atrial Tissue by Using Multi-Electrode Arrays	81
4.1 Introduction	82
4.2 Methods	82
4.2.1 Unicellular Models	82
4.2.1.1 Electrical Remodelling	82
4.2.1.1.1 Paroxysmal Atrial Fibrillation	83
4.2.1.1.2 Chronic Atrial Fibrillation	84
4.2.2 Sheet of Atrial Tissue	85
4.2.2.1 Tissue Geometrical Meshes	86
4.2.2.2 Electrical Propagation	87
4.2.3 Mapping the Electrical Activity	88
4.2.3.1 3D-Block Meshes	88
4.2.3.2 Virtual Electrodes	89
4.2.3.2.1 Virtual Central Electrode	89
4.2.3.2.2 Virtual Multi-electrode Array Configurations	90
4.2.3.3 Computation of the EGMs, Phase Maps and Dominant Frequency Maps	91
4.2.3.3.1 Unipolar EGMs	91
4.2.3.3.2 Phase Maps and Rotor Tracking	91
4.2.3.3.3 Dominant Frequency Maps	93
4.3 Results	94
4.3.1 Simulation of the Electrical Activity in a 3D Sheet of Atrial Tissue	95
4.3.2 Influence of the Torso in the EGMs Computation	95
4.3.3 Near and Far Field Contributions	98
4.3.4 Mapping Reentries by using Multi-Electrode Arrays	100
4.3.4.1 Accuracy of the Multi-electrode Arrays Configuration	100
4.3.4.2 Differentiation Between Functional and Anatomical Reentry	106

4.3.5	Differences between Rotors in pAF and cAF	109
4.4	Discussion	111
4.4.1	Electrical Remodelling: pAF and cAF	111
4.4.2	Influence of the Torso in the EGMs Computation	112
4.4.3	Contribution of the Near and Far Field Sources	112
4.4.4	Accuracy of the Multi-Electrode Arrays	113
4.4.5	Ability of Multi-Electrode Arrays to Differentiate Functional and Anatomical Reentries	114
4.4.6	Differences between Rotors in pAF and cAF	115
5	Mapping Reentries in a 3D Human Atrial Model by Using a Basket Catheter	117
5.1	Introduction	118
5.2	Methods	119
5.2.1	Generation of Reentries	119
5.2.2	Endocardial Phase Maps and Rotor Tracking	120
5.2.3	Mapping Basket Catheter	122
5.3	Results	124
5.3.1	The Simulated Propagation Patterns	124
5.3.2	Effect of Electrode-to-Endocardium Distance on Mapping	126
5.3.2.1	Mapping at Three Different Basket Positions	128
5.3.2.2	Effect of Ectopic and Rotor Activity on IMPSs	136
5.3.3	Effect of the Far-Field Sources on Mapping	137
5.3.4	Effect of Inter-electrode Interpolation on Mapping	141
5.4	Discussion	143
5.4.1	Effect of the Electrode-Endocardium Distance	144
5.4.2	Effect of Basket Catheter Electrode Density	145
6	Limitations	147
7	Conclusions	151

8 Future Research Work	157
9 Contributions	159
9.1 Publications	160
9.1.1 Journal Papers	160
9.1.2 Conference Papers and Communications	161
9.2 Collaborations	162
9.3 Research projects	163
A CRN Model Formulation	165
B Propagation Patterns in the Basket Catheter for Sinus Rhythm	175
Bibliography	181

List of Figures

2.1	Structure of the heart and blood flow	8
2.2	Views of the atria	9
2.3	Anatomy of the atria	10
2.4	Schematic representation of the atrial structures	10
2.5	Position of the heart in the torso	11
2.6	Electrical conduction system and action potentials	13
2.7	Atrial myocytes	14
2.8	Ionic exchange through the cell membrane	14
2.9	Atrial action potential	15
2.10	Electrical heterogeneity in the atria	16
2.11	Generation of the waves in the electrocardiogram	17
2.12	12 standard ECG leads	18
2.13	Intracardiac EGMs	19
2.14	Generation of unipolar and bipolar EGMs	20
2.15	Commercial mapping systems	21
2.16	Console of the RHYTHMIA HDx TM Mapping System	22
2.17	ECG recording of a premature atrial contraction	23
2.18	ECG recordings during atrial tachycardia	24
2.19	Disorganized activation of the atria and ECG recording during atrial fibrillation	25
2.20	Principal mechanisms underlying AF	26

2.21	APs in control and remodelling	28
2.22	Number of publications related to computational analysis of AF	31
2.23	Comparison of the five most relevant human atrial myocyte models	33
2.24	Cell in the CRN model	34
2.25	Patient-specific atrial and torso models	36
2.26	Spherical torso models	39
3.1	Variation of the ionic intracellular concentrations for the CRN model	49
3.2	Simulated APs obtained after pacing the CRN model with a BCL of 1000 ms	50
3.3	Action potentials (AP) in control conditions	52
3.4	Geometrical mesh corresponding to a 3D block of atrial tissue	53
3.5	Threshold stimuli for the CRN model	54
3.6	Propagation patterns corresponding to different atrial tissues	55
3.7	3D atrial geometrical mesh	57
3.8	Atrial regions in the 3D model	58
3.9	Atria-blood and torso models	59
3.10	Diagram of the bidomain approximation	61
3.11	Closed outer surface to mesh the atria-blood model	62
3.12	Atria-blood tetrahedral mesh	63
3.13	Atria-blood mesh quality	63
3.14	Torso mesh comprised of tetrahedral elements	64
3.15	Torso mesh quality	65
3.16	EGM properties for clustering	66
3.17	Atrial activation times	67
3.18	Endocardial EGMs and BSPM	68
3.19	EGM in the RA and LA computed with the atria-blood model	68
3.20	Clustering of the endocardial RA EGMs computed in the atria-blood model	70
3.21	Clustering of the endocardial LA EGMs computed in the atria-blood model	71

3.22	EGM in the RA and LA computed with the atria-torso model . .	72
3.23	Clustering of the endocardial RA EGMs computed in the atria-torso model	73
3.24	Clustering of the endocardial LA EGMs computed in the atria-torso model	74
3.25	P-waves at the precordial leads simulated with the atria-torso model	75
4.1	Action potentials (AP) under pAF conditions	84
4.2	Action potentials (AP) under cAF conditions	86
4.3	Geometrical meshes corresponding to the LA, PV and MVR tissues	86
4.4	3D block meshes to compute unipolar EGMs	88
4.5	Tetrahedral elements size depending on the location of the multi-electrode arrays	89
4.6	Regions of tissue defined as near- and far-field sources	89
4.7	Virtual multi-electrode array configurations	90
4.8	PS detection on the multi-electrode arrays phase maps	92
4.9	EGM before and after filtering, PSD of the filtered EGM and resultant DF	93
4.10	Propagation of the APs in the simulations performed with sheets of atrial tissue	94
4.11	Comparison of the EGMs computed with the TTB and TB meshes	96
4.12	Attenuation of the EGMs with the electrode-to-tissue distance .	98
4.13	NF and FF contributions	99
4.14	Effect of the EGMs interpolation on the phase maps and PSs detection	101
4.15	Phase maps corresponding to Sim2 for each multi-electrode array configuration	102
4.16	Rotor trajectory corresponding to Sim2 detected by each multi-electrode array configuration	103
4.17	Phase maps corresponding to Sim3 for each multi-electrode array configuration	104
4.18	Rotors trajectories corresponding to Sim3 detected by each multi-electrode array configuration	105

4.19	Tetrahedral meshes built for the EGM calculation in order to differentiate functional from anatomical reentries	106
4.20	V_m , phase maps and rotor tracking	107
4.21	EGMs corresponding to functional and anatomical reentries . . .	108
4.22	DF maps corresponding to functional and anatomical reentries .	108
4.23	Meandering corresponding to functional reentries in pAF and cAF	109
4.24	DF maps corresponding to functional reentries in pAF and cAF .	110
5.1	Location of the ectopic foci close to the CS	119
5.2	PS detection on the endocardium-blood interface	121
5.3	Basket positions in the RA	122
5.4	Basket inter-electrode distances	123
5.5	Improvement of basket phase maps after EGMs interpolation . .	123
5.6	Electrical propagation and phase maps	125
5.7	Plots of the phases in the endocardium	126
5.8	RA and the CT rotor meandering area in relationship with the near and far basket electrodes	127
5.9	Basket mapping for the SVC position	129
5.10	Traces of the phases in the basket for the SVC position	131
5.11	Basket mapping for the CT position	132
5.12	Phases at the basket's south pole	133
5.13	Traces of the phases in the basket for the CT position	133
5.14	Basket mapping for the CS position	134
5.15	Traces of the phases in the basket for the CS position	135
5.16	AP propagation following secession of pacing	136
5.17	Basket phase maps of simulation following secession of pacing . .	137
5.18	Effect of the far-field sources	138
5.19	Sources regions to analyse the effect of FF	139
5.20	Sensitivity of the phase maps	140
5.21	Effect of EGMs interpolation in the phase maps	141

A.1 Schematic representation of a cardiomyocyte modelled by the CRN model	173
B.1 Basket propagation pattern in SR for the SVC position	177
B.2 Basket propagation pattern in SR for the CT position	178
B.3 Basket propagation pattern in SR for the CS position	179

List of Tables

2.1	Anatomical dimensions of thoracic cage and organs	11
2.2	Electrical remodelling experimentally observed in cAF	29
2.3	Multiscale modelling	30
3.1	APD at 50% and 90% repolarization for the CRN model	50
3.2	Ionic channel conductances and APD distribution under control conditions	51
3.3	Stimuli applied to unicellular and multicellular simulations	53
3.4	Cellular model, longitudinal conductivity, anisotropy ratio and CVs for each atrial region	56
3.5	Longitudinal conductivity and anisotropy ratio used in the 3D atrial model	58
3.6	Tissue conductivities for the torso model	65
3.7	Amplitude and duration of the simulated P-waves at the precordial leads	75
4.1	Ionic currents variations and APD ₉₀ under pAF conditions	83
4.2	Ionic currents variations and APD ₉₀ under cAF conditions	85
4.3	Summary of simulations performed with the 3D sheets of atrial tissue	87
4.4	Amplitude of the EGMs computed with the TTB and TB meshes	97
4.5	Meandering areas in pAF and cAF	110

5.1	Longitudinal conductivity and anisotropy ratio used in the 3D atrial model in cAF	120
5.2	PS detections for different densities of electrodes	142

Acronyms

ACh	Acetylcholine
AF	Atrial Fibrillation
AP	Action Potential
APD	Action Potential Duration
APD ₅₀	Action Potential Duration at 50% of repolarization
APD ₉₀	Action Potential Duration at 90% of repolarization
APD ₉₅	Action Potential Duration at 95% of repolarization
AT	Atrial Tachycardia
AV	Atrio-Ventricular
BB	Bachmann's Bundle
BBRA	Bachmann's Bundle in the Right Atrium (right side)
BBLA	Bachmann's Bundle in the Left Atrium (left side)
BCL	Basic Cycle Length
BEM	Boundary Elements Method
bpm	beats per minute
BSPM	Body Surface Potential Maps
cAF	chronic Atrial Fibrillation
CL	Cycle Length
C_m	Cell membrane capacitance
COR	Cellular Open Resource
CRN	Courtemanche-Ramirez-Nattel
CS	Coronary Sinus
CT	Crista Terminalis
CT rotor	Rotor on the CT
CV	Conduction Velocity
CV _L	Longitudinal Conduction Velocity
CV _T	Transversal Conduction Velocity
DF	Dominant Frequency

d_{ie}	Inter-electrode distance
ECG	Electrocardiogram
EGM	Electrogram
FEM	Finite Elements Method
FF	Far Field
FFT	Fast Fourier Transform
FIPS	False Interpolation Phase Singularity
FO	Fossa Ovalis
HR	Heart Rate
HT	Hilbert Transform
I_{bCa}	Background Ca^{2+} current
I_{bNa}	Background Na^{+} current
I_{CaL}	L-type inward Ca^{2+} current
I_{ion}	Total ionic current
I_{K1}	Inward rectifier K^{+} current
I_{KACH}	Acetylcholine activated inward rectifier K^{+} current
I_{Kr}	Rapid delayed rectifier K^{+} current
I_{Ks}	Slow delayed rectifier K^{+} current
I_{Kur}	Ultrarapid delayed rectifier K^{+} current
IMPS	Imaginary Phase Singularity
IM-RWE	Imaginary Rotor Wave Extension
I_{Na}	Fast inward Na^{+} current
I_{NaCa}	Na^{+}/Ca^{2+} exchanger current
I_{NaK}	$Na^{+}-K^{+}$ pump current
I_{pCa}	Sarcoplasmic Ca^{2+} pump current
I_{st}	Stimulus current
I_{to}	Transient outward K^{+} current
IVC	Inferior Vena Cava
IVCR	Inferior Vena Cava Reentry
JSR	Junctional Sarcoplasmic Reticulum
LA	Left Atrium
LAA	Left Atrial Appendage
LFO	Limbus of Fossa Ovalis
LLPV	Left Lower Pulmonary Vein
LPV	Left Pulmonary Veins
LUPV	Left Upper Pulmonary Vein
LV	Left Ventricle
MV	Mitral Valve
MVR	Mitral Valve Ring

NF	Near Field
NSR	Network Sarcoplasmic Reticulum
ODE	Ordinary Differential Equation
PAC	Premature Atrial Contraction
pAF	paroxysmal Atrial Fibrillation
PDE	Partial Differential Equation
PM	Pectinate Muscles
PS	Phase Singularity
PSD	Power Spectral Density
PV	Pulmonary Veins
RA	Right Atrium
RAA	Right Atrial Appendage
RLPV	Right Lower Pulmonary Vein
RPV	Right Pulmonary Veins
RUPV	Right Upper Pulmonary Vein
RV	Right Ventricle
RWE	Rotor Wave Extension
SR	Sinus Rhythm
SAN	Sino-Atrial Node
SVC	Superior Vena Cava
SVCR	Superior Vena Cava Reentry
TB	Tissue-Blood
TTB	Torso-Tissue-Blood
TV	Tricuspid Valve
TVR	Tricuspid Valve Ring
V_m	Transmembrane potential
2D	Two-Dimensional
3D	Three-Dimensional
$\partial\Omega_T$	Torso-air non-flux boundary
ϕ_e	Extracellular potential
ϕ_i	Intracellular potential
σ_L	Longitudinal Conductivity
σ_T	Transversal Conductivity
θ	Instantaneous phase

CHAPTER 1

Introduction

1.1 Motivation

Cardiovascular diseases are responsible for approximately 17 million deaths per year around the world (31% of the major causes of death). Among them, cardiac arrhythmias, i.e. disorders of the electrical conduction system of the heart, can be life threatening and cause medical emergencies.¹ Atrial fibrillation (AF) is one of the most common cardiac arrhythmias seen in clinical practice and is the most important cause of embolic stroke.^{2,3} Its prevalence increases with advancing age and it is also commonly associated with congestive heart failure. In 2030 between 14 and 17 million people will suffer AF in the European Union.⁴ Therefore, it is of vital importance to develop new technologies aimed at diagnosing and terminating cardiac arrhythmias such as AF in order to improve the quality of life of patients and to reduce costs to national health systems.

Historically, the standard and non-invasive procedure to detect AF or any other cardiac arrhythmia has been the electrocardiogram (ECG). Two major approaches have been used to terminate AF: drug therapy (non-invasive) and ablation procedures (invasive). Recently, catheter ablation has been recommended as a first-line treatment for AF termination,⁴ since it has been demonstrated to be superior to antiarrhythmic therapy for the maintenance of sinus rhythm (SR).⁵⁻⁷ Traditionally, ablation procedures aimed at terminating AF have been primarily focused on isolating the pulmonary veins (PV)⁸⁻¹⁰ often complemented by linear ablation of the posterior left atrium (LA).¹¹ On the contrary, recent approaches based on mapping the electrical activity of the atria during AF are patient-specific and take into account the underlying mechanism and target the AF drivers. These drivers can be focal sources or rotors,^{12,13} as demonstrated through high-resolution optical mapping of AF in animal models¹⁴⁻¹⁷ and explanted human hearts.^{18,19} Unfortunately, optical mapping cannot be employed in humans because the voltage sensitive dyes used to record membrane potentials are toxic. Therefore clinical mapping approaches are limited to the use of low resolution multi-electrode systems (contact and non-contact).^{12,20-26} The use of panoramic contact multi-electrode basket catheters to map the atria in search for AF drivers enabled $> 80\%$ success rates compared to 20-50% obtained by conventional ablation.^{2,20,27} However, the descriptions of rotors as AF drivers are still controversial^{23,24,28,29} and the usage of this new mapping approach to target those drivers needs further studies to determine its accuracy.

A significant drawback of the basket mapping approach is that direct contact between a given electrode on the basket and the atrial tissue is not always possible, and the effect of distance between electrode and endocardium has not been deeply studied.^{30,31} Lack of direct contact likely affects recording accuracy, as it occurs with non-contact catheters, whose center cannot be separated from the endocardium by more than 4 cm or the signal resolution

would decline.²⁵ In addition, it is important to more clearly understand the effect of far-field sources on the basket catheter recordings, due to the ability of unipolar recordings to detect not only local but also remote electrical activity. Furthermore, atrial electrical activity maps built from basket catheter recordings are of limited resolution. To our knowledge only the minimum spatial resolution to localize rotors has already been studied.²¹ Interpolation of the signals before building such maps seems useful. However, interpolation can also introduce artifacts.^{22,32}

For all the above reasons, there is a need to map the electrical activity of the atria and target the AF drivers to restore the SR. Nevertheless, the new systems available to map the atria have not been systematically analysed for accuracy and further analyses are required. Yet, the ability to conduct such analyses in clinical practice during an ablation procedure is limited. Therefore, computer simulations can be an excellent and valuable tool as a first approach to overcome these limitations since they can reproduce with fidelity experimental observations, allow the splitting of the problem to treat into more simple sub-studies and the possibility of performing preliminary investigations impossible to carry out in the clinical practice.

1.2 Objectives

The main objective of this PhD thesis is to study the accuracy of multi-electrode mapping systems when mapping the electrical activity of the human atria, concretely reentrant activity, through computational models and simulations. Due to the complexity of the atrial anatomy, and multi-electrode systems such as basket catheters, there is a need to first consider a simpler scenario to analyse the accuracy of a flat grid of equidistant electrodes when mapping a sheet of atrial tissue; and then, to study the accuracy of a basket catheter when mapping the electrical activity in a three-dimensional (3D) realistic human atrial model. Hence, the main objective has been splitted into the following specific objectives:

1. To develop and validate a realistic and multiscale 3D atrial-torso model as a tool for computing intracavitary atrial electrograms (EGMs):
 - Adjustment of atrial unicellular models under control conditions to carry out simulations ranging from cellular level to organ.
 - Evaluation of the effect of the torso in the computations of the intracavitary EGMs.
2. To analyse the factors affecting the accuracy of a multi-electrode system with equidistant inter-electrode distance when mapping reentries in a sheet of atrial tissue.

- Adjustment of atrial unicellular models under remodelling conditions to carry out simulations ranging from cellular level to organ.
 - Evaluation of the ability of multi-electrode systems to differentiate between anatomical and functional reentries.
3. To analyse the factors affecting the accuracy of a multi-electrode system (basket catheter) when mapping reentries in the atria.

1.3 Structure of the Thesis

This thesis is structured in the following chapters:

Chapter 1. Introduction: In this chapter we expose the motivation to develop this research work, the objectives of this PhD thesis and the structure of the document.

Chapter 2. State of the art: This chapter is a review that reflects the state of the art in the different disciplines that are involved in this work. First of all, the anatomy and electrophysiology of the heart are detailed. Then, cardiac arrhythmias and the systems to map them are summarized in this chapter. And finally, a background concerning computational models and the methods employed in the literature to perform cardiac simulations are explained.

Chapter 3. Three-Dimensional Multiscale Atria-Torso Model: In this chapter the methods developed to perform and validate atrial electrical simulations ranging from cell level to organ are described, followed by the methods to compute the EGM inside the atria. Lastly, the importance of having the atria immersed into a torso model in order to compute the intracavitary EGMs is evaluated.

Chapter 4. Mapping Reentries in a Sheet of Atrial Tissue by Using Multi-electrode Arrays: In this chapter we describe, in first place, the methods developed to generate and map the reentrant electrical activity in a sheet of atrial tissue. In second place, we report and discuss the results obtained regarding the accuracy of the mapping systems and their ability to differentiate functional from anatomical reentries.

Chapter 5. Mapping Reentries in a 3D Human Atrial Model by Using a Basket Catheter: In this chapter the methods used to generate and map electrical reentrant activity in the atria are described. In addition, results of the evaluation of factors affecting the basket accuracy when mapping complex atrial activation containing reentries are reported and discussed.

Chapter 6. Limitations: The potential limitations of this PhD thesis are listed in this chapter.

Chapter 7. Conclusions: The main conclusions of this work are listed in detail in this chapter, and also the fulfilment degree of the objectives established in Section 1.2 is analysed.

Chapter 8. Future Research Work: In this chapter some guides for future work to overcome the limitations of this PhD thesis and to extract the maximum profit from it are provided.

Chapter 9. Contributions: Finally, the main scientific contributions derived from the work developed in this dissertation are listed in this chapter. The scientific framework in which this work has been involved is also described, including national and international collaborations and related research projects.

CHAPTER 2

State of the Art

2.1 The Heart

2.1.1 Structure of the Heart

The heart is the main organ of the circulatory system. It is located in the middle of the thoracic cavity, between the lungs, and surrounded by a membrane called pericardium. It is composed of four chambers, two upper called atria and two lower called ventricles. The atrioventricular valves connect atria and ventricles: tricuspid valve (TV) connects right atrium (RA) and right ventricle (RV), and mitral valve (MV) connects left atrium (LA) and left ventricle (LV). The atria are separated by a wall or interatrial septum, and the ventricles by the interventricular septum. Both partitions are continuous with each other and form the medial septum, a muscular-membrane wall which separates the heart chambers in two right and two left chambers. Accordingly, the heart can be considered two separate pulsatile pumps. The right heart collects, through the vena cava, the deoxygenated blood from the organism into the RA. Then, the blood goes into the RV, which contracts and pump it through the pulmonary artery into the lungs to perform gas exchange. Afterwards, the left heart collects oxygenated blood from the lungs into the LA through the pulmonary veins (PV), to the LV by pressure difference, and pumps it through the aorta artery into the peripheral organs³³⁻³⁵ (Figure 2.1).

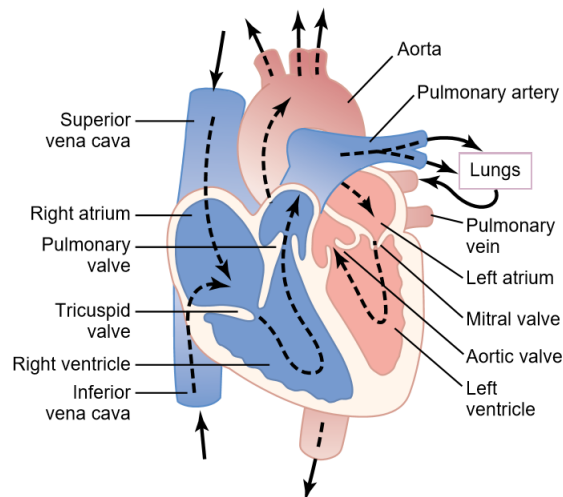


Figure 2.1: Structure of the heart, and course of blood flow through the heart chambers and heart valves.³³

2.1.1.1 Atrial Anatomy

The atrial anatomy has rigorously been studied over the years. Numerous experimental studies describe all the anatomical structures comprising the atria, among others the right and left atrial appendage (RAA and LAA), the crista terminalis (CT), the pectinate muscles (PM), the muscle fibers, the coronary sinus (CS), the fossa ovalis (FO), the Bachmann's bundle (BB) and both atrioventricular (AV) valves, TV and MV.³⁶⁻⁴⁰ Although both atria differ in their shape, they consist of the same structures supported by the atrial body: a venous component, an appendage and the atrioventricular valve, together with the septum and the adjacent walls between the chambers.^{36,39} Figure 2.2 depicts different views from the atria with the main structures.

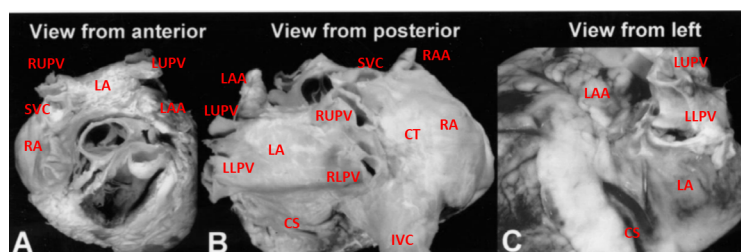


Figure 2.2: Anterior (A), posterior (B) and left (C) views of the atria (modified from Ho et al³⁷). RUPV/RLPV/LUPV/LLPV: right upper/right lower/left upper/left lower pulmonary vein; SVC/IVC: superior/inferior vena cava; RA/LA: right/left atrium; RAA/LAA: right/left atrial appendage; CS: coronary sinus; CT: crista terminalis.

The RA is a muscular sack composed of the RAA, the intercaval area, the septum and the vestibule. The RAA has a triangular shape and is located anterior and laterally. Along the intercaval area is located the CT, which is a prominent muscle on the internal surface which separates the PM from the smooth walls of the venous area, and can be seen along the lateral wall. The CT is the largest and strongest muscular bundle in the RA. PM spread from the CT throughout the entire wall of the RAA and reach the lateral and inferior walls (see Figure 2.3, left). Near the CT is located the sinoatrial node (SAN), natural pacemaker of the heart, close to the cavoatrial junction. The atrial septum, which separates RA and LA, consists mainly of the flap valve of the FO. The vestibule in the RA surrounds the TV orifice. The venous region in the RA comprises the SVC, IVC and CS. The CS drains the cardiac venous blood into the RA but also has an important relationship to the LA, since there are muscular connections between the wall of the LA and the CS.^{36,37,39} The thickness of the RA wall is not uniform due to the CT and the PM. However, experimental measures differ among studies: Wang et al³⁶ described the wall thickness between 5 and 8 mm in the thickest region and 2 mm in the thinnest one, while Zhao et al¹⁹ affirmed the maximum wall thickness was 11.7 mm and

the minimum 0.4 mm, with a mean value throughout the RA of 4.2 mm.

Similarly to the RA, the LA consists of a venous region, comprising the PV, a vestibule surrounding the MV orifice and an appendage with a tubular shape (LAA). Besides, the LA shares the septum with the RA and is connected to it through the BB, FO and CS. Nevertheless, the BB is the most significant electrical interatrial connection due to its proximity to the CT and therefore, to the SAN. The BB is the main bundle in the LA and extends from the right of the orifice of the SVC and crosses the vessel and the anterior wall of the LA until it reaches the LAA, where it divides into upper and lower branches (see dashed yellow lines in Figure 2.3, right).^{36,37,39} The body of the LA is more obvious than the body of the RA and also the LA thickness is more uniform (data reported by Wang et al³⁶ provide a wall thickness between 3 and 5 mm, while data reported by Zhao et al¹⁹ gives a wall thickness among 1.1 and 8.6 mm, with a mean value of 3.7 mm). In Figure 2.4 is depicted a schematic representation of the main structures in the atria, together with the fibers orientation.

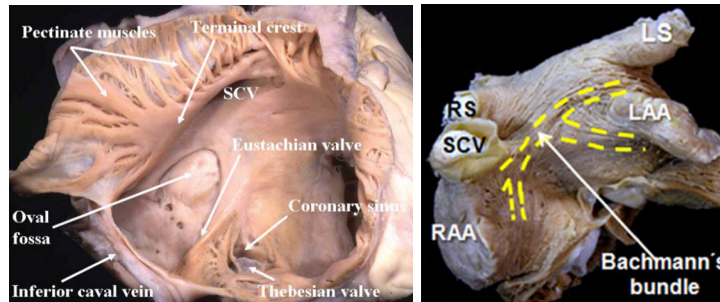


Figure 2.3: Anatomy of the atria. Endocardial face of the RA³⁹ (left) and location of the Bachmann's bundle on the epicardial face of the LA⁴¹ (right). SCV: superior caval vein; RS/LS: right superior/left superior pulmonary vein; RAA/LAA: right/left atrial appendage.

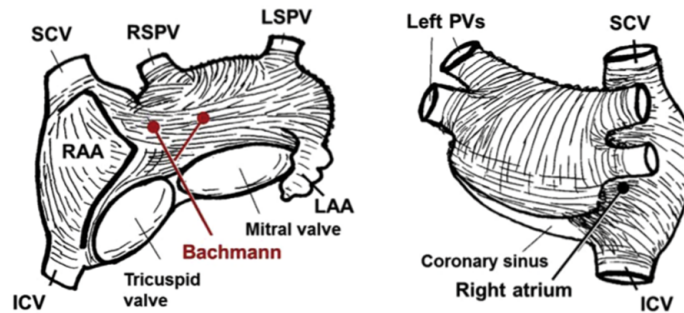


Figure 2.4: Schematic representation of the atrial structures and fibers orientation.⁴² SCV/ICV: superior/inferior caval vein; RAA/LAA: right/left atrial appendage; RSPV/LSPV: right/left superior pulmonary vein; PVs: pulmonary veins.

2.1.1.2 Position of the Heart in the Torso

The vital organs of the human body, except for the brain, are contained in the torso. The viscera in the thoracic cavity are protected by the thoracic cage, also named rib cage. This cage is longitudinally limited by the vertebral column on his posterior face and by the sternum on the upper and anterior side, and transversally by twelve pair of ribs that surround the torso. The sternum is located almost parallel to the vertebral column. The twelve pairs of ribs are independently placed on both sides of the trunk.⁴³ As shown in Figure 2.5, the heart is located in the middle of the thoracic cavity.

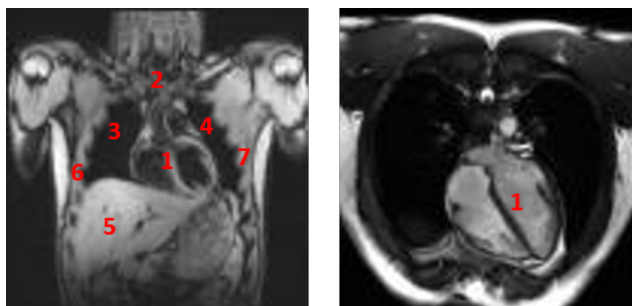


Figure 2.5: Position of the heart in the torso (left: coronal plane; right: transverse plane). 1: heart; 2: sternum; 3-4: lungs; 5: liver; 6-7: ribs. Images modified from <https://medicine.uiowa.edu/mri/facility-resources/scanner-images>.

The anatomical dimensions of the thoracic cage and the organs placed inside have been previously collected in a doctoral thesis developed in our research group,⁴⁴ and are shown in Table (2.1).

Region	Size (cm)
Shoulder breadth	39.90 - 50.50 ⁴⁵
Abdomen circumference	70.70 - 110.40 ⁴⁵
Averaged torso breadth	26.35 - 28.61 ⁴⁶
Shoulder depth	17.70 - 25.30 ⁴⁵
Waist depth	17.70 - 26.90 ⁴⁵
Averaged torso depth	13.27 - 16.27 ⁴⁶
Diaphragm height	20.46 - 26.12 ⁴⁶
Lung height	25.00 ⁴⁷
Lung posteroanterior diameter	16.00 ⁴⁷
Lung base transverse diameter	10.00 (right) - 7.00 (left) ⁴⁷
Spine length	56.94 ⁴⁸
Sternum length	29.36 - 36.54 ⁴⁹
Sternum angle	158.97 - 173.73 ⁴⁹
Rib angle	49.15 - 62.75 ⁵⁰
Liver diameter	9.40 - 21.30 ^{51,52}

Table 2.1: Anatomical dimensions of thoracic cage and organs.⁴⁴

2.1.2 Electrophysiology of the Heart

The heart behaves as a biomechanical pump. On the one hand, the cardiac cells are excitable, generate and propagate electrical impulses, and on the other hand, they contract as a response to them. The generated and transmitted electrical impulse that governs cardiac contraction is called action potential (AP).³⁴

The heart is mainly composed of three types of cells: working, nodal and conduction cells. In addition, other elements can be found in the heart, such as fibroblasts, proteins (collagen, elastin, connexin) or cardiac stem cells. The atrial and ventricular muscle, comprised of working cells, is striated and contracts similarly to skeletal muscle, although the duration of contraction is much longer. It includes myofibrils containing actin and myosin filaments, which are responsible for contraction. On the contrary, the nodal (SAN and AV node) and conduction (Purkinje system) cells contain few contractile fibrils and therefore contract slightly. However, they exhibit automatic rhythmical electrical impulses, which excite the cardiac cells, providing an excitatory system that controls the rhythmical beating of the heart.^{33,35}

The muscle fibres comprising the cardiac muscle consist of many individual cells, connected in series and in parallel with one another. The cell membranes that separate individual cardiac muscle cells are called intercalated discs. These discs yield a much lower resistance than the resistance of the membrane of the muscle fiber due to the fusion of the membranes of the individual cells, which form permeable unions called gap junctions. The gap junctions allow almost totally free diffusion of ions. Thereby, ions move easily in the intracellular fluid along the longitudinal axes of the cardiac muscle fibers, and as a consequence, the electrical impulse also propagates easily from one cell to the next through the intercalated discs. Summing up, cardiac muscle can be considered a syncytium of many heart muscle cells and the heart can be considered composed of two syncytia: the atrial syncytium and the ventricular syncytium. Accordingly, the atria contract before the ventricles, which is important for effectiveness of heart pumping.^{33,34}

2.1.2.1 Electrical Conduction System

Regarding its electrical properties, the heart is considered an autonomous organ since it starts its own beat. Among the regions containing pacemaker cells which exhibit intrinsic rhythmical excitation, we find the cells in the SAN, the AV node and the Purkinje fibers. However, the natural pacemaker of the heart in physiological conditions is the SAN due to the fact that the myocytes in this region have the shortest period of spontaneous electrical activity initiation, and therefore they control the heart rate (HR). Accordingly, each heartbeat originates in the SAN, where APs are generated

at a rate of approximately 70-80 beats per minute (bpm) in physiological conditions. Then, the AP spreads from cell to cell throughout the atria, first in the RA and then into the LA, mainly through the BB, causing their contraction. Later, AP propagates towards the AV node, where cells are similar to the cells in the SAN, but their excitation rate is slower (40-60 bpm). In accordance, they don't excite spontaneously under physiological conditions as they are excited through the propagation of the APs coming from the neighbouring cells, which is initiated by the SAN at its excitation rate. Only in case of pathological conditions, if the propagation through the atria is too slow or interrupted, or the initiation of the impulse in the SAN fails, the cells in the AV node will behave as a pacemaker and will spontaneously excite, in order to propagate the impulse to the ventricles. The AV node is not only responsible for the electrical connection between atria and ventricles, but also for normal conduction delays between atrial and ventricular contractions, since the conduction velocity (CV) in the AV node is slower than in the atria and it delays the impulse propagation. These delays optimize the atrial pump activity and protect the ventricles from too early stimulation, also assuring a sequential contraction (first of the atria and then of the ventricles) and an optimal blood pumping in the ventricles. Later, the electrical impulse is reconducted from the AV node through the His bundle and then the Purkinje system ramification in order to reach the ventricles and cause their synchronized contraction. The excitation arrives first to the endocardial surface of the ventricles and then propagates towards the epicardial surface. Only in case of lack of stimuli coming from neighbouring cells, the cells in the Purkinje fibers auto-excite at a rate between 15-40 bpm.^{33-35, 53}

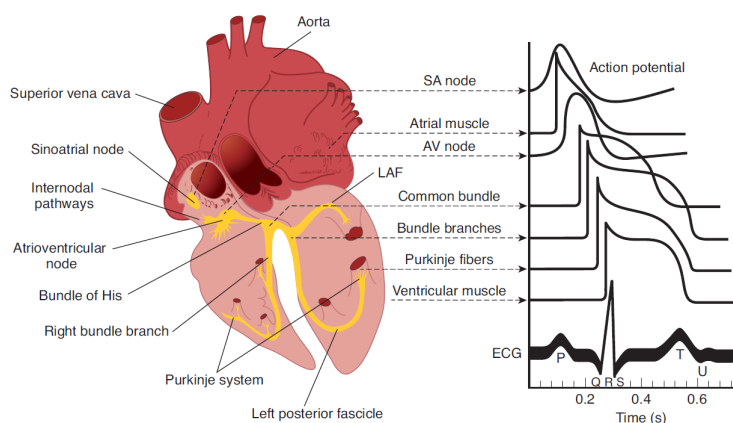


Figure 2.6: Electrical conduction system of the heart, action potentials corresponding to each type of cardiac cell and its relation to the electrocardiogram.⁵⁴

Figure 2.6 shows a simplified representation of the electrical conduction

system of the heart with the APs corresponding to each type of cardiac cell. The superposition of all the APs corresponding to the cells of the whole heart yields an electrical signal known as electrocardiogram (ECG), which can be registered on the body surface and it will be explained in detail in Section 2.1.2.3.

2.1.2.2 Action Potential

Cardiomyocytes morphology is cylindrical, with a length ranging between 50-150 μm and a diameter of about 10-20 μm , depending on the region of the heart³⁵ (see Figure 2.7). They have a semipermeable cellular membrane which separates the intracellular and extracellular space and allows ionic fluxes between them. The cell membrane has a thickness of about 5-7 nm. It consists of a lipid bilayer and some proteins which form the ion channels, pumps and exchangers embedded into it, which allow the active and passive ionic exchange between both spaces (Figure 2.8), generating a difference in the ionic concentrations at both sides of the membrane and yielding as a result an electrical potential called transmembrane potential (V_m).^{33,54}

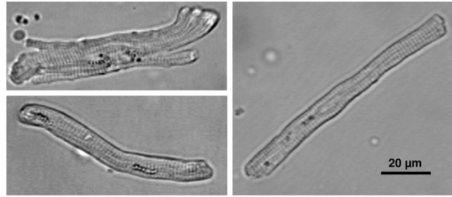


Figure 2.7: Atrial myocytes (modified from⁵⁵).

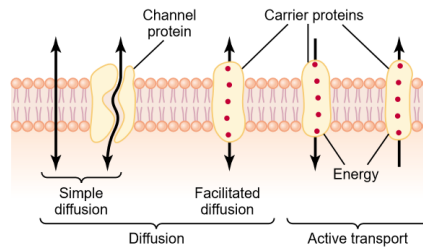


Figure 2.8: Ionic exchange through the cell membrane.³³

V_m is described by Equation 2.1. In rest, the electrical potential of the intracellular space (ϕ_i) is lower than the extracellular potential (ϕ_e). Therefore, V_m is set to negative values (resting potential). The excitation of the cardiomyocytes causes a rapid variation of its V_m . If the stimulus which excites the cell is below a threshold value, the V_m returns to its resting value after the stimulus ends, but if it is above the threshold, an AP is generated: the cell membrane depolarizes and V_m increases from the resting value

(approximately -80 mV for atrial myocytes⁵⁶) to a value above zero, remains around this value for a certain interval and then returns to the resting value after the membrane repolarizes.³⁵

$$V_m = \phi_i - \phi_e \quad (2.1)$$

Figure 2.9 depicts the AP phases of an atrial myocyte, which are described below, as well as the main fluxes of ions affecting in each phase:^{33,34,54}

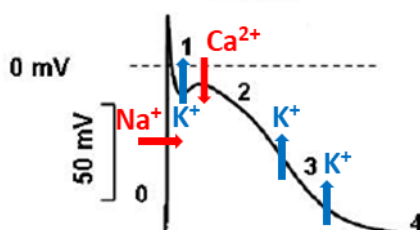


Figure 2.9: Atrial action potential and main ionic fluxes during its phases.

- **Phase 0. Depolarization:** The initial upstroke is mainly generated by the inward flux of Na^+ ions due to the quick opening of the corresponding ion channels when an external stimulus is applied. Cardiac cells, polarized in rest, depolarize because the intracellular potential increases with the inward flux of ions and V_m reaches the zero value (intracellular and extracellular potentials are equal). These Na^+ channels immediately close, generating the fast Na^+ current, I_{Na} .
- **Phase 1. Initial fast repolarization:** The decrease in the V_m is caused by the inactivation of Na^+ channels and the activation of transient outward K^+ currents (I_{to}) that try to return the cell to its resting state.
- **Phase 2. Plateau:** Inward Ca^{2+} ion flux creates slow Ca^{2+} currents that compensate the outward K^+ currents I_{Kr} (rapid delayed rectifier current) and I_{Ks} (slow delayed rectifier current), and therefore slow down the decrease in the potential. The activation is slower for Ca^{2+} channels than for Na^+ channels. Thereby, they affect mainly in this phase, although they start their activation in phase 0.
- **Phase 3. Repolarization:** Ca^{2+} channels begin to close while I_{K1} (inward rectifier K^+ current) starts acting until the cell recovers its initial resting state.
- **Phase 4. Resting potential:** During this phase, the cell remains at its resting state when there is no external stimulation. The cell is again

polarized due to the activity of the NaK pump and the I_{K1} channels remain also slightly activated.

As shown in Figure 2.6, APs differ depending on the part of the conduction system of the heart where myocytes belong. However, there also might be differences in the same region. Several studies carried out in humans and other animal species demonstrate the existence of different AP morphologies depending on the anatomical region in the ventricles (base, apex, epicardium, endocardium...) ^{57,58} and the atria (CT, PM, LA, PV...) ^{56,59-64}. An example of experimentally observed atrial electrical heterogeneity is shown in Figure 2.10.



Figure 2.10: Electrical heterogeneity in the atria registered in experimental measurements in dogs reported by Feng et al ⁶⁰ (A) and Cha et al ⁶² (B). CT: crista terminalis; APG: appendage; PM: pectinate muscles; AVR: atrio-ventricular ring; LA: left atrium; PV: pulmonary vein.

2.1.2.3 Electrocardiogram and Electrogram

The electrical potential propagates from the heart to the rest of the torso, which can be considered as a conductive volume. This electrical potential, named extracellular potential, can be recorded in order to analyse the electrical activity of the heart. If the registration of the extracellular potentials is carried out on the body surface, we obtain the electrocardiogram (ECG), while if it is registered inside the heart cavities, the resultant signal is called electrogram (EGM).

The ECG, the recording of the electrical activity of the heart on the body surface, is the result of the APs generated throughout the whole heart, as shown in Figure 2.6. It reflects the depolarization and repolarization of the cardiac cells. Figure 2.11 depicts in detail the generation of the ECG and its waves. P-wave corresponds to the depolarization of the atria, before their contraction, while the QRS complex corresponds to the depolarization of the ventricles. The QRS complex consists of the Q-, R- and S-waves. T-wave reflects the repolarization of the ventricles, and therefore their relaxation. The repolarization of the atria is masked by the QRS complex since the ventricular muscle is thicker than the atrial muscle. As a consequence, the superposition

of the ventricular APs provides a QRS complex of higher amplitude than the wave corresponding to the atrial repolarization.^{33,54}

In physiological conditions, the atrial depolarization and conduction through the AV node is ranged between 0.12 and 0.20 s, and it is measured from the beginning of the P-wave to the beginning of the QRS complex (PR interval). However, the ventricular depolarization and atrial repolarization (QRS duration) is approximately 0.10 s.⁵⁴

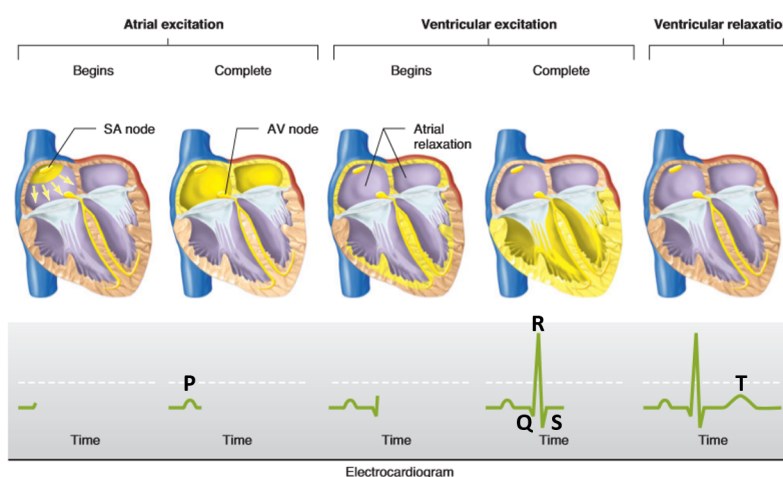


Figure 2.11: Generation of the waves in the electrocardiogram. After the SAN excitation, atrial depolarization begins and, as a result, P-wave appears in the ECG. Once all the atrial myocytes are depolarized and the stimulus reaches the AV node (P-wave is complete), the atrial repolarization starts at the same time than the ventricular depolarization. Therefore, in the ECG we can see the QRS complex, regarding the ventricular depolarization, but not the atrial repolarization, which is masked by the QRS complex. After the ventricles are completely depolarized, the repolarization starts and T-wave is detected in the ECG. Yellow color denote the depolarized regions (modified from⁵⁴).

2.1.2.3.1 Electrocardiographic Leads

The ECG may be an unipolar or a bipolar recording. In the first case, it is recorded between an active electrode and a reference electrode, and in the second case, it is recorded by using two active electrodes. Depolarization moving towards an active electrode in a volume conductor produces a positive deflection, whereas depolarization moving in the opposite direction produces a negative deflection.

Nowadays, the standard ECG consists of 12 leads: the three standard limb leads, the three augmented limb leads and the six precordial leads (see Figure 2.12). The first standard leads in electrocardiography were the three bipolar

limb leads (I, II and III) used by Einthoven in the first half on XXth century.⁶⁵ They record the differences in potential between two limbs. The electrodes are set at the right arm, left arm and left leg, forming the Einthoven's triangle, and provide information about the propagation of the electrical activity of the heart in the frontal plane. In lead I, the positive terminal of the electrocardiograph is connected to the left arm and the negative to the right arm. In lead II, the electrodes are on the right arm and left leg, with the leg being positive. Finally, in lead III the electrodes are on the left arm and left leg, with the leg being positive (see Figure 2.12). The Einthoven's law affirms that at any given instant, the potential in lead II is equal to the sum of the potentials in leads I and III.^{33,54}

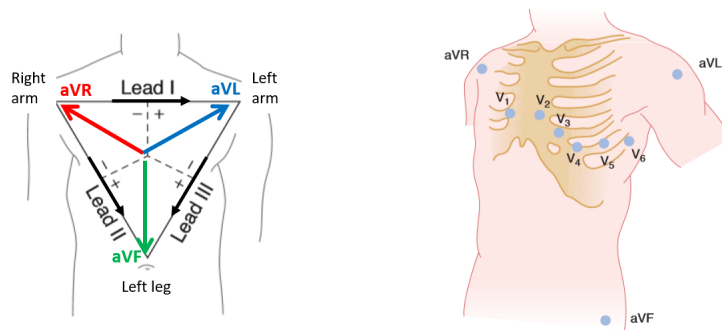


Figure 2.12: 12 standard ECG leads. Standard bipolar limb leads I, II and III (left); unipolar augmented limb leads aVR, aVL and aVF (left and right); and unipolar precordial leads V1-V6 (right). Modified from.⁵⁴

The three augmented limb leads are unipolar, and the active electrodes are set at the right arm (aVR), left arm (aVL) and left foot (aVF). They are recordings of the difference of potential between one limb and the combination of other two limbs, and provide higher amplitudes compared to the standard limb leads. They also yield the propagation of the electrical activity of the heart in the frontal plane (Figure 2.12).^{33,54}

The precordial leads are six unipolar leads (V1-V6) which provide information about the propagation of the electrical activity of the heart in the transverse plane (see Figure 2.12). Each of the six electrodes is connected to the positive terminal of the electrocardiograph, while the negative one is connected to the central terminal of Wilson, whose potential value is zero.⁶⁶ Figure 2.12 (right) shows the electrode placement described below:^{33,54}

- V1: fourth intercostal space, on the right border of the sternum.
- V2: fourth intercostal space, on the left border of the sternum.
- V3: midpoint between V2 and V4.

- V4: fifth left intercostal space, in the middle clavicular area.
- V5: fifth left intercostal space, anterior axillary line.
- V6: fifth left intercostal space, in the middle axillary line.

Due to their proximity to the heart, each of the precordial leads mainly records the activity of a particular heart region.

2.1.2.3.2 Intracavitary Recordings and Mapping Systems

The electrical activity of the heart can be recorded inside the atrial or ventricular chambers, yielding as a result the EGM (see Figure 2.13). These intracavitary signals are recorded by using measurement electrodes attached to catheters, which are inserted by physicians into the femoral vein, guided under fluoroscopy towards the RA (through the IVC), and if needed, positioned into the LA after puncture of the septum.⁶⁷

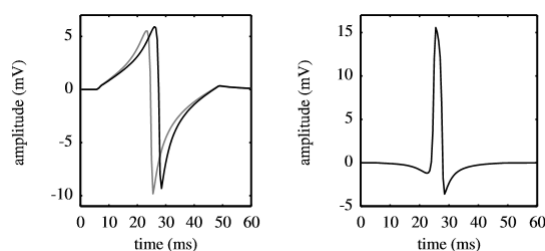


Figure 2.13: Intracardiac EGMs. Unipolar EGMs from locations at the endocardium 3 mm distant from each other (left) and bipolar EGM resulting from the difference of the unipolar EGMs (right).⁶⁸

Similarly to the ECG, the intracavitary recordings can also be unipolar or bipolar. Unipolar EGMs are measured between an electrode positioned at the endocardial surface and a reference electrode ideally placed at infinity (in the practice, at the body surface or the central terminal of Wilson). When the wavefront approximates to the measuring electrode, creates a positive potential (R-wave of the unipolar EGM); when the wavefront is exactly reaching the electrode, it forms a negative deflection associated with the local activation time; and finally, when the wavefront moves away from the electrode, a negative S-wave results (see Figure 2.14A). The main drawback of the unipolar EGMs is the fact that in addition to local activation, they also contain far field contributions. Unlike unipolar EGMs, bipolar recordings are measured by two electrodes near the endocardium, separated a distance of few millimeters, using the same reference. This configuration cancels most of the far field contributions but also limits the field of view to the local electrical activity in the vicinity of the electrodes. Moreover, the interpretation of

bipolar EGMs is more complicated because they are strongly susceptible to changes in morphology and amplitude depending on catheter orientation with respect to the direction of wavefront propagation on the endocardium. This is a consequence of the difference in electrical potentials between distal and proximal electrodes (see Figure 2.14B).⁶⁸⁻⁷⁰

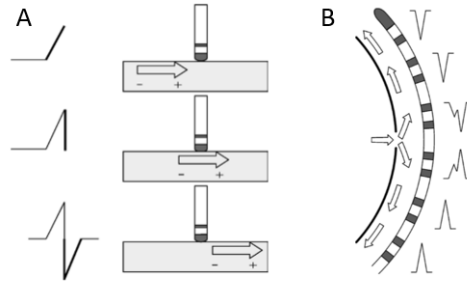


Figure 2.14: Generation of unipolar and bipolar EGMs. A) Unipolar EGMs: when the wavefront approximates to the measuring electrode, a positive wave is formed while when it moves away, a negative wave is formed. When the wavefront reaches the electrode, a deflection appears on the EGM (it indicates the local activation time). B) Bipolar EGMs: polarity reverses at the breakthrough point of the wavefront. In case of bipolar EGMs, the maximum absolute peak indicates the local activation time (modified from⁷⁰).

Nowadays, in the clinical practice there is a need to acquire multiple intracardiac recordings simultaneously in order to reduce the duration of the procedures and exposition to fluoroscopy, as well as to map the electrical activity of a full chamber. Accordingly, numerous commercial multi-electrode systems have appeared lately. In Figure 2.15 are shown some of them:

- AdvisorTM FL Circular Mapping Catheter (St. Jude Medical/Abbott): 10 poles catheter, with 15 mm of loop diameter (3 mm electrode spacing) or 20 mm of loop diameter (5 mm electrode spacing).
- PentaRayNAV[®] Eco catheter (Biosense Webster): 20 poles catheter (2, 4 or 6 mm electrode spacing) to map atrial tachycardias, ventricular tachycardias and complex fractionated EGMs in AF.
- DecaNAV[®] catheter (Biosense Webster): 10 poles catheter (2 and 8 mm electrode spacing) designed for multi-electrode mapping of the LV and RA. It facilitates access to complex anatomy areas difficult to reach.
- ORBITER[®] PV Variable Loop Mapping Catheter (Boston Scientific): 14 poles (5 mm electrode spacing) catheter with an adjustable diameter. It is capable to reach challenging anatomy.

- Constellation[®] Full Contact Mapping Catheter (Boston Scientific): 64 poles basket catheter, which provides full RA and LA maps in a single beat to diagnose complex atrial arrhythmias. Several sizes are available, ranging from 31 mm of diameter (2 mm electrode spacing) to 75 mm of diameter (7 mm electrode spacing).
- INTELLAMAP ORION[®] Mapping Catheter (Boston Scientific): 64 poles basket catheter (2.5 mm electrode spacing). It provides a variable diameter ranging from 3 to 22 mm, which allows its use in different anatomical structures.
- LassoNAV[®] Eco catheter (Biosense Webster): 10 or 20 poles catheter for targeted AF therapy, as for example to validate PV isolation. It also allows pacing from any electrode and sample multiple points of cardiac mapping data simultaneously for reduced procedure and fluoroscopy time.

Among the mapping catheters described before, basket catheters allow to map the electrical activity of a whole chamber in just one beat (they provide a wider field of view), in comparison with the rest of systems, which only are able to map a part of it. Therefore, despite their low spatial resolution, basket catheters would detect rotors missed by other multi-electrode arrays (with better spatial resolution) in the unmapped regions.⁷¹ This is the reason why basket catheters became so popular lately, although their accuracy when mapping the electrical activity remains still controversial and there is a need of further studies to analyse them systematically.

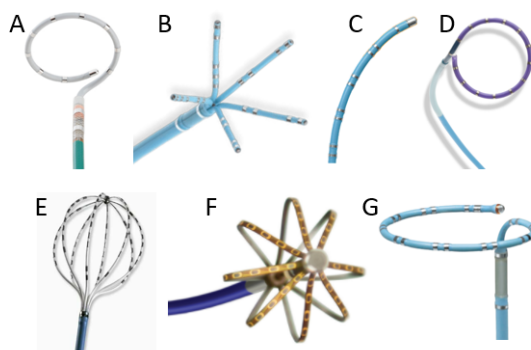


Figure 2.15: Commercial mapping systems. A) Advisor[™] FL Circular Mapping Catheter. B) PentaRayNAV[®] Eco catheter. C) DecaNAV[®] catheter. D) ORBITER[®] PV Variable Loop Mapping Catheter. E) Constellation[®] Full Contact Mapping Catheter. F) INTELLAMAP ORIO[®] Mapping Catheter. G) LassoNAV[®] Eco catheter.

The multi-electrode mapping catheters described previously are used

together with 3D mapping and navigation systems in the electrophysiology procedures. These systems, like RHYTHMIA HDx™ Mapping System (Boston Scientific), CARTO® 3 System (Biosense Webster) or EnSite NavX™ (St. Jude Medical/Abbott), among others, allow the generation of the cardiac chamber models and display on them information such as the activation times or voltage maps. They also permit the real-time visualization of the intracardiac catheters and the acquired patient signals (ECG and intracavitary EGM) on the screen. Figure 2.16 illustrates the screen of the RHYTHMIA HDx™ Mapping System during an atrial procedure.

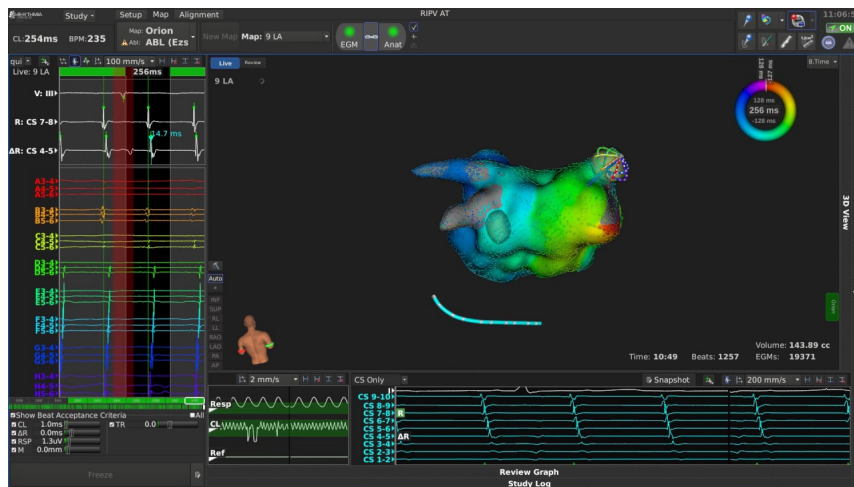


Figure 2.16: Console of the RHYTHMIA HDx™ Mapping System during an atrial procedure. A basket catheter is observed in the atrial chambers.

2.2 Cardiac Arrhythmias

Cardiac arrhythmias are defined as an abnormal electrical activity in the heart, in which the rhythm of the heartbeat may be too fast or too slow, regular or irregular.¹ Among all the possible cardiac arrhythmias, focal atrial tachycardia (AT) and AF are the ones of interest for this PhD thesis, so they are described in the following sections.

2.2.1 Premature Atrial Contractions

An extrasystole is a premature contraction of the heart, i.e. the heart contracts before than expected. It is also called premature or ectopic beat and can be isolated or multiple. Most of them result from ectopic foci in the heart. In case of the premature atrial contractions (PACs), the P-wave appears too soon in the ECG (see Figure 2.17). The PR interval might shorten, indicating that

the heart beat originates due to an ectopic foci near the AV node. Therefore, the stimulus needs less time to reach the ventricles. Besides, after the atrial premature contraction there is a compensatory pause, which means that the next contraction of the heart delays as a consequence of the impulse travelling from the ectopic foci through the muscle to discharge the SAN. Accordingly, as the SAN excites late in the premature beat, next stimulus originated in the SAN and propagated throughout the atria will be also delayed.³³ PACs are common in healthy people, however at high percentages they can be a predictor of atrial arrhythmias and stroke.⁷²⁻⁷⁵ If the ectopic foci excitation repeatedly occurs, it becomes the pacemaker of the heart and can trigger a tachycardia or a fibrillation. AT and AF might be both paroxysmal, which means that they would begin suddenly, last for a short period of time (minutes, hours or a few days) and then also suddenly stop.³³

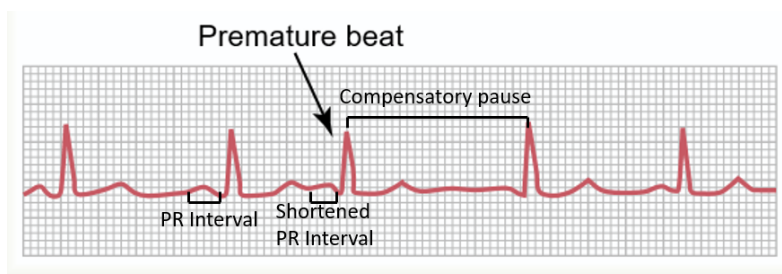


Figure 2.17: ECG recording of a premature atrial contraction (lead I). PR interval shortens and there is a compensatory pause after the premature beat (modified from³³).

2.2.2 Focal Atrial Tachycardia

A focal AT is a supraventricular tachyarrhythmia characterized by a fast atrial activation, initiated by an automatic, triggered or reentrant mechanism.⁷⁶ Focal ATs can have single or multiple foci. In the first case, it is usually characterized by regular and organized atrial activity with HR ranging between 100 and 250 bpm.⁷⁷ P-wave morphology will change with respect to physiological conditions, depending on the position of the foci throughout the atria, as shown in Figure 2.18A.⁷⁸ However, in case of the multifocal AT, besides a change in the P-wave morphology with respect to physiological conditions, the morphology will change from one beat to another (at least 3 different P-wave morphologies, as shown in Figure 2.18B), depending on the position of the different foci in the atria. It is also characterized by irregular rhythm and several patterns of atrial activation (HR higher than 100 bpm).^{78,79} Focal ATs usually appear throughout certain anatomic regions, like the CT, TVR and CS in the RA, or PVs and MVR in the LA, among others.⁸⁰

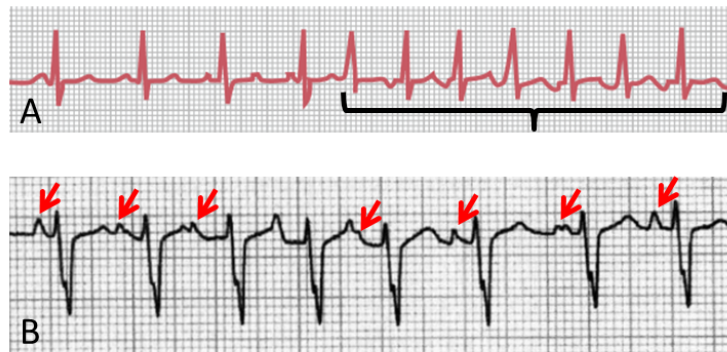


Figure 2.18: ECG recordings during atrial tachycardia. A) Paroxysmal focal AT (lead I): sudden increase of the HR to about 150 bpm, P-wave superimposed onto the T-wave with inversion of its morphology, indicating that the ectopic foci is not near the SAN (modified from³³). B) Multifocal AT (lead II): different P-wave morphologies, some of them partially or completely superimposed onto the T-wave, and irregular rhythm (modified from⁸¹).

2.2.3 Atrial Fibrillation

AF is a supraventricular tachyarrhythmia characterized by uncoordinated atrial activation, which provokes a deficient mechanical contraction of the atria and therefore, a deficient atrial function.⁸² During AF, the disorganized electrical waves (see Figure 2.19A) cause the irregular contraction of both atria at rates higher than 300 bpm, usually ranging from 400 to 600 bpm.⁸³ Due to their high rates and desynchronized activation, the atria are not able to contract properly and they do not pump blood. As blood flows passively through the atria into the ventricles, ventricular pumping also becomes inefficient (only up to 30%). However, unlike ventricular fibrillation, AF is not lethal and a person can live months or even years with AF, although it increases the risk of suffering diseases like heart failure and stroke.^{4, 33, 54} AF is frequently caused by the enlargement of the atria, as a consequence of heart valve lesions or ventricular failure. Under this scenario, atrial walls are dilated and provide a long conductive pathway along with slow conduction.³³

AF can be diagnosed on an ECG recording due to two main changes (see Figure 2.19B). On the one hand, the disorganized waves spreading throughout the atria can be of opposite polarity and it is common that most of them annihilate each other, so P-waves are not longer recognizable and f-waves could appear. On the other hand, HR is irregular because atrial impulses get the AV node at a fast and irregular rate, so ventricles are also irregularly excited (irregular RR segments). QRS complexes are normal unless ventricles have a disorder in the conduction. Often, due to the fibrillatory impulses in



Figure 2.19: Disorganized activation of the atria and ECG recording during atrial fibrillation. A) Depolarization waves propagate simultaneously in different directions throughout the atrial muscle. B) Episode of AF recorded at lead I:³³ irregular rhythm and lack of P-waves. SAN: sino-atrial node; AVN: atrio-ventricular node.

the atria, ventricles are also driven at fast HR (125-150 bpm).^{33, 54, 84}

Nowadays, mechanisms initiating and maintaining AF are still not well understood and theories to explain them remain controversial. At the early 20th century, AF was considered for first time as the disease we know today. Mackenzie⁸⁵ observed the lack of the A-wave in the jugular venous pulse in a patient with irregular rhythm by using a polygraph. In 1909, Lewis⁸⁶ established that AF was the cause of the irregular pulse. Some years later, in 1962, Moe⁸⁷ suggested one of the most supported theories regarding AF, based on the chaotic coexistence of multiple reentrant waves that spread and collide throughout the excitable atrial tissue. They fragment and annihilate, so they constantly generate new circuits of self-perpetuation and block a normal propagation of the wavefront. This hypothesis was supported for many years and was also experimentally demonstrated.⁸⁸ Later, Jalife proposed the mother rotor theory,⁸⁹ in which AF seems an organized process with uninterrupted periodic activity of discrete reentrant sites, instead of a chaotic and disorganized process like in the Moe's multiple wavelets hypothesis. In the mother rotor theory, activity is maintained by shorter reentrant circuits acting as dominant frequency (DF) sources and wavefronts emanating from these sources propagate and interact with anatomic and functional obstacles in the atria, leading to its fragmentation and wavelet generation. Rotors have been experimentally observed in animal hearts by using optical mapping, as published in studies carried out by Jalife's research group.^{14, 15} Recently, rotors have also been observed in humans, as reported by Narayan,²⁰ but in this case they remain stable, unlike the meandering rotors proposed by Jalife. Simultaneously to the mother rotor theory, Haïssaguerre et al⁸ postulated the focal theory, in which they affirmed that AF is spontaneously initiated and maintained by ectopic beats originating in the PVs. At present, AF is considered to be initiated and maintained by a combination of all these theories (see Figure 2.20). Focal activity might be a trigger to initiate an AF or, together with a vulnerable substrate, could initiate and maintain AF. After a certain period of time, AF initially maintained by ectopic activity or a single-circuit reentry might induce remodelling and as a consequence, the

heterogeneous shortening of the atrial refractoriness also may lead to a multiple-circuit reentry, which itself could become the maintenance mechanism.⁹⁰ Summing up, triggers are responsible for AF initiation, substrate is necessary for maintenance and perpetuators are needed for the progression of AF from paroxysmal to persistent forms. Electrical remodelling appears within the first few days of AF and manifest as shortening of the atrial refractoriness and slower CV. Ion channels variations have also been described in animal models and humans under electrical remodelling, and in addition, persistent forms of AF usually lead to structural remodelling.⁹¹

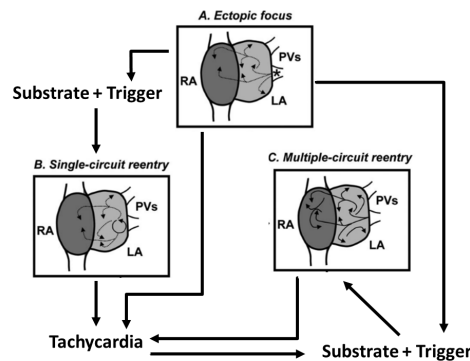


Figure 2.20: Principal mechanisms underlying AF (modified from⁹⁰). Focal activity (A) may lead to tachycardia or, in presence of a vulnerable substrate, to AF (B or C). At the first stages, AF is usually initiated by the focal activity or single-circuit reentry (B), and after inducing remodelling by itself, it could be maintained by multiple-circuit reentry (C). RA/LA: right/left atrium; PVs: pulmonary veins.

Depending on its duration and progression, AF is classified in the following categories:^{4,84,91}

- First-diagnosed: any AF that has not been diagnosed before, regardless of the duration.
- Paroxysmal: self-terminating AF, in most cases within 48 h, although some episodes can last up to 7 days. Paroxysmal AF (pAF) episodes are triggered often by extrasystoles in the PV (focal AF).⁸ It could also be asymptomatic (silent AF).
- Persistent: it lasts longer than 7 days and less than 1 year (early persistent AF if lasts less than 3 months). Besides extrasystoles, is highly dependent on the underlying substrate.
- Long-standing persistent: it lasts longer than 1 year and the outcomes to treatment (drugs therapy, electrical cardioversion or ablation) are worse

than in the previous types. This type of AF is dependent on the substrate and perpetuation factors.

- Permanent: it is always present and there is no intention of recovering the SR. If a rhythm control strategy is adopted, it should be reclassified as long-standing persistent AF.

Chronic AF (cAF) is also a term commonly used,^{92–96} although it has variable definitions and therefore this term is not included in the classification.⁹¹ However, it usually refers to long-standing forms of AF.⁹⁷ In this PhD thesis, the term cAF will also refer to long-standing forms of AF.

2.2.3.1 Paroxysmal Atrial Fibrillation

Experimental studies suggest that the remodelling present in the LA and RA is different under pAF conditions. In fact, sources triggering AF tend to appear mostly in the LA. As a consequence, it has been observed a left-to-right gradient of frequency, with the highest frequencies appearing in the LA.^{30, 98–101}

Sarmast et al¹⁰¹ studied, in isolated sheep hearts, the hypothesis that myocytes are more sensitive to acetylcholine (ACh) in the LA than in the RA and, therefore, there is a left-to-right frequency gradient under pAF conditions. They found out that DFs increased in both atria with an increase of ACh concentration. However, LA frequency predominated at all concentrations and rotors were more often in the LA. They also demonstrated that the acetylcholine activated inward rectifier K^+ current (I_{KAC_h}) density was greater in LA than RA sheep myocytes. Later, Voigt et al⁹⁸ demonstrated, by measuring I_{KAC_h} and the inward rectifier K^+ current (I_{K1}) in human cardiomyocytes from RAA and LAA, that pAF patients had inward rectifier current densities 2-fold larger in LA than in RA, yielding a left-to-right gradient that contributes to the existence of high frequencies in the LA and the maintenance of pAF. They also found that the right-to-left gradient of I_{KAC_h} observed in control conditions disappeared in pAF.

2.2.3.2 Chronic Atrial Fibrillation

Similarly to pAF conditions, experimental studies suggest that electrical remodelling is also different in the LA and RA under cAF conditions. However, the electrical remodelling existent after a long period of time under fibrillating conditions seems to be stronger in both atria. Therefore, a larger number of ionic channels are involved and the shortening of the AP duration (APD) is larger in cAF than in pAF (62% vs 15%), as shown in Figure 2.21.

In Table 2.2 a summary of the most relevant and frequent changes experimentally observed in cAF conditions is shown. On the one hand, there are studies that demonstrated the presence of electrical remodelling in cAF with

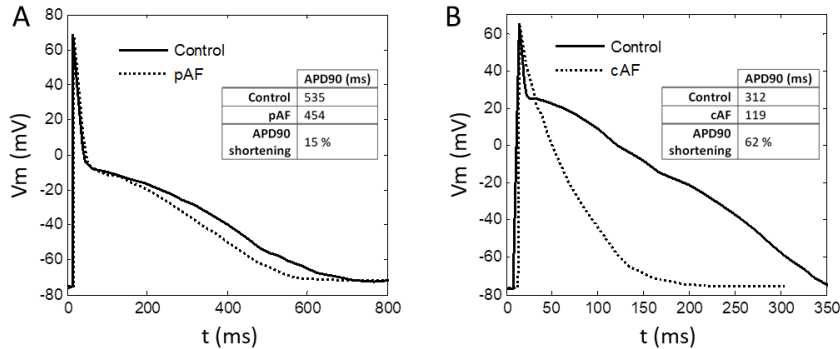


Figure 2.21: APs in control and remodelling, recorded at a stimulation frequency of 0.5 Hz. A) APs digitalized from Voigt et al.¹⁰² in pAF there is a slight APD reduction with respect to control conditions (15%). B) APs digitalized from Bosch et al.⁹⁴ the APD reduction in cAF is much stronger than in pAF (62%).

respect to SR conditions, through the variations observed in the ionic channels current and/or their protein expression. After the isolation of cardiomyocytes from the RAA, a decrease in the I_{to} ,^{93,94,103} L-type inward Ca^{2+} current (I_{CaL}),^{93,94,104,105} I_{KACH} ^{106,107} (Bosch et al.⁹⁴ provided a controversial measurement) and ultrarapid delayed rectifier K^+ current (I_{Kur})¹⁰³ was observed, whereas I_{K1} presented an increase.^{93,94,106,107} On the other hand, there are studies which, in addition to the remodelling in cAF compared to SR conditions, analysed the differences among the remodelling suffered by the RA and LA. Voigt et al.⁹⁸ found out in cAF patients that despite registering greater basal inward rectifier currents compared to SR, there were no significant LA-RA differences and I_{K1} and I_{KACH} were similar in the RA and LA (I_{KACH} was greater in the RA in SR, but it suffered a decrease in cAF). Caballero et al.⁹² were also interested in describing the electrical remodelling under cAF conditions, so they took cardiomyocytes from the RAA and LAA in humans and observed a decrease in I_{to} and I_{Kur} as well as an increase in I_{Ks} in both atria for cAF compared to SR, with differences among RA and LA. Van Wagoner et al.¹⁰⁸ demonstrated with isolated cardiomyocytes from RAA and LAA that outward K^+ currents I_{to} and I_{Kur} were reduced in cAF with respect to SR conditions in both atria, while I_{K1} increased only in the LA.

Under AF conditions, the electrical remodelling is usually accompanied by structural remodelling. Atrial fibrosis provides the structural substrate for AF maintenance and it is associated with worse outcomes in the ablation procedures (lower efficacy associated to extensive fibrosis).^{109,110} However, the variability of fibrosis among patients with AF is high and there are no significant differences in the extent of fibrosis among patients with pAF and cAF.⁹⁶

	cAF: LA	cAF: RA	Literature
I_{to}	-61% -78%	-70% -66% -44% -60/-65% -44%	Bosch et al ⁹⁴ Van Wagoner et al ¹⁰⁸ Caballero et al ⁹² Workman et al ⁹³ Brandt et al ¹⁰³
I_{CaL}		-70% -63% -60/-65% -72%	Bosch et al ⁹⁴ Van Wagoner et al ¹⁰⁴ Workman et al ⁹³ Skasa et al ¹⁰⁵
I_{K1}	+106% +100%	+100% +0% +100% +73% +100% +75%	Dobrev et al ¹⁰⁶ Van Wagoner et al ¹⁰⁸ Voigt et al ⁹⁸ Dobrev et al ¹⁰⁷ Bosch et al ⁹⁴ Workman et al ⁹³
I_{KACH}	0%	-47/-50% -x% -54% +45%	Dobrev et al ¹⁰⁶ Voigt et al ⁹⁸ Dobrev et al ¹⁰⁷ Bosch et al ⁹⁴
I_{Kur}	-53% -45%	-44% -60% -55%	Van Wagoner et al ¹⁰⁸ Caballero et al ⁹² Brandt et al ¹⁰³
I_{Ks}	+85%	+166%	Caballero et al ⁹²

Table 2.2: Electrical remodelling experimentally observed in cAF. Variation of different ionic currents (I_{to} , I_{CaL} , I_{K1} , I_{KACH} , I_{Kur} and I_{Ks}) reported in the literature. x represents the reduction of the I_{KACH} observed by Voigt et al⁹⁸ in the RA in cAF, yielding as a result the same density of current than in the LA.

2.3 Modelling the Heart Electrical Activity

Computational models of the heart were developed in order to improve understanding of cardiac electrophysiology and arrhythmias. They perfectly complement experimental approaches since they allow us to test hypothesis difficult to bring to experimental procedures. Among others, they permit to compare different types of ablation in the same patient (ablation is not reversible and only through computational simulations you can perform each type of ablation for first time),^{19,111} to test the effect of several drugs,¹¹² or to map the electrical activity of the heart by artificially isolating different factors that might affect.¹⁹ However, mathematical models emulating the electrical behaviour of the heart are not only a set of equations. They need to be developed according to experimental observations and then, they have to be validated.³⁴ The evolution of technology and computers science has allowed to develop, on the one hand, techniques such as patch or voltage clamp to get the experimental data needed, and, on the other hand, complex numerical methods to accurately and efficiently solve the complex systems of equations

in the mathematical models. In addition, computers have now high computational and storage capacity.¹¹³ Therefore, nowadays, the electrical activity of the heart can be multiscale modelled not only for the forward but also for the inverse problem in electrocardiography. The forward problem tries to determine the potentials distribution on the body surface from a known source in the heart,¹¹⁴ while in the inverse problem, the aim is to predict the cardiac activity based on the potentials recorded on the body surface.¹¹⁵


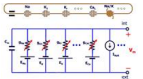
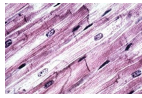
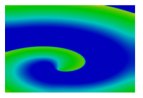

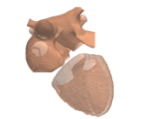
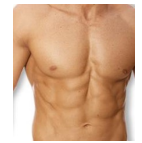
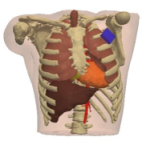
Scale	Biology	Model
Cellular		
Tissue		
Organ		
Body		

Table 2.3: Multiscale modelling. At cellular level, models simulate the electrical activity of isolated cells; at tissular or organ level, models also incorporate the electrical interaction between cells; and at body level, models simulate the propagation of the electrical signals from the heart throughout the torso.

As shown in Table 2.3, the electrical activity of the heart can be multiscale modelled from cellular level to body surface. At cellular level, a model simulates the electrical activity of the isolated cells (flux of currents through the ionic channels in the cellular membrane and the resultant V_m). However, at tissular or organ level, models also need to account for the electrical interaction between cells, which yields the spreading of the APs throughout the myocardium. It also becomes necessary to assign a cellular ionic model of an isolated cell to each node in a geometrical mesh corresponding to a tissue or organ. Finally, at body level, there are torso models which propagate the electrical signals generated by the heart and permit their registration at both, the cardiac cavities and the torso surface.³⁴ Once the electrical activity of the heart has been modelled and simulated, and the signals inside the atrial cavities (EGM) or on the body surface (ECG) have been obtained, they can be processed in order

to characterize propagation patterns corresponding to normal or pathological conditions. These patterns are useful to help physicians to study, diagnose and even treat patients suffering several arrhythmias.

The first model in simulating the electrical behaviour of the cellular membrane and the flux of ionic currents through it was formulated by Hodgkin and Huxley more than 50 years ago.¹¹⁶ They used a squid axon to study the excitation and conduction in neurons and to develop a mathematical model comprising a set of non-linear differential equations that approximates the electrical characteristics of excitable cells. They considered the cellular membrane to be comprised of ionic channels (proteins embedded into the membrane) whose gates allow or block the flux of ions, yielding as a result an electrical current flowing through them. Their model still remains the basis for many modern neuronal and cardiac AP models. Some years later, in 1960, Noble¹¹⁷ developed the first model of cardiac AP based on Hodgkin and Huxley's work. However, this field of research did not boom until techniques such as voltage¹¹⁸ or patch¹¹⁹ clamp were improved and allowed to measure the current generated by each type of ions flowing through the membrane in isolated cardiac cells. Since then until today, numerous cardiac computational models have been developed. Although at the beginning most of them were focused on the ventricular electrophysiology, recently the interest in atrial models has increased. Among the applications of atrial models, AF remains the most common and the number of publications related to AF has increased exponentially,¹²⁰ as shown in Figure 2.22.

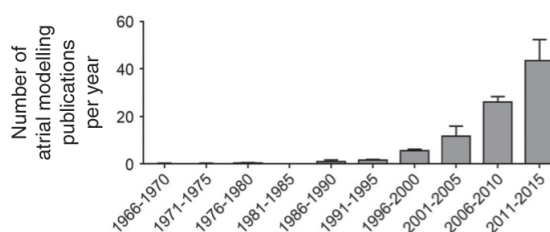


Figure 2.22: Number of publications related to computational analysis of AF.¹²⁰ There has been an exponential growth since the second half of the 20th century.

2.3.1 Cellular Atrial Models

Experimental data obtained from human atrial myocytes have not been always available. For this reason, first computational models were based on experimental data from animals. In 1987, Hilgemann and Noble¹²¹ developed a rabbit atrial cardiomyocyte model that reconstructed extracellular calcium transients and typical AP changes during steady-state and non-steady-state stimulation. It provided a better understanding of electrical activity, contracti-

le function and trans-sarcolemmal calcium movements. Some years later, Lindblad et al¹²² improved this rabbit atrial myocyte model and added several ionic currents in order to analyse the ionic basis of the atrial AP. This model formulation was based on cellular voltage clamp data and provided information about the intracellular Ca^{2+} concentration transient during the AP and the interactions between the membrane currents involved in the repolarization. Rasmusson et al¹²³ developed an atrial model, based on voltage clamp measurements obtained from isolated atrial bullfrog cells, that showed that AP characteristics change depending on the presence or absence of certain ionic currents. Other animal species such as dog or mouse have also been used to model the atrial electrical activity.^{124–126}

In 1998, when human atrial electrophysiological data were available, two different human atrial models appeared.^{127,128} Nygren et al¹²⁷ developed an accurate model to predict electrophysiological responses of the human atrial cell, mainly the role of the K^+ currents in the repolarization phase of the AP, excitability, refractoriness and channel blocking drugs. Similarly to Nygren et al, Courtemanche et al¹²⁸ developed a model (hereinafter, called CRN model) to investigate the mechanisms of AP rate dependence, the changes in AP morphology in the presence of pharmaceutical blockers of the I_{CaL} and the $\text{Na}^+/\text{Ca}^{2+}$ exchanger, and the variability in experimentally observed AP morphology. Both models approach ion channels through Hodgkin and Huxley formulation and include the atrial current I_{Kur} . However, although they were partially based on the same human atrial experimental data, they yield very different AP morphologies (see Figure 2.23A) and rate dependence. Besides, while the CRN model includes the Luo and Rudy calcium description,¹²⁹ the Nygren et al model is based on the calcium handling from Lindblad et al.¹²² Some of the differences might be due to the inclusion of formulations based on data from animal species as well as the choices made during model generation. As a consequence of all their differences, both models have different properties and, therefore, reentrant activity generation in tissue and organ level simulations is also different. But despite their differences, both models have been frequently used for single cell as well as multicellular simulation studies for years.^{130–132}

Recently, Maleckar et al¹³³ published an improved version of the Nygren model regarding excitability and repolarization. It incorporates new available experimental data and I_{to} and I_{Kur} were re-formulated. However, similarly to Nygren and CRN models, this new model was developed without detailed information about the Ca^{2+} handling in human atrial cardiomyocytes. Other newer models, such as Koivumäki et al¹³⁴ (based on the Nygren et al model) and Grandi et al,¹³⁵ are focused on the simulation of the Ca^{2+} handling in human atrial cardiomyocytes. These two models account for the importance of the interactions between Na^+ and Ca^{2+} , as well as their role in rate dependent

APD changes. The main five human atrial myocyte models and their electrophysiological properties have been meticulously compared.¹³⁰ In Figure 2.23A the APs are depicted and in Figure 2.23B a schematic representation of the modelled human atrial cardiomyocyte is shown, highlighting the differences among these five models. On the one hand, one of the most relevant differences presented in this study is the fact that in the Maleckar, Koivumäki and Grandi models, the AP reaches the steady state in the first minutes of the simulation, whereas the CRN and Nygren models do not reach it within the first 20 minutes of the simulation. On the other hand, rotor generation in a sheet of atrial tissue under control conditions was impossible for the CRN and Grandi models, while rotors with DFs between 3 and 4 Hz appeared for the Nygren, Maleckar and Koivumäki models. Under cAF conditions, every model yielded rotors, with highest DFs for the CRN and Grandi models (around 8 Hz compared to 6-7 Hz for the Nygren, Maleckar and Koivumäki models).

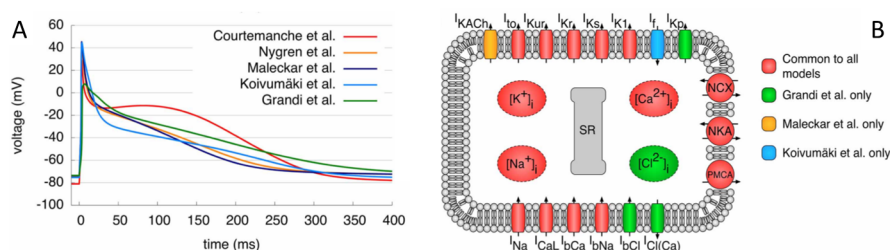


Figure 2.23: Comparison of the five most relevant human atrial myocyte models (modified from¹³⁰). A) APs after pacing for 50s with a BCL of 1s. B) Schematic of the cell membrane including the different modelled ionic currents and intracellular ion concentrations.

In this PhD thesis we use the CRN model to simulate the human atrial electrical activity because of its simplicity and low computational cost compared to newer models with a more detailed Ca^{2+} handling.^{134,135} Thus, in Section 2.3.1.1 we describe the CRN model in more detail.

2.3.1.1 CRN Model

The CRN model yields the state of a virtual atrial cardiomyocyte at each time step of a simulation. State variables account for the dynamic quantities changing over time and are represented by a system of non-linear ordinary differential equations. Computed changes in the cardiomyocyte state are used to update the current state vector, which is also used for the computation of the individual ion currents and intracellular ion fluxes. Finally, ion currents and intracellular ion fluxes are used to calculate the state variables, so the intracellular ion concentrations and V_m are updated.¹²⁰ In the CRN model, the cellular membrane is modelled as a capacitance connected in parallel with

variable resistances and voltage sources representing the ionic channels, and current sources corresponding to pumps and exchangers (see Figure 2.24, top). The time derivative of the V_m is described by Equation 2.2:

$$\frac{dV_m}{dt} = \frac{-(I_{ion} + I_{st})}{C_m} \quad (2.2)$$

C_m is the total membrane capacitance (100 pF) and I_{ion} and I_{st} are the total ionic current and stimulus current, respectively, flowing across the cell membrane.

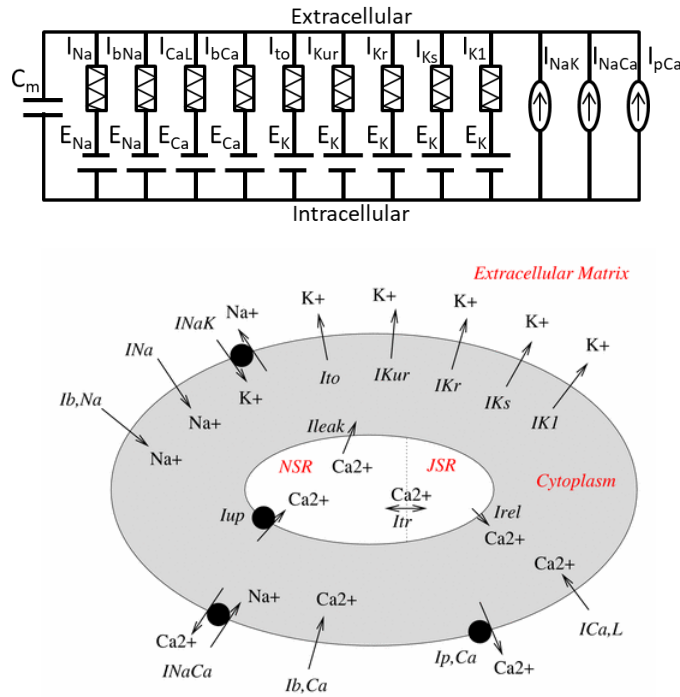


Figure 2.24: Cell in the CRN model. Electrical circuit equivalent to the cell membrane (top) and schematic representation of the currents, pumps, and exchangers included in the model (bottom¹²⁸).

The total ionic current is composed of all the currents flowing through the membrane, as defined in Equation 2.3:

$$I_{ion} = I_{Na} + I_{K1} + I_{to} + I_{Kur} + I_{Kr} + I_{Ks} + I_{CaL} + I_{pCa} + I_{NaK} + I_{NaCa} + I_{bNa} + I_{bCa} \quad (2.3)$$

where I_{pCa} is the sarcoplasmic Ca^{2+} pump current, I_{NaK} is the Na^+ - K^+ pump current, I_{NaCa} is the Na^+ / Ca^{2+} exchanger current, I_{bNa} is the background Na^+ current and I_{bCa} is the background Ca^{2+} current. For further information regarding the currents formulation as well as the equations of intracellular ion concentrations ($[Ca^{2+}]_i$, $[Na^+]_i$, $[K^+]_i$) or any other equation in the model, see the Appendix A.

Ion currents are characterized by three elements: a fixed conductance, the dynamic open probability and the driving force or difference between V_m and the equilibrium potential of permeant ions.¹³⁶ The ion channel open probability can be approached by three different formulations. For ion channels with fast kinetics, open probabilities can be treated as instantaneous, which mathematically means that they are time-independent functions of V_m or any other state variable, for instance, I_{K1} in the CRN model. For other channels, the kinetics properties such as activation or inactivation can be approached by the Hodgkin and Huxley formulation or by using Markov models. In the first case, each single state variable changes based on activation and inactivation rates, which depend on the V_m or other state variable in the model. In the second case, ion channels are represented by a number of states. Each Hodgkin and Huxley formulation has an equivalent Markov formulation.¹³⁷ The CRN model follows the Hodgkin and Huxley approach for currents whose open probabilities cannot be treated as instantaneous, as for example the I_{Na} current, which contains gating variables m , h and j . Gates allow or block the flux of ions depending on different factors such as V_m , time, pH, ion concentrations... If a gate is open, ions (Na^+ , Ca^{2+} or K^+) flow through the channel in the membrane because of the diffusion forces (concentration gradients between both sides of the membrane) or by electric field.

In addition, the CRN model includes the following intracellular compartments: myoplasm, sarcoplasmic reticulum release compartment (or junctional sarcoplasmic reticulum, JSR) and sarcoplasmic reticulum uptake compartment (or network sarcoplasmic reticulum, NSR), as shown in Figure 2.24 (bottom). However, no extracellular cleft spaces are included, i.e. extracellular ion concentrations are fixed.

2.3.2 3D Atria and Torso Models

The study of the cardiac electrophysiology through computational models is not only focused on isolated cells, but also on the whole atrial anatomy and even the influence of the human torso on the propagation of the electrical potential from the atria to the torso surface and inner the atrial cavities. Therefore, in a first phase, atrial cellular models can be anatomically and electrically coupled in order to simulate the AP propagation in a layer of atrial tissue or in the whole atrial anatomy. Then, the electrical heart-torso coupling

allows the propagation of the potential throughout the torso. And finally, the outcome is the registration of the electrical potential on the torso surface (ECG) and inside the atria (EGM). For this purpose, atrial and torso geometrical meshes are needed.

Geometrical meshes are usually constructed from the segmentation of organs in medical images (magnetic resonance imaging, computed tomography scans or ultrasounds).^{138–140} The segmentation can be manual, automatic or most commonly a combination of both techniques.¹³⁸ Once the mesh is built, it is usual to refine it to achieve a better spatial resolution in the domain in which the problem is going to be solved. Elements in the geometrical mesh are comprised of nodes (their vertices) and the value of a magnitude in an element is usually obtained by linear interpolation of the values in their nodes. In 3D meshes, the most commonly used elements are tetrahedrons and hexahedrons.³⁴ Once the geometrical model is constructed, in case of cardiac models, where there is an active propagation, an electrical cellular model should be assigned to each node comprising the mesh to solve the system of differential equations and to obtain the electrical propagation in the myocardium. Nowadays, the tendency in the field of cardiac electrophysiology modelling is the patient-specific approach, i.e. to develop specific models in order to help physicians to personalize the diagnosis and treatment for any patient (see Figure 2.25). In this case, models reflect the anatomy and pathologies of each patient.^{140, 141}

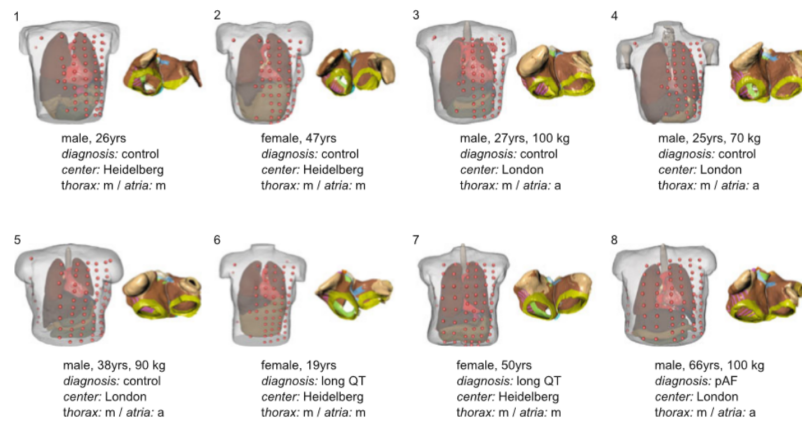


Figure 2.25: Patient-specific atrial and torso models (from¹³⁸).

2.3.2.1 3D Atrial Models

Over the last years, atrial electrophysiology modelling has been trending towards the development of realistic 3D atrial models. However, there are still studies carried out in tissue models. For instance, Pandit et al¹⁴² provided

novel insights into the ionic bases of a sustained rotor in a cAF substrate through simulations in a two-dimensional (2D) homogeneous and isotropic atrial tissue. Sánchez et al¹⁴³ reported a systematic characterization of the importance of transmembrane ionic currents in modulating the electrophysiological properties and reentrant activity in 2D simulations of human atrial isotropic and homogeneous tissue. Aguilar et al¹⁴⁴ used 2D simulations to study the rate-dependent role of I_{Kur} and the effect of blocking it on the atrial AP. Keller et al¹⁴⁵ used a 3D isotropic planar patch of myocardium to establish a model for acute ablation lesions in order to study the changes in the EGMs during radio-frequency ablation procedures. Meanwhile, several 3D atrial models have been developed in order to carry out different studies in the atria. In 2000, Harrild and Henriquez¹⁴⁶ developed one of the first anatomically detailed 3D geometrical human atrial models, by incorporating both atria, their major muscle bundles (CT, PM, limbus of the FO (LFO) and BB) as anisotropic structures with fiber directions aligned with the bundle axes, and different regional conductivities to give realistic local CV. They coupled the electrical unicellular model proposed by Nygren et al¹²⁷ to simulate the propagation of the APs. As a result, they provided a realistic 3D atrial model to perform *in silico* investigations of macroscopic atrial conduction under normal and abnormal conditions. This model has been the basis of more recently developed models.¹⁴⁷⁻¹⁴⁹ In 2010 Ruiz-Villa¹⁴⁷ and Tobón¹⁵⁰ developed, in this research group, an anatomically realistic 3D atrial model based on the atrial surfaces of the Harrild and Henriquez model. This new model improved the anatomy and the electrophysiology proposed by Harrild and Henriquez and was one of the first models in including realistic fiber orientation. It was comprised of the main anatomical structures (LA, RA, twenty PM in the RA free wall, the FO in the septum with its limbus, BB, CT, LAA, RAA, LPV, RPV, SCV, ICV, the isthmus of RA, TVR, MVR and CS) and reproduced the atrial electrophysiological heterogeneity through variations of the Nygren et al model.¹²⁷ It was developed and validated to study the vulnerability to reentries in the atria¹⁴⁷ as well as the efficiency of radio-frequency ablation procedures to finish atrial arrhythmias.¹⁵⁰ This 3D atrial model was published by Tobón et al¹⁵¹ and has been improved some years later in the framework of a recent PhD thesis,⁴⁴ with a mesh of higher spatial resolution comprised of regular elements (voxels instead of hexahedrons) and more accurate electrophysiological heterogeneity.

Among the models which were not based on Harrild and Henriquez's work, there is one developed by Vigmond et al¹⁵² in 2001. Although it is anatomically simpler, this 3D atrial model incorporates electrical connections between RA and LA, fiber orientation, CT, PM and AV valves, and it was built to study the role of specific anatomic structures on reentry induction and maintenance. In 2006, Seemann et al¹⁵³ developed a 3D atrial model incorporating main anatomical structures (geometry extracted from the visible

female dataset), electrophysiological heterogeneity added through variations of the CRN model,¹²⁸ and anisotropic conduction. In 2012, Deng et al¹⁵⁴ developed a detailed 3D atrial model to study biatrial conduction via different pathways during SR. Simultaneously, in this research group, a whole heart model anatomically detailed was developed, which incorporates fiber orientation as well as atrial and ventricular conduction systems.¹³⁹

Lately, several groups carried out studies with patient-specific models. In Dössel's group, Krüger et al^{138,141} developed the methods for the personalization of models of atrial anatomy, electrophysiology and excitation conduction to study atrial repolarization in normal and AF conditions. Trayanova's research group is also focused in patient-specific models. For instance, Zahid et al¹⁵⁵ built 20 patient-specific atrial models to test the hypothesis that AF reentrant drivers only persist in regions with specific fibrosis patterns; Deng et al¹⁵⁶ used fibrotic atrial computational models to predict optimal ablation targets in patients with persistent AF; and Boyle et al¹⁵⁷ used them to study the termination of reentrant AT via optogenetic stimulation.

2.3.2.2 3D Torso Models

In nature, unlike in models, the heart is not isolated but immersed in the torso, surrounded by organs presenting different conductivities. This is one of the reasons why torso models became necessary to analyse the effect of torso inhomogeneities in the ECG and EGM recordings, as well as to more faithfully reproduce reality.¹¹⁴ Therefore, many studies are focused on the correlation between the electrical activity of the heart and the ECG or the body surface potential maps (BSPM) after its propagation through the torso.^{44,114,141,158} BSPM yield the distribution of electrical potentials on the body surface along time, providing more information than the standard 12-leads ECG. In this sense, computational torso models are a useful tool for a first approach. Nevertheless, it is important to enhance that BSPM might attenuate, distort and smooth the actual activity of the heart. In fact, some of the events appearing in the heart could be not recognizable on the torso surface.¹¹⁵

First torso models did not reproduce with fidelity the anatomical and electrical properties of tissues and organs. In 1980, Rudy and Plonsey¹⁵⁹ developed a spherical model comprised of a spherical heart eccentrically placed in a spherical torso (lung region bounded by muscle and fat layers). Even recently, studies such as the one published by Rodrigo et al¹⁶⁰ modelled heart and torso through spheres (see Figure 2.26). Buist and Pullan worked on 2D slices of torso and took benefit from the strengths of two of the most popular methods to solve the problem, the finite elements method (FEM) and the boundary elements method (BEM), by applying them in the appropriate region of the torso. They studied the effect of torso impedance on epicardial

and body surface potentials.¹¹⁴ However, the vast majority of models tend to be increasingly realistic and anatomically detailed.

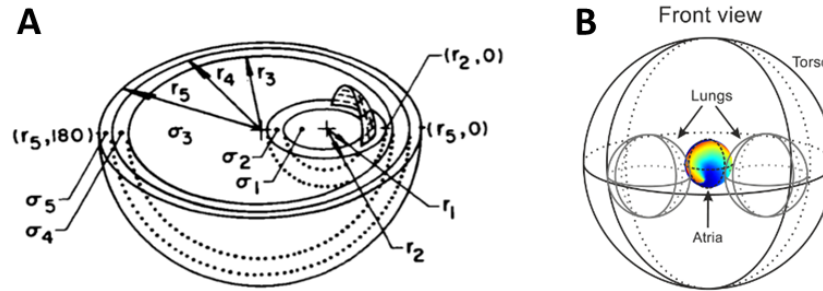


Figure 2.26: Spherical torso models. Models proposed by Rudy and Plonsey¹⁵⁹ (A) and Rodrigo et al¹⁶⁰ (B).

In 1991, MacLeod et al¹⁶¹ built one of the most detailed human torso models. It included tissue heterogeneities accounting for skin, muscles, bones, blood vessels and fat, as well as specific conductivity values from organs. They constructed it based on magnetic resonance images. First of all, they digitized the images, then interpolated the resulting points and automatically generated triangulated surfaces, and finally tetrahedralized volumes. They presented several variations of the model with different spatial resolutions between nodes, ranging from 5.31 mm (high resolution model) to 9.85 mm. These models allowed the calculations for the forward and inverse problem in electrophysiology, and yielded solutions using both methods, FEM and BEM, as well as provided a 3D framework to display the results: potential maps on the epicardium and the body surface. Ferrer et al¹⁴⁸ developed an anatomically detailed 3D torso model based on the dataset from the online open repository provided by the Centre for Integrative Biomedical Computing (CBIC) from the University of Utah, i.e. the MacLeod et al torso model,¹⁶¹ and adapted it to their 3D atrial model. Ferrer et al used this torso model to establish the relationship between atrial electrical signals and BSPM in SR conditions, differentiating each region of the atria,¹⁴⁸ and to localize ectopic beats in the atria through BSPM.¹⁶² Keller et al¹⁵⁸ developed a tetrahedron torso model based on the Visible Man dataset to solve the forward problem in cardiac electrophysiology, containing the following tissue types: myocardium, blood (both intracavitary and in the main vessels), lungs, fat (both visceral and subcutaneous), anisotropic skeletal muscle, intestine, liver, kidneys, bone, cartilage and spleen. They studied the influence of tissue conductivities on the ECG. Krüger et al approach was not only personalized for atrial models but also for torso models,^{138,141} which included the heart, cardiac blood, aorta, lungs, spine, stomach, intestines, liver and kidneys.

2.3.3 Numerical and Computational Methods

At tissue or organ scale, the propagation of the electrical activity of the heart has to be defined in terms of flux of currents between a cell and its neighbours, not only in terms of the behaviour of the ionic currents with respect to the V_m . Cardiac models describe the electrophysiology of one single cell with a system of ordinary differential equations (ODE) and the propagation of the stimuli throughout the tissue with a system of partial differential equations (PDE). Therefore, a reaction-diffusion equation is used, in which the reactive part refers to the ionic currents and the diffusive part accounts for the propagation to neighbouring cells. The mathematical formulation of the electrical activity of the heart has been described by the bidomain model,¹⁶³ in which the cardiac tissue is composed of two continuous domains (intracellular and extracellular) coexisting in the same space and with unequal anisotropy ratios. Furthermore, there is a need to discretize in time and space the domains in which the problem is going to be solved.¹⁶⁴

2.3.3.1 Bidomain Formalism

In the bidomain formulation, both the intracellular and extracellular domains behave as a volumetric conductor with different conductivities and potentials. Therefore, there is a flux of currents between them through the cell membrane governed by the Ohm's law, as follows:¹⁶⁴

$$J_i = -M_i \nabla \phi_i \quad (2.4)$$

$$J_e = -M_e \nabla \phi_e \quad (2.5)$$

where J_i and J_e are the intracellular and extracellular currents, and M_i and M_e correspond to the intracellular and extracellular conductivity tensors, respectively. Since the membrane behaves as a capacitor, and due to its thin thickness, the charge accumulated at one side is immediately compensated on the other side. As a consequence, there is no charge accumulated at any point belonging to the membrane (Equation 2.6) and the current flow at each point must be a balance between the incoming and the outgoing currents (Equations 2.7 and 2.8).

$$\frac{\partial}{\partial t}(q_i + q_e) = 0 \quad (2.6)$$

$$-\nabla J_i = \frac{\partial q_i}{\partial t} + \chi I_{ion} \quad (2.7)$$

$$-\nabla J_e = \frac{\partial q_e}{\partial t} - \chi I_{ion} \quad (2.8)$$

q_i and q_e are the charges in the intracellular and extracellular domains, and χ is the area of the membrane per unit volume. After combining Equations 2.6-2.8, we obtain the equation for the charge conservation (Equation 2.9), and replacing it in Equations 2.4 and 2.5, we deduce Equation 2.10:

$$\nabla J_i + \nabla J_e = 0 \quad (2.9)$$

$$\nabla(M_i \nabla \phi_i) + \nabla(M_e \nabla \phi_e) = 0 \quad (2.10)$$

On the other side, the charge at the membrane directly depends on V_m , as follows:

$$V_m = \frac{q}{\chi C_m} = \frac{q_i - q_e}{2\chi C_m} \quad (2.11)$$

After calculating the time derivative of Equation 2.11, in combination with Equation 2.6, we obtain:

$$\chi C_m \frac{\partial V_m}{\partial t} = \frac{\partial(q_i - q_e)}{2\partial t} = \frac{\partial q_i}{\partial t} = -\frac{\partial q_e}{\partial t} \quad (2.12)$$

By replacing Equation 2.12 and 2.7 in Equation 2.4, and combining it with Equation 2.13, the resultant Equation is 2.14:

$$D_i = \frac{M_i}{\chi} \quad (2.13)$$

$$\nabla(D_i \nabla \phi_i) = C_m \frac{\partial V_m}{\partial t} + I_{ion} \quad (2.14)$$

where D_i is the intracellular diffusion vector. Finally, if we remove the dependency with respect to ϕ_i in Equations 2.10 and 2.14 by combining them with Equation 2.1, we obtain the bidomain formulation presented by Tung (Equations 2.15 and 2.16):¹⁶⁵

$$\nabla(D_i \nabla V_m) + \nabla((D_i + D_e) \nabla \phi_e) = 0 \quad (2.15)$$

$$\nabla(D_i \nabla V_m) + \nabla(D_i \nabla \phi_e) = C_m \frac{\partial V_m}{\partial t} + I_{ion} \quad (2.16)$$

where D_e is the extracellular diffusion vector. Assuming that the heart is surrounded by a non-conductive medium, the normal component of the intracellular and extracellular currents must be equal to zero along the boundary. Therefore, the boundary conditions of the bidomain model are:

$$n(D_i \nabla V_m + D_e \nabla \phi_e) = 0 \quad (2.17)$$

$$n \nabla (D_e \nabla \phi_e) = 0 \quad (2.18)$$

where n is the normal component outward the heart domain. As described in this section, the bidomain formalism represents the electrical currents in the intracellular and extracellular spaces and allows the computation of the potential at each cell membrane (V_m), as well as the extracellular potentials at any point belonging to the domain (ϕ_e).

2.3.3.2 Monodomain Formalism

The bidomain model is numerically complex and computationally demanding, as it consists of a non-linear parabolic equation coupled with an elliptic equation, which is difficult to solve and analyse. Therefore, it is common to use a simplification when computing the V_m , known as the monodomain model, due to its lower numerical and computational complexity.^{164,166} In this approach, we assume, on the one hand, that variations in ϕ_e are negligible and therefore $V_m \approx \phi_i$; and on the other hand, that the effect of ϕ_e on V_m is also negligible and then it is possible to uncouple the equations of the bidomain model. As a consequence, we can consider that the conductivity tensor presents equal anisotropy ratios ($D_e = \lambda D_i$, being λ a scalar) and D_e can be removed from Equation 2.15, so it can be rewritten as follows:

$$\nabla(D_i \nabla \phi_e) = -\frac{\nabla(D_i \nabla V_m)}{1 + \lambda} \quad (2.19)$$

After combining Equation 2.19 with 2.16, and substituting D_i with Equation 2.20, we obtain the monodomain formulation (Equation 2.21). This parabolic PDE equation perfectly describes the reaction-diffusion phenomena produced in the cardiac tissue.

$$D = \frac{\lambda}{1 + \lambda} D_i \quad (2.20)$$

$$\nabla(D \nabla V_m) = \frac{C_m \partial V_m}{\partial t} + I_{Ion} \quad (2.21)$$

The boundary condition in the monodomain formalism is:

$$n\nabla(D\nabla V_m) = 0 \quad (2.22)$$

2.4 Phase Analysis

A signal can be characterized by three parameters: amplitude, frequency and phase. Among them, phase can be considered a useful descriptor to track the electrical progression of a myocardial region through signals such as AP, EGM or ECG.³²

Mainly, phase analysis has been applied to cardiac fibrillation and reentrant activity. This type of analysis in cardiac fibrillation was introduced for first time by Winfree in the 80s.¹⁶⁷ However, his methodology was valid only for equal periods of activation in the whole surface to map, which is not common during fibrillation. Later, Gray et al¹⁶⁸ introduced the spatio-temporal codification concept for non-linear dynamics, concretely applied to the phase analysis in cardiac fibrillation, which better reflects reality. Nowadays, in order to study the spatial distribution of the phase, a spatio-temporal codification of two variables is used. APs, EGMs or ECGs are treated as the output of a non-linear dynamic system characterized by a finite number of states. Thereby, we can obtain a phase trajectory in the space around a central point (attractor). Unfortunately, it is not always possible to have two different state variables of the system, mainly in experimental procedures. Therefore, another possibility is to reconstruct the attractor with only one variable, in case it is represented versus itself after applying to it a phase shift.^{32, 169, 170}

A drawback of the phase analysis might be the absence of the origin in the phase trajectories or a non-optimal phase shift. Therefore, there would be mistakes when analysing the phase singularities (PS). Some authors shifted the signal about the 25% of the cycle length.^{171, 172} Other authors preferred to choose the value that minimized the correlation function between the original variable and the shifted one in order to assure lineal independence among both.^{168, 173, 174} Finally, Bray et al¹⁷⁵ concluded that the representation of a variable versus its Hilbert Transform (HT) produced an optimal phase shift, which avoids mistakes in the analysis of the PS, being centred at the origin of the resultant phase trajectory.

Some of the terms commonly used in a phase analysis are:^{172, 174}

- Wavebreak: block of a part of the wavefront when colliding with an obstacle (anatomical or functional), while the remaining wavefront continues the propagation.

- Phase singularity (PS): it appears after the block and break of a wavefront. It is the pivoting point around which all phases converge.
- Chirality: it is the direction of rotation around the PS. By convention, a positive chirality (+) indicates clockwise rotation and a negative chirality (-) means a counter-clockwise rotation.
- Rotor: wave rotating around a PS for one or more cycles.

Under regular conditions, an obstacle do not provoke wavebreaks nor PS generation and, therefore, reentrant activity. This only occurs when the tissue excitability is low enough and thereby, the heterogeneous excitability gradients propitiate reentrant waves as a consequence of the collision between a wavefront and an obstacle. This obstacle can be anatomical, for instance a scar or a vein orifice, or functional (difference among the tissue refractoriness).³²

2.4.1 Phase Maps

A map can be considered as a data structure containing discrete time series from different spatial locations.¹⁷¹ Similarly to the representation of the APs or the EGMs through color-coded maps along time, it is also possible to build a phase map, which provides temporal and spatial information about the phenomena occurring. For this purpose, it is needed to obtain the signals for the phase computation. Experimentally, it is common to use the optical mapping technique to register APs (sometimes also pseudo-EGMs),^{14, 16, 171, 174} or to register EGMs through electrodes.^{32, 176}

In this PhD thesis all the phase maps will be built based on simulated signals. First, we will compute the HT for each signal, as described in Equation 2.23, and then we will calculate the instantaneous phase (Equation 2.24):

$$HT[x(t)] = \frac{1}{\pi} \int_{-\infty}^{\infty} \frac{x(\tau)}{t - \tau} d\tau \quad (2.23)$$

$$\theta = \tan^{-1} \left(\frac{HT[x(t)]}{x(t)} \right) \quad (2.24)$$

2.5 Frequency Analysis

Cardiac signals are frequently analysed in the frequency domain^{99, 177, 178} to determine the local frequencies of excitation, as the measurement of local activation times can become difficult during arrhythmias. For this purpose, the spectral analysis of signals such as the EGMs or APs, can be performed on their power spectra obtained by a Fast Fourier Transformation (FFT).

The dominant frequency (DF) of a recording is defined as the frequency corresponding to the highest peak in the power spectrum. Colour-coded DF maps can be built in order to obtain the activation frequencies of the mapped regions. For example, it has been demonstrated that regions with the highest DFs coincide with the meandering area of rotors during AF.¹⁶ Although DF maps are a valuable tool that provide the spatial organization of AF, they have limitations in tracking the temporal variations commonly observed during AF.

Three-Dimensional Multiscale Atria-Torso Model

The content in this chapter was partially published in:

L. Martínez-Mateu et al. Factors affecting basket catheter detection of real and phantom rotors in the atria: A computational study. *PLoS Comput Biol*, 14(3):e1006017, 2018.

A. Ferrer-Albero, E.J. Godoy, M. Lozano, **L. Martínez-Mateu**, et al. Non-invasive location of atrial ectopic beats by using body surface P-wave integral maps, *PLoS ONE*, 12(7): e0181263, 2017.

3.1 Introduction

The general aim of this PhD thesis was to study the accuracy of multi-electrode mapping systems when mapping the electrical activity of the human atria through computational models and simulations. For this purpose, there was a need to develop a 3D multiscale model as a tool to carry out our simulations. In this chapter, we describe all the methods used to achieve the first specific objective of this PhD thesis: the development and validation of a realistic and multiscale 3D atria-torso model as a tool for computing intracavitary atrial EGMs.

First, we will detail all the steps followed in order to adjust atrial unicellular models under physiological conditions to perform simulations ranging from cellular level to organ. Second, we will compute intracavitary EGMs by using a model which comprises the atrial myocardium and the blood inner the atria (atria-blood model). However, the heart is not isolated but immersed in the torso, and we still do not know how the modelling of isolated atria could affect the propagation of the electrical signals. To our knowledge, the effect of the torso and its inhomogeneities has already been studied regarding the P-wave generation.^{148,158} Nevertheless, the effect that the torso absence might have on the generation of the intracavitary recordings has not yet been analysed. Therefore, we will evaluate the effect of the torso in the computation of intracavitary EGMs by using a complete 3D atria-torso model. Finally, we will discuss our findings and limitations with the aim of establishing the best tools to carry out the studies exposed within the following chapters.

3.2 Methods

3.2.1 Unicellular Models

The cellular electrical activity of a human atrial myocyte was modeled by the CRN ionic model.¹²⁸ We chose it among the five main human atrial available models (see Section 2.3.1) for two main reasons: its simplicity in terms of implementation and its moderate computational cost in terms of time required to carry out the simulations.

3.2.1.1 Stabilization of the Ionic Model

As reported by the authors, the CRN model has a stable resting potential of approximately -81 mV and all intracellular concentrations are stable at rest ($[Ca^{2+}]_i = 0.1\mu\text{M}$, $[Na^+]_i = 11.2$ mM and $[K^+]_i = 139.0$ mM).¹²⁸ However, they didn't provide any information about the stability and the variations in these concentrations, and therefore in the AP morphology and duration after stimulating the cell. For this purpose, we used the Cellular

Open Resource (*COR*), developed at the Oxford University, as the environment for modelling a single cell cardiac electrophysiology with the CRN model. We simulated the electrical activity of an atrial myocyte for 120 minutes, stimulating at a basic cycle length (BCL) of 1000 ms with a stimulus of 2 nA amplitude and 2 ms duration (same stimulation conditions as in Courtemanche et al¹²⁸). The variation of the intracellular concentrations for the whole simulation time is shown in Figure 3.1A.

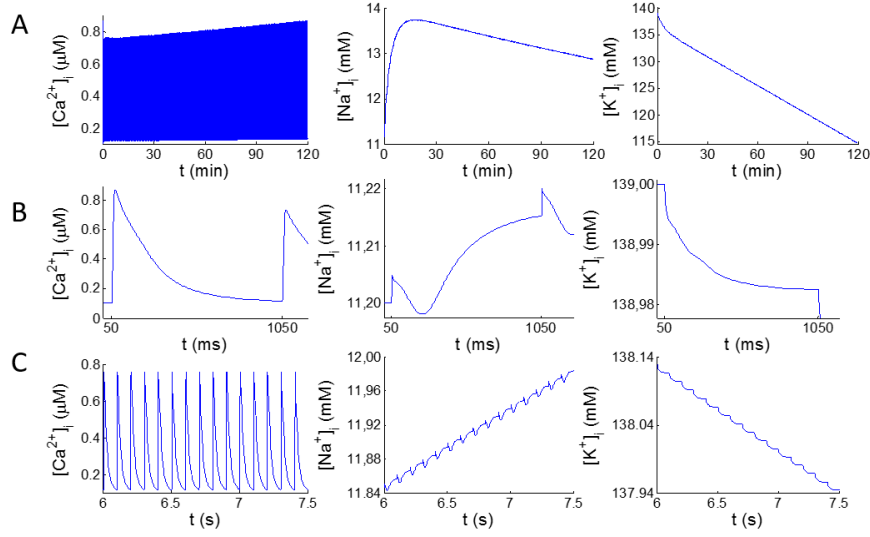


Figure 3.1: Variation of the ionic intracellular concentrations for the CRN model after pacing with a BCL of 1000 ms for 120 min. Traces of the concentrations are shown for the 120 min (A), the two first stimuli (B) and 15 s after 1 min (C) of the simulation.

On the one hand, we considered the intra-beat variation of the concentrations, i.e. the variation of the concentration within a beat. As depicted in panel B, the trace of the $[Ca^{2+}]_i$ increases after the stimulus ($t=50$ and 1050 ms) and then decreases to the rest level. The amplitude of this variation of concentration within a beat was not stable along the whole simulation. As seen in panel A and B, it first decreased from first to second beat and then increased along time. However, this intra-beat variation remained stable along the simulation time for the $[Na^+]_i$ and $[K^+]_i$. On the other hand, we considered the inter-beat variation of the concentrations, i.e. the variation of the value of concentrations in resting potential along the whole simulation time, before applying each stimulus. In this case, the resting value varied significantly for the $[Ca^{2+}]_i$: $0.1 \mu\text{M}$ before the first stimulus and $0.13 \mu\text{M}$ before the last one, which is a variation of 30%. However it varied 15% for $[Na^+]_i$ (11.2 and 12.87 mM before the first and last stimulus, respectively)

and 17% for $[K^+]_i$ (139 and 114.6 mM before the first and last stimulus, respectively). The resting level of $[Na^+]_i$ increased after each stimulus for about 18 min, then decreased compared to the prior beat for the rest of the simulation (see panel A).

As a consequence of the intracellular concentrations variation along the simulation time, the amplitude of the AP decreased and the prominent spike-and-dome morphology smoothed. APs after 1, 10, 30, 60, 90 and 120 minutes of pacing are shown in Figure 3.2A. Besides the morphology, APD also varied along the simulation. APDs at 50% (APD_{50}) and 90% (APD_{90}) of repolarization are shown in Table 3.1.

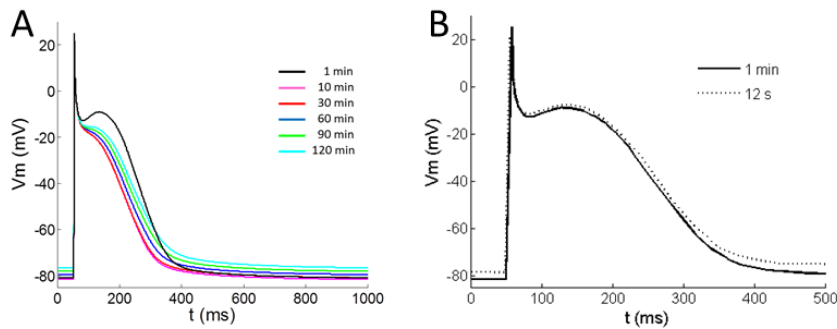


Figure 3.2: Simulated APs obtained after pacing the CRN model with a BCL of 1000 ms. A) APs after 1, 10, 30, 60, 90 and 120 minutes of stimulation. B) Comparison of the AP after 12 s¹²⁸ and 1 minute of stimulation.

Simulation time	APD_{50} (ms)	APD_{90} (ms)
12 s	178	297
1 min	180	300
10 min	167	305
30 min	115	246
60 min	125	272
90 min	134	286
120 min	143	289

Table 3.1: APD at 50% and 90% repolarization for the CRN model after 12 s (data reported by the authors¹²⁸), and 1, 10, 30, 60, 90 and 120 minutes of stimulation with a BCL of 1000 ms.

In order to maintain the pronounced spike-and-dome morphology and the APD reported by the authors ($APD_{90} = 297$ ms for the 12th AP with pacing at BCL = 1000 ms), we decided to stabilize the model for only 1 minute (see Figure 3.2B and Table 3.1) and check if the variation of the concentrations was negligible in the period of time needed to carry out our simulations. Panel

C in Figure 3.1 depicts the intracellular concentrations for the first 15 s after 1 minute of stabilization. In this period of time the variation in the resting value of the concentrations (before first and last stimulus) was 1% for $[Ca^{2+}]_i$ and $[Na^+]_i$, and 0.07% for $[K^+]_i$. As there are no abrupt changes, which could imply non-physiological conditions, these variations can be considered negligible. Therefore the CRN model after 1 min of stimulation can be considered stable at least in simulations up to 15 s of duration.

3.2.1.2 Atrial Heterogeneity

In order to reproduce the experimentally observed heterogeneity in AP morphology and duration of different regions in the atria,^{56,60-63} the maximum conductance of three ionic currents (I_{to} , I_{CaL} and I_{Kr}) was adjusted as previously described^{138,148,151,153,179} (Table 3.2). The adjustment consisted of applying multiplicative factors with respect to the default values in the CRN model, in order to increase or reduce the channel conductance and maintain the tendency on the relative regional variations of the APD seen experimentally (ΔAPD_{90} and ΔAPD_{95}). This procedure yielded nine cellular models (RA/PM, LA, CT/BBRA, BBLA, PV, MVR, TVR, RAA and LAA) whose APs are depicted in Figure 3.3. APs were recorded after 1 minute of stimulation at a BCL of 1000 ms; pulse amplitude and duration were 2 nA and 2 ms, respectively. BB was divided into right (BBRA) and left (BBLA) sides.

	RA/PM	CT/BBRA	TVR	RAA	LA	BBLA	MVR	LAA	PV
$g_{to_{max}}$ ^a	1.00	1.00	1.00	0.68	1.00	1.00	1.00	0.68	1.00
$g_{CaL_{max}}$ ^a	1.00	1.67	0.67	1.00	1.00	1.67	0.67	1.00	1.00
$g_{Kr_{max}}$ ^a	1.00	1.00	1.53	1.00	1.60	1.60	2.44	1.60	2.20
APD ₉₅ (ms) ^b	339	375	264	325	299	324	228	281	268
ΔAPD_{95} (%) ^c	0	10	-22	-4					
Exp. ΔAPD_{95} (%) ^d		42 ⁶⁰	-15 ⁶⁰	-5 ⁶⁰					
APD ₉₀ (ms) ^e	295	311	227	278	256	261	193	236	227
ΔAPD_{90} (%) ^f					-13				-11
Exp. ΔAPD_{90} (%) ^g					-10 ⁶¹				-11 ⁶²

^a Relative values with respect to the g_{max} in the original CRN model¹²⁸

^b APD₉₅ after 1 minute of stimulation at BCL = 1000ms

^c Variation of the APD₉₅ with respect to the APD₉₅ in the RA/PM region

^d Experimental value for ΔAPD_{95}

^e APD₉₀ after 1 minute of stimulation at BCL = 1000ms

^f Variation of the APD₉₀ in LA with respect to the APD₉₀ in RA/PM and in PV with respect to the LA

^g Experimental value for ΔAPD_{90}

Table 3.2: Ionic channel conductances used to reproduce the atrial heterogeneity and the APD distribution under control conditions. Variations of the channels conductances (second to fourth rows) in each region (first row) used to reproduce the atrial heterogeneity; APD₉₀ and APD₉₅ obtained in each atrial region (eighth and fifth rows) and their respective increments (ninth and sixth rows); and comparison with the experimental variation of APD between regions (seventh and tenth rows).

APDs to 90% and 95% repolarization (APD₉₀ and APD₉₅) are shown in

Table 3.2. The APD variation among regions was similar to experimental observations:^{60–62} the APD was longer in the CT region than in the RA region, where it was longer than in the TVR, RAA and LA regions, and the APD was shorter in the PV region than in the LA region.

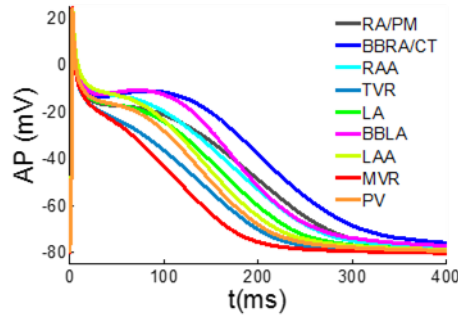


Figure 3.3: Action potentials (AP) corresponding to each variation of the CRN model¹²⁸ in control conditions.

3.2.2 3D Atrial Model

Once the unicellular models were adjusted in control conditions for each region of the atria, we needed to couple them into the 3D atrial geometrical mesh. However, before using the 3D realistic atrial model, we analysed the behaviour of the cellular models at tissue scale to characterize the stimulation needed for the propagation in a multicellular simulation as well as the CV in each atrial region.

3.2.2.1 Block of Atrial Tissue

We used a geometrical mesh comprised of $50 \times 50 \times 3$ hexahedral elements with a spatial resolution of $300 \mu\text{m}$ between nodes (see Figure 3.4) to simulate the electrical propagation in a 3D block of atrial tissue, with the aim of adjusting the stimulus and the regional CVs needed in multicellular simulations. Once these electrical parameters were characterized, we used them for simulations with the 3D realistic atrial model.

In order to simulate the AP of each cell (node) in the mesh and their electrical propagation within the tissue, we coupled the corresponding variation of the unicellular CRN model to each node. Then, we solved the monodomain formalism (see Section 2.3.3.2) by using the *ELVIRA* software,¹⁸⁰ a pseudo-adaptive FEM in space and time to solve anisotropic reaction-diffusion equations with highly non-linear reactive terms, based on the operator splitting numerical scheme.

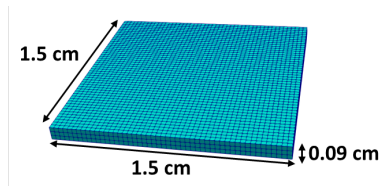


Figure 3.4: Geometrical mesh corresponding to a 3D block of atrial tissue. Size: $1.5 \times 1.5 \times 0.09 \text{ cm}^3$.

3.2.2.1.1 Adjustment of the Stimulation

The threshold needed for the depolarization of a cell varies depending on the amplitude and duration of the stimulus, as shown in Figure 3.5. In our single cell simulations solving the CRN model with *COR*, we employed a stimulus of 20 pA/pF amplitude and 2 ms duration, which is almost 2-fold the minimum amplitude needed for a stimulus of 2 ms duration (see Figure 3.5A, blue trace). However, in the case of multicellular simulations, the stimulus has to depolarize the cell and also promote the propagation along the tissue. Then, the threshold might vary depending on the geometrical mesh used in the simulations and should be calculated for any specific mesh. In Figure 3.5 the minimum (A) and maximum (B) threshold stimuli needed for a single cell (blue), the block of atrial tissue described previously (green) and the 3D atrial model, which will be described in Section 3.2.2.2 (red), are depicted. In case of our multicellular simulations, which were performed with *ELVIRA*, and according to the values shown in the traces, we decided to apply a stimulus of 2 ms duration and 50 pA/pF for the 3D block of atrial tissue and 28 pA/pF for the 3D atrial model (approximately 2-fold the threshold, respectively). In all simulations (unicellular and multicellular) the CRN model was solved with a time step of $dt = 0.01 \text{ ms}$. The stimuli used for the simulations performed in this PhD thesis are summarized in Table 3.3.

Type of Simulation	Stim.Amplitude (pA/pF)	Stim.Duration (ms)
Unicellular	20	2
Atrial Tissue	50	2
3D Atrial Model	28	2

Table 3.3: Stimuli applied to unicellular and multicellular simulations.

3.2.2.1.2 Adjustment of Conduction Velocity

CVs for each atrial region were calculated by adjusting the longitudinal conductivities (σ_L) and the anisotropy ratios (σ_T/σ_L) in the 3D block of tissue. Therefore, each atrial region was characterized by three different properties: unicellular model, σ_L and σ_T/σ_L . For this characterization, we chose an ionic model among the 9 available models described in Section 3.2.1.2, and one of the

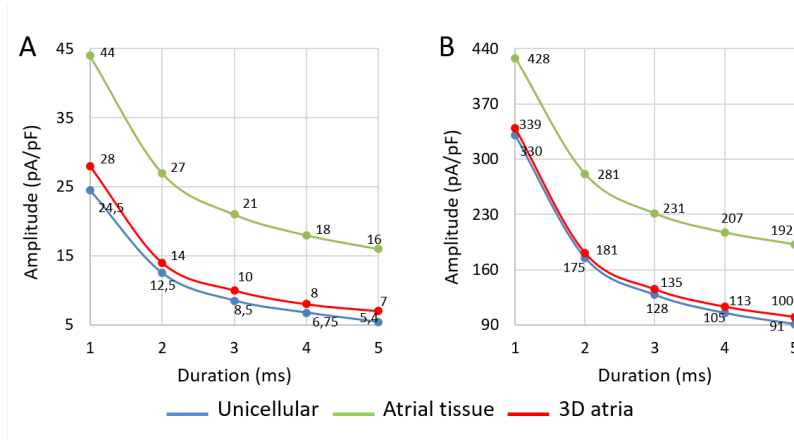


Figure 3.5: Threshold stimuli for the CRN model (RA/PM variation) when simulating the electrical activity in a single cell (blue), a 3D block of atrial tissue (green) and the whole organ (red). A) Minimum stimulus necessary to depolarize the cell, and also get propagation in case of the atrial tissue and organ. B) Maximum stimulus permitted by the ionic model.

8 types of tissue defined by the combination of σ_L and σ_T/σ_L (see Table 3.4).

According to experimental observations,^{181,182} the preferential conduction bundles (LFO, BB, PM and CT) were defined as regions with a high anisotropy ratio, so we set this value to 0.15. In case of the RA/LA (including the TVR, RAA, MVR and LAA structures), the PV/CS and the SAN/FO/Isthmus regions, the anisotropy ratio assigned was 0.35, 0.5 and 1.0 (isotropy) respectively, as in previous computational works.^{44,151,153} In relation to σ_L , the preferential conduction bundles (BB, PM, CT and LFO) were assigned with higher values, since they have faster CVs (0.0071 and 0.0081 S/cm·pF). The CS region, which has an important role in the electrical connection among both atria, was set to an intermediate value (0.0052 S/cm·pF). Lower values were assigned to the RA/LA and structures within them (0.003 S/cm·pF) and PV/Isthmus regions (0.0017 and 0.0014 S/cm·pF). Finally, while the FO is an isolating tissue and its conductivity was set to zero, the SAN conductivity was set to 0.0008 S/cm·pF because it is the region where the stimulus is applied and needs a very low conductivity value to trigger the activation of neighbouring tissue.

As a result of the simulations performed to determine the CV in each atrial region, we obtained the propagation patterns depicted in Figure 3.6 after stimulation in the center of the tissue. Longitudinal and transversal directions were defined in the vertical and horizontal axis, respectively, and longitudinal CV (CV_L) and transversal CV (CV_T) were computed as the spatial variation

(ΔS) between two points in the vertical (P1 and P2) and horizontal (P3 and P4) axis, divided by the temporal variation (Δt) between the two local activation times (see Figure 3.6.A), as follows:

$$CV_L = \frac{\Delta S}{\Delta t} = \frac{\Delta S}{t_2 - t_1} \text{ (cm/s)} \quad (3.1)$$

$$CV_T = \frac{\Delta S}{\Delta t} = \frac{\Delta S}{t_4 - t_3} \text{ (cm/s)} \quad (3.2)$$

where t_1 , t_2 , t_3 and t_4 were the local activation times at points P1, P2, P3 and P4, respectively.

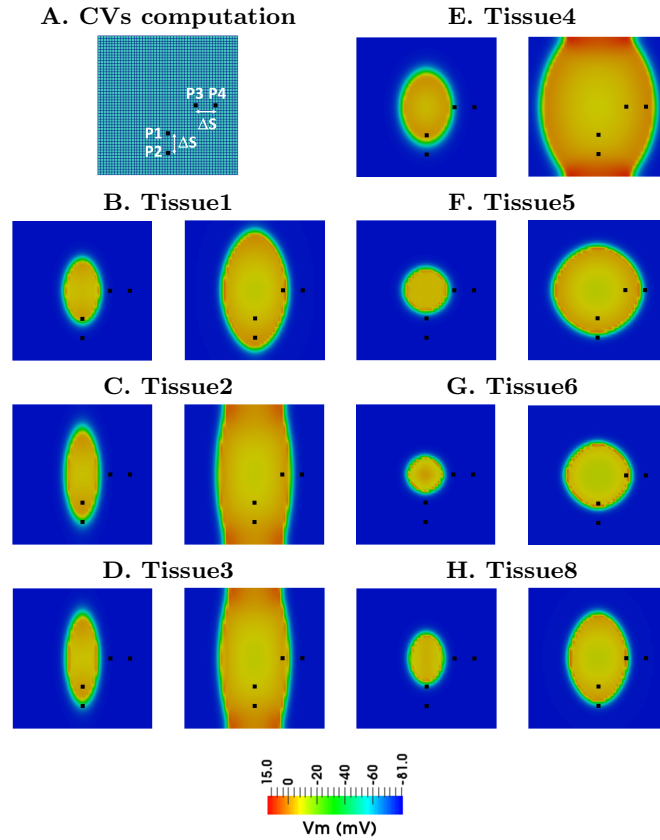


Figure 3.6: Propagation patterns corresponding to different atrial tissues. A) Nodes used to compute CV_L (P1 and P2) and CV_T (P3 and P4). B-H) Propagation patterns obtained after simulating the electrical activity in the types of tissue defined in Table 3.4 (snapshots at 5 (left) and 10 (right) ms after the stimulation). Type of tissue 7 (FO) is not shown since σ_L was set to zero and there is no propagation.

Cellular model	RA	TVR	RAA	LA	MVR	LAA	CT	BBRA	PM	LFO	BBLA	CS	Isthmus	SAN	FO	PV	
	RA/PM	TVR	RAA	LA	MVR	LAA	CT/BBRA	RA/PM	BBLA	RA/PM							PV
Type of tissue	tissue1						tissue2	tissue3		tissue4	tissue5	tissue6	tissue7	tissue8			
σ_L (S/cm-pF)	0.0030						0.0081	0.0071		0.0052	0.0014	0.0008	0.0000	0.0017			
σ_T/σ_L	0.35						0.15	0.15		0.50	1.00	1.00	1.00	0.50			
CV_L (cm/s)	72.66						120.00	112.30		96.77	48.28	33.93	0.00	53.03			
CV_T (cm/s)	41.10						45.36	41.75		69.08	48.28	33.93	0.00	35.77			

Table 3.4: Cellular model (second row), type of tissue (third row) defined by the longitudinal conductivity σ_L (fourth row) and the anisotropy ratio σ_T/σ_L (fifth row), longitudinal CV (sixth row) and transversal CV (seventh row) for each atrial region (first row).

Figure 3.6, panels B to H, depict the propagation patterns corresponding to the types of tissue shown in Table 3.4. Faster CV_L were obtained for tissues with high conductivity values, for example 120 cm/s or 112.3 cm/s in the CT and BB/PM/LFO regions, followed by 96.77 cm/s in the CS, 72.66 cm/s in the general RA/LA tissue, 53.03 cm/s in the PV and 48.28 in the isthmus. The slowest CV_L was measured in the SAN (33.93 cm/s). In Figure 3.6 can also be observed the difference between anisotropic (panels B-E and H) and isotropic (panels F-G) propagation patterns.

3.2.2.2 Atrial Geometrical Mesh

In order to perform a simulation with the whole atria under physiological conditions, we used a recently developed realistic 3D model of the human atria,⁴⁴ which comprises the main anatomical regions with their respective fiber orientation. Atrial regions are, among others: RA, LA, CT, FO, PV (divided into left/right and upper/lower PVs: LUPV, LLPV, RUPV, RLPV), BB (divided into left and right sides: BBLA, BBRA), PM, isthmus, SAN, CS, MVR, TVR, RAA, LAA, SVC and IVC (see Figure 3.7). This computational finite element model, composed of linear hexahedral elements with a regular spatial resolution of 300 μm , has a homogeneous wall thickness between 600 and 900 μm (754893 nodes and 515010 elements). See reference⁴⁴ for additional details about the geometrical mesh.

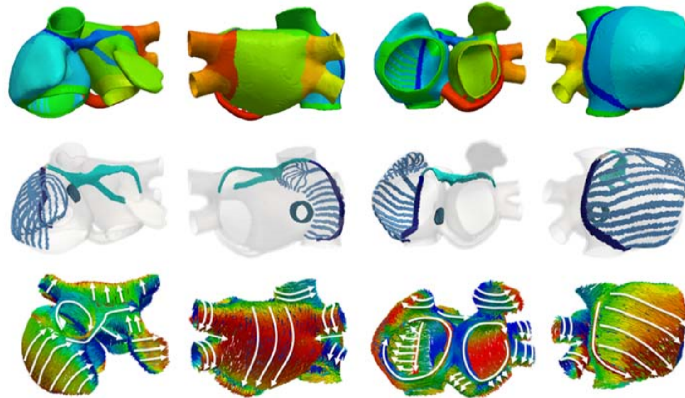


Figure 3.7: 3D atrial geometrical mesh (from⁴⁴). First row: 21 atrial regions; second row: preferential conduction bundles; third row: fibers direction (from left to right columns: frontal, rear, inferior and right lateral views).

The nine cellular models described in Section 3.2.1.2 were assigned to the nodes in the 3D geometrical mesh, following the distribution shown in Figure 3.8.A. Conductivities adjusted for each type of atrial tissue (see Table 3.4) were tuned as in¹⁴⁸ to match the activation sequences in the atria to the

experimental data,¹⁸³ as well as the P-wave duration in the ECG.¹⁸⁴ In Table 3.5 the regional values for σ_L and σ_T/σ_L assigned to the elements in the 3D model are summarized and their geometrical distribution is shown in Figure 3.8.B.

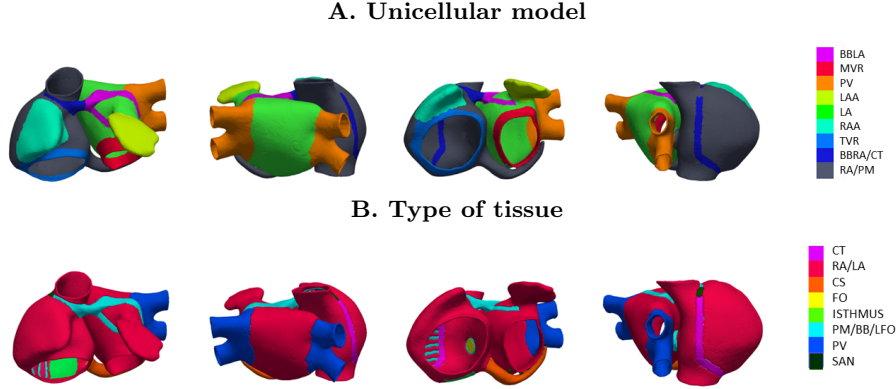


Figure 3.8: Atrial regions in the 3D model defined by: A) the unicellular models assigned to each node in the mesh; B) the types of tissue assigned to each element in the mesh.

Region	σ_L (S/cm·pF)	σ_T/σ_L	Region	σ_L (S/cm·pF)	σ_T/σ_L		
RA	0.0030	0.35	BBRA	0.0075	0.15		
TVR			PM				
RAA			LFO				
LA			BBLA				
MVR			CS			0.0060	0.50
LAA			Isthmus			0.0015	1.00
CT	0.0085	0.15	PV	0.0017	0.50		
SAN	0.0008	1.00	FO	0.0000	1.00		

Table 3.5: Longitudinal conductivity σ_L (second and fifth columns) and anisotropy ratio σ_T/σ_L (third and sixth columns) for each atrial region (first and fourth columns) in the 3D atrial model.

3.2.2.3 Numerical/Computational Methods and Stimulation Protocol

Once the unicellular ionic models and the electrical properties of the tissue accounting for the atrial heterogeneity were assigned to the nodes and elements comprising the 3D atrial mesh, the electrical activity in our 3D model was solved by the monodomain formalism. For this purpose we used the operator splitting

numerical scheme with *ELVIRA* software¹⁸⁰ with a constant time step $dt=0.01$ ms. Simulations of 11 s of atrial activity took 37 hours on a computing node with eight 6-core AMD Opteron Processors 6234 clocked at 2.4 GHz.

To initiate the electrical activity, we applied 11 stimuli (BCL 1000 ms, amplitude 28 pA/pF, duration 2 ms) to the SAN region. Although ionic models were previously stabilized in single cell simulations (1 min, BCL=1000 ms; see Section 3.2.1.1), the first 10 stimuli were carried out in order to stabilize them in 3D simulations and smooth transitions between neighbouring regions. After 10 s of stabilization, the 11th stimulus was used to analyse the electrical propagation pattern in control conditions and measure the activation times, with the aim of validate our 3D atrial model. Results are reported in Section 3.3.

3.2.3 Computation of Intracavitary EGMs

Unipolar intracavitary EGMs were computed through the extracellular potentials (ϕ_e) calculation on the endocardium-blood interface with a temporal resolution of 1 ms. For this purpose, we used two different models for the calculations with the aim of studying the differences among the EGMs computed with them, as well as the validity of both models:

1. A 3D isolated atria-blood model, comprised of 2 regions: atrial myocardium and blood inner the atria (Figure 3.9.A).
2. A 3D torso model with the atria immersed in it, comprised of 7 regions: chest, lungs, liver, bones, blood (in the vessels and inside the atria), ventricles and atria (Figure 3.9.B).

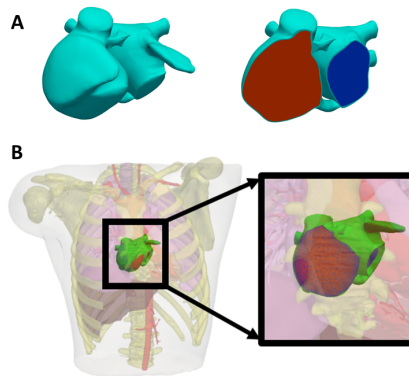


Figure 3.9: Atria-blood and torso models. A) Atria-blood model comprising 2 regions: atrial myocardium and blood inner the atria. B) Torso model comprising 7 regions: chest, lungs, liver, bones, atria, ventricles and blood.

3.2.3.1 Numerical and Computational Methods

ϕ_e were computed by an approximation of the bidomain formalism in two steps.¹⁵⁸ By assuming equal anisotropy ratio for D_i and D_e , the bidomain equations can be decoupled into an equation describing the changes in the V_m , and another equation describing the ϕ_e in the heart domain,¹⁶³ i.e., the well-known monodomain model (see Section 2.3.3.2):

$$\nabla(D\nabla V_m) = C_m \frac{\partial V_m}{\partial t} + I_{ion} \quad \text{in } \Omega_H \quad (3.3)$$

$$\nabla(D\nabla \phi_e) = -\frac{1}{1+\lambda} \nabla(D\nabla V_m) \quad \text{in } \Omega_H \quad (3.4)$$

where D is the equivalent conductivity tensor (see Equation 2.20) and Ω_H is the heart domain. Equations 3.3 and 3.4 are subjected to the following boundary conditions in Ω_H :

$$n(D\nabla V_m) = 0 \quad \text{on } \Omega_H \quad (3.5)$$

$$n(D\nabla \phi_e) = 0 \quad \text{on } \Omega_H \quad (3.6)$$

where n is the outward normal to $\partial\Omega_H$. Equations 3.3 and 3.5 allow for solving the V_m in the cardiac tissue, whereas Equations 3.4 and 3.6 recast the ϕ_e in the heart tissue after V_m has been calculated. Note that boundary conditions 3.5 and 3.6 consider the heart to be immersed in a non-conducting bath.

To accurately calculate the EGMs inside the atria, we need to place the heart within the torso and solve for the ϕ_e in the entire domain (the heart Ω_H and the torso Ω_T outside the heart). Therefore, we define our 3D space problem to include the governing equations for the solid conductor associated with the torso, and modify accordingly the boundary conditions at the heart/torso interface, i.e., $\partial\Omega_H$. Under the hypothesis of equal anisotropy ratio for D_i and D_e , the ϕ_e in the domain $\Omega_H \cup \Omega_T$, after obtaining V_m as solution of Equations 3.3 and 3.5, is found as the solution of the following Laplace Equation:

$$\nabla(D_T \nabla V_T) = 0 \quad \text{in } \Omega_T \quad (3.7)$$

where V_T and D_T are the ϕ_e and the heterogeneous conductance tensor in the torso, respectively. Equation 3.7 is subjected to the following boundary and

continuity conditions:

$$\phi_e = V_T \quad \text{in } \partial\Omega_H \quad (3.8)$$

$$n(D\nabla V_T) = 0 \quad \text{in } \partial\Omega_T \quad (3.9)$$

where $\partial\Omega_T$ is the torso-air non-flux boundary. Then, V_T is the EGM inner the atrial cavity or the ECG on the torso surface. It should be noted that in case of the atria-blood model, the torso domain Ω_T described along this formulation corresponds only to the blood inside the atria.

The approximation of the bidomain formulation was computed with custom-made software routines in *MatLab* (MathWorks, Natick, MA), developed in collaboration with *Politecnico di Milano*. First V_m was obtained, after solving the monodomain formalism with the *ELVIRA* software, at the nodes of the 3D atrial model comprised of hexahedral elements. Then, there was a need to interpolate V_m into the nodes belonging to the myocardial region in the 3D tetrahedral mesh for both, the atria-blood and the torso model¹⁸⁵ (see Figure 3.10), before initiating the computation of ϕ_e . This interpolation consists of assigning the centroid of each hexahedral element (3D atrial model) to the nearest neighbour node in the final mesh (atrial region in the tetrahedral mesh corresponding the atria-blood model or the torso model). Then, for each node in the atrial region (tetrahedral elements), the V_m values of the hexahedral elements (3D atrial model) assigned to this node are taken and the V_m mean value is computed. Finally, once all the nodes in the atrial myocardium of the tetrahedral mesh have assigned a V_m value, ϕ_e can be computed at each node in the tetrahedral mesh.

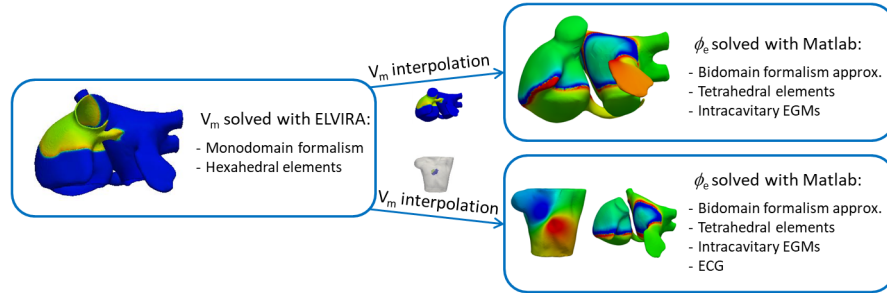


Figure 3.10: Diagram of the bidomain approximation.

3.2.3.2 3D Atria-Blood Model

We needed to develop a geometrical mesh comprised of tetrahedral elements to compute the intracavitary EGMs with the bidomain formalism

approximation. However, besides building a complete torso model, we also built an atria-blood model due to the following reasons:

- We were not interested in the ECG, so we did not need the propagation throughout the torso to the surface.
- We wanted to increase as much as possible the spatial resolution inside the atrial cavities, and the elimination of torso regions out of the atrial myocardium maintained the total number of nodes at lower values.
- We wanted to evaluate the viability and usefulness in the intracavitary EGMs computation of both, an isolated atria model and a complete torso model.

3.2.3.2.1 Generation of the Atria-Blood Geometrical Mesh

We built an atria-blood tetrahedral mesh in which atrial myocardium overlapped with our 3D atrial hexahedral model. First, we took the outer and inner surfaces from which our 3D atrial model was developed⁴⁴ to delimit the region corresponding to the atrial myocardium in our new tetrahedral mesh. Then, we closed those surfaces with the *Remesh 2.1* software (see Figure 3.11), since the *TetGen* software used to generate our tetrahedral model only meshes inside closed surfaces. Elements located between the outer and inner atrial surface correspond to the atrial myocardium, while elements located inside the inner atrial surface correspond to the blood (Figure 3.12). They were automatically labelled by localizing their centroids within the region corresponding to the myocardium or the blood. Elements labelled as atrial myocardium were assigned with the corresponding conductivity depending on the atrial region (see Table 3.5), and elements corresponding to the blood were assigned with a conductivity of 7.0 mS/cm.¹⁸⁶

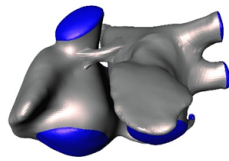


Figure 3.11: Closed outer surface to mesh the atria-blood model. Grey: outer atrial myocardium surface. Blue: added surfaces with Remesh to close the orifices.

After running the *TetGen* software, we obtained a mesh in VTK format comprised of 225042 nodes (100950 belonging to the myocardium; 61771 to the RA blood; and 62321 to the LA blood) and 951087 tetrahedral elements (322618 belonging to the myocardium; 311186 to the RA blood; and 317283 to the LA blood). The endocardium-blood interface had 24224 nodes in the RA and 23476

nodes in the LA. As shown in Figure 3.12, the element size is not constant: smaller elements are located within the myocardium and bigger elements in the middle of the atrial cavities, which yields a spatial resolution among nodes of approximately 0.5 mm on the endocardium and 5.8 mm in the center of the cavities. The elements size growth towards the center of the atrial cavities allows a high spatial resolution in the region close to the endocardium, where the EGMs will be measured, while it maintains a moderate spatial resolution in the middle of the cavities. Therefore, the total number of nodes in the mesh do not become exorbitant.

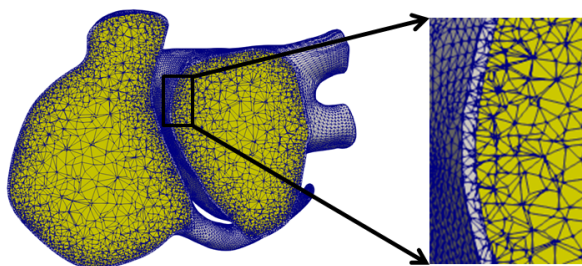


Figure 3.12: Atria-blood tetrahedral mesh: myocardial elements in white and blood elements in yellow (elements edges in blue).

Once the mesh was built, we analysed its quality by using the *Mesh Quality Filter* in the visualization software *ParaView 5.4.1*. The jacobian is one of the most important indicators regarding the mesh quality. If it presents negative values, the numerical problem (ϕ_e calculation) will not be solved. As shown in Figure 3.13.A, for our mesh all values are positive. Figure 3.13.B depicts the histogram corresponding to the distortion of the tetrahedral elements, which are not distorted since the value is around 1.

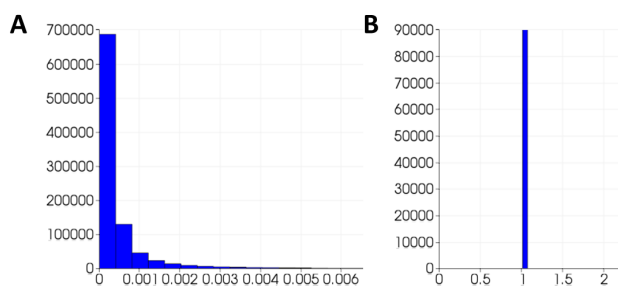


Figure 3.13: Atria-blood mesh quality. Histograms corresponding to the jacobian (A) and distortion (B) of the tetrahedral elements. Vertical axis: number of elements.

3.2.3.3 3D Torso Model

After computing the EGMs on the endocardium with the atria-blood model, we also computed them with the torso model. For this purpose and to achieve a better spatial resolution, we modified a previous torso model developed in this research group,¹⁴⁸ which was comprised of 190804 nodes and 1149531 tetrahedral elements (only around 34000 nodes pertained to the vicinity of the myocardial region).

3.2.3.3.1 Generation of the Torso Geometrical Mesh

The torso model developed by Ferrer et al¹⁴⁸ was re-meshed in order to improve the spatial resolution at the endocardium-blood interface and the inner atrial blood with the *TetGen* software (see Figure 3.14). Accordingly, the resulting torso mesh had 254976 nodes (94230 corresponding to the myocardium; 61142 to the RA blood; and 57523 to the LA blood) and 1554255 tetrahedral elements (326866 corresponding to the myocardium; 303662 to the RA blood; and 281565 to the LA blood) with a spatial resolution ranging approximately from 0.5 mm on the atrial endocardium-blood interface to 5.8 mm on the torso surface and the center of the atrial cavities (elements size in the remaining organs was wider, as shown in Figure 3.14, right). The number of nodes belonging to the endocardium-blood interface were 25175 in the RA and 24819 in the LA.

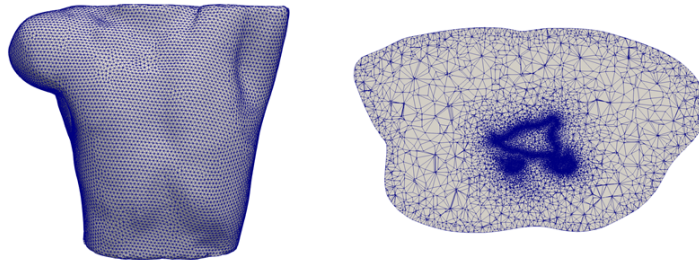


Figure 3.14: Torso mesh comprised of tetrahedral elements. Frontal view (left) and transversal view (right). Spatial resolution ranging from 0.5 mm on the atrial endocardium-blood interface to 5.8 mm on the torso surface and the center of the atrial cavities.

Each tetrahedral element in the model was labelled as lung, bone, liver, atrium, ventricle, blood or general torso. The labelling algorithm computed the centroid of each element and located it inside the surface meshes delimiting each organ. Therefore, elements were labelled accordingly. It should be noted that a tetrahedron cannot be labelled twice so each of them have a unique identifying label and, then, they are unique within the torso mesh. This labelling was used to assign the corresponding organ conductivity to each region in the torso, as

reported in previous studies.^{161,186–188} Our inhomogeneous torso model has the conductivities shown in Table 3.6, which are in accordance with values reported in the literature. In case of the elements pertaining to the atrial myocardium, conductivities are assigned depending on the atrial region and following the values shown in Table 3.5.

Organ	Model conductivities (mS/cm)	Literature conductivities (mS/cm)
Ventricular myocardium	4.590	0.537, ¹⁸⁶ 4.830, ¹⁸⁹ 5.000 ¹⁸⁸
Lungs	0.389	0.389, ¹⁸⁶ 0.500, ¹⁸⁸ 1.340 ¹⁸⁹
Bones	0.200	0.200, ¹⁸⁶ 0.050-0.600 ¹⁹⁰
Blood	7.000	4.350, ¹⁸⁹ 7.000, ¹⁸⁶ 10.000 ¹⁹¹
Liver	0.277	0.277, ¹⁸⁶ 2.000 ¹⁹⁰
General torso	2.390	2.160, ¹⁹² 2.200, ¹⁸⁸ 2.390, ¹⁸⁷ 2.410 ¹⁹³

Table 3.6: Tissue conductivities for the torso model and comparison with values reported in the literature.

We also performed a quality analysis in *ParaView* (*Quality Mesh Filter*) similarly to the atria-blood mesh. The jacobian provided positive values and elements were not distorted (distortion value at about 1), as illustrated in Figure 3.15.

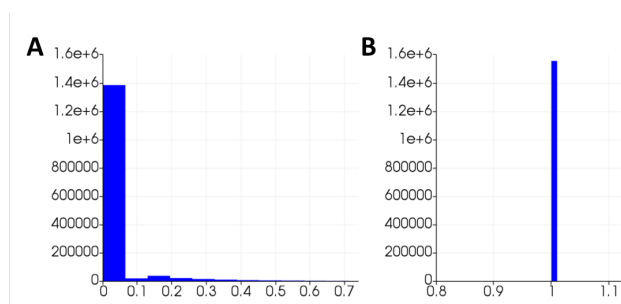


Figure 3.15: Torso mesh quality. Histograms corresponding to the jacobian (A) and distortion (B) of the tetrahedral elements. Vertical axis: number of elements.

3.2.3.4 Clustering of the EGMs on the Endocardial Surface

The EGMs computed on the endocardium-blood interface with both, the atria-blood and atria-torso models, were clustered through custom-made routines in *MatLab*, based on the following properties (see Figure 3.16):

- EGM integral
- Maximum amplitude: $A = V_{max} - V_{min}$

- Temporal difference between V_{max} and V_{min} : $\Delta t = |t_{V_{max}} - t_{V_{min}}|$

This clustering was performed in order to group the EGMs similar to each other and show the regions containing them on the endocardium-blood interface through colour-coded maps. In addition, the distribution of the 10 clusters obtained for the atria-blood and the atria-torso models was compared.

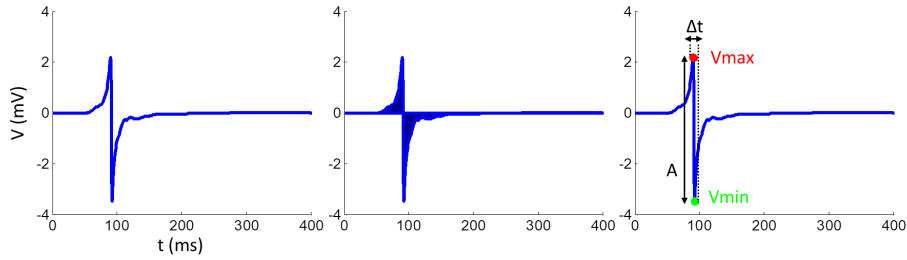


Figure 3.16: EGM properties for clustering. Trace of a computed intracavitary EGM (left); integral of the EGM in A (middle); maximum amplitude (A) and temporal difference between V_{max} and V_{min} (Δt) of the EGM in A (right).

3.3 Results

3.3.1 Simulation of the Electrical Propagation in the Human Atria Under Physiological Conditions

First, we stabilized the CRN model (1 minute, BCL=1000 ms) and carried out the modifications needed to obtain the atrial heterogeneity with unicellular simulations. Then, we coupled the unicellular models into the 3D atrial model, and after stabilizing for 10 s, we finally performed a simulation of the electrical propagation in the human atria by solving the monodomain formalism with the *ELVIRA* software. As a result of this simulation, we validated our model based on the activation times reported by Lemery et al.¹⁸³ As illustrated in Figure 3.17, the electrical propagation in our simulation reached the different parts of the atrial anatomy at time instants matching the experimental observations. The beat started in the SAN. Then, the stimulus spread out along the CT, reached the BB and FO, and propagated towards the LA. Last regions being depolarized were the PV. The whole atria was depolarized after 119 ms.

3.3.2 Simulation of the Intracavitary EGMs

Once our simulation of the electrical activity in the atria under physiological conditions was validated by comparison with the activation times, we proceeded

to compute the intracavitary EGMs, first with the atria-blood model and lastly with the atria-torso model. Results are described in the following sections.

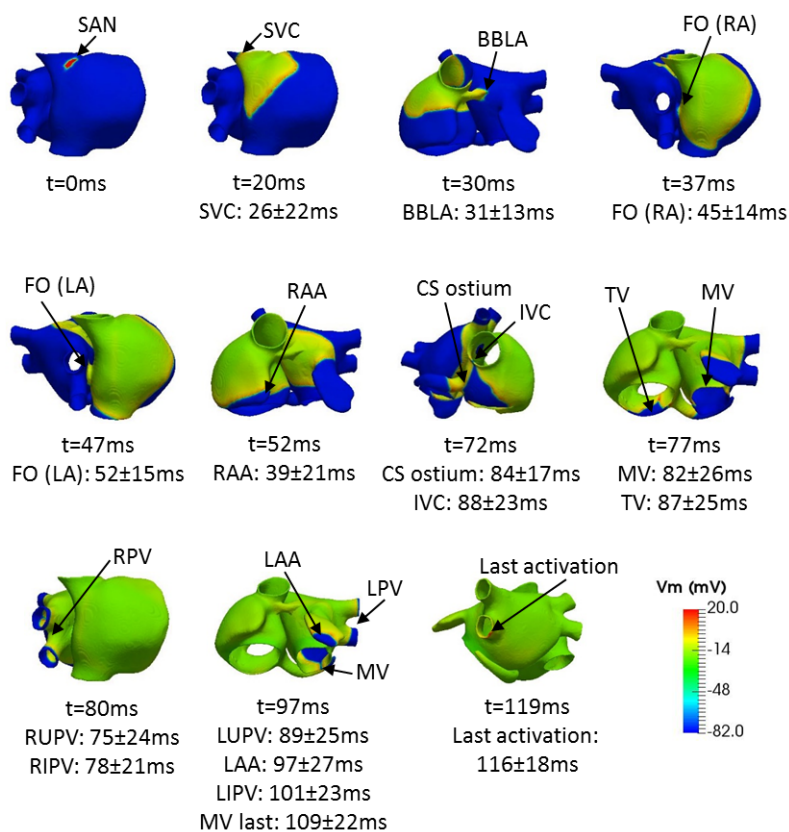


Figure 3.17: Atrial activation times. Snapshots of the atrial activation and comparison of the simulated activation times at different points of the atria with the experimental activation times reported by Lemery et al.¹⁸³

3.3.2.1 EGMs in the Atria-Blood Model

After computing the ϕ_e with the atria-blood model and obtaining the unipolar intracavitary EGMs, we built colour-coded maps of them on the endocardium-blood interface, as shown in Figure 3.18.A. After the stimulus was applied, the propagation pattern matched with the pattern of the V_m in the 3D atrial model. At rest, ϕ_e remained at 0 mV (green area on the colour-coded maps). However, the depolarization wavefront was identified by the transition between the blue and red zones, since the approximation of the wavefront to the measurement point yields an increase of the EGM to positive

values (red in the colour-coded maps) and after the wavefront passes over the point, the EGM decreases (blue region in the colour-coded maps). Nevertheless, although the propagation pattern on the EGMs map matched with the depolarization of the atria at the beginning (snapshot at $t=15$ ms), the effect of the absence of torso in the computations yielded deformed EGMs, as shown at $t=30$ ms (Figure 3.18A). The EGMs in the whole RA suffered a negative deflection at about $t=25$ ms (Figure 3.19), while the EGMs in the whole LA suffered a positive deflection, without respecting the propagation pattern. After approximately 20 ms ($t=45$ ms) the propagation pattern returned to normality. This deformation of the EGMs is clearly shown in Figure 3.19.

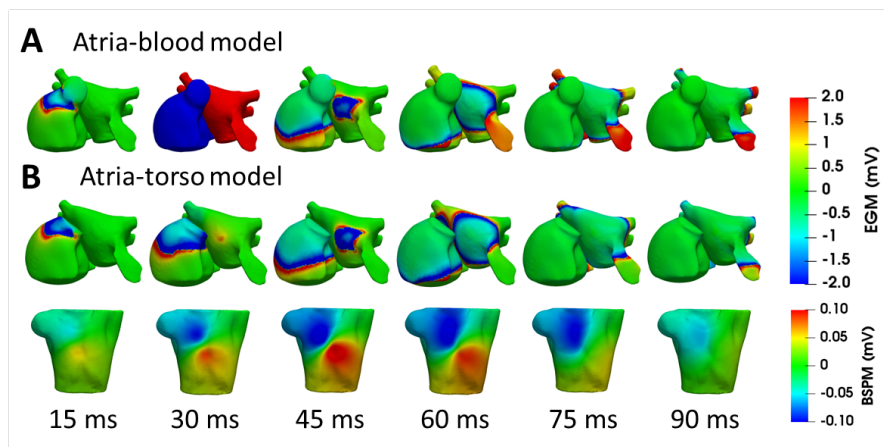


Figure 3.18: Endocardial EGMs and BSPM. A) Colour-coded maps of the EGMs on the endocardium-blood interface corresponding to the atria-blood model. B) Colour-coded maps of the EGMs on the endocardium-blood interface and BSPM corresponding to the atria-torso model. For both models are shown snapshots at 15, 30, 45, 60, 75 and 90 ms.

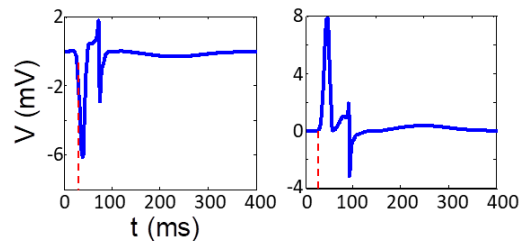


Figure 3.19: EGM in the RA (left) and LA (right) computed with the atria-blood model. At approximately $t=25$ ms a deflection is observed (negative on the left plot; positive on the right plot), which does not match the depolarization pattern.

Once the propagation patterns were analysed on the EGM maps, we revised the clustering obtained for the EGMs in the RA and the LA (Figures 3.20 and 3.21). Panel A in both figures depicts a color-coded map with the regions corresponding to each cluster. As illustrated in panel B, traces of the EGMs within a cluster perfectly match for the deflection (negative in the RA and positive in the LA) due to the deformation of the EGMs. Therefore, the mean value of the EGMs pertaining each cluster (black trace) completely overlaps the EGMs in the period of time in which the abnormal deflection occurs. Since the clustering was mainly governed by this deflection, instead of the morphology of the rest of the signals, it was not possible to detect significant amplitude differences among the EGMs in the different clusters.

3.3.2.2 EGMs in the Atria-Torso Model

After computing the ϕ_e in the atria-torso model, and obtaining the intracavitary unipolar EGMs, we built their colour-coded maps on the endocardium-blood interface, as previously done for the atria-blood model (Figure 3.18.B, top row). In this case, after the application of the stimulus, the wavefront in the EGMs map matched the V_m propagation pattern for each time step, i.e. no deformation of the EGMs was found (Figure 3.22 shows one EGM from the RA and one from the LA as an example). Tissue at rest remained at 0 mV (green) and the wavefront was identified by the transition among the blue and red regions. Red colour indicated a positive deflection in the EGM (wavefront approximating to the measure point), while blue colour indicated a negative deflection (wavefront moving away from the measure point). In comparison with the EGMs map obtained for the atria-blood model, there are not significant differences in the propagation patterns apart from the abnormal deflection between time instants 25 and 45 ms (see Figure 3.18.A).

In the case of the atria-torso model, clusters obtained in the RA and LA differ from those ones in the atria-blood model, as depicted in Figures 3.23 and 3.24. In panel A we can observed the distribution of the clusters on the colour-coded maps, and in panel B the traces of the EGMs pertaining to each cluster (black trace represents the mean value of the EGMs in each cluster). As expected, the EGMs computed in regions of the endocardium-blood interface located in the middle of wide orifices, i.e. points far from the tissue, have smaller amplitudes, for instance cluster 10 in the RA (TV orifice) and cluster 5 in the LA (MV orifice). Our computed EGMs ranged between -8 and 6 mV, which is in accordance with the order of magnitude of experimental unipolar EGMs reported in the literature.^{68,145}

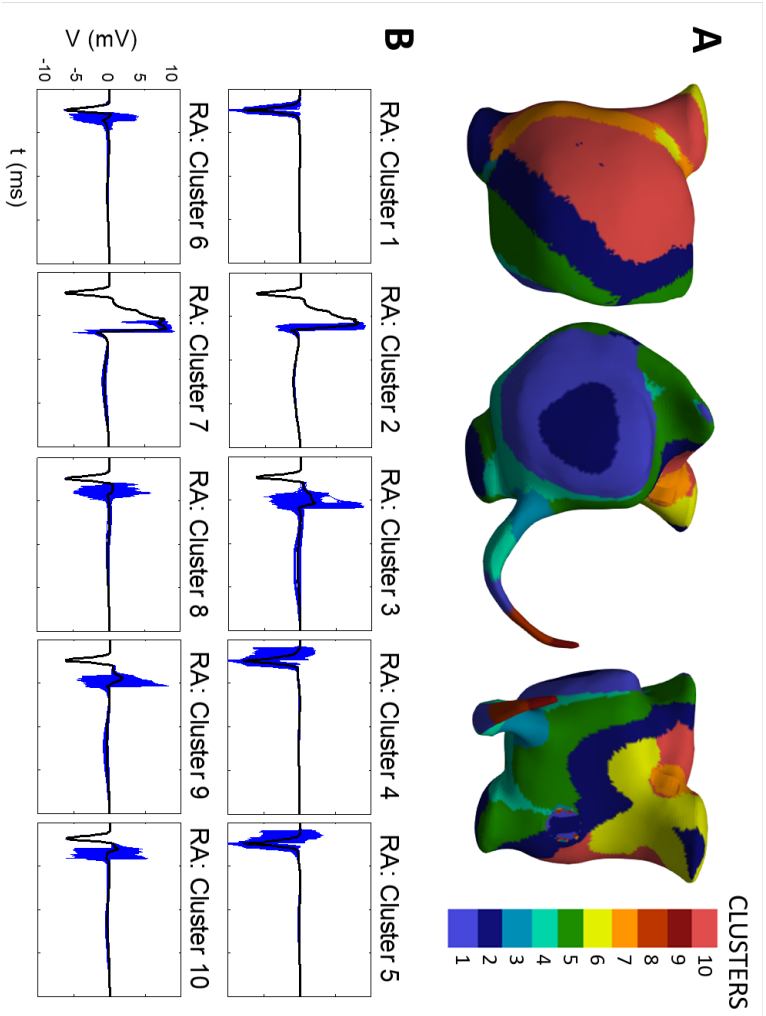


Figure 3.20: Clustering of the endocardial RA EGMs computed in the atria-blood model. A) Colour-coded maps of the 10 clusters on the endocardium-blood interface in the RA. B) Traces of all the EGMs belonging to each cluster (blue) and mean value (black). For each cluster, traces were aligned based on the maximum value.

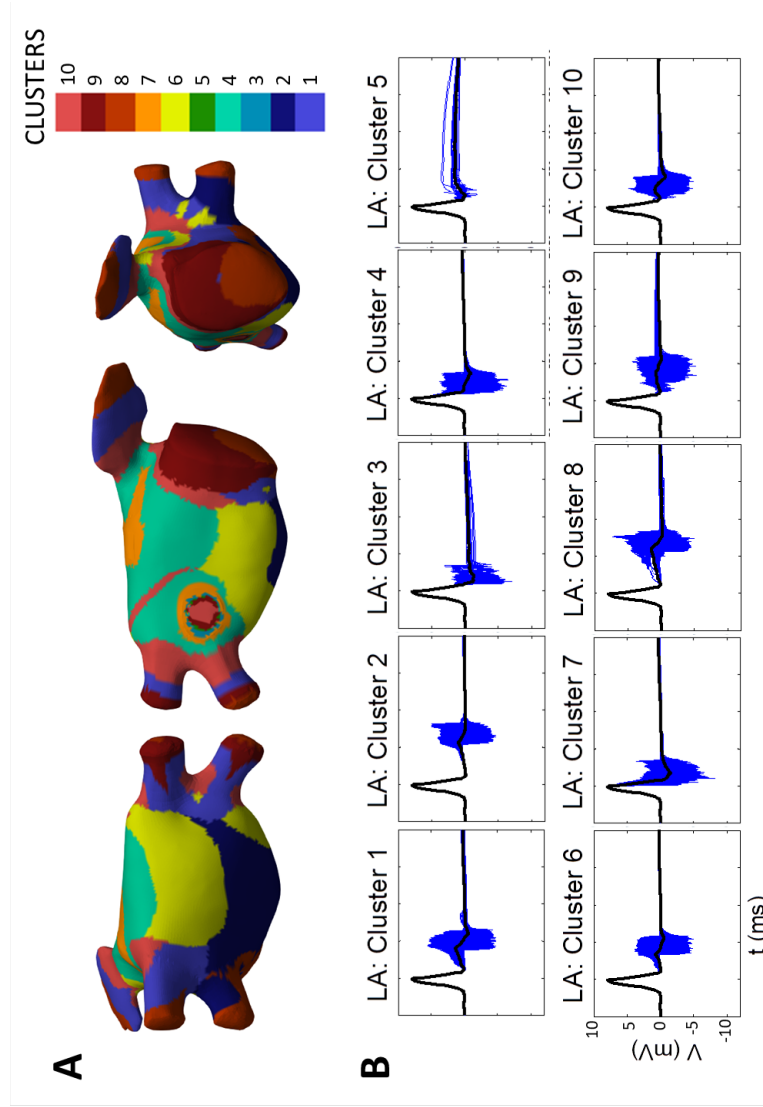


Figure 3.21: Clustering of the endocardial LA EGMs computed in the atria-blood model. A) Colour-coded maps of the 10 clusters on the endocardium-blood interface in the LA. B) Traces of all the EGMs belonging to each cluster (blue) and mean value (black). For each cluster, traces were aligned based on the maximum value.

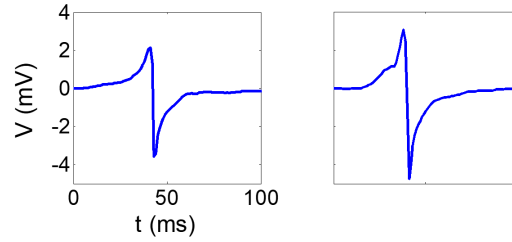


Figure 3.22: EGM in the RA (left) and LA (right) computed with the atria-torso model. No deformations of the EGM are observed.

3.3.3 Simulation of the Electrical Propagation on the Torso Surface

The propagation in our 3D atrial model was validated by comparison with the activation times in the atria, as well as through the duration of the P-waves. Therefore, we show in this section the complete propagation on the torso surface and concretely, the P-waves obtained at the precordial leads. The electrical propagation on the torso surface is shown in Figure 3.18.B (bottom row) through the BSPM. The wavefront spread throughout the atria yielded a dipole on the torso surface. At rest, the torso surface remained at 0 mV (green). After the SAN depolarization, when the wavefront started spreading through the atria, a visible dipole appeared on the BSPM. Atrial depolarization produced the maximum potential registered on the torso surface at $t = 45$ ms, while at $t = 90$ ms the atria was almost entirely depolarized and the potential on the torso surface decreased until reaching the resting potential (once the atria was completely depolarized at about $t = 120$ ms).

The right upper quadrant of the torso yields negative values of the P-waves (for example precordial lead V1, as shown in Figure 3.25), which means that the wavefront moved away. This negative deflection in the potentials is colour-coded in blue on the BSPM. However, the wavefront approximated towards left lower quadrant of the torso and, therefore, P-waves in this region presented positive values (precordial leads V2-V6 in Figure 3.25), colour-coded in red on the BSPM. Other regions on the torso were less sensitive to the atria depolarization and remained at low potential values or practically at rest (green regions on the BSPM).

Precordial leads, shown in Figure 3.25, are in accordance with experimental data reported in the literature,¹⁸⁴ as described in Table 3.7. The P-wave amplitude was measured as the difference among the maximum and minimum values for each lead, while the duration was measured as the period of time between the first and last values different to 0 mV.

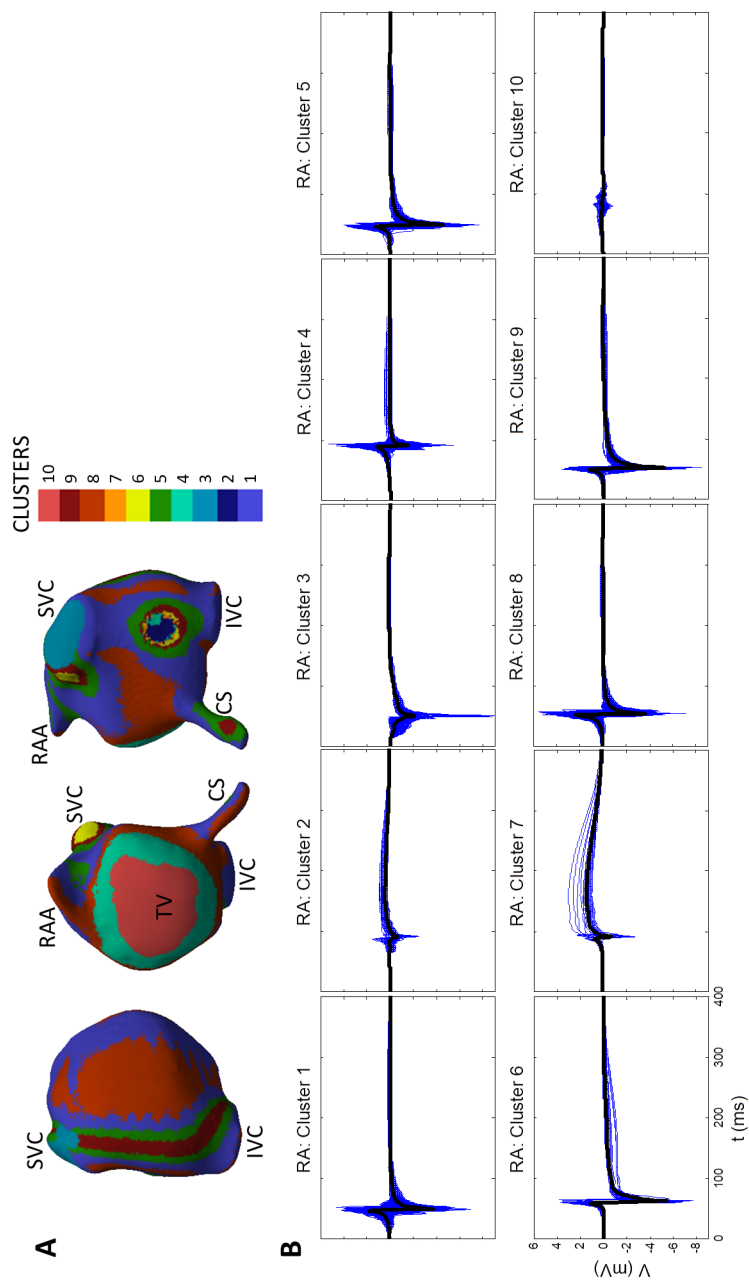


Figure 3.23: Clustering of the endocardial RA EGMs computed in the atria-torso model. A) Colour-coded maps of the 10 clusters on the endocardium-blood interface in the RA. B) Traces of all the EGMs belonging to each cluster (blue) and mean value (black).

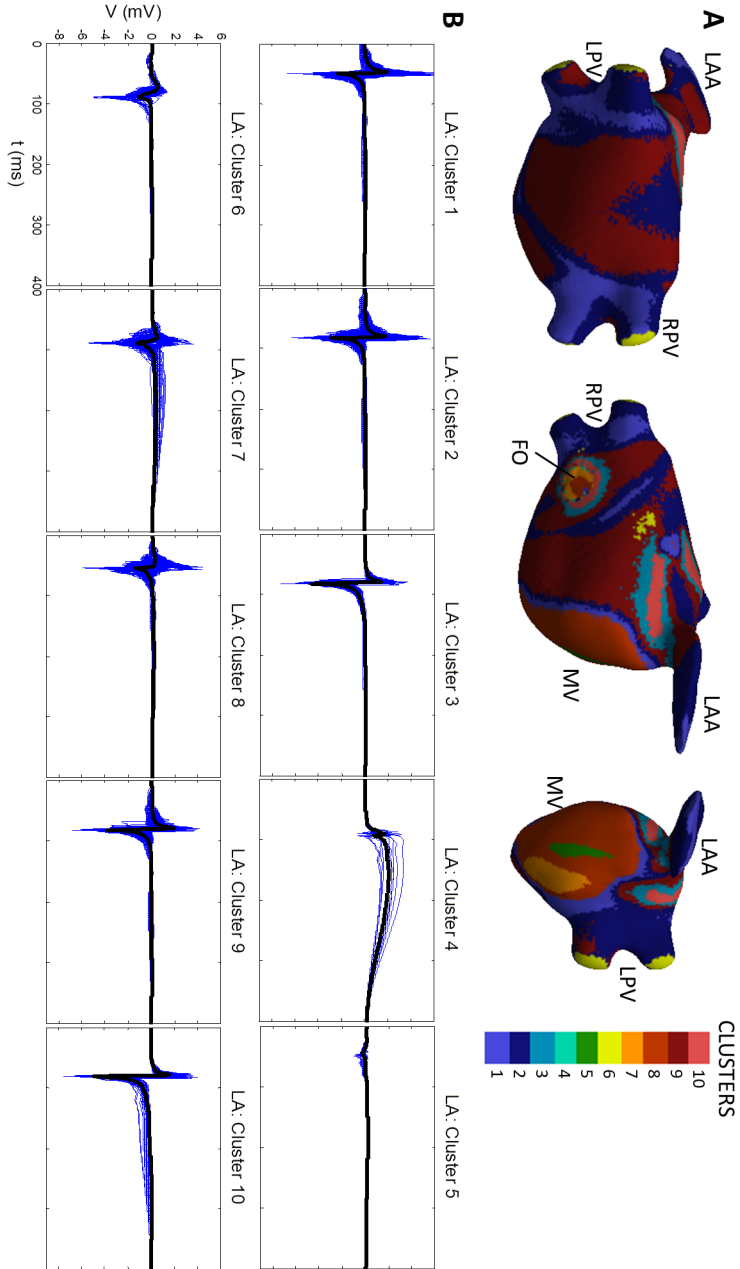


Figure 3.24: Clustering of the endocardial LA EGMs computed in the atria-torso model. A) Colour-coded maps of the 10 clusters on the endocardium-blood interface in the L.A. B) Traces of all the EGMs belonging to each cluster (blue) and mean value (black).

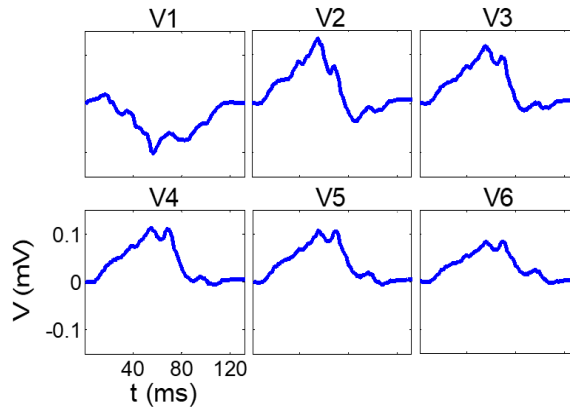


Figure 3.25: P-waves at the precordial leads simulated with the atria-torso model.

	Simulated P-waves		Experimental P-waves	
	Amplitude (mV)	Duration (ms)	Amplitude (mV)	Duration (ms)
V1	0.12	120	0.13 ± 0.06	105 ± 20
V2	0.17	116	0.12 ± 0.05	100 ± 21
V3	0.13	118	0.10 ± 0.04	104 ± 20
V4	0.12	114	0.09 ± 0.03	103 ± 18
V5	0.11	110	0.08 ± 0.03	103 ± 18
V6	0.09	113	0.07 ± 0.02	106 ± 18

Table 3.7: Amplitude and duration of the simulated P-waves at the precordial leads, and comparison with experimental data reported by Lin et al.¹⁸⁴

3.4 Discussion

The aim of this chapter was to develop a realistic model as a tool for mapping the atrial electrical activity in humans. For this purpose, firstly we had to adjust the unicellular models to reproduce the human atrial APs in physiological conditions. Secondly, we had to build the geometrical meshes corresponding to a sheet of atrial tissue and a realistic 3D atrial model in order to couple the unicellular electrophysiological models and simulate the electrical propagation of the APs. Thirdly, we had to compute the EGMs in the atrial cavities, so we developed two different models for the computation of the ϕ_e : on the one hand, an atria-blood model; and on the other hand, an atria-torso model comprising 7 regions. Finally, we compared the differences between the simulated intracavitary unipolar EGMs obtained with the isolated atria-blood model (not immersed in the torso) and the complete 3D multiscale atria-torso model, in order to select the best approach to map the electrical activity of the atria by using multi-electrode systems in the following chapters.

3.4.1 Unicellular Models

In this PhD thesis, we chose the CRN model to simulate the single cell electrophysiology because of its simplicity, as well as its low computational cost. Despite the fact that it is not stable, as described in Section 3.2.1.1, the CRN model has been frequently used in simulation studies.^{153,185,194} Besides, we demonstrated that after 1 minute of stimulation the changes in the AP characteristics are negligible with respect to the 12th AP reported by the authors in their work,¹²⁸ and also that for simulations up to 15 s of duration, there is only a slight variation in the concentrations and, therefore, it can be considered stable. In addition, we did not use any other available atrial models due to the following reasons. On the one hand, Malekar model¹³³ auto-stimulates under BCLs below 1000 ms even if no external stimulus is applied.⁴⁴ As a consequence, we discarded the Malekar model and its close relatives, the Nygren¹²⁷ and Koivumäki¹³⁴ models. On the other hand, since the aim of this PhD thesis was not the study of calcium dynamics or the mechanisms generating and maintaining AF, but it was focused on evaluating the ability of multi-electrode systems to map the atrial electrical activity, we also discarded the Grandi model,¹³⁵ which better describes the calcium dynamics but presents a prohibitively high computational cost in 3D simulations.

3.4.2 3D Atrial Model

Firstly, the atrial heterogeneity adjusted at unicellular level through the variation of the maximum conductance of the I_{to} , I_{CaL} and I_{Kr} currents, which was based on experimental data and previous computational works (see Section 3.2.1.2), yielded a variation in the APD among regions with the same trend of the experimental data.⁶⁰⁻⁶² Secondly, the σ_L and σ_T/σ_L adjusted in the block of atrial tissue provided different CVs with different anisotropy ratios depending on the atrial region, as shown in Table 3.4, which permitted fine tune the CVs in the realistic 3D atrial model. It should be noted that although each atrial region is described by the unicellular model together with the type of tissue (combination of σ_L and σ_T/σ_L), it is actually the type of tissue what plays the main role in the computation of the CV and mainly modifies its value. Same type of tissue and different unicellular models yielded the same CV value, while same unicellular model but different types of tissue yielded different CV values, as reported in Table 3.4.

As a result, once we simulated V_m propagation in the 3D atria, activation times and patterns were in accordance with the experimental observations reported by Lemery et al.¹⁸³ and Zhao et al.¹⁹⁵ The electrical wavefront originated at the SAN and propagated from the RA to the LA through inter-atrial preferential conduction bundles such as BB and LFO. It should be highlighted that activation times reported by Zhao et al.¹⁹⁵ are shorter because

in their study the isolated heart was exposed to 10 nM isoproterenol perfusion (HR of 115 bpm). However, similarly to the propagation patterns in our simulation, as well as to data reported by Lemery et al,¹⁸³ last regions to be activated in the atria were the MV, LAA and LPV.

3.4.3 Intracavitary EGMs

Since in this PhD thesis we are not focused on mechanisms of activation in the atria but in mapping their electrical activity, to solve the V_m propagation we adopted the monodomain formalism, which is less computationally demanding than the bidomain formalism.¹⁸⁰ However, we did use a bidomain formalism to compute the ϕ_e (EGM and ECG). To accomplish this in a more computationally efficient way, we solved the bidomain formalism by splitting the problem into two steps by decoupling the V_m and ϕ_e computations, as done in previous studies.^{158,185} This is allowed since the monodomain approach provides sufficient accuracy in the absence of external currents,^{166,196} as for example those which would be generated by a defibrillator.

3.4.3.1 Atria-Blood Model and Atria-Torso Model

One of the specific objectives of this PhD thesis was to build a realistic multiscale 3D model to compute the intracavitary EGMs in order to map the electrical activity of the human atria. Therefore, in this chapter we developed the atria-blood and the atria-torso models to compare their outcomes and obtain the best tool to carry out our simulations. This involves obtaining the most realistic intracavitary EGMs with the lowest computational cost.

The reason why we built the atria-blood and the atria-torso models for the computation of the intracavitary EGMs was the fact that we wanted to increase the spatial resolution between nodes on the endocardial surface, as well as the inner atrial blood, of the torso developed by Ferrer et al,¹⁴⁸ which had only approximately 34000 nodes surrounding the myocardial region. With our atria-blood model, the nodes belonging to the endocardium-blood interface ascended to 47700 (24224 nodes in the RA and 23476 in the LA), which means an increase of 40% with respect to the atrial region in Ferrer et al,¹⁴⁸ whereas in the case of the atria-torso model the nodes belonging to the endocardium-blood interface ascended to 49994 (25175 nodes in the RA and 24819 in the LA), i.e. an increase of 47%. However, although the amount of nodes was slightly higher on the endocardium-blood interface for the atria-torso model, the spatial resolution remained the same (0.5 mm).

Regarding the total number of nodes in the mesh for the atria-blood and atria-torso models, compared to the torso developed by Ferrer et al,¹⁴⁸ there was an increase of 18% and 34%, respectively (the atria-blood model had 11.7% less

nodes than the atria-torso model, i.e. 225042 vs 254976 nodes). Therefore, the atria-blood model seems to be computationally more efficient since it provides the same spatial resolution on the endocardium-blood interface with a smaller number of nodes comprising the entire mesh. However, due to the influence of the absence of torso in the computations, it is not the best tool (see below).

3.4.3.2 Influence of the Torso in the Computation of Intracavitary EGMs

First, the difference in the number of nodes belonging to the atrial myocardium in both models, the atria-blood model (100950 nodes) and atria-torso model (94230 nodes), seemed to have no effect in the propagation patterns observed through the EGMs maps (Figure 3.18). Therefore, the V_m interpolation was satisfactory for both models. However, the approximation made by leaving the atria isolated instead of immersed in the torso did have an effect on the computation of the EGMs, as it provoked a deformation in the EGMs at 25 ms after the SAN stimulation, with a duration of about 20 ms. This distortion of the EGMs was due to the lack of current flux from the atrial myocardium towards the torso. The $\partial\Omega_T$ in the case of the atria-blood model does not correspond to the torso-air non-flux boundary, but to the atria-air non-flux boundary since the atria is isolated instead of immersed in the torso. Therefore, the flux of currents which should flow through the torso have to flow back to the atrial cavities, yielding as a result the distortion of the EGMs. Although a small flux of current towards the atrial cavities was expected, we did not expect that the effect was strong enough to alter the morphology of the EGMs and, therefore, to invalidate the use of our isolated atria-blood model for the calculation of intracavitary unipolar EGMs (which is computationally more efficient than the atria-torso model because the mesh is comprised by a smaller number of nodes).

Second, as a consequence of the EGMs distortion, the clustering carried out with the EGMs on the endocardium-blood interface in the atria-blood model did not provide any valuable information, as they were matched depending on the deflection corresponding to the deformation. Therefore, no difference in amplitude or morphology can be observed for the different atrial regions. However, the deformation of the EGMs might be mitigated in case of bipolar EGMs, as long as both electrodes are contacting the endocardial surface, because the abnormal deflection has the same amplitude and appears at the same time instant. However, in case of bipolar EGMs corresponding to 2 electrodes at different distances to the tissue, the abnormal deflection would be smoothed but not eliminated, since at each distance from the tissue the amplitude of the signal would be different.

Unlike the atria-blood model, the atria-torso model did yield valid intracavitary unipolar EGMs, ranging between -8 mV and 6 mV of amplitude,

with a duration of approximately 50-60 ms corresponding to the depolarization phase. They are in the order of magnitude of experimental data reported in the literature (measured unipolar EGMs ranging between -2 mV and 1 mV, with a duration of approximately 70 ms during the depolarization,¹⁴⁵ or ranging between -4 mV and 3 mV, with a duration of 50 ms¹⁹⁷). Our atria-torso model validation was based on the obtained EGMs, but also on the P-waves obtained at the precordial leads on the torso surface, whose amplitude and duration were in agreement with data reported in the literature.¹⁸⁴ Moreover, the torso model allowed us to carry out a second validation of our simulation of the V_m propagation with the 3D realistic atrial model under physiological conditions. Although it had already been validated through the experimental activation times and patterns in the atria,^{183,195} the propagation was also validated through the EGMs and P-waves computed with the torso model since the outcomes are in accordance with experimental observations.^{145,184,197}

Finally, it should be noted that the effect of an homogeneous or inhomogeneous torso in the computation of the P-waves¹⁵⁸ or the torso impedance on the epicardial signals and the BSPM¹¹⁴ had been studied before. However, the effect that the absence of torso could have in the computations of intracardiac signals had not been studied. For example, Potse et al¹⁶⁶ used an isolated ventricular model to study if there were differences between monodomain and bidomain simulations when computing the ϕ_e . They found out that there were no significant differences regarding the used approach (mono- or bidomain), but ϕ_e were highly influenced by the presence or absence of blood inside the ventricles. Although they compared the epicardial and endocardial EGMs with the EGMs from an isolated heart perfused with a Langendorff system and, therefore, in their simulations they needed an isolated heart model, if their model had been immerse in a torso, they might have observed a similar effect to the one caused by the presence or absence of blood in the cavities due to the flux of currents spreading out of the myocardium towards both, the blood inside the cavities and the torso. In our study, the high influence of the torso in the computation of intracavitary EGMs has been demonstrated.

To sum up, although in this PhD thesis we are not focused on the computation of ECG signals but in the intracavitary EGMs, we consider that the best tool to carry out further simulations with the aim of mapping the atrial electrical activity in humans is a complete realistic multiscale atria-torso model due to the influence of the torso in the computations of unipolar intracavitary EGMs.

Mapping Reentries in a Sheet of Atrial Tissue by Using Multi-Electrode Arrays

The content in this chapter was partially published in:

L. Martínez et al. *Effect of Multi-Electrode Configurations on Accuracy of Rotor Detection in the Atria. Computing in Cardiology, 43:1085-1088, 2016.*

L. Martínez et al. *Are Multi-electrode Arrays able to Differentiate Anatomical from Functional Reentries in an Excitable Sheet? Computing in Cardiology, 42:865-868, 2015.*

4.1 Introduction

Lately, multi-electrode array systems are increasingly being used to map the atrial electrical activity in humans, with the aim of reconstructing spatiotemporal maps to identify focal sources as well as rotors during AF. They are being used as a tool for the diagnosis during ablation procedures in order to improve their outcomes.^{20,21,32,198} However, they have not been systematically analysed for accuracy. Although the minimum inter-electrode distance (d_{ie}) necessary to detect the rotors has already been studied,²¹ the common variation in distance between the electrodes and the tissue present in the clinical setting was not considered. In fact, the analysis of the accuracy of such systems with a real anatomy and non-constant d_{ie} might be difficult. Therefore, although in Chapter 3 we developed a realistic and multiscale atria-torso model as a tool to map the atrial electrical activity by using multi-electrode catheters, we considered necessary a first approach with a simpler scenario in which we can afford several factors separately. This scenario corresponds to the second specific objective of this PhD thesis: the analysis of the factors affecting the accuracy of multi-electrode systems with equidistant d_{ie} when mapping reentries in a sheet of atrial tissue.

In this chapter we describe all the methods needed to achieve the second specific objective of the thesis. First, we will detail all the steps followed to adjust the electrical remodelling at cellular level under pAF and cAF conditions. Second, we will develop several configurations of the sheet of atrial tissue model in order to initiate physiological electrical propagation as well as reentrant activity. Finally, we will compute the unipolar EGMs in order to study the effect on the near- and far-field contributions, the effect of the multi-electrode configurations and the electrode-to-tissue distance on the mapping accuracy, as well as the ability of the multi-electrode systems to differentiate between anatomical and functional reentries.

4.2 Methods

4.2.1 Unicellular Models

As in Chapter 3, the cellular electrical activity of a human atrial myocyte was modeled by the CRN ionic model.¹²⁸ However, it faithfully reflects the electrophysiology of the healthy human atrial myocyte. Therefore, it had to be modified to simulate the remodelling associated to atrial arrhythmias.

4.2.1.1 Electrical Remodelling

In this section we modified the CRN model to account for the remodelling suffered by atrial cells under pAF and cAF conditions.

4.2.1.1.1 Paroxysmal Atrial Fibrillation

According to the experimental data reported in the literature under pAF conditions, the variations performed in the CRN model were different in the RA and the LA.^{30,98–101} As shown in Table 4.1, the remodelling of the LA was applied to the ionic models corresponding to all the structures within the LA (LA, LAA, BBLA, PV and MVR), while the remodelling in the RA was applied to the models corresponding to the structures within the RA (RA/PM, RAA, TVR, CT/BBRA).

	RA/PM	CT/BBRA	TVR	RAA	LA	BBLA	MVR	LAA	PV	Exp.Data
I_{KACH}^a	$0.25I_{KACH-CtrlRA}$				$I_{KACH-CtrlLA}$					^{98,101}
I_{K1}^b	$I_{K1-Ctrl}$				$2I_{K1-Ctrl}$					98
APD _{90-Ctrl} ^c	266	295	197	252	230	253	170	216	204	193 ⁹³ /218 ⁹⁴
APD _{90-pAF} ^c	266	295	197	252	162	198	112	160	147	
Δ APD _{90-pAF}	0	0	0	0	-30	-22	-34	-26	-28	

^a $I_{KACH-CtrlLA} = I_{KACH}$, $I_{KACH-CtrlRA} = 2I_{KACH}$, where I_{KACH} is the formulation in Equation 4.1.

^b $I_{K1-Ctrl}$ is the value of I_{K1} in the CRN model.¹²⁸

^c APD₉₀ (ms) after 1 minute of stimulation at BCL = 500ms.

Table 4.1: Variations in the ionic currents I_{KACH} and I_{K1} used to reproduce the electrical remodelling experimentally observed under pAF conditions; APD₉₀ in control (APD_{90-Ctrl}) and pAF (APD_{90-pAF}) conditions; and variation of the APD₉₀ in pAF with respect to control conditions (Δ APD_{90-pAF} (%)). Exp.Data: experimental data reported in the literature.

The first variation applied to the CRN model was the addition of the I_{KACH} since this model does not consider it and this current plays an important role in the pAF electrical remodelling. We used the formulation from the Grandi et al model,¹³⁵ based on the experimental data from Koumi et al.¹⁹⁹ This current is time independent and voltage and dose dependent, as follows:

$$I_{KACH} = \frac{1}{1 + \left(\frac{0.03}{[ACH]}\right)^{2.1}} \left(0.08 + \frac{0.04}{1 + e^{\left(\frac{V_m + 91}{12}\right)}}\right) (V_m - E_K) \quad (4.1)$$

where [ACh] is the concentration of acetylcholine, ranging from 10^{-4} to 1 μ mol/L, and E_K the equilibrium potential for K^+ , as described in Equation 4.2:

$$E_K = \frac{RT}{zF} \log \frac{[K^+]_o}{[K^+]_i} \quad (4.2)$$

R is the universal gas constant (8.3143 J/mol·K), T is the temperature (310 K), z is the ion charge, F is the Faraday constant ($9.64867 \cdot 10^4$ C/mol), and $[K^+]_o$ and $[K^+]_i$ are the extracellular and intracellular K^+ concentrations, respectively.

In our implementation of the I_{KAC_h} , we set the $[ACh]$ to $0.0001 \mu M$, and the value of the current in the regions within the LA was 2-fold the value in the regions within the RA^{98,101}(Table 4.1):

$$I_{KAC_h-pAF_{LA}} = 2I_{KAC_h-pAF_{RA}} \quad (4.3)$$

In addition, we modified I_{K1} , which is expected to be 2-fold in the regions within the LA under pAF conditions compared to control conditions, while in the RA remains the same⁹⁸ (Table 4.1). All the changes in the ionic currents due to the pAF electrical remodelling were applied after the changes corresponding to the atrial heterogeneity. As in control conditions (see Chapter 3, Section 3.2.1.1), unicellular models were stabilized for 1 minute, but this time with a $BCL = 500$ ms.

After all the remodelling, the maximum dispersion of APD_{90} due to heterogeneity increased under pAF conditions (183 ms versus 125 ms under control conditions). As shown in Table 4.1, with a $BCL = 500$ ms, the longest APD_{90} was the same for control and pAF conditions (295 ms corresponding to the CT/BBRA ionic model), whereas the shortest APD_{90} corresponded to 170 ms in control and 112 ms in pAF conditions, both for the MVR ionic model. Remodelling in the regions within the RA yielded no variations in the APD with respect to control conditions. However, remodelling was stronger within the regions in the LA and, therefore, APD variations were only visible in those regions. As a result, we obtained the APs shown in Figure 4.1.

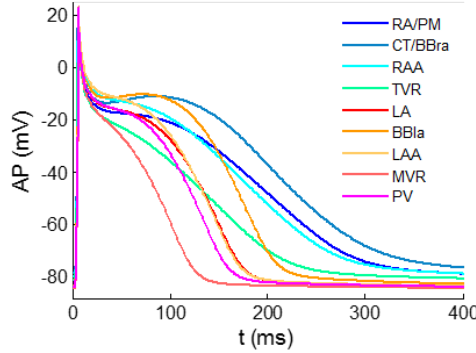


Figure 4.1: Action potentials (AP) corresponding to each variation of the CRN model¹²⁸ under pAF conditions. The shortening of the APs corresponding to the ionic models of the regions within the LA is visible.

4.2.1.1.2 Chronic Atrial Fibrillation

Atrial electrical remodelling corresponding to cAF was introduced through the variation of the maximum conductances of I_{to} , I_{CaL} , I_{K1} , I_{Kur}

and I_{Ks} , in agreement with experimental observations,^{92–94,98,104,106} and similarly to other computational studies.^{130,135,136,151,200,201} As illustrated in Table 4.2, remodelling in the RA (comprising the RA, CT/BBRA, TVR and RAA regional models) was different to that in the LA (which comprises the LA, BBLA, MVR, LAA and PV regional models), according to experimental data reported in the literature. The changes in the ionic currents due to the cAF electrical remodelling were applied after the changes corresponding to the atrial heterogeneity. Unicellular models were stabilized for 1 minute with a BCL = 500 ms.

	RA/PM	CT/BBRA	TVR	RAA	LA	BBLA	MVR	LAA	PV	Exp.Data
I_{to}		0.55					0.25			92
I_{CaL}		0.35					0.35			93,104
I_{K1}		2.00					2.00			94,98,106
I_{Kur}		0.40					0.55			92
I_{Ks}		2.50					2.00			92
APD _{90-ctrl} ^a	266	295	197	252	230	253	170	216	204	193 ⁹³ /218 ⁹⁴
APD _{90-cAF} ^a	127	156	106	133	119	135	99	119	109	93 ⁹³ /100 ⁹⁴
Δ APD _{90-cAF}	-52	-47	-46	-47	-48	-46	-42	-45	-47	-52 ⁹³ / ⁻⁵⁴ 94

^a APD₉₀ (ms) after 1 minute of stimulation at BCL = 500ms

Table 4.2: Variations in the ionic currents (I_{to} , I_{CaL} , I_{K1} , I_{Kur} , I_{Ks}) used to reproduce the electrical remodelling experimentally observed under cAF conditions; APD₉₀ in control (APD_{90-ctrl}) and cAF (APD_{90-cAF}) conditions; and reduction of the APD₉₀ in cAF with respect to control conditions (Δ APD_{90-cAF} (%)) in each atrial region, compared to the experimental data (Exp.Data) reported in the literature.

After the remodelling, APD shortening was within the range of the available experimental observations, around the 50% as in Workman et al⁹³ and Bosch et al⁹⁴ (see Table 4.2). The maximum dispersion of APD₉₀ due to heterogeneity was 57 ms under cAF conditions, compared to 125 ms under control conditions. The longest APD₉₀ was obtained with the CT/BBRA model (295 ms in control vs 156 ms in cAF), while the shortest APD₉₀ corresponded to the MVR ionic model (170 ms in control vs 99 ms in cAF). Resulting APs after cAF remodelling for each atrial region are depicted in Figure 4.2.

4.2.2 Sheet of Atrial Tissue

As explained in Chapter 3, to carry out multicellular simulations there is a need to couple the unicellular models to a geometrical mesh. In this chapter, in order to analyse the effects of the geometrical configuration in the multi-electrode arrays, as well as their ability to distinguish between functional and anatomical reentries, we will perform computer simulations in three different 3D sheets of atrial tissue, whose geometrical meshes will be describe in the following section.

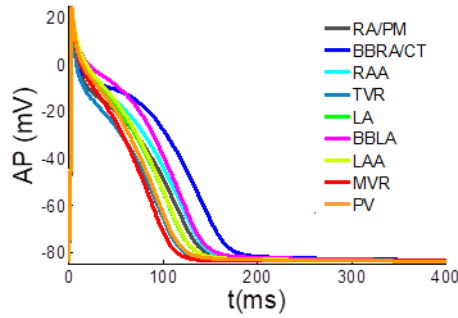


Figure 4.2: Action potentials (AP) corresponding to each variation of the CRN model¹²⁸ under cAF conditions. The APD shortening is visible in all the regions within the RA and the LA, as a consequence of the strong electrical remodelling suffered in cAF.

4.2.2.1 Tissue Geometrical Meshes

In order to carry out computer simulations in three different 3D sheets of atrial tissue, we built three different geometrical meshes corresponding to the LA, PV and MVR tissues (LA_{tissue} , PV_{tissue} and MVR_{tissue} , respectively). As depicted in Figure 4.3, these meshes are a 3D square block of dimensions $4.98 \times 4.98 \times 0.03 \text{ cm}^3$, comprised of hexahedral elements with a spatial resolution between nodes of $300 \mu\text{m}$: 27556 hexahedral elements in the LA_{tissue} , 26612 in the PV_{tissue} and 23916 in the MVR_{tissue} . The number of nodes were 55778, 54024 and 48768 for the LA_{tissue} , PV_{tissue} and MVR_{tissue} meshes, respectively.

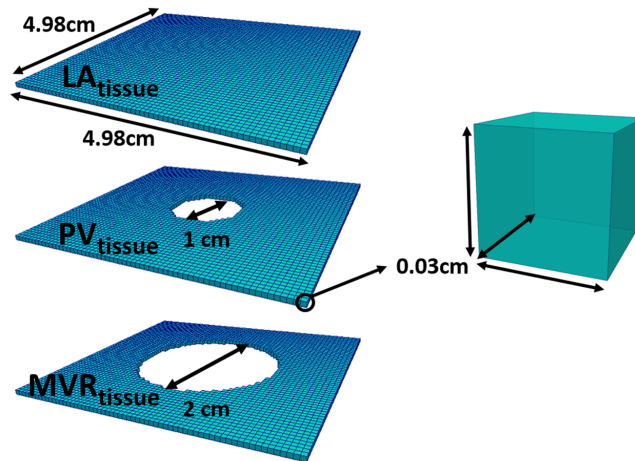


Figure 4.3: Geometrical meshes corresponding to the LA, PV and MVR tissues.

The LA_{tissue} geometrical mesh was built to simulate the electrical propagation under physiological conditions, as well as reentrant activity corresponding to functional reentries. Nevertheless, PV_{tissue} and MVR_{tissue} geometrical meshes were built to simulate anatomical reentries around the PV and MV orifices. The diameter of such orifices was set to 1 cm for the PV and 2 cm for the MV to match with the experimental values reported by Cohen et al.²⁰² 1.1 ± 0.2 cm (mean value \pm standard deviation), ranging from 0.7 to 1.6 cm for the PV; 2.9 ± 0.4 cm, ranging from 2.0 to 3.8 cm.

4.2.2.2 Electrical Propagation

In order to simulate the AP of each cell (node) and their electrical propagation within the tissue, we coupled the corresponding unicellular CRN model to each node in the mesh (LA, PV or MVR unicellular model, in control, pAF or cAF conditions, depending on the simulation). The type of tissue, defined by the σ_L and σ_T/σ_L values, was assigned based on atrial regions in Table 3.4. Then, we solved the monodomain formalism by using the *ELVIRA* software,¹⁸⁰ as explain in Chapter 3, Section 3.2.2. A summary of the simulations performed in this Chapter is detailed in Table 4.3.

Simulations	Stimuli	Conditions	Mesh	Cellular model	N. reentries
Sim1	S1 ^a	Control	LA_{tissue}	LA	0
Sim2	S1-S2 ^b	pAF	LA_{tissue}	LA	1
Sim3	S1-2S2 ^c	pAF	LA_{tissue}	LA	2
Sim4	S1-S2 ^b	pAF	PV_{tissue}	PV	1
Sim5	S1-S2 ^b	pAF	MVR_{tissue}	MVR	1
Sim6	S1-S2 ^b	cAF	LA_{tissue}	LA	1
Sim7	S1-2S2 ^c	cAF	LA_{tissue}	LA	2

^a S1: planar stimulus

^b S1-S2 crossfield stimulation protocol: S1 a planar stimulus and S2 a square stimulus

^c S1-2S2 crossfield stimulation protocol: S1 a planar stimulus and 2S2 two square stimuli

Table 4.3: Summary of simulations performed with the 3D sheets of atrial tissue. Sim1 lasted 500 ms and Sim2-Sim7 lasted 5000 ms.

Electrical activity was initiated by applying: in the case of Sim1, a planar stimulus S1 at the lower edge of the tissue; in the case of Sim2, Sim4, Sim5 and Sim6, a crossfield stimulation protocol S1-S2, S1 being a planar stimulus applied at the lower edge of the tissue and S2 a square stimulus applied at the bottom left corner of the tissue; in the case of Sim3 and Sim7, a crossfield stimulation protocol S1-2S2, S1 being a planar stimulus applied at the lower edge of the tissue and 2S2 two square stimuli, each applied at the bottom left and right corners of the tissue. The crossfield stimulation protocols in Sim2 to Sim7 were performed in order to obtain reentrant activity, i.e. functional and anatomical reentries. In all the simulations, the S1 stimulus was applied 10 ms after the

initiation of the simulation, while S2 was applied at instant 158 ms (Sim2 and Sim3), 160 ms (Sim4), 130 ms (Sim5), 142 ms (Sim6) and 151 ms (Sim7). All the simulations lasted 5000 ms, except for Sim1 which was run for 500 ms.

4.2.3 Mapping the Electrical Activity

In order to map the electrical activity of the atrial sheets of tissue, we first calculated the unipolar EGMs through the computation of the ϕ_e and, then, performed a phase and/or frequency analysis, depending on the sub-study within this chapter. For this purpose, we built two new geometrical meshes, comprised of tetrahedral elements, which are described in the following section.

4.2.3.1 3D-Block Meshes

First, we built two different meshes to check if the effect provoked by the absence of torso in the computation of the EGMs, observed in Chapter 3 with the realistic atria-blood model, can also be observed when computing the EGMs with a block of tissue. The first mesh had the elements distributed in three regions: torso, tissue and blood (TTB mesh); the second mesh in two regions: tissue and blood (TB mesh). Both meshes are depicted in Figure 4.4.

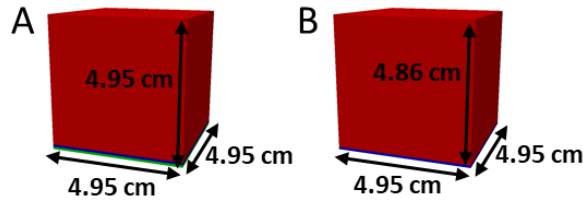


Figure 4.4: 3D block meshes to compute unipolar EGMs. A) TTB mesh: torso (green), atrial tissue (blue) and blood (red) regions. B) TB mesh: atrial tissue (blue) and blood (red) regions.

The dimensions of the TTB mesh were $4.95 \times 4.95 \times 4.95 \text{ cm}^3$, whose torso and tissue regions were a layer of dimensions $4.95 \times 4.95 \times 0.09 \text{ cm}^3$ and whose blood region was a block of dimensions $4.95 \times 4.95 \times 4.77 \text{ cm}^3$. Similarly, the TB mesh dimensions were $4.95 \times 4.95 \times 4.86 \text{ cm}^3$ (the dimensions of the tissue and blood regions remained as for the TTB mesh). In both cases, the distance between nodes was not constant for the entire mesh. However, for the torso and blood layers it corresponded to 0.09 cm, and in the block of blood it varied between 0.09 cm and 0.5 cm (see Figure 4.5 A). This variation was intentioned in order to have the same spatial resolution at the multi-electrode arrays locations.

The conductivities assigned to each region within the TTB and TB meshes

corresponded to the values shown in Table 3.6: 7 mS/cm for the blood and 2.39 mS/cm for the torso. In case of the atrial tissue, conductivity values depended on the type of tissue (LA, PV or MVR) and were the ones defined in Table 3.4 for such regions.

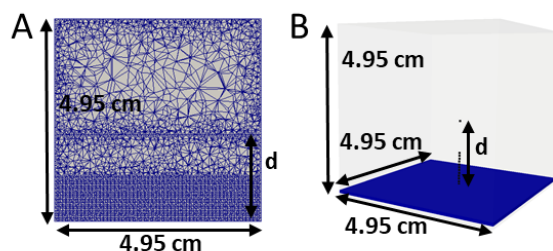


Figure 4.5: Tetrahedral elements size depending on the location of the multi-electrode arrays. A) Variation of the spatial resolution between nodes depending on the size of the tetrahedral elements (vertical slice). B) Virtual electrode located in the center of the mesh at several distances from the tissue (in blue).

4.2.3.2 Virtual Electrodes

4.2.3.2.1 Virtual Central Electrode

First, in order to analyse the effect of the presence and absence of the torso layer in the 3D block model under physiological conditions (Sim1), we computed the unipolar EGMs at a virtual central electrode located in the centre of the atrial tissue at several distances (see Figure 4.5B). An electrode was located at the epicardium, at the endocardium and at a distance of 0.9 mm, 1.8 mm, 2.7 mm, 3.6 mm, 4.5 mm, 5.4 mm, 6.3 mm, 7.2 mm, 8.1 mm, 9.0 mm, 9.9 mm and 19.8 mm from the endocardium. This central electrode was also used to study the contribution of the near- and far-field sources in the computation of the EGMs. For this purpose, we defined near-field (NF) and far-field (FF) regions, as illustrated in Figure 4.6. The radius of the disc corresponding to the NF sources ranged from 0.25 cm to 2 cm.

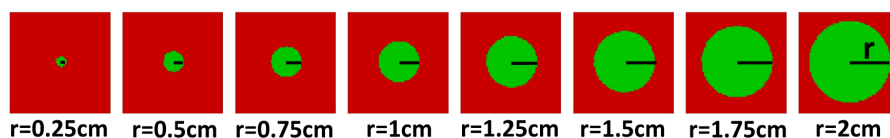


Figure 4.6: Regions of tissue defined as near- and far-field sources. Near-field sources: green disc, with variable radius ranging from 0.25 cm to 2 cm; Far-field sources: remaining tissue (in red).

4.2.3.2.2 Virtual Multi-electrode Array Configurations

In order to map the reentrant electrical activity in the sheet of atrial tissue, we built different multi-electrode array configurations with constant d_{ie} . Then, we studied the accuracy of such configurations when mapping reentries. On the one hand, we located the arrays at different distances from the tissue. The locations were at the endocardium and at a distance of 0.9 mm, 2.7 mm, 5.4 mm, 9.9 mm and 19.8 mm from the endocardium. On the other hand, we varied the spatial resolution of the arrays, i.e. we varied the d_{ie} from 0.9 mm to 18 mm. All the multi-electrode array configurations are summarized in Figure 4.7.

Multi-electrode Array Configurations				
Atrial myocardium: blue				
Multi-electrode Array: black dots				
Array	d_{ie} (mm)			
d (mm)	0.9	4.5	9	18
0.9				
2.7				
5.4				
9.9				
19.8				

Figure 4.7: Virtual multi-electrode array configurations. The constant inter-electrode distance (d_{ie}) ranged between 0.9 and 18 mm, while the distance from the array to the endocardium (d) ranged from 0.9 to 19.8 mm.

4.2.3.3 Computation of the EGMs, Phase Maps and Dominant Frequency Maps

4.2.3.3.1 Unipolar EGMs

In our simulations, the electrical propagation of the APs was solved by the monodomain formulation and the unipolar EGMs were computed through the ϕ_e calculation by an approximation of the bidomain formulation in two steps, as explained in Chapter 3, Section 3.2.3.1, with a temporal resolution of 1 ms. First, we interpolated the V_m obtained for the atrial sheets of tissue onto the atrial layer in the finite-element tetrahedron mesh. Then, the unipolar EGMs were computed, on the one hand, in the atrial blood block at the specific coordinates where the virtual electrodes (single central electrode and multi-electrode arrays) were located. On the other hand, EGMs were also computed at the epicardium/endocardium.

4.2.3.3.2 Phase Maps and Rotor Tracking

The spatial resolution of the tissue in the tetrahedral mesh (distance between nodes), as well as the best spatial resolution among the multi-electrode array configurations, was 0.9 mm. Therefore, first, computed EGMs were linearly interpolated to achieve a spatial resolution of 0.3 mm in order to obtain a better visualization of the phase maps and a more accurate detection of the PSs. Second, we applied the HT to the interpolated EGMs (Equation 4.4), as in prior studies,^{15, 203, 204} and computed the instantaneous phase θ , whose values ranged from $-\pi$ to π radians (Equation 4.5):

$$HT[EGM(t)] = \frac{1}{\pi} \int_{-\infty}^{\infty} \frac{EGM(\tau)}{t - \tau} d\tau \quad (4.4)$$

$$\theta = \tan^{-1} \left(\frac{HT[EGM(t)]}{EGM(t)} \right) \quad (4.5)$$

To visualize the phase maps corresponding to the interpolated EGMs recorded by the virtual multi-electrode array configurations, we built a 2D mesh comprised of square elements, and assigned the instantaneous phase value (θ) of each interpolated signal to its corresponding node in the mesh (see Figure 4.8). We excluded the first and last 500 ms of the signals to avoid transformation artifacts, resulting in phase maps as frames of movies of 4 s long.

Finally the PS points, where all phases converge, were computed to track rotor's trajectory:^{168, 205-207}

$$\oint \nabla \theta dr = \pm 2\pi \quad (4.6)$$

where r is the close curve surrounding the PS at the center of the reentry. To approximate Equation 4.6 and automatically localize PSs, we adapted the method proposed by Rogers.¹⁷¹ As shown in Figure 4.8, each node in the mesh has a θ value. Thereby, we computed for each element in the mesh and all simulation time steps, the variations of phase among its nodes (space gradients). The automatic PS detection algorithm was implemented as follows:

1. Computation of the variation of phase among the nodes comprising each edge in the element:

$$\begin{cases} Edge_1 = Phase_B - Phase_A \\ Edge_2 = Phase_C - Phase_B \\ Edge_3 = Phase_D - Phase_C \\ Edge_4 = Phase_A - Phase_D \end{cases} \quad (4.7)$$

2. Adjustment of the variation of phase values within the range $[-\pi, \pi]$:

$$Edge'_i = \begin{cases} Edge_i, & \text{if } Edge_i \in [-\pi, \pi] \\ Edge_i + 2\pi, & \text{if } Edge_i < -\pi \\ Edge_i - 2\pi, & \text{if } Edge_i > \pi \end{cases} \quad (4.8)$$

where $i = 1, 2, 3, 4$

3. Computation of the complete variation of phase along the element:

$$Phase_{Variation} = Edge'_1 + Edge'_2 + Edge'_3 + Edge'_4 \quad (4.9)$$

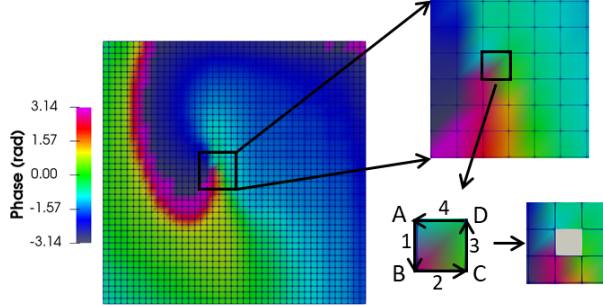


Figure 4.8: PS detection on the multi-electrode arrays phase maps. θ was assigned to each node in the 2D mesh. Magnifying the region of the rotor, we observe its tip within one of the elements in the mesh, whose nodes have been named as A-D and edges as 1-4. The arrows indicate the direction to surround the elements and compute the phase variations. The element detected as a PS ($\pm 2\pi$) was white coloured and overlapped to the phase map to track the rotor trajectory. Snapshot of the phase map corresponds to Sim2.

For those elements around which all phases converged, the summed phase variation along a closed surrounding path was $\pm 2\pi$. Those elements were designated as PSs and white coloured superimposed on the phase maps (as shown in Figure 4.8). EGMs interpolation, HT of the EGMs, θ computations and automatic PS detection algorithms were implemented in custom-made software routines in *MATLAB*.

The accuracy of detecting rotors and its meandering by the multi-electrode array configurations was evaluated by the sensitivity and the specificity of the PS pixel-by-pixel location match between the array and the atrial layer.

4.2.3.3 Dominant Frequency Maps

To study the ability of multi-electrode arrays to distinguish between anatomical and functional reentries, in addition to the phase maps and the PSs detection, we also computed the DF maps. For this purpose, the interpolated EGMs were processed as in Tobón et al.¹⁵¹ First, we band-pass filtered the EGMs between 40 and 250 Hz through a 4th order Butterworth filter. Then, we rectified the signals and applied a low-pass filter at 20 Hz (4th order Butterworth filter). After this, we computed the power spectral density (PSD) with Welch's method and looked for the local maxima. The DF of each EGMs was defined as the frequency corresponding to the highest peak of the PSD. The algorithm to generate the DF maps was implemented in custom-made software routines in *MATLAB*. An example of an EGM before and after the filtering as well as its PSD and the corresponding DF is shown in Figure 4.9.

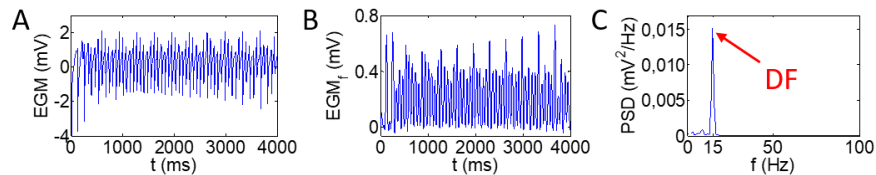


Figure 4.9: EGM before (A) and after (B) filtering, PSD of the filtered EGM and resultant DF (C).

Finally, all the DF values were assigned to the 2D mesh of square elements to visualize the DF maps, similarly to the phase maps.

4.3 Results

In this chapter we performed different simulations in order to carry out several sub-studies. First, in control conditions, we analysed the influence of a torso layer in the 3D block of tissue and blood when computing the EGMs. In addition, we also studied the effect of the NF and FF sources in the generation of the EGMs. Second, we simulated pAF conditions with two aims: to analyse the accuracy of the multi-electrode array systems when mapping functional reentries depending on their configuration, and their ability to differentiate between functional and anatomical reentries. Finally, we analysed the differences in the reentries generated under pAF and cAF conditions. All the results yielded from these studies are exposed in the following sections.

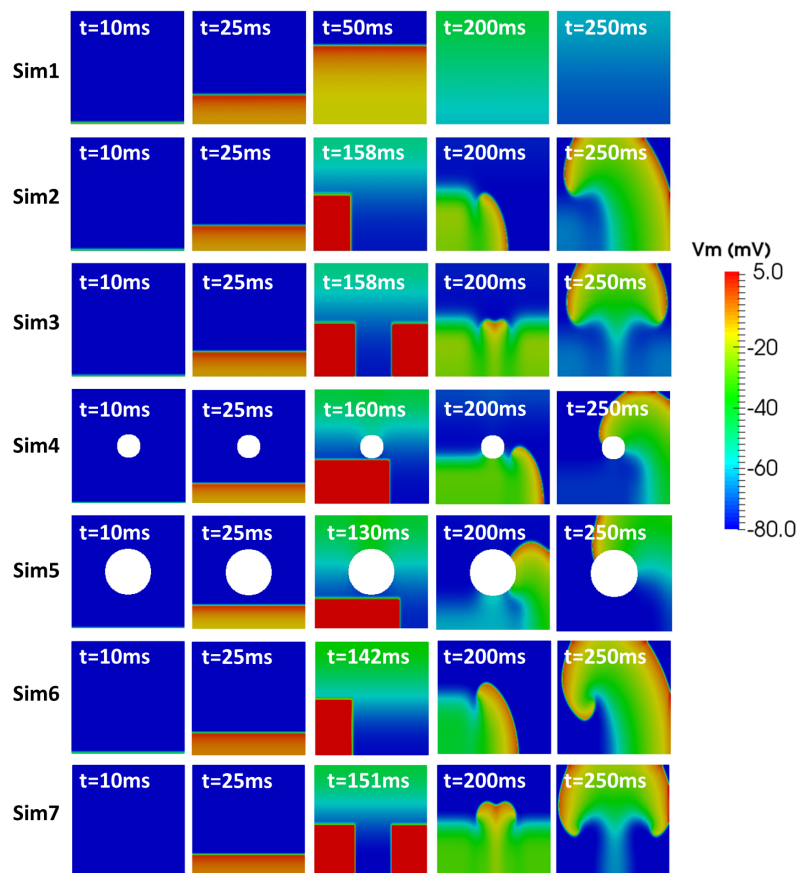


Figure 4.10: Propagation of the APs in the simulations performed with sheets of atrial tissue: LA (Sim1, Sim2, Sim3, Sim6, Sim7), PV (Sim4) and MVR (Sim5).

4.3.1 Simulation of the Electrical Activity in a 3D Sheet of Atrial Tissue

As explained in Section 4.2.2.2, we performed different simulations (see Table 4.3). As a result of solving the APs with the monodomain formalism by using the *ELVIRA* software with a time step of 0.01 ms, we obtained the APs propagation patterns shown in Figure 4.10.

Sim1 corresponded to a simulation of 500 ms of duration under physiological conditions, where a planar stimulus was applied at the lower edge of the LA_{tissue} . In the snapshots shown in Figure 4.10 the propagation of the planar wavefront can be observed. The remaining simulations had a duration of 5000 ms. In Sim2, we simulated a functional reentry in the LA_{tissue} under pAF conditions. Electrical activity was initiated by the S1-S2 stimulation protocol. After the stimulation, activity was maintained due to the auto-perpetuation of the reentry for the whole simulation time. Sim3 was similar to Sim2, except for the fact that the stimulation protocol applied was the S1-2S2 and, therefore, we obtained two functional reentries in the LA_{tissue} during the whole simulation time. Electrical activity was also self-maintained once the stimulation ended. Sim4 and Sim5 had the same stimulation protocol than Sim2, but the tissue corresponded to PV_{tissue} and MVR_{tissue} , respectively. Thereby, for both cases we obtained an anatomical reentry rotating around the orifice, self-maintained after the stimulation. Finally, Sim6 and Sim7 corresponded to functional reentries in the LA_{tissue} , but in this case under cAF conditions. Electrical activity was also initiated by the S1-S2 and S1-2S2 stimulation protocols and then self-maintained for the whole simulation time.

4.3.2 Influence of the Torso in the EGMs Computation

Similarly to Chapter 3, we wanted to study the influence of the torso in the computation of the EGMs, but in this case by using a 3D block of atrial tissue and intracavitary blood. For this purpose, we performed Sim1 and computed the unipolar EGMs at the coordinates of a virtual electrode located in the center of the tissue at the epicardium, at the endocardium and at a distance of 0.9 mm, 1.8 mm, 2.7 mm, 3.6 mm, 4.5 mm, 5.4 mm, 6.3 mm, 7.2 mm, 8.1 mm, 9.0 mm, 9.9 mm and 19.8 mm from the endocardium. After the computation of ϕ_e by using the bidomain approximation (see Section 3.2.3.1) with the TTB and TB meshes, we obtained the unipolar EGMs shown in Figure 4.11. Unlike the 3D realistic atria-blood and atria-torso models, differences were slight with the TTB and TB models. In the absence of a torso layer (TB mesh) the EGMs were not distorted, as occurred with the atria-blood model in Chapter 3. However, the absence of torso provoked an increase in the EGM amplitude. The strongest variation among the EGMs computed with the TTB and TB models can be observed at the epicardium, as illustrated in Figure 4.11A. When the electrode

was set at a distance of 19.8 mm from the endocardium, differences between both EGMs (TTB and TB meshes) were negligible (Figure 4.11N).

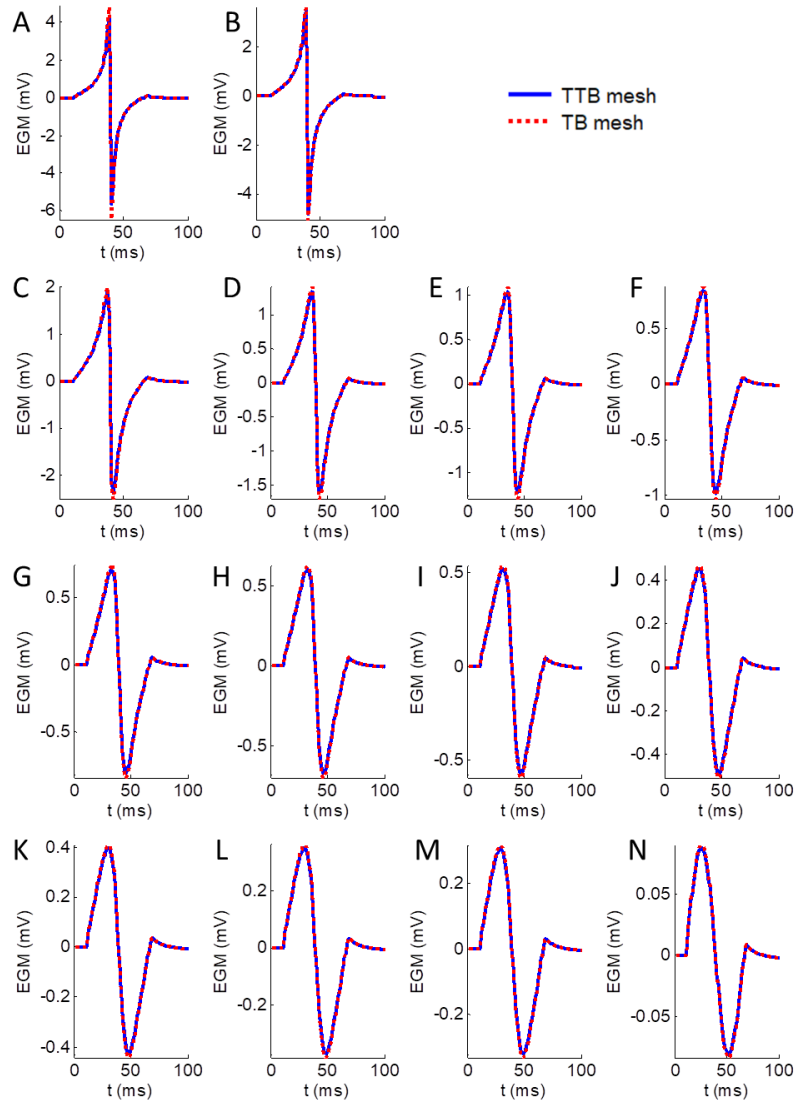


Figure 4.11: Comparison of the EGMs computed with the TTB and TB meshes. EGMs correspond to the virtual electrode located at the epicardium (A), at the endocardium (B), and at a distance of 0.9 mm (C), 1.8 mm (D), 2.7 mm (E), 3.6 mm (F), 4.5 mm (G), 5.4 mm (H), 6.3 mm (I), 7.2 mm (J), 8.1 mm (K), 9.0 mm (L), 9.9 mm (M) and 19.8 mm (N) from the endocardium.

In order to quantify the influence of the torso layer on the amplitude of the EGMs, the maximum amplitude (A_{max}), the minimum amplitude (A_{min}) and the peak-to-peak amplitude (A_{pp}) of the EGMs computed with the TTB and TB meshes for all electrode locations are summarized in Table 4.4. The increase in the A_{pp} for each EGM computed using the TB mesh with respect to its corresponding EGM computed using the TTB mesh was defined as ΔA_{pp} .

	TTB mesh			TB mesh			ΔA_{pp} (%)
	A_{max} (mV)	A_{min} (mV)	A_{pp} (mV)	A_{max} (mV)	A_{min} (mV)	A_{pp} (mV)	
Epi	4.19	-5.66	9.85	4.82	-6.46	11.28	+14.52
Endo	3.54	-4.84	8.38	3.66	-5.04	8.70	+3.82
d=0.9mm	1.88	-2.36	4.24	2.01	-2.49	4.50	+6.13
d=1.8mm	1.34	-1.60	2.94	1.41	-1.69	3.10	+5.44
d=2.7mm	1.05	-1.23	2.28	1.10	-1.30	2.40	+5.26
d=3.6mm	0.84	-0.98	1.82	0.88	-1.01	1.89	+3.85
d=4.5mm	0.70	-0.80	1.50	0.74	-0.84	1.58	+5.33
d=5.4mm	0.60	-0.67	1.27	0.62	-0.70	1.32	+3.94
d=6.3mm	0.52	-0.57	1.09	0.54	-0.59	1.13	+3.67
d=7.2mm	0.45	-0.49	0.94	0.47	-0.51	0.98	+4.25
d=8.1mm	0.39	-0.42	0.81	0.41	-0.44	0.85	+4.94
d=9.0mm	0.34	-0.37	0.71	0.36	-0.38	0.74	+4.22
d=9.9mm	0.30	-0.32	0.62	0.32	-0.33	0.65	+4.84
d=19.8mm	0.09	-0.08	0.17	0.09	-0.08	0.17	+0.00

Table 4.4: Amplitude of the EGMs computed with the TTB and TB meshes at each electrode location. A_{max} : maximum amplitude; A_{min} : minimum amplitude; A_{pp} : peak-to-peak amplitude; ΔA_{pp} : increase in the A_{pp} of the EGM computed using the TB mesh with respect to the A_{pp} of the EGM computed using the TTB mesh. d : electrode-to-endocardium distance.

The strongest increase in the amplitude due to the lack of a torso layer was measured at the epicardium (+14.52%), which is reasonable since for the TB mesh there was no flux of current towards the torso. At the endocardium and at a distance from it up to 9.9 mm, the increase in the amplitude of the EGMs ranged from 3.67 to 6.13 % (it was not inversely proportional to the distance). At a distance of 19.8 mm there were no differences between the EGMs, so the absence of a torso layer did not affect the computation of the EGMs. As expected, for both groups of EGMs (those computed with the TTB and the TB meshes), the amplitude decreased with the distance to the tissue. In addition to the values shown in Table 4.4, this effect can also be noticed in Figure 4.12. Besides the attenuation of the amplitude with the distance to the tissue, the magnification of the amplitude for the EGMs computed with the TB mesh can also be observed in panel A, compared to those computed with the TTB mesh. Panel B quantifies the attenuation with the distance to the tissue. For both meshes, the amplitude of the EGM was attenuated to less than 50% at a distance of 0.9 mm from the endocardium, compared to the epicardium; to less than 10% from 7.2 mm away; and to less than 5% from distances higher than 9.9 mm.

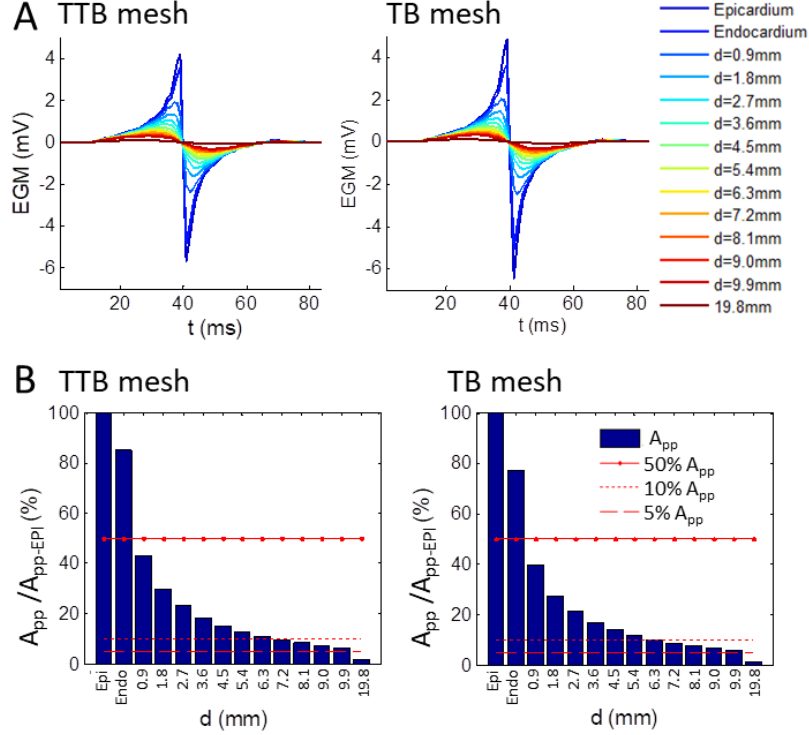


Figure 4.12: Attenuation of the EGMs with the electrode-to-tissue distance. A) Plots of the EGMs at each location of the virtual electrode. B) Ratio of the peak-to-peak amplitude of the EGM at each electrode (A_{pp}) with respect to the peak-to-peak amplitude of the EGM at the epicardium (A_{pp-EPI}).

4.3.3 Near and Far Field Contributions

Sim1 was also performed to analyse the influence of the NF and FF sources in the computation of the EGMs. For this purpose, we divided the LA_{tissue} in two regions, as shown in Figure 4.6. The radius (r) of the disc corresponding to the NF sources region ranged from 0.25 to 2 cm in order to vary the extension considered as NF contribution. For each of the NF-FF configurations of the tissue and all the virtual electrode positions, the EGMs were computed accounting only for the NF sources (EGM_{NF}), with the aim of being compared to the regular EGMs computed in the previous section with the whole LA_{tissue} at the same electrode positions. Results are illustrated in Figure 4.13. First, we computed the percentage of peak-to-peak amplitude that represents the EGM_{NF} with respect to the regular EGM at the same

electrode position (Figure 4.13A). Second, in order to quantify the resemblance of both signals at each electrode position, we calculated the correlation (Figure 4.13B). For a certain value of r , the contribution of the NF sources to the whole signal decreased with the distance to the tissue (a decrease in A_{ppNF}/A_{pp} and correlation values can be observed), which means that FF sources contribution increased. Finally, based on the data in panels A and B, we defined the minimum r needed to achieve 90% for the A_{ppNF}/A_{pp} and 0.9 for the correlation (black dashed lines in A and B) at each electrode position (Figure 4.13C). As depicted, the radius had to increase with the distance to the tissue to maintain the 90% and 0.9 values in the computations. When the electrode was located at a distance of 19.8 mm from the endocardium, none of the tested r yielded the 90% of A_{ppNF}/A_{pp} .

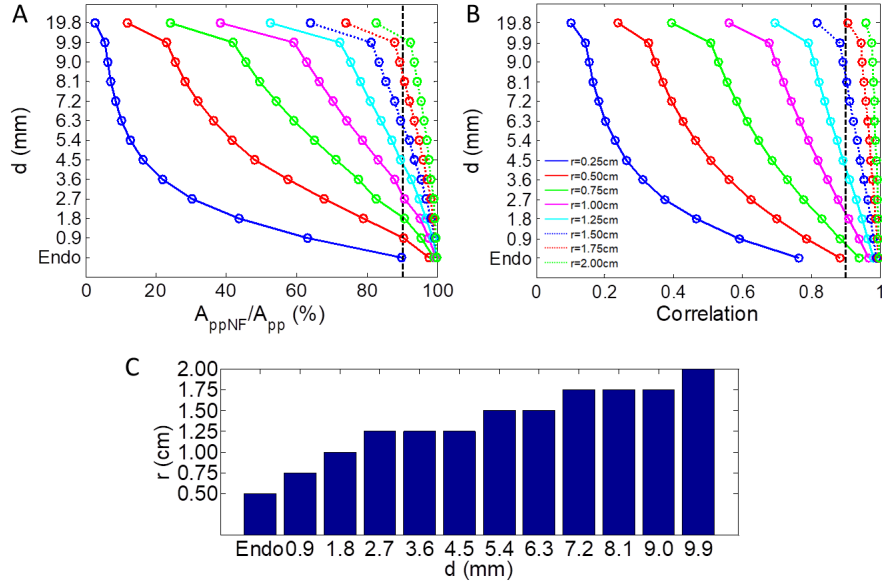


Figure 4.13: NF and FF contributions. Ratio of the A_{pp} (A) and correlation (B) between the EGM computed with the whole atrial tissue and the EGM computed only with the NF sources (EGM_{NF}) for each electrode and each radius defining the NF sources. Black dashed line indicates a value of 90% in A and 0.9 in B. C) Radius r needed to achieve the 90% for the A_{ppNF}/A_{pp} and 0.9 for the correlation, depending on the electrode-to-tissue distance. Endo: $d=0$ mm.

We considered that in contact to the tissue, the major contribution of the signal had to be due to the NF sources. For this purpose, we established as an acceptable threshold a value of 90% for the A_{ppNF}/A_{pp} and 0.9 for the correlation. Therefore, in our study, in which we varied the radius of the NF region, among all the possible NF sources configurations, we assumed that the

NF sources had to be at least a region defined by $r \geq 0.50$ cm. In an scenario where the NF region was defined by $r = 0.5$ cm, when the electrode was located at the endocardium, the regions of tissue at distances greater than 0.50 cm from the electrode were considered as FF sources and they provided a small contribution to the complete EGM (less than 5% of the A_{ppNF}/A_{pp} and around 0.1 of the correlation). However, when we increased the electrode-to-tissue distance, both A_{ppNF}/A_{pp} and correlation decreased, so the FF contribution gained importance with respect to the whole EGM. For instance, the amplitude ratio and correlation values were below 50% and 0.5, respectively, at $d = 5.4$ mm and below 30% and 0.4 at $d = 9.9$ mm. This means that the higher the distance to the tissue, the stronger the FF sources contribution. This pattern is observed in all NF region sizes, although we observed weaker FF contributions for bigger NF regions at the distances tested in the study.

4.3.4 Mapping Reentries by using Multi-Electrode Arrays

In this section we used simulations Sim2 and Sim3 to characterize the effects of the multi-electrode array configurations, including variations in both the d_{ie} and the electrode-to-tissue distance d , on the accuracy of localizing rotors and their meandering (4.3.4.1); and simulations Sim2, Sim4 and Sim5 to study if it is possible to distinguish properly between anatomical and functional reentries by using multi-electrode array systems (4.3.4.2).

4.3.4.1 Accuracy of the Multi-electrode Arrays Configuration

As explained in the methodology (Section 4.2), unipolar EGMs were computed at the endocardium and at the specific coordinates where the electrodes of the multi-electrode array were located within the blood. They were linearly interpolated to obtain a continue visualization of the phase maps, based on the HT, and a more accurate tracking of the trajectories through the PS detection. In Figure 4.14 the effect of the EGMs interpolation in the phase maps and the PSs detection at the endocardium is depicted. Panel A corresponds to the original spatial resolution (900 μm) and panel B to the resolution after the interpolation (300 μm). An improvement of the spatial resolution yielded a more accurate detection of the rotor trajectory. This fact was due to the smaller size of the element used to detect the PSs corresponding to the tip of the rotor at each time step of the simulation.

We analysed rotors detection through various multi-electrode array configurations by varying the electrode-to-tissue distance d from 0.9 mm to 19.8 mm and the inter-electrode distance d_{ie} from 0.9 mm to 18 mm (see Figure 4.7). Results obtained by each multi-electrode array configuration as well as their comparison with the phase maps and rotors tracking at the endocardium (our ground-true reference) are summarized in Figures 4.15 to 4.18. As expected, for both simulations (Sim2 and Sim3), phase maps of the

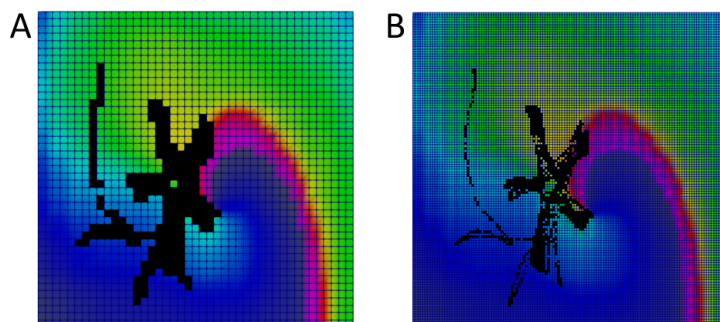


Figure 4.14: Effect of the EGMs interpolation on the phase maps and PSs detection. Phase map and superimposed rotor trajectory (black) obtained for a spatial resolution of $900 \mu\text{m}$, i.e. without EGMs interpolation, (A) and for a spatial resolution of $300 \mu\text{m}$, i.e. with EGMs interpolation, (B) at the endocardium.

multi-electrode array configuration with the minimal $d=d_{ie}=0.9 \text{ mm}$ are the ones that resemble most the endocardial phase map (see Figure 4.15 and 4.17). However, the effects of increasing d_{ie} on the phase maps seem to be stronger when the electrode is closer to the tissue (smaller d).

Thereafter, rotors were tracked through the PSs detection for each multi-electrode array configuration for both simulations (Sim2 and Sim3). Resultant trajectories are shown in Figure 4.16 and 4.18. Sensitivity and specificity were calculated by matching the trajectories detected by the arrays and the ones detected on the endocardium. As expected from Figures 4.15 and 4.17, Figures 4.16 and 4.18 reveal that the best trajectory detection was obtained at $d=d_{ie}=0.9 \text{ mm}$ with a sensitivity $\sim 85\%$ for both simulations. Moreover, increasing d decreased the sensitivity (to a minimum of 31.4% and 58.8% at $d=19.8 \text{ mm}$ for Sim2 and Sim3, respectively). Surprisingly for the highest d_{ie} (18 mm) the sensitivity increased from 5.9% to 20.3% (Sim2) and from 29.9% to 53% (Sim3) by increasing d . Specificity also decreased by increasing d and d_{ie} with respect to $d=d_{ie}=0.9 \text{ mm}$. Nevertheless, it was $\geq 84\%$ in all cases for both Sim2 and Sim3.

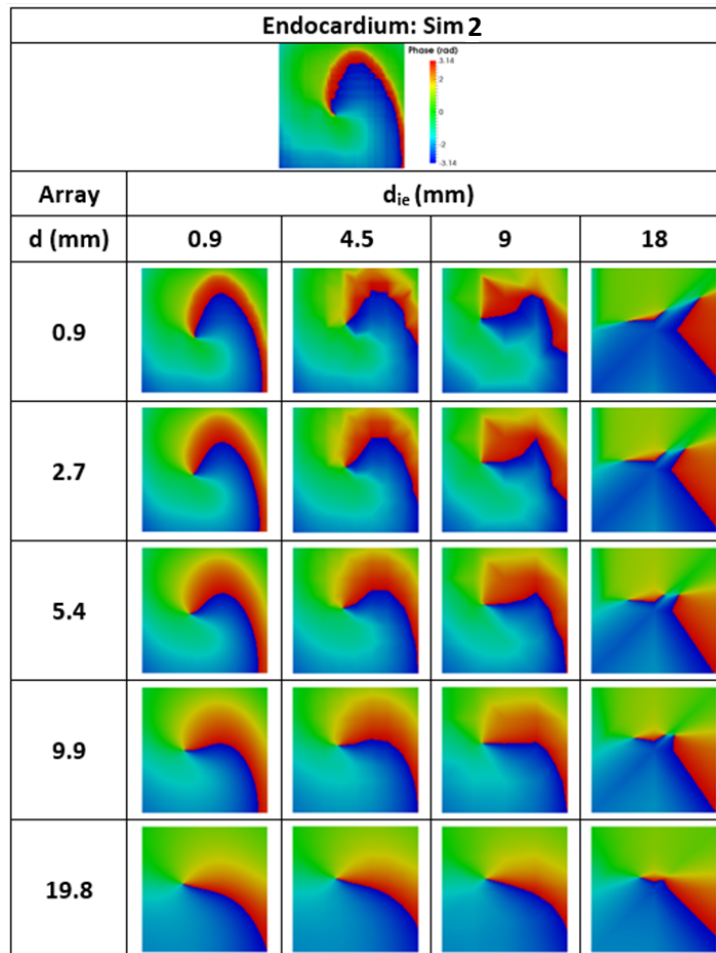


Figure 4.15: Phase maps corresponding to Sim2 for each multi-electrode array configuration. On top, phase map at the endocardium.

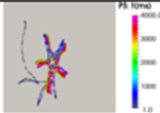
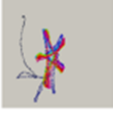

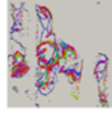
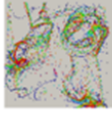

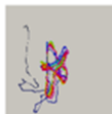
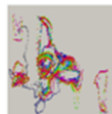
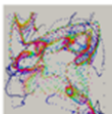


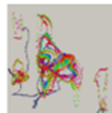
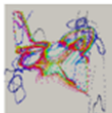
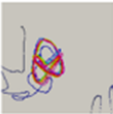

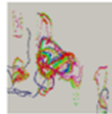
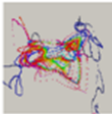


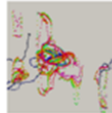
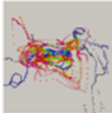
Endocardium: Sim 2				
				
Array	d_{ie} (mm)			
d (mm)	0.9	4.5	9	18
0.9	 Sens=85.7% Spe=99.2%	 Sens=62.4% Spe=98.0%	 Sens=17.5% Spe=89.4%	 Sens=5.9% Spe=85.6%
2.7	 Sens=64.6% Spe=98.0%	 Sens=58.6% Spe=97.7%	 Sens=25.8% Spe=92.0%	 Sens=7.6% Spe=84.0%
5.4	 Sens=48.6% Spe=96.9%	 Sens=45.0% Spe=96.6%	 Sens=24.9% Spe=92.1%	 Sens=11.4% Spe=87.2%
9.9	 Sens=35.4% Spe=95.7%	 Sens=35.5% Spe=95.8%	 Sens=22.8% Spe=92.0%	 Sens=14.9% Spe=89.9%
19.8	 Sens=31.4% Spe=96.8%	 Sens=33.1% Spe=96.9%	 Sens=24.3% Spe=92.9%	 Sens=20.3% Spe=92.0%

Figure 4.16: Rotor trajectory corresponding to Sim2 detected by each multi-electrode array configuration. On top, the trajectory detected on the endocardial phase maps. Trajectories are colour-coded along time: from start (blue) to end (magenta) of the simulation. Sens: sensitivity, Spe: specificity.

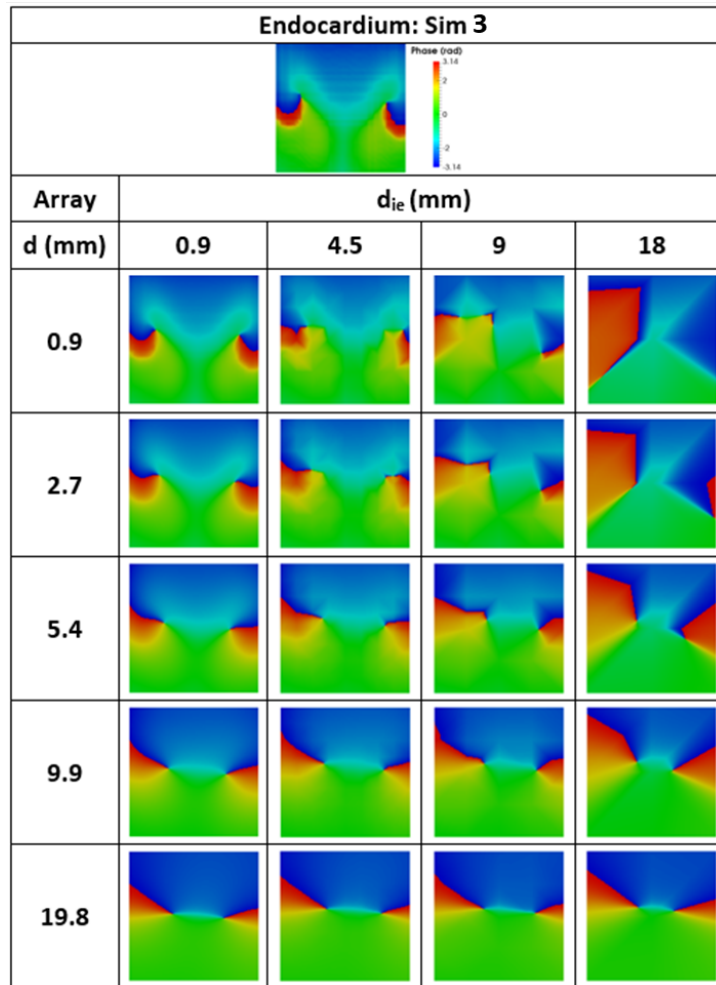


Figure 4.17: Phase maps corresponding to Sim3 for each multi-electrode array configuration. On top, phase map at the endocardium.

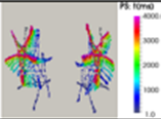
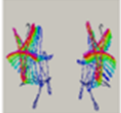
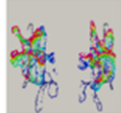
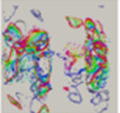
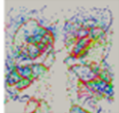
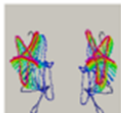
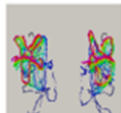
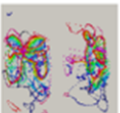
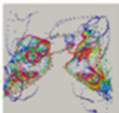
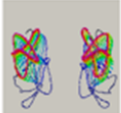
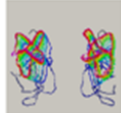
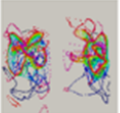
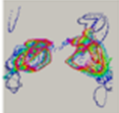
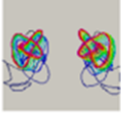
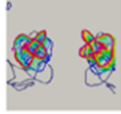
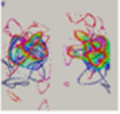
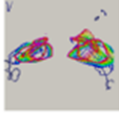
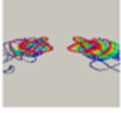

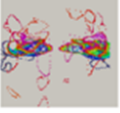

Endocardium: Sim 3				
				
Array	d_{ie} (mm)			
d (mm)	0.9	4.5	9	18
0.9	 Sens=84.7% Spe=97.7%	 Sens=66.3% Spe=95.0%	 Sens=42.3% Spe=87.4%	 Sens=29.9% Spe=84.3%
2.7	 Sens=68.5% Spe=95.0%	 Sens=62.9% Spe=94.3%	 Sens=49.7% Spe=90.4%	 Sens=40.0% Spe=88.6%
5.4	 Sens=57.4% Spe=93.1%	 Sens=56.5% Spe=93.0%	 Sens=50.8% Spe=91.0%	 Sens=44.3% Spe=91.3%
9.9	 Sens=57.1% Spe=93.4%	 Sens=58.1% Spe=93.7%	 Sens=52.0% Spe=92.0%	 Sens=49.4% Spe=94.1%
19.8	 Sens=58.8% Spe=95.8%	 Sens=59.5% Spe=95.8%	 Sens=53.5% Spe=93.8%	 Sens=53.0% Spe=95.4%

Figure 4.18: Rotors trajectories corresponding to Sim3 detected by each multi-electrode array configuration. On top, the trajectories detected on the endocardial phase maps. Trajectories are colour-coded along time: from start (blue) to end (magenta) of the simulation. Sens: sensitivity, Spe: specificity.

4.3.4.2 Differentiation Between Functional and Anatomical Reentry

In this section, we used simulations Sim2 (functional reentry in the LA_{tissue}), Sim4 (anatomical reentry around a PV) and Sim5 (anatomical reentry around the MVR), all three corresponding to pAF conditions with a S1-S2 stimulation protocol (see Figure 4.10) in order to study the ability of multi-electrode arrays to distinguish between functional and anatomical reentries. Unlike in Section 4.3.4.1, in this section we only used one of the multi-electrode array configurations ($d_i e = 0.9\text{mm}$) and at a unique location (see Figure 4.19). EGMs were linearly interpolated to improve phase maps visualization and rotor tracking ($300\ \mu\text{m}$ of spatial resolution).

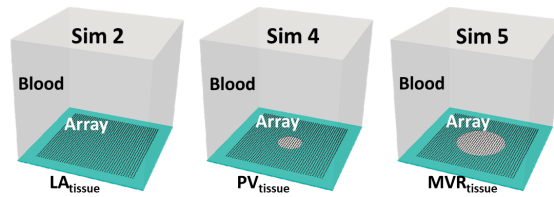


Figure 4.19: Tetrahedral meshes built for the EGM calculation in order to differentiate functional from anatomical reentries. Tissue (blue), blood (grey) and multi-electrode array (black dots).

After applying the cross-field stimulation protocol S1-S2, we obtained three different reentries for Sim2, Sim4 and Sim5, as shown in Figure 4.20. First column corresponds to the V_m , second column to phase maps and third column to rotors trajectories. As expected, phase maps generated by the recordings of the multi-electrode array exhibited the functional reentry as a rotor (Figure 4.20A, second column) and its trajectory was detected through the PSs detection on the LA_{tissue} phase maps (Figure 4.20A, third column). Surprisingly, anatomical reentries were also exhibited as rotors (Figure 4.20B-C, second column) and, therefore, a meandering was detected for them (Figure 4.20B-C, third column). However, in case of both anatomical reentries, their trajectories were spatially located inside the anatomical orifice, where there was no tissue. This fact implies that phase maps based on the HT of the unipolar EGMs have a high sensitivity regardless the amplitude of the EGMs. As illustrated in Figure 4.21, the amplitude of the EGMs recorded at the black points depicted in Figure 4.20 (first column), i.e. electrodes in contact to the tissue, is much higher than the amplitude of the EGMs recorded at the red points in Figure 4.20 (first column), i.e. electrodes at a certain distance from the tissue. Once the reentries stabilized, these peak-to-peak amplitudes were approximately 5 mV (Figure 4.21A) versus 0.25 mV (Figure 4.21B).

The cycle length (CL) of the V_m signals at the black dots was calculated as the interval between excitations. The CL ranged between 105 ms and 132 ms

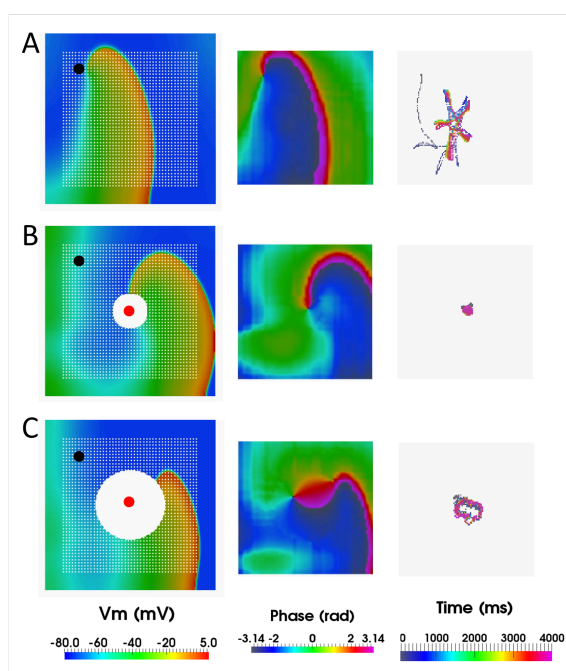


Figure 4.20: V_m , phase maps and rotor tracking for Sim2 (A), Sim4 (B) and Sim5 (C). Multi-electrode array corresponds to white dots superimposed on V_m ; black and red dots indicate the point of measure of the EGMs shown in Figure 4.21. Rotor tracking was performed through the detection of PSs along time.

for the functional reentry in the LA (Sim2), between 107 ms and 122 ms for the anatomical reentry around the PV (Sim4) and between 148 ms and 149 ms for the anatomical reentry around the MVR (Sim5), the mean value being 115 ms, 113 ms and 148 ms, respectively. The frequency of the electrical activation on those black points, computed as the inverse value of the time interval between excitations (CL), ranged from 7.57 to 9.51 Hz for Sim2, from 8.20 to 9.35 Hz for Sim4 and from 6.71 to 6.76 Hz for Sim5. The mean value of the activation frequency was 8.72 Hz for Sim2, 8.88 Hz for Sim4 and 6.75 Hz for Sim5.

As explained before, phase maps based on the HT of the unipolar EGMs registered by multi-electrode arrays do not differentiate between functional and anatomical reentries. All of them appear as rotors on the phase maps. Although the amplitude seems to be very different at the recording sites, as shown in Figure 4.21, it would be difficult to set a threshold to differentiate between both types of reentries since the EGMs close to the tip of the rotor also might be of very low amplitude. Therefore, we performed DF analysis in order to study if any difference can be observed. DF maps, shown in Figure 4.22, ranged from 8.7 to 14.6 Hz for Sim2, from 1 to 9 Hz for Sim4 and from 1 to 6.8 Hz for

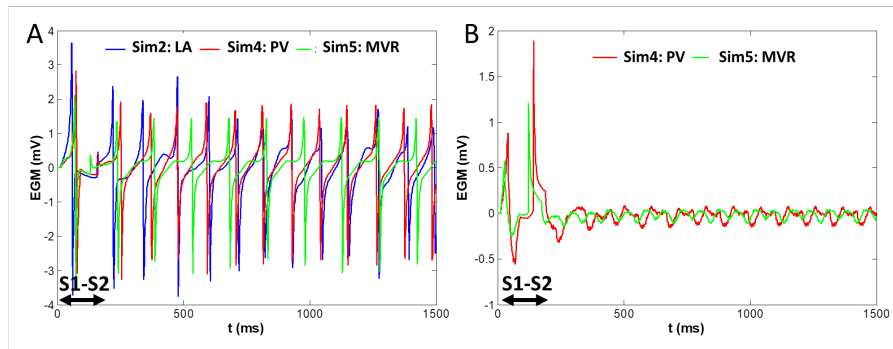


Figure 4.21: EGMs corresponding to functional and anatomical reentries. EGMs recorded at black points (A) and red points (B) depicted in Figure 4.20.

Sim5. The highest frequencies were located in the center of the meandering area (part of the trajectory most populated of PSs) for the functional reentry (Sim2). However, the meandering area coincided with the lower frequencies region for the anatomical reentries (Sim4 and Sim5) and in addition, it was located in the middle of the anatomical orifice.

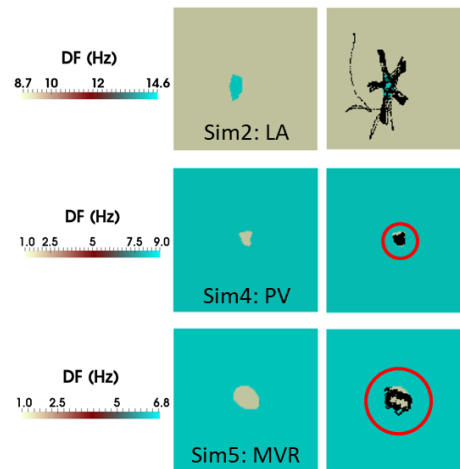


Figure 4.22: DF maps corresponding to functional and anatomical reentries (left) and rotor trajectory superimposed on the DF maps (right). Red circles: anatomical orifice.

These results demonstrated that, although multi-electrode array systems are not able to differentiate functional from anatomical reentries when using phase analysis based on the HT of the unipolar EGMs, they were capable of differentiating between both types of reentries when we combined phase and frequency analysis.

4.3.5 Differences between Rotors in pAF and cAF

In order to analyse the meandering of rotors under pAF and cAF conditions, we performed simulations Sim6 and Sim7, both containing functional reentries in the LA_{tissue} (see Figure 4.10), which were compared with simulations Sim2 and Sim3, respectively. For Sim2 and Sim6, electrical activity was initiated by applying the same stimulation protocol S1-S2, although S2 was applied at different instants to get the reentry (158 ms for Sim2 and 142 ms for Sim6). For Sim3 and Sim7, electrical activity was initiated by applying the same stimulation protocol S1-2S2, although the S2 stimuli were applied at different instants (158 ms for Sim3 and 151 ms for Sim7). After solving the APs with the monodomain formalism by using *ELVIRA* software with a time step of 0.01 ms (propagation patterns are shown in Figure 4.10), we calculated the unipolar EGMs through the computation of the ϕ_e with the approximation of the bidomain formalism (see Section 3.2.3.1). Afterwards, we linearly interpolated the EGMs to achieve a spatial resolution of 300 μm and built the phase maps based on the HT of the interpolated EGMs. Finally, we tracked rotors through the PSs detection. As a result, we obtained the rotors trajectories depicted in Figure 4.23.

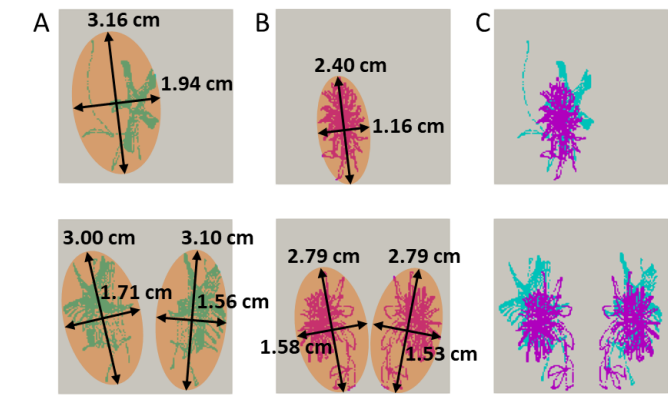


Figure 4.23: Meandering corresponding to functional reentries in pAF and cAF. A) Rotors trajectories in pAF: single rotor (top, Sim2) and two rotors (bottom, Sim3). B) Rotors trajectories in cAF: single rotor (top, Sim6) and two rotors (bottom, Sim7). C) Trajectories in A and B are superimposed: Sim2 and Sim6 (top) and Sim3 and Sim7 (bottom). Orange ellipses in panels A and B delimit the area where the rotor meanders. Simulations were performed in the LA_{tissue} .

As illustrated in panels A and B, we delimited each meandering area by an ellipse encompassing the rotor trajectory (orange ellipse superimposed on the trajectories). Then, the area of those ellipses was computed as follows:

$$A_{\text{Ellipse}} = \pi r_1 r_2 \quad (4.10)$$

where r_1 and r_2 were the major and minor radius of the ellipse. In Table 4.5 the values for the major/minor radius and the area of each ellipse corresponding to the meandering of rotors in all four simulations are shown. Although for both the pAF and the cAF simulations we always obtained star-shaped trajectories, the area encompassing rotors meandering delimited by the ellipses was wider under pAF conditions than under cAF conditions (see Figure 4.23 and Table 4.5). Therefore, cAF remodelling seemed to spatially stabilise rotors, while pAF remodelling seemed to yield wider meandering areas.

	pAF			cAF			
	r_1 (cm)	r_2 (cm)	A_{Ellipse} (cm ²)	r_1 (cm)	r_2 (cm)	A_{Ellipse} (cm ²)	
Sim2	1.58	0.97	4.81	1.20	0.58	2.19	Sim6
Sim3	1.50	0.85	4.03	1.39	0.79	3.45	Sim7
	1.55	0.78	3.80	1.39	0.76	3.34	

Table 4.5: Meandering areas in pAF and cAF. Major (r_1) and minor (r_2) radius, as well as area (A_{Ellipse}) of the ellipses delimiting rotors meandering. Meandering area was smaller in cAF than in pAF (comparison between coloured cells with the same colour).

In addition to rotors tracking, we also computed the DF maps in order to evaluate if differences among frequencies in pAF and cAF were found. Results are depicted in Figure 4.24. For all cases, the region with the highest DF coincided with the rotor trajectory. However, the maximum DF was higher than for pAF simulations in the case of cAF simulations (15.6 vs 14.6 Hz).

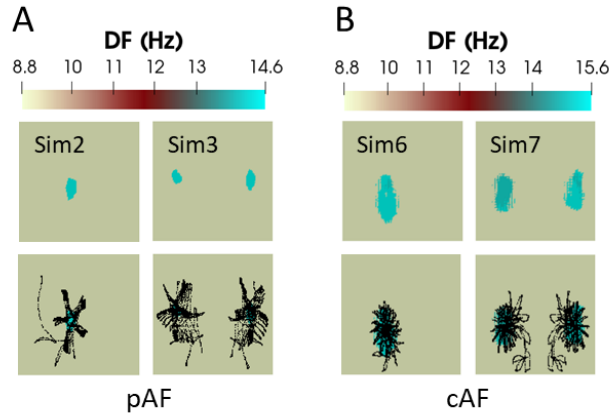


Figure 4.24: DF maps corresponding to functional reentries in pAF and cAF. DF maps (top) and rotor trajectories superimposed on the DF maps (bottom) in pAF (A) and in cAF (B). Simulations performed in the LA_{tissue} .

4.4 Discussion

The main goal of the study described in this chapter was to analyse the factors affecting the accuracy of a multi-electrode system with equidistant d_{ie} when mapping reentries in a sheet of atrial tissue. For this purpose, we first adjusted the electrical remodelling under pAF and cAF conditions. Second, we evaluated the influence of the torso in the computation of the EGMs with the block of atrial tissue and blood. Subsequently, we characterized the contribution of the NF and FF sources in the computation of the EGMs. Finally, we analysed the accuracy of the multi-electrode arrays to map the electrical activity in the atria and detect rotors by studying:

1. The influence of the inter-electrode and electrode-to-tissue distances in the rotors trajectories tracking.
2. Their ability to differentiate functional from anatomical reentries.

In addition, we also analysed the differences in the meandering of functional reentries performed under pAF and cAF conditions.

4.4.1 Electrical Remodelling: pAF and cAF

The pAF remodelling provoked strong differences among the APD_{90} of the LA and RA structures since it mainly shortened the APs in the regions within the LA. Therefore, the dispersion of the APD_{90} increased with respect to control conditions (183 ms vs 125 ms). No differences were seen in the APD_{90} corresponding to the regions within the RA with respect to control conditions. These results are in accordance with the experimental data reported in the literature.^{102,208} Voigt et al¹⁰² did not observe any difference among control and pAF APDs of cardiomyocytes extracted from the RAA. Similarly, Schmidt et al²⁰⁸ did not reported any APD reduction in pAF cardiomyocytes. Although they measured APs in cardiomyocytes from the LAA and the RAA, we assume that on average they did not observe a shortening of the APD due to the unequal number of samples proceeding from each region (33 samples from RAA and 6 samples from LAA) and in case they had observed the LAA samples separately, they might have seen a reduction of the APD.

In the case of cAF remodelling, changes in the ionic models were stronger than in pAF and affected both, the structures within the LA and the RA. Therefore, APDs shortened highly in every atrial region (between 42 and 52% of reduction), yielding a slight dispersion of the APD_{90} compared to control conditions (57 ms vs 125 ms). Our results are in agreement with the literature. Schmidt et al²⁰⁸ observed an APD_{90} shortening of about 43% in patients with cAF compared with subjects in SR; Workman et al⁹³ reported a reduction of 52%; and Bosch et al⁹⁴ a reduction of 54%.

Finally, our results match with the experimental observations regarding

the left-to-right frequency gradients observed in pAF but not in cAF,^{99,100} as well as the higher DFs observed in cAF with respect to pAF.^{98,99} On the one hand in pAF, shortening of APDs in the LA might generate reentries at higher excitation rates than in the RA and thereby higher DFs can be observed. And on the other hand in cAF, the APD shortening throughout the whole atria (more severe even for the LA structures than in pAF) might propitiate the lack of a left-to-right frequency gradient, as well as higher DFs compared to the ones obtained in pAF. As expected, electrical remodelling produces the abbreviation of the APDs and as a consequence, it may help to stabilize reentrant circuits.²⁰⁹

4.4.2 Influence of the Torso in the EGMs Computation

As we did in Chapter 3, we wanted to analyse the influence of the torso in the computation of the EGMs, but instead of by using the realistic models of atria and torso, by using the 3D-block models: TTB (torso-tissue-blood) and TB (tissue-blood). For this purpose, we computed the unipolar EGMs at the coordinates where a virtual electrode should be placed at the epicardium, at the endocardium and varying the distance to the tissue from 0.9 to 19.8 mm. As expected, in absence of torso we observed variations in the computation of the EGMs. However, unlike with the realistic atria-blood and atria-torso models in Chapter 3, these differences were slight and did not alter the morphology of the EGMs; only a small variation in the amplitude was observed. In addition, in absence of a torso layer, the strongest amplification of the EGM was seen at the epicardium, while at a distance of 19.8 mm the variation of the EGM was negligible.

We consider that the amplification of the EGMs in absence of torso is due to the diffusive part of the bidomain formulation. The lack of torso precludes a flux of currents towards it and therefore, those currents have to diffuse along the tissue and towards the blood region. This is the reason why we noticed a stronger effect in the variation of the EGMs at the epicardium. If we compare our results in this chapter with those in Chapter 3, is evident that in the absence of torso, the geometry of the model influences the variation of the EGMs. Although EGMs can be strongly deformed when using a whole atrial anatomy, differences are slight when using a layer of atrial tissue. In fact, our unipolar EGMs for both cases, presence and absence of torso, are in accordance with experimental EGMs reported in the literature (around a peak-to-peak amplitude of 8 mV in our simulations and 7 mV in experimental observations¹⁹⁷). Therefore, there is no need to include a torso region in the 3D blocks of tissue and blood to compute intracavitary EGMs.^{145, 196, 197}

4.4.3 Contribution of the Near and Far Field Sources

On the one hand, we assumed that the major contribution of an unipolar EGM in contact to the tissue should be provided by the NF sources. On the

other hand, in our simulations we considered that in contact to the tissue, the NF sources should yield an amplitude ratio of 90% and a correlation value of 0.9, as they were expected to be the major contribution of the EGM. From these premises, in our study we decided that the NF sources region should be defined by $r \geq 0.50$ cm. Then, for a NF sources region of fixed size, the NF contribution decreased by increasing the electrode-to-tissue distance and therefore, the greater the distance, the higher the contribution of the FF. This fact implies that at certain distances from the tissue, an electrode is mainly recording remote electrical activity and despite the low amplitude of the signals recorded, they might have a strong effect when using a phase analysis, since phase is a parameter not directly dependent of the amplitude of the EGMs.³²

4.4.4 Accuracy of the Multi-Electrode Arrays

To establish a clear baseline understanding before localizing rotors in the atria, we first evaluated the effects of the geometrical configuration of the multi-electrode systems with constant d_{ie} on the accuracy of localizing rotors in a 3D cube comprised of a torso and LA_{tissue} layers and a block of blood (TTB model). We simulated several rotors in the atrial tissue and analysed their detection by varying the multi-electrode array configurations. To build our phase maps we decided to represent the EGMs versus their HT instead of themselves with a phase shift, because this way we assured an optimal phase shift selection and avoided mistakes in the PSs detection,¹⁷⁵ which was used for rotors tracking.

Our results suggested that when the spatial resolution of the electrodes was poor, rotors detection improved by increasing the electrode-to-tissue distance d . In this study it occurred for $d_{ie} \geq 9$ mm where the sensitivity and the specificity started to increase when increasing d . Nevertheless, $d_{ie} < 9$ mm seemed to be a sufficient spatial resolution to detect rotors with a relatively high sensitivity (approximately 62% if $d_{ie}=4.5$ mm and 85% if $d_{ie}=0.9$ mm) for low distances to the tissue ($d=0.9$ mm). These results are in accordance to a previous study that demonstrated that rotors could be detected with a spatial resolution of 1 mm to 1 cm.²¹ However, we provide further insight and conclude that the minimum spatial resolution depends on the distance between the array of electrodes and the tissue.

Overall, the results obtained with the simple 3D block (TTB model) are not directly applicable to more complex atrial geometries and multi-electrode configurations with non-equidistant d_{ie} , as for example in the spherical basket catheter case, where the distance between the electrodes and the endocardium, as well as the distance to the rotor, are non-constant. This case will be studied in Chapter 5. Nevertheless, our results suggest that localization of a rotor with high density multi-electrode arrays placed in a cavity parallel to a flat endocardium can be accurate when the array is placed closest to the endocardium. For low density arrays, however, accuracy can be maintained by

increasing the distance to the tissue.

4.4.5 Ability of Multi-Electrode Arrays to Differentiate Functional and Anatomical Reentries

In this chapter we demonstrate that when mapping functional reentries with multi-electrode arrays by using phase maps based on the HT of unipolar EGMs, the best trajectory tracking (through the PSs detection) was obtained for the minimum d_{ie} tested, as long as the array is placed as close as possible to the tissue ($d=d_{ie}=0.9$ mm). Therefore, we used this multi-electrode array configuration to evaluate the ability of this kind of systems to distinguish between functional and anatomical reentries.

On the one hand, results showed that on phase maps either functional and anatomical reentries are registered by the multi-electrode array as a rotor, i.e. as a functional reentry, and also their meandering can be detected through the PSs detections. In the anatomical reentries the trajectory appeared more concentrated spatially, while in the functional reentry it was wider. This was probably due to the effect of the orifice around which the anatomical reentry occurred. Phases existing in the edge of the orifice converged inside and formed a false PS, always located within the edge of the orifice. Therefore the trajectory of anatomical reentries was spatially concentrated within the orifice.

On the other hand, as expected, results obtained from the DF maps in combination with those resulting from the PSs detection showed that the trajectory location coincided spatially with the region of highest frequencies for a functional reentry.¹⁶ This fact is in accordance with the literature since the core of a rotor has shorter CV and APD than its tail, which also implies a shorter CL and, therefore, a higher frequency of activation.²¹⁰ However, the trajectory coincided with the region of lowest frequencies (region inside the orifice where there was any excitable tissue) in the case of anatomical reentries. Thereby, although we detected a meandering in all cases, it was possible to differentiate the functional reentry from the anatomical ones due to the spatial coincidence of the trajectory with the highest DF region, as the trajectory coincided with the lowest DF region in anatomical reentries. Even in the case of having spatially stable functional reentries (with concentrated trajectories), we consider that they would still have been differentiated from the anatomical reentries (also with very concentrated trajectories because they appeared inside the orifice). This type of functional reentries with concentrated trajectories would have still presented the highest DFs region superimposed on the trajectory, unlikely anatomical reentries, which yield the trajectories superimposed to the lowest DF region. In fact, in our simulations, multi-electrode arrays are located close to the tissue and, therefore, they record local electrical activity, which yield high frequencies. However, for the anatomical reentries there are some electrodes far from the tissue (over the

orifice region) which might register remote electrical activation, characterized by lower frequencies compared to the local activation.⁶⁹ It should be highlighted that in our simulations we generated a single reentry in a sheet of homogeneous tissue instead of fibrillatory conduction in an heterogeneous sheet of tissue with multiple rotors migrating and colliding, so frequencies are quite homogeneous all along the tissue.

It should be noted that although DF maps do not provide any temporal information about the evolution of the reentrant activity, they seem to be very useful when combined with the phase analysis in order to differentiate functional from anatomical reentries. It would be of interest to perform further studies with our 3D realistic human atrial model and multi-electrode basket arrays, in order to check whether the results obtained with excitable tissue sheets are consistent with those obtained in the atria. In this case, both the geometry of the multi-electrode systems (non-equidistant d_{ie} , low spatial resolution and need of interpolation, which could produce false rotors²¹¹) and the propagation patterns throughout the atria would be more complex.

4.4.6 Differences between Rotors in pAF and cAF

In our simulations performed with the CRN model under cAF conditions, we obtained regular meanderings with star-shaped trajectories, also named as rosette in the literature, which is in accordance with previous simulation works.^{130,142} However, our star-shape trajectories have a more elongated aspect, not so circular, probably due to the anisotropy of the tissue in our simulations compared with the isotropic tissue used in those works.

In the case of our pAF simulations, we still can observe star-shaped trajectories but less spatially concentrated. This fact could be a consequence of the differences between pAF and cAF electrical remodelling in the LA. Pandit et al¹⁴² obtained a rotor with a rosette trajectory (2.6 cm of meandering) and a DF of 5.7 Hz in cAF. They observed that when increasing I_{K1} (2-fold), rotor frequency also increased (8.4 Hz) and meandering reduced (1.7 cm), i.e. rotor stabilized due to the APD shortening and enhanced cardiac excitability. They also observed that when decreasing I_{CaL} by 75%, rotor accelerated (DF of 6.3 Hz vs 5.7 Hz) and meandering reduced (2 cm vs 2.6 cm). In addition, they tested I_{Ks} and I_{Kr} block, which seemed to have no effect in rotor meandering and frequency, while I_{Kur} and I_{to} block (90% of reduction) led to rotor termination. Although the authors performed all these variations in the currents under cAF conditions, they could be comparable to the ionic currents variations produced in cAF with respect to pAF for the LA in our simulations. Despite the fact that we decreased I_{to} and I_{Kur} , they are far away of being blocked (-75% and -45% of reduction, respectively) and, therefore, our rotors did not terminate. Regarding I_{K1} , there are no differences between pAF and cAF since in both cases it was 2-fold the value in

control conditions. However, I_{CaL} was reduced by 65% in cAF with respect to pAF. Therefore, the increase in the DF (1 Hz) and reduction of the meandering area (between 0.46 and 2.62 cm², depending on the rotor; see Table 4.5) observed in our cAF simulations with respect to our pAF simulations could be due to the variation of I_{CaL} .

Additionally, our results are in accordance with experimental observations, in which the DFs are greater for cAF than for pAF⁹⁹ and also the location of the trajectories coincide spatially with the region of the highest frequencies.¹⁶

Mapping Reentries in a 3D Human Atrial Model by Using a Basket Catheter

The content in this chapter was partially published in:

L. Martínez-Mateu et al. *Factors affecting basket catheter detection of real and phantom rotors in the atria: A computational study.* *PLOS Comput Biol*, 14(3):e1006017, 2018.

L. Martínez et al. *Effect of Multi-Electrode Configurations on Accuracy of Rotor Detection in the Atria.* *Computing in Cardiology*, 43:1085-1088, 2016.

L. Martínez et al. *Far field induces false rotors when mapping complex atrial arrhythmias.* *EP Europace*; 18 (suppl1): i141, 2016.

5.1 Introduction

The knowledge gained from the 3D-block simulations in Chapter 4 was used to establish a clear baseline understanding about the geometrical configuration of the multi-electrode systems on the accuracy of localizing rotors before approaching the actual basket problem, much more complex. Although such systems yield better success rates in the ablation procedures than the conventional ablation ($>80\%$ vs $20-50\%$ ^{2,20,27}), there is still controversy about them^{23,24,28,29} and their use to target rotors needs further studies to validate their accuracy and applicability in clinical practice. On the one hand, basket catheters have non-equidistant inter-electrode distances and it is not always possible to locate all their electrodes in full contact to the tissue. Therefore, one third of the electrodes might provide a voltage below the low voltage threshold. It is also common to observe splines bunching when the basket is deployed in the atria, which yields distances between consecutive splines ranging from 1.7 to 64.0 mm in the RA and from 1.5 to 85.08 mm in the LA. On the other hand, they provide a panoramic coverage of the chamber but limited to low spatial resolutions.²¹²

The effect of the distance between electrode and endocardium on the accuracy of basket catheters has not been studied yet.^{30,31} In addition, there is a need to understand the influence of far-field sources on the basket catheter recordings, since unipolar recordings are more sensitive than bipolar recordings to detect remote electrical activity. Furthermore, atrial electrical activity maps built from basket catheter recordings are of limited resolution and interpolation of signals before building such maps to improve visualization and rotors tracking might introduce artifacts.^{22,32} All these facts evidence the need to analyse the accuracy of basket catheters. However, the possibility of performing such analyses in clinical practice during an ablation procedure is limited. Therefore, in this chapter we use computer simulations to analyse how the following factors:

1. Electrode-endocardium distance
2. Distant electrical sources
3. Inter-electrode interpolation

affect the accuracy of basket catheters in mapping atrial electrical activity and detect rotors. For this purpose, we simulated reentrant activity in the whole atria by using the 3D realistic model developed in Chapter 3 under cAF conditions remodelling explained in Chapter 4. Subsequently, we computed the intracavitary unipolar EGMs at the endocardial surface, as well as at the electrodes of the basket catheter, and built phase maps based on the HT of the EGMs. Finally, we tracked rotors through the PSs detection.

5.2 Methods

To accomplish our aims in this study and easily track rotors by isolating the factors that might influence in their detection when using a basket catheter, we preferred spatially stable rotors. Therefore, we decided to simulate reentrant activity under cAF conditions instead of pAF conditions since rotors meandering was more concentrated in cAF than in pAF, as explained in Chapter 4. In this section all the methods used to perform our study are described.

5.2.1 Generation of Reentries

In order to simulate the electrical propagation under cAF conditions, we coupled the nine remodeled cellular models (Table 4.2) into the 3D realistic atrial model, like in control conditions in Chapter 3 (Figure 3.8A), with approximately 15% reduced intracellular conductivity to account for gap junctional remodelling^{213,214} as in other simulation studies.^{130,201,215} The reduced σ_L as well as the σ_T/σ_L values are shown in Table 5.1. Then, we applied 21 stimuli (BCL 500 ms, amplitude 28 pA/pF, duration 2 ms) to the SAN region to stabilize models in neighboring regions. The electrical and gap junctional remodelling produced a reduction of 17% in the CV with respect to control, consistent with experimental observations.²¹³ To generate reentrant activity, after the 21 stabilization pulses, we paced the CS using a continuous high frequency train of ectopic foci (CL 110 ms), as shown in Figure 5.1. Then, the simulation was run for 12 additional seconds, in which the simulated activity was driven by 2 stable sources: the pacing train near the CS and a stable rotor near the CT.

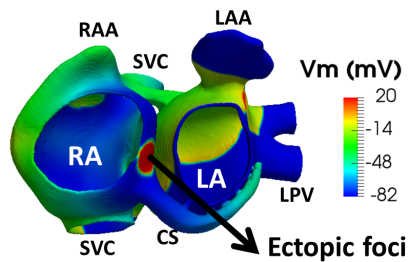


Figure 5.1: Location of the high frequency train of ectopic foci close to the CS.

Stimulation from the SAN was stopped upon starting the ectopic pacing from the CS because, in test simulations, when SAN stimulation was maintained, its discharge propagation was overridden by the faster ectopy rate (110 ms vs 500 ms) and differences in the propagation patterns were negligible.

Region	σ_L (S/cm·pF)	σ_T/σ_L	Region	σ_L (S/cm·pF)	σ_T/σ_L
RA	0.00260	0.35	BBRA	0.00640	0.15
TVR			PM		
RAA			LFO		
LA			BBLA		
MVR			CS	0.00510	0.50
LAA			Isthmus	0.00130	1.00
CT	0.00720	0.15	PV	0.00144	0.50
SAN	0.00068	1.00	FO	0.00000	1.00

Table 5.1: Reduced longitudinal conductivity σ_L (second and fifth columns) and anisotropy ratio σ_T/σ_L (third and sixth columns) for each atrial region (first and fourth columns) for cAF conditions in the 3D atrial model.

5.2.2 Endocardial Phase Maps and Rotor Tracking

Unipolar EGMs inside the atrial cavity and on its endocardial boundaries (endocardium-blood interface) were computed as extracellular potentials (see Section 3.2.3.1) with a temporal resolution of 1 ms in the whole atria-torso model developed in Chapter 3. Next, endocardial and cavity EGMs at the coordinates of the basket’s electrodes were bandpass filtered (7-10 Hz) in order to allow rotor tip tracking similarly to Rodrigo et al.¹⁶⁰ Phase maps were calculated from the EGMs during the last 11 s of the simulation, as the reentrant activity during the first second was not stable. In the custom-made software routines implemented in *MATLAB*, we applied the HT to the filtered EGMs (Equation 5.1), as in prior studies,^{15,203,204} and computed the instantaneous phase θ , whose values ranged from $-\pi$ to π radians (Equation 5.2).

$$HT[EGM_f(t)] = \frac{1}{\pi} \int_{-\infty}^{\infty} \frac{EGM_f(\tau)}{t - \tau} d\tau \quad (5.1)$$

$$\theta = \tan^{-1} \left(\frac{HT[EGM_f(t)]}{EGM_f(t)} \right) \quad (5.2)$$

We excluded the first and last 500 ms of the signals to avoid filtering and transformation artifacts, resulting in phase maps as frames of movies of 10 s long. Finally the PSs, where all phases converge, were computed to track the rotor’s trajectory on the endocardium-blood interface^{168,205–207} as in Section 4.2.3.3.2. To approximate Equation 4.6 and automatically localize PSs, as in Chapter 4, we adapted the method proposed by Rogers.¹⁷¹ Accordingly, the endocardium-blood interface corresponded to a 3D surface mesh of triangular elements (see Figure 5.2) and each node in the mesh had a phase value. For each element in the mesh and for all simulation time steps, we computed the

spatial variations of phase among its nodes (space gradients). The automatic PS detection algorithm was implemented in *MATLAB*, as follows:

1. Computation of the variation of phase among the nodes comprising each edge in the element:

$$\begin{cases} Edge_1 = Phase_B - Phase_A \\ Edge_2 = Phase_C - Phase_B \\ Edge_3 = Phase_A - Phase_C \end{cases} \quad (5.3)$$

2. Adjustment of the variation of phase values within the range $[-\pi, \pi]$:

$$Edge'_i = \begin{cases} Edge_i, & \text{if } Edge_i \in [-\pi, \pi] \\ Edge_i + 2\pi, & \text{if } Edge_i < -\pi \\ Edge_i - 2\pi, & \text{if } Edge_i > \pi \end{cases} \quad (5.4)$$

where $i = 1, 2, 3$

3. Computation of the complete variation of phase along the element:

$$Phase_{variation} = Edge'_1 + Edge'_2 + Edge'_3 \quad (5.5)$$

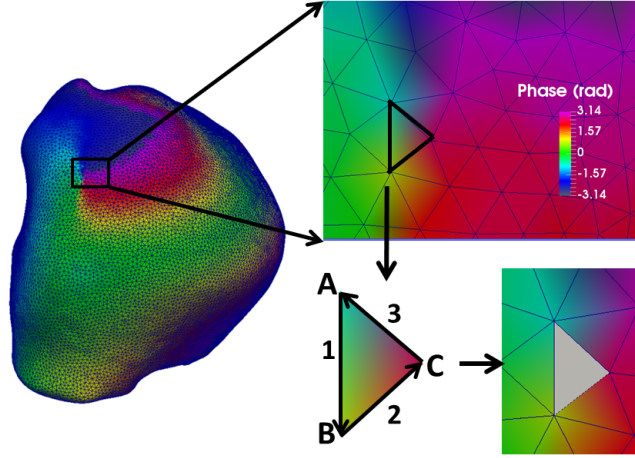


Figure 5.2: PS detection on the endocardium-blood interface. Phase map in the RA displayed a rotor. Magnification of the rotor region allowed the visualization of the triangular elements in the mesh. Elements detected as a PS ($\pm 2\pi$) were white coloured on the phase map to track the trajectory. Arrows indicate the direction to surround the element and compute the phase variation among nodes (A-C). Element edges: 1-3.

For those elements around which all phases converged, the summed phase variation along a closed surrounding path was $\pm 2\pi$. Those elements were

designated as PSs and white coloured superimposed on the phase maps, as illustrated in Figure 5.2. Rotors were defined as an excitatory wave pivoting around a PS for at least one cycle of rotation and were visually detected in phase map movies.

5.2.3 Mapping Basket Catheter

A virtual intracardiac 64-pole mapping basket catheter formed by 8 splines (A-H) each containing 8 electrodes (1-8) was placed in three different positions in the RA of our atrial model: close to the SVC, CT and CS (Figure 5.3, first and second columns). The diameter of the modelled 8×8 electrode basket was 31 mm, corresponding to the smallest Constellation mapping catheter (Boston Scientific). Electrodes were equidistant along the splines with d_{ie} of 4.8 mm. The distances between electrodes at neighboring splines varied from 5.4 mm for the electrodes near the poles to 11.7 mm for the electrodes near the equator (Figure 5.4A).

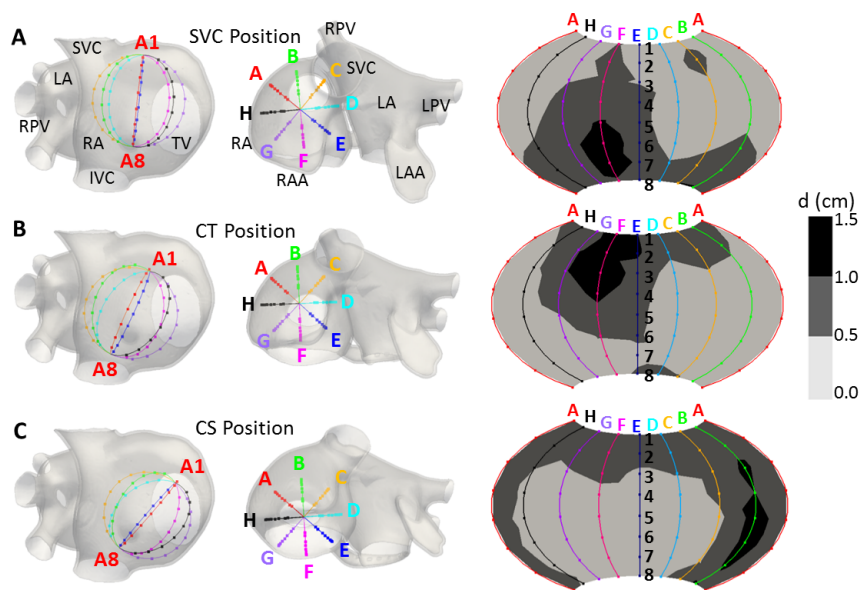


Figure 5.3: Positions of the 64-pole basket mapping catheter in the RA. SVC (A), CT (B) and CS (C) position (first and second column) and electrode-to-endocardium distance (d) maps for the 64 electrodes in each basket position (last column).

The distribution of the distance (d) between each electrode in the basket and the closest point on the endocardial surface differed for the three basket positions within the atria (see 2D projections of the basket in Figure 5.3, last

column), but the number of electrodes located at $d \leq 0.5$ cm and $0.5 < d \leq 1$ cm was approximately similar. In the first case the percentage of electrodes was 53%, 58% and 50%, and in the second case 41%, 34% and 42%, for the SCV, CT and CS positions, respectively.

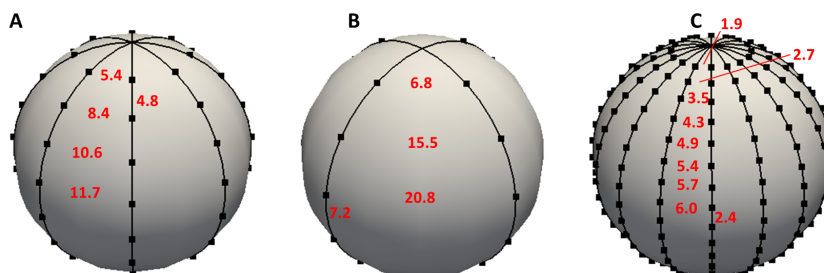


Figure 5.4: Basket inter-electrode distances. Inter-electrode distances for 8×8 (A), 4×6 (B) and 16×16 (C) basket configurations.

EGMs were computed at the 64 electrodes' coordinates and linearly interpolated on 57600 points on a periodic 2D projection of the basket to improve phase maps visualization (see Figure 5.5) and rotor tracking. The same signal processing explained for the endocardial EGMs in Section 5.2.2 was applied to the basket's EGMs in order to obtain the phase maps and PSs detection. The PSs detection algorithm was also performed on the basket phase maps, but in this case the closed path integral was computed along the edges of each triangular element of the 2D projection of the basket, with a perimeter of approximately 0.5 mm, instead of along the elements of the endocardial-blood surface (perimeter of 2 mm).

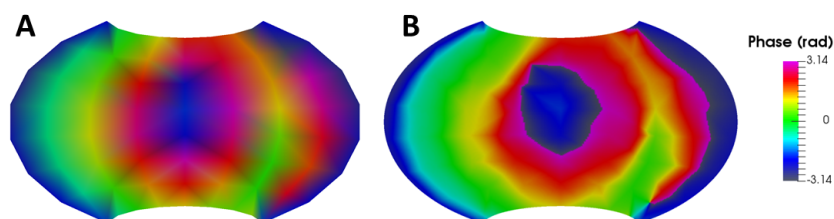


Figure 5.5: Improvement of the basket phase maps after EGMs interpolation. Phase map based on the HT of 64 EGMs (A) and 57600 EGMs (B).

Finally, to analyze the effect of electrode density, we varied the number of electrodes in the basket between 4×6 and 16×16 for each of the three positions (see Figure 5.4B-C).

5.3 Results

The goal of this simulation study was to evaluate how each of the following three factors:

1. Electrode-endocardium distance
2. Distant electrical sources
3. Inter-electrode interpolation

affected the detection of rotors when using a basket mapping catheter in the atria. To accomplish that goal, the basket phase maps were compared to the activation patterns of AP simulated on the atrial wall, which served as our ground-true reference.

5.3.1 The Simulated Propagation Patterns

To evaluate how the three above listed factors affected the detection of rotors by the basket, we carried out a simulation in which the RA was paced by a high frequency train of stimuli close to the CS (see Section 5.2.1). Stimulation led to a complex propagation pattern maintained by a stable rotor on the crista terminalis (CT rotor) accompanied by a distal rotor wave extension (RWE) reentry around the IVC. The CT rotor migrated back and forth between the SVC and the IVC along the CT, while its RWE persistently collided and merged with the wavefront generated by the CS stimuli. Propagation in the LA was more regular. The LA was repeatedly excited by two wavefronts from the RA: one moving toward the roof through BB and spreading to the posterior wall and the other moving toward the inferior wall through the FO limb and extending to the posterior wall. Both wavefronts collided between the posterior and inferior walls, with the precise location of the collision line varying throughout the simulation. Figure 5.6A is a snapshot at 5125 ms showing the CT rotor (clockwise white arrow), the RWE (counterclockwise dashed white arrow), the direction of the propagation in the LA (dotted white arrows), the wavefront corresponding to the high frequency train of stimuli applied near the CS (dashed orange arrows), the collision between the CS stimuli wavefront and the RWE (black line close to the FO) and the collision in the LA (black line between the posterior and inferior walls).

The EGMs and their corresponding phase maps were calculated at the endocardium-blood interface (25175 signals in the RA and 24819 signals in the LA). The trajectory described by the CT rotor tip detected through the PSs calculations was depicted in white superimposed on the phase maps. All the events described above in the propagation maps were also identified on the phase maps, as shown in Figure 5.6B. Furthermore, not only the CT rotor but also the RWE circulating around the IVC, whose tip was located in the middle of the orifice, appeared as a rotor.

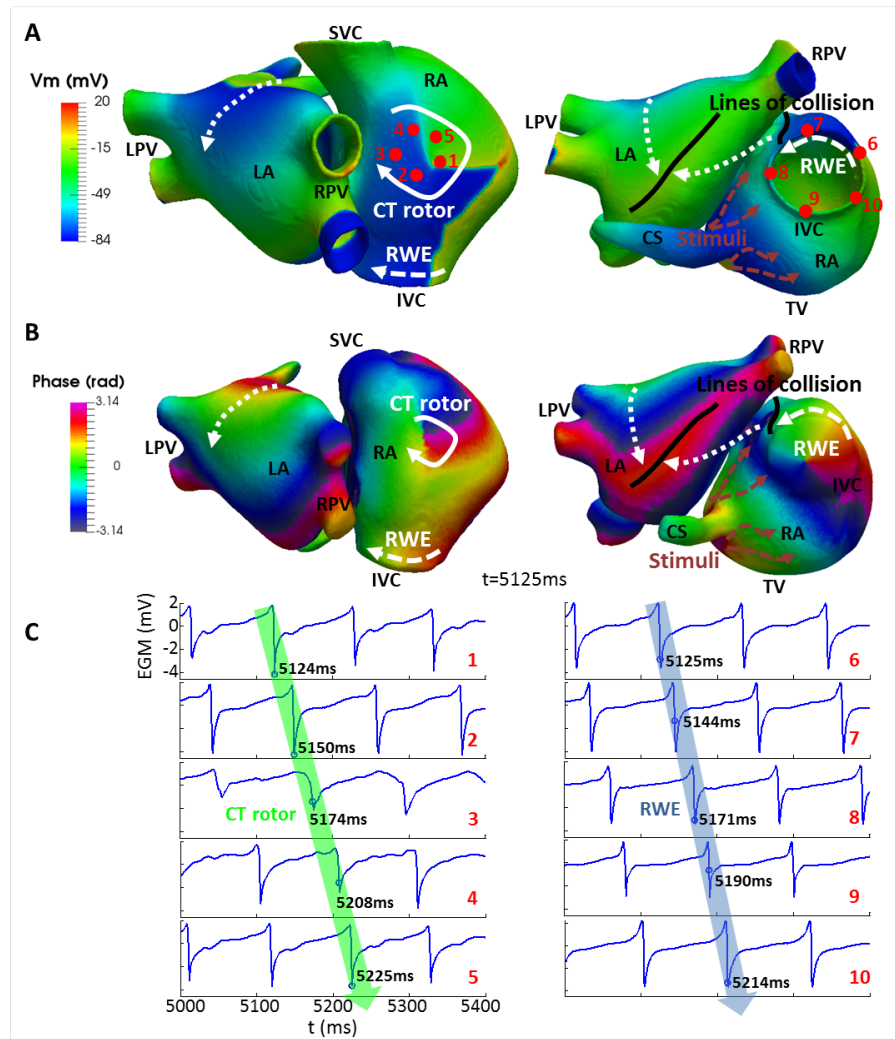


Figure 5.6: Snapshot of the electrical propagation and phase map at $t=5125$ ms. A) Simulated V_m in the 3D atrial model. CT rotor (white arrow), RWE (dashed white arrow), CS stimuli wavefront (orange dashed arrows), wavefronts in the LA (dotted white arrows) and lines of collision (black lines). B) Phase maps computed on the endocardium-blood interface after filtering. C) EGM traces corresponding to points 1-10 in panel A. Blue circles on the traces show the closest activation times to $t=5125$ ms. Green and blue arrows superimposed over the EGMs demonstrate the sequential activation times of the tissue at points 1-5 (CT rotor) and 6-10 (RWE), respectively.

The rotational activation of the tissue can be observed in the EGMs shown in Figure 5.6C. The EGMs on the left correspond to red points 1-5 (CT rotor), while the EGMs on the right correspond to red points 6-10 (RWE) in panel A. Their corresponding phases are shown in Figure 5.7.

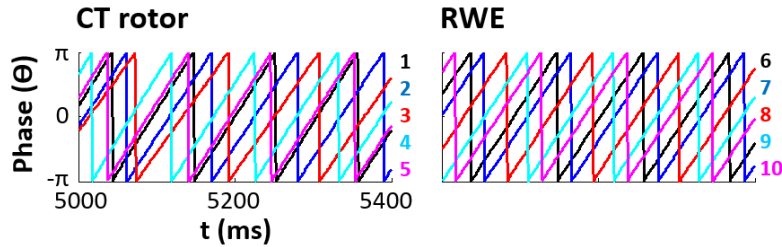


Figure 5.7: Plots of the phases in the endocardium, computed based on the HT of the filtered EGMs. They correspond to points 1-5 (left) and 6-10 (right) in Figure 5.6.

5.3.2 Effect of Electrode-to-Endocardium Distance on Mapping

For all three different basket positions (SVC, CT and CS) we analyzed the effect of the electrode-endocardium distance (d) at each electrode location by computing EGMs for all 64 electrode coordinates to build phase maps. We also evaluated the RA and the meandering area coverages for each basket position. First, the RA coverage was defined as the percentage of endocardium at a distance $d \leq 0.5$ cm (red) or $0.5 < d \leq 1.0$ cm (green) from at least one electrode of the basket (Figure 5.8A) over the whole atrial tissue. RA coverage was similar for the three basket positions ($\sim 20\%$ for $d \leq 0.5$ cm and $\sim 45\%$ for $0.5 < d \leq 1.0$ cm, as shown in Figure 5.8B). Second, the meandering area coverage was defined as the percentage of CT rotor meandering area (black area in panel A, corresponding to the region of the endocardium comprising the rotor trajectory) superimposed on the RA coverage (red or green area in panel A) over the whole CT rotor meandering area. Meandering area coverage was $\sim 60\%$ for $d \leq 0.5$ cm and $\sim 40\%$ for $0.5 < d \leq 1.0$ cm for the SVC and CT positions (Figure 5.8A, top and middle, and Figure 5.8C), while it remained completely uncovered for the CS position (Figure 5.8A, bottom, and Figure 5.8C).

The amplitude of the EGMs depends on the dipole strength and the source-to-electrode distance. As an example of the variation of amplitude regarding the distance to the tissue, the traces on the right-hand side in panel A show EGMs on electrodes set at $d \leq 0.5$ cm (red traces; A3, A5 and F8 for the SVC, CT and CS positions, respectively) and at $0.5 < d \leq 1.0$ cm (green traces; B7, C1 and A1 for the SVC, CT and CS positions, respectively). The maximum

root mean square value (V_{rms}) was 0.74 mV among all the EGMs corresponding to the electrodes set at $d \leq 0.5$ cm, while it was 0.33 mV for the electrodes set at $0.5 < d \leq 1.0$ cm. Interestingly, a relatively large variation on the nearest EGMs amplitude at electrodes A3 and A5 is observed in the SVC and CT position which could be related to rotor meandering.

5.3.2.1 Mapping at Three Different Basket Positions

Before analysing the rotor detection by the basket, we analysed the propagation patterns in control conditions for all three basket positions. For this purpose, we computed the basket EGMs and phase maps based on them in the case of the simulation in SR described in Section 3.3.1. These propagation patterns are shown in Appendix B. As expected, during SR no rotors were detected by the basket.

Once we were familiar with the basket phase maps, we analysed the effects of the three different positioning of the basket within the RA on the characteristics of its rotor mapping, which are illustrated in Figures 5.9, 5.11 and 5.14. Surprisingly, in addition to the CT with its RWE on the atrial surface (see Figure 5.6), the basket phase maps also showed phantom PSs at various locations that have no corresponding reentrant AP on the atria. We classified the false PSs either as an imaginary phase singularity (IMPS), when activation occurred sequentially in the surrounding electrodes, or as a false interpolation phase singularity (FIPS), when the electrodes surrounding the singularity did not register the activation sequentially. FIPs appeared because of the inter-electrode interpolation of the EGMs prior to the computation of the phase maps (see Section 5.3.4). For the three basket positions tested, a comparison between the PSs locations on the phase maps and the electrode-to-endocardial surface distance maps (Figures 5.3 and 5.8) showed that PSs, IMPSs and FIPs appear at various distances, including $d \leq 0.5$ cm, suggesting that NF and FF sources have an influence on the generation of PSs.

SVC position

Starting from the SVC position in Figure 5.9, panel A illustrates the location of the basket at the high RA (top row), the phase maps on the endocardium-blood interface (middle row) and the phase map corresponding to the basket recordings (bottom row) at $t = 10000$ ms. White coloured PS trajectories are superimposed on the phase maps. The basket phase map was visually more like the endocardium-blood interface map at splines A-B-C-D than at splines E-F-G-H, where a higher number of electrodes were at $d > 0.5$ cm from the tissue (see Figures 5.3 and 5.8). The CT rotor was detected 94% of the simulation time at splines A-B-C (white clockwise arrow in Figure 5.9A). The CT rotor was not detected when it migrated closer to the IVC (6%

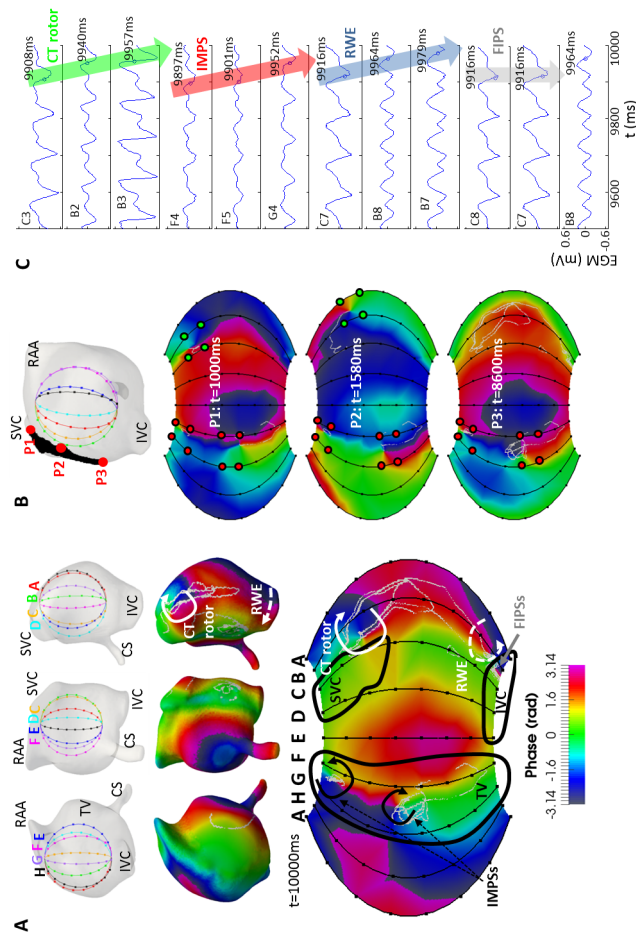


Figure 5.9: Basket mapping for the SVC position. A) Views of the location of the basket in the RA (top), snapshots of the phase maps in the endocardium-blood interface (middle) and of the phase map computed from the basket’s recordings (bottom) at $t = 10000$ ms. PSSs in white over the phase maps (middle and bottom row). Black curves: SVC, IVC and TV orifices. B) Selection of points (P1, P2 and P3) belonging to the CT rotor meandering area (top); snapshots when the CT rotor was moving through the points P1-P3 (second to bottom row). Green points: electrodes surrounding the CT rotor; red points: electrodes surrounding the IMPs. C) EGMs at electrodes detecting the CT rotor (C3-B3), IMPs (F4-G4), RWE (C7-B7) and FIPs (C8-B8). Blue circles on the plot of the EGMs indicate the activation time closest to $t = 10000$ ms. Green, red and blue arrows over the EGMs enhance the sequential activation of the electrodes detecting the CT rotor, IMPs and RWE, respectively; grey arrow, the non-sequential activation of the electrodes detecting the FIPs.

of the simulation time). A counter-rotating wave to the CT rotor was found to rotate around the IVC and is termed in this study as a "rotor wave extension" (RWE). The basket map detected the RWE mostly uninterruptedly around the IVC, near the basket's south pole (dashed white counterclockwise arrow). However, the corresponding PS appeared on the phase map only over 7% of the simulation time. Other times, the RWE was represented at the basket phase map as a wave encircling the south pole without a PS. Additionally, false PSs were also found, as follows: at splines E-F-G the basket detected a pair of IMPs (black curved arrows in Figure 5.9A, bottom) during the entire simulation time (splines near the TV orifice), and the basket phase map pattern differed from the phase map pattern at the endocardium-blood interface. On the other hand, at electrodes B7-B8-C8-C7, the basket phase map displayed FIPs 57% of the simulation time (grey arrow in Figure 5.9A bottom).

Figure 5.9B depicts a selection of points (P1, P2 and P3) belonging to the CT rotor meandering area (top) as well as snapshots of the basket phase maps when the CT rotor tip was located at or near each of these points. As demonstrated by the three sequential basket phase maps at 1000, 1580 and 8600 ms, the CT rotor (green dots) was not detected when it moved toward the IVC, whereas the IMPs (red dots) appeared for the entire simulation time.

Figure 5.9C shows the EGMs at some of the electrodes detecting the CT rotor (C3, B2 and B3), a IMPs (F4, F5 and G4), the RWE (C7, B8 and B7) and FIPs (C8, C7 and B8). Green, red and blue arrows superimposed on the plots of the EGMs illustrate the sequential activation of the electrodes for the CT rotor, IMPs and RWE respectively (blue circles on the EGM plot depict the activation times). However, grey superimposed arrow shows the non-sequential activation of the electrodes in case of FIPs. At $t = 10000$ ms, the basket phase map (Figure 5.9A, bottom) showed the RWE and a FIP between electrodes B7, B8, C7 and C8. As demonstrated by the EGMs in panel C, the counterclockwise activation corresponded to the RWE, being the FIP an artifact due to the interpolation of the EGMs. The phases corresponding to EGMs in Figure 5.9C are shown in Figure 5.10.

CT position

The basket phase map also differed substantially from the endocardium-blood interface phase map when the basket was set at the CT position (Figure 5.11). At splines A-B-C, the CT rotor was detected 90% of the simulation time. During the other 10% the CT rotor had migrated closer to the SVC from which all basket electrodes were at $d > 0.5$ cm (Figure 5.11A). As for the RWE, its propagation was detected uninterruptedly at electrodes located at the basket's south pole, although no corresponding PSs appeared on the phase map because the south pole (as well as the north pole) area was not interpolated (see Figure 5.12). Greater discrepancies between the endocardium

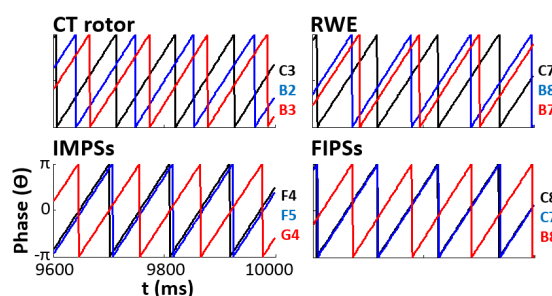


Figure 5.10: Traces of the phases, computed based on the HT of the filtered EGMs, at some electrodes in the basket for the SVC position.

and the basket maps are visible at splines E-F-G, since in the CT position of the basket a higher number of electrodes corresponding to such splines were located at $d > 0.5$ cm (see Figure 5.3) from the atrial surface. Moreover, an IMPS was noticed at splines E-F-G-H 100% of the simulation time. Finally, FIPSSs appeared at electrodes B1-B2-C1-C2 and D4-D5-E4-E5 13% of the simulation time. Figure 5.11B shows that the CT rotor (green points) was not detected when it was near the SVC. In contrast the IMPS (red points) was always present. In Figure 5.11C are shown the EGMs at some electrodes detecting the CT rotor (B6, C6 and C5), the IMPSs (F2, G2 and G1) and FIPSSs (B1, B2 and C1). Results are in accordance with those obtained for the basket in the SVC position: the activation arrived sequentially to the electrodes in case of the CT rotor and the IMPSs (illustrated by the green and red arrows superimposed on the EGMs traces), but not in case of FIPSSs (grey arrow). Phases corresponding to these EGMs are shown in Figure 5.13.

CS position

Figure 5.14 illustrates the mapping when the basket was set at the CS position. The CT rotor was detected in this basket position only 35% of the simulation time at splines H-A-B between the first and second ring of electrodes in the basket (see Figure 5.14A, bottom). Detection of the CT rotor was poor because the rotor meandering area was relatively far ($d > 1$ cm) from splines A-B-C of the basket in this position (compare panel A, bottom, and Figure 5.3). The RWE was detected at electrodes B7-C7-C8-B8 61% of the simulation time. In addition, IMPSs were located along spline B (electrodes covering the SVC orifice) during 31% of the simulation time. And also, some FIPSSs were detected 40% of the simulation time at electrodes E2-E3-E4-F2-F3-F4 and A7-A8-C7-C8.

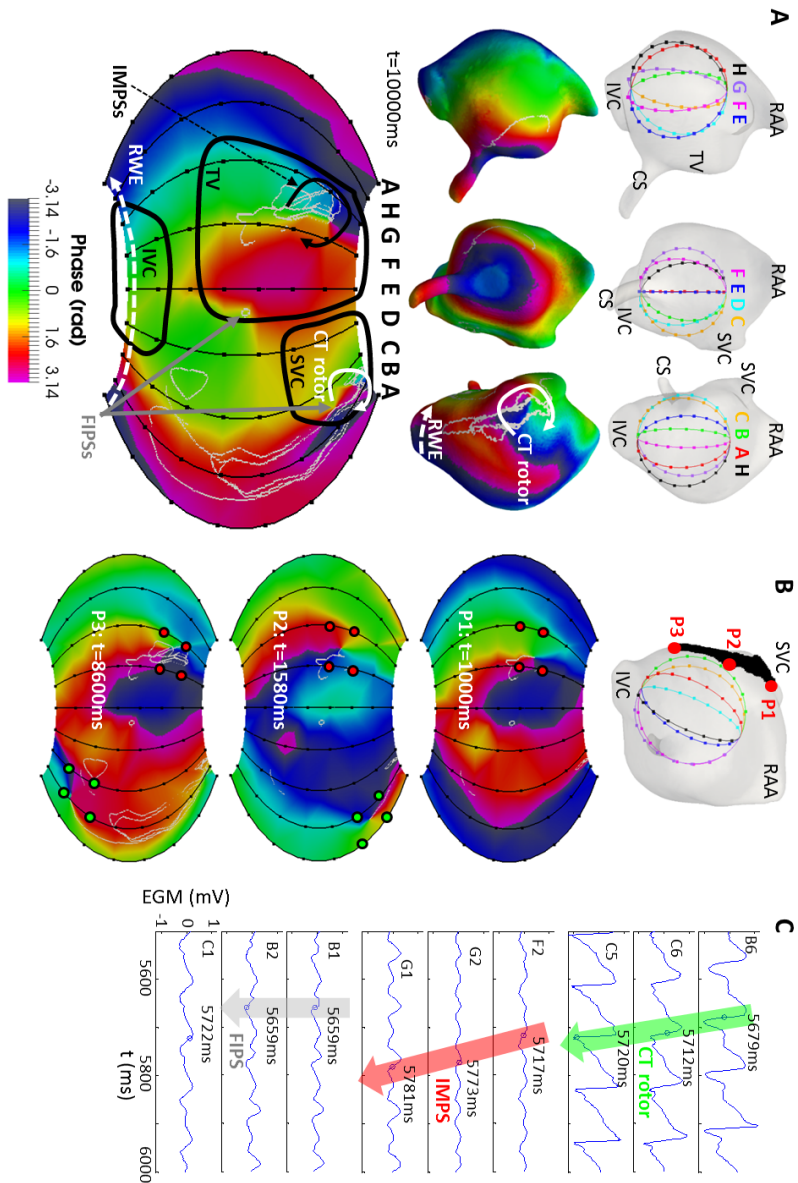


Figure 5.11: Basket mapping for the CT position. The layout of this Figure is the same as in Figure 5.9.

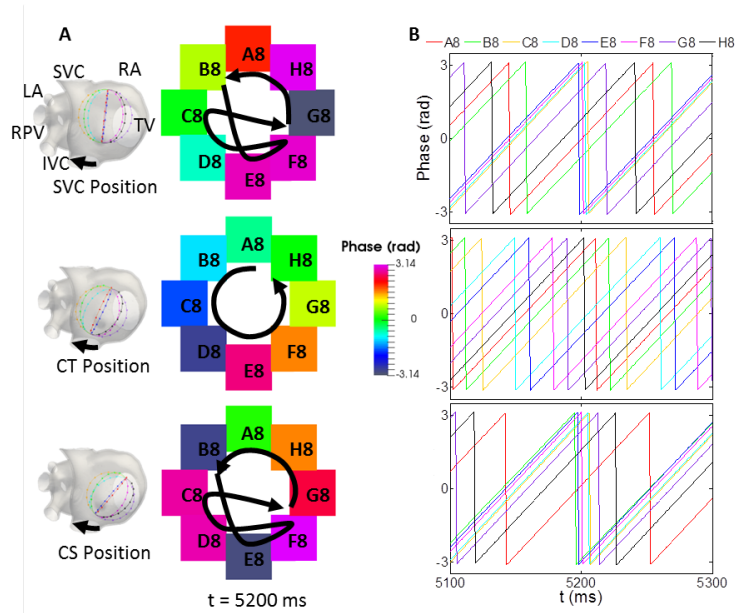


Figure 5.12: Phases at the basket's south pole. A) Phases in the last (south-most) ring of electrodes (A8 to H8) at $t = 5200$ ms when the basket was located at the SVC, CT and CS positions. Only in case of the CT position a circulating activation corresponding to the RWE (black arrow) can be observed, as shown by the phases' colour code. In case of the SVC and CS positions we are detecting the collision between the CS stimuli wavefront and the RWE and we are not observing the RWE due to the lack of electrodes at the basket's south pole. B) Plot of the phases in the last ring of electrodes (SVC position: top; CT position: middle; CS position: bottom).

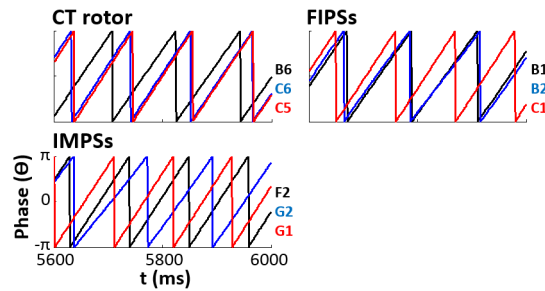


Figure 5.13: Traces of the phases, computed based on the HT of the filtered EGMs, at some electrodes in the basket for the CT position.

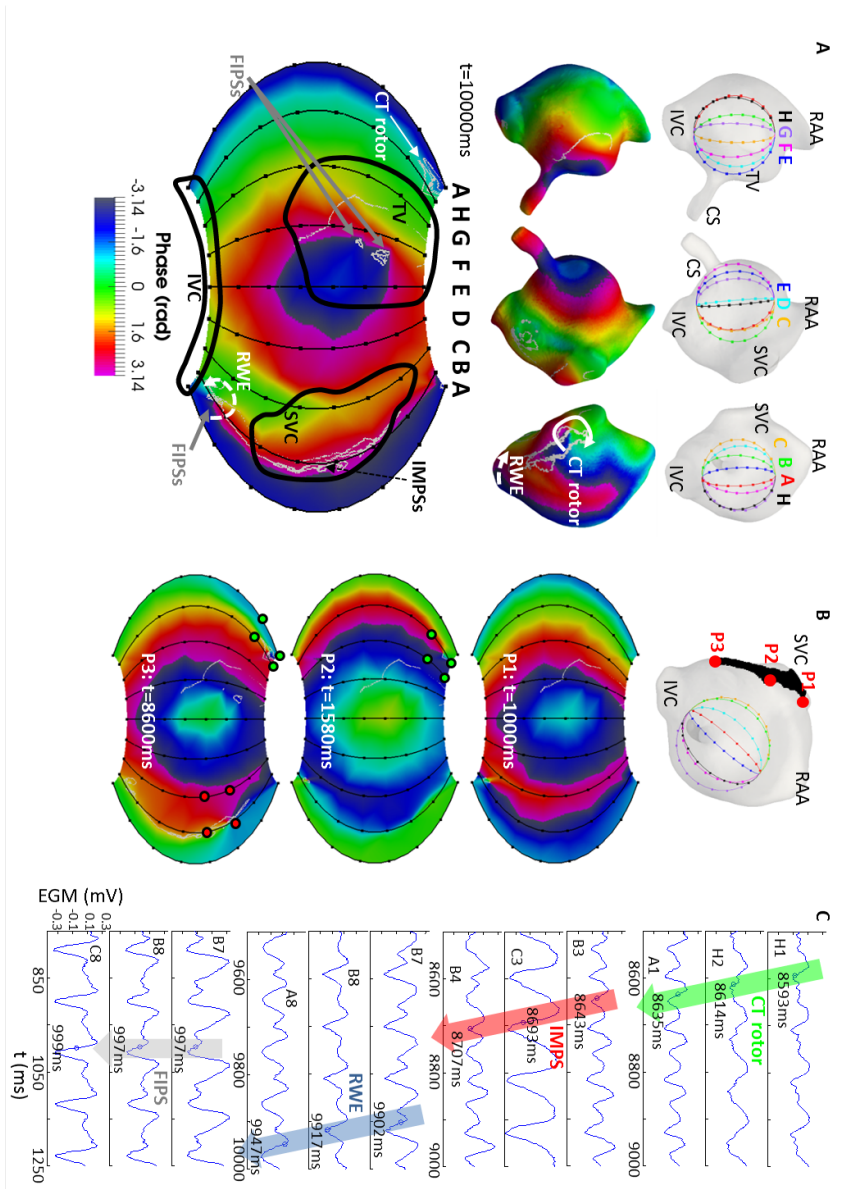


Figure 5.14: Basket mapping for the CS position. The layout of this Figure is the same as in Figure 5.9.

As in the previous cases, when comparing the basket phase map to the map on the endocardium-blood interface there were some differences, especially at splines A-B-C. As shown in Figure 5.14B, neither the CT rotor (green points) nor the IMPs (red points) were always detected. As in the other 2 basket's positions, Figure 5.14C shows the EGMs at some of the electrodes detecting the CT rotor (H1, H2 and A1), IMPs (B3, C3 and B4), the RWE (B7, B8 and A8) and FIPs (B7, B8 and C8). As in those basket's positions, activation arrived sequentially to the electrodes in case of the CT rotor, IMPs and RWE, and there was not sequential activation of the electrodes in case of the FIPs (see coloured arrows superimposed on the EGMs plots in panel C). The phases corresponding to the EGMs in Figure 5.14C are shown in Figure 5.15.

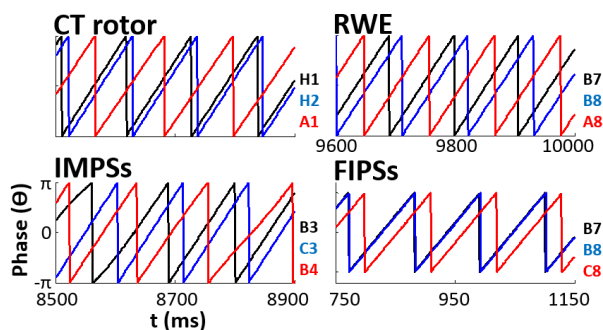


Figure 5.15: Traces of the phases, computed based on the HT of the filtered EGMs, at some electrodes in the basket for the CS position.

The detailed analysis of basket detection for the three considered positions yielded a high detection rate ($\sim 90\%$ of the simulation time) of the real rotor, i.e. the CT rotor, when the basket was closely covering the rotor meandering area (SVC and CT positions, as shown in Figure 5.8A). In the case of the basket at the CS position, detection of the CT rotor was poor due to the electrodes distance from the meandering area (see Figure 5.8A). However, basket-based phase maps in our simulated setting always generated a number of phantom rotors (IMPs and FIPs) in the presence of only one real rotor (CT rotor) for each of the basket positions. It should be noted that the PS associated with the RWE around the IVC is not to be considered false due to the fact that multi-electrode recording systems will produce a PS for both anatomical and functional reentries. Furthermore, after computing the instantaneous location of the CT rotor on the endocardial surface along the simulation time, as well as the location of the CT rotor detected by the basket in the three different positions studied, we calculated the distance between the real and detected trajectory of the rotor at any moment of the simulations and obtained that for the SVC position, this distance was between 0.37 and 1.38 cm (median 0.69 cm); for the

CT position, it was between 0.43 and 2.48 cm (median 0.94 cm); and for the CS position it was between 2.53 and 3.97 cm (median 2.88 cm). This supports the fact that rotor localization is more accurate when the basket is properly located inside the atrium in close proximity to the region of the rotor.

5.3.2.2 Effect of Ectopic and Rotor Activity on IMPs

To rule out the possibility that IMPs result from the ectopic pacing close to the CS, the simulation was prolonged for additional 5000 ms following secession of the pacing. The activation patterns in the atria changed (see Figure 5.16). They became dependent on a drifting reentry alternating between anatomical and functional cores. Nevertheless, we observed clear IMPs on the phase maps of the basket at SVC and CT positions, as in the simulation that includes the CS pacing.

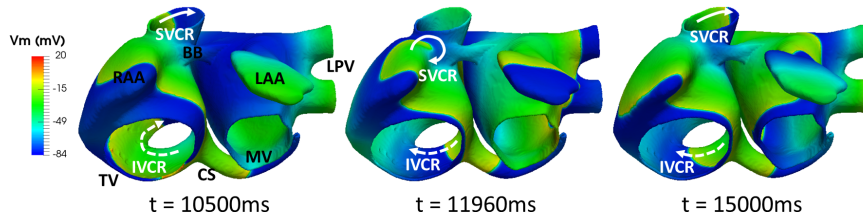


Figure 5.16: AP propagation in the atria following secession of the high frequency pacing close to the CS. Snapshots at $t = 10500$, 11960 and 15000 ms.

After two rotation cycles, the CT rotor became a reentry around the SVC (SVCR). Then at instant 11000 ms it migrated to the area between the BBRA and the RAA, where it kept rotating for about 20 cycles as a rotor. Later, at instant 12500 ms it came back to the SVC and behaved again as a reentry circulating around the SVC until the end of the simulation. The RWE became the extension of the SVCR and kept circulating around the IVC for the whole simulation time (IVCR). Snapshots of the basket's phase maps based on the HT of the filtered EGMs in this simulation without pacing are depicted in Figure 5.17. As demonstrated in these basket phase maps, IMPs are still generated even though the train of ectopic foci was not active. On the basket's phase maps, we observe the SVCR (white arrow) and the IVCR (white dashed arrow) for the three basket's positions. However, we observe IMPs (black arrows) in the TV region just in the case of SVC (panel A) and CT (panel B) positions, as occurred in the previous simulation with the CS pacing. For the CS position (panel C) the percentage of IMPs was completely negligible (also somewhat negligible presence of FIPs). This evidence suggests that high frequency pacing shouldn't be considered the leading cause of IMPs generation, although it might help depending on the position of the pacing with respect to the basket.

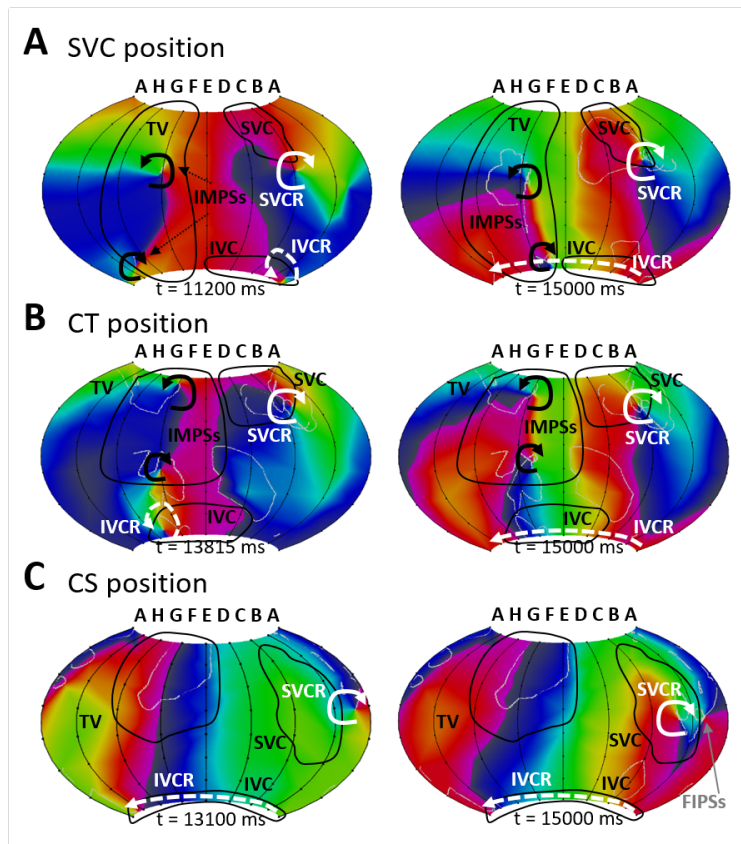


Figure 5.17: Basket phase maps of simulation following secession of the high frequency pacing close to the CS. Snapshots for the SVC (A), CT (B) and CS (C) basket positions are shown for 11200 and 15000 ms time points and demonstrate IMPSSs presence as in the simulation that includes the stimuli train.

5.3.3 Effect of the Far-Field Sources on Mapping

To verify the importance of FF sources in the genesis of IMPSSs, we computed the endocardial and basket phase maps when considering activity generated by decreasing areas of endocardial wall. As an example, Figure 5.18 shows results at $t=4935$ ms for the CT position of the basket. The left most column displays the three spatial extensions of AP sources considered in the analysis: A1 includes the entire atrial tissue, B1 includes only tissue encompassing the CT rotor and its RWE, and C1 considers only tissue closely encompassing the CT rotor. A2, B2 and C2 display endocardial-blood interface EGM; A3, B3 and C3 display endocardial-blood phase maps; and A4, B4 and C4 display the basket phase maps.

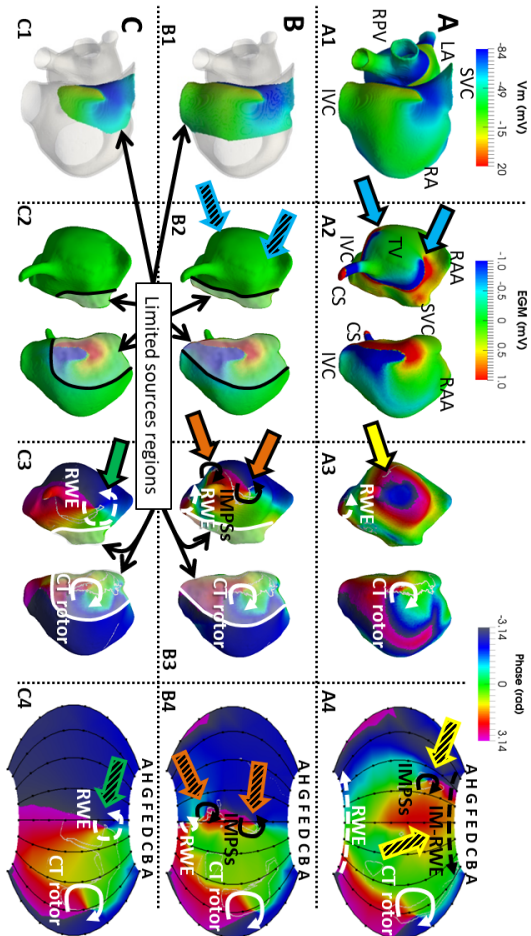


Figure 5.18: Effect of the FF sources. Maps for the endocardial and CT positioned basket were generated for 3 different distributions of sources (shown at $t=4935$ ms). Sources include the whole RA and LA tissue (A1); only tissue encompassing the CT rotor (C1); and only tissue encompassing the TVC (B1); and limited atrial sources (B2 and C2). Voltage maps of the EGMs computed on the endocardium-blood interface corresponding to the whole (A2) and limited atrial sources (B2 and C2). Blue arrows (A2) indicate edges of EGM wave propagating around the TV. Hatched blue arrows (B2) indicate that no significant voltage gradients are visible after removing sources from the TV region. A3, B3 and C3: Phase maps computed from the EGMs maps on the endocardium-blood interface. Yellow arrow (A3) indicates a short living PS at earlier time (no PS is visible at the moment of this analysis). Orange arrows (B3) indicate PS outside of the sources region (IMPS resulting from FF sources). Green arrow (C3) indicates a dramatic shift of the RWVE into a region outside of the sources region. A4, B4 and C4: Phase maps from the recordings of the virtual basket. Hatched yellow arrows (A4) show IMPS in the region of the TV and an imaginary rotor wave extension (IM-RWE) around the basket north-pole. Hatched orange arrows (B4) indicate the IMPS on the basket phase map. Hatched green arrow indicates a PS corresponding to the RWVE, but with a dramatic shift in location relative to A4. White/black lines on B2-3 and C2-3: limits of the sources regions.

When considering the whole atrial tissue (A1), the CT rotor (white curved arrow) and the RWE (dashed white curved arrow) were detected in both the endocardium-blood interface (A3) and the basket phase maps (A4). Additionally, an IMPS and an imaginary extension of that rotor (IM-RWE, hatched yellow arrows) appeared on the basket phase map in an area close to where the endocardial-blood EGMs showed propagation around the TV annulus (blue arrows in A2). As the IMPS was not detected on the endocardium-blood interface phase map (A3) but was detected on the basket mapping (A4) we further investigated whether IMPSs are formed by FF signals by excluding the nearby sources. When considering the sources as the activity at the CT rotor and RWE alone (B1), the EGMs in the TV area show very small voltage amplitude (hatched blue arrows in B2) that gives rise to IMPSs on the endocardium-blood surface (orange arrows in B3), as well as on the basket phase maps (hatched orange arrows in B4). These orange arrows (B3) indicate PSs outside of the sources region; that is, they are IMPSs resulting from FF sources. In Figure 5.19A the location of the IMPSs with respect to the area of the sources considered in the computations is shown more in detail.

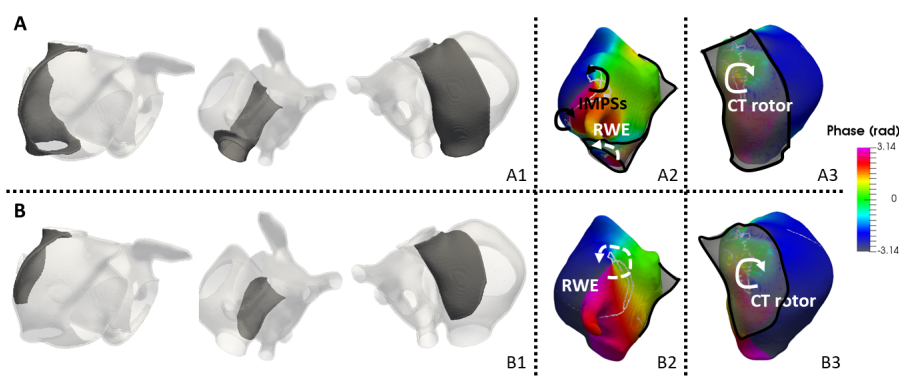


Figure 5.19: Sources regions to analyse the effect of FF. A) Views of the tissue encompassing the CT rotor and the RWE (A1), IMPSs and RWE (A2) and CT rotor (A3) on the endocardial phase maps. B) Views of the tissue encompassing only the CT rotor (B1), RWE (B2) and CT rotor (B3) on the endocardial phase maps. Black lines enhance the border of the sources region overlapped to the endocardial phase maps.

A magnification of the amplitude scale of the EGMs reveals that the IMPSs in this case arise from the high sensitivity of the phase analysis to low amplitude waves far from the sources (see Figure 5.20). Finally, phase maps of sources confined to only close vicinity of the CT rotor core (Figure 5.18, C1) removed the IMPSs and detected the CT rotor and its extension reentry toward the boundary of the source region (Figure 5.18, C3-C4), also termed RWE. The PS corresponding to the CT rotor remained close to its original location, shown

in panels A3 and A4 in Figure 5.18. However, the RWE suffered a dramatic shift in location relative to its origin, shown in Figure 5.18 (A3-A4), and resided outside of the active sources region (see Figure 5.19).

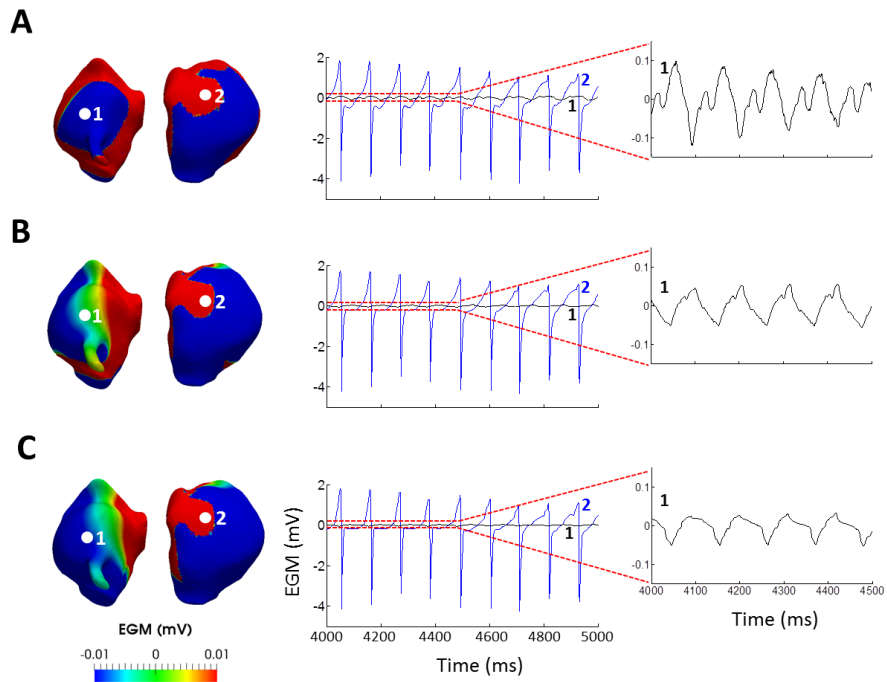


Figure 5.20: Sensitivity of the phase maps. Color scale magnification in the EGMs maps shown in Figure 5.18 (first and second column) and corresponding traces of the EGMs at points 1 and 2 when considering for the computations the limited sources regions as shown in Figure 5.18: whole atrial tissue (A1), tissue encompassing the CT rotor and the RWE (B1) and tissue encompassing the CT rotor (C1). Point 1 is located on the TV area, while point 2 is on the CT rotor meandering area.

The data in Figure 5.18 demonstrate that basket IMPs were a consequence of the distal atrial tissue activation at either the CT rotor and the IVC RWE, or at the TV region. In the example provided, FF sources interfered with the recordings when electrodes were at distances greater than about 0.5 cm from the endocardial wall activity. The effect was observed in the basket phase map when considering the whole atrial tissue (5.18A), and on the endocardium-blood interface and the basket phase maps when considering the tissue encompassing the CT rotor and its RWE (5.18B). However, if distance keeps increasing or source shrinking, the influence of FF sources is not enough to generate IMPs, as demonstrated by considering only the tissue encompassing the CT rotor (5.18C).

5.3.4 Effect of Inter-electrode Interpolation on Mapping

We hypothesized that reducing the inter-electrode distance would reduce the percentage of FIPs. Therefore, we analyzed the effect of modifying the number of electrodes in the basket by decreasing it to 4×6 or increasing it to 16×16 (Figure 5.21A). Figure 5.21 B-D are snapshots of the basket phase maps for each of the three positions: SVC position at $t = 5550$ ms (B); CT position at $t = 6110$ ms (C); and CS position at $t = 5040$ ms (D) for the 4×6 (left), 8×8 (middle) and 16×16 (right) electrodes density. Results are summarized in Table 5.2.

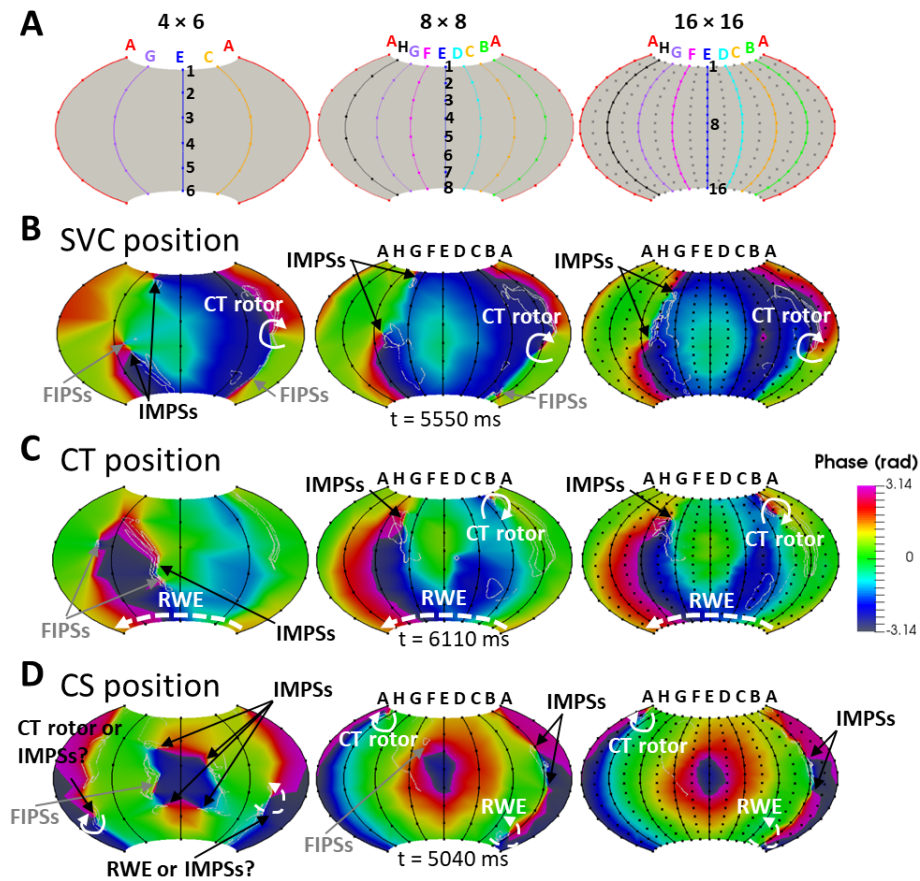


Figure 5.21: Effect of EGMs interpolation in the phase maps. 2D projection of the baskets (A) and phase maps for the SVC (B), CT (C) and CS (D) positions with a density of electrodes of 4×6 (left), 8×8 (middle) and 16×16 (right).

Increasing the electrodes density at the SVC position improved the ability to detect the CT rotor from 85% (4×6) to 94% (8×8) and 97% (16×16) of the time; at the CT position from 46% (4×6) to 90% (8×8) and 94% (16×16); and at the CS position from 35% (4×6 and 8×8) to 63% (16×16). Clearly, detection was less accurate in the CS position because the basket was located farthest from the CT rotor meandering area. Notably, at an electrode density of 4×6 in either the SVC or CS position, the detection of the RWE was impaired by the appearance of the FIPs. Increasing the electrode density from 8×8 to 16×16 , improved detection slightly (7 to 9%) for the SVC position, but remained unchanged for the CS position (61%). For the CT position, despite the fact that the RWE rotated at the south pole during the entire simulation time, no PS was detected at any of the electrode densities (see Figure 5.12). Whereas in the SVC and CT positions IMPs were present 100% of the simulation time regardless of the electrode density, the percentage of time during which FIPs were present went down considerably (from 70% to 57% and 0% for the SVC position and from 59% to 13% and 8% for the CT position) when increasing the electrode density. In the CS position, in addition to a poor detection of the CT rotor, the 4×6 electrode basket yielded an extremely high percentage of FIPs and IMPs during the entire simulation time and it was almost impossible to differentiate between them. Increasing the density of electrodes allowed differentiating IMPs from FIPs, so the FIPs percentage was reduced to 40% for 8×8 electrodes and eliminated for the 16×16 electrode basket density.

	SVC position			CT position			CS position		
	4×6	8×8	16×16	4×6	8×8	16×16	4×6	8×8	16×16
CT rotor	85	94	97	46	90	94	35	35	63
RWE	0 ^b	7	9	100 ^a	100 ^a	100 ^a	0 ^b	61	61
IMPs	100	100	100	100	100	100	— ^c	31	44
FIPs	70	57	0	59	13	8	— ^c	40	0

^a No PSs but sequential activation from A8 to H8

^b Detection possibly masked by the FIPs at electrodes A4-A5-A6-B4-B5-B6

^c The low density of electrodes renders a poor detection through the whole simulation period, including IMPs and FIPs

Table 5.2: PS detections with baskets with various densities of electrodes. Percentage time of detection of the CT rotor, RWE, IMPs and FIPs for the 3 positions of the basket when the density of electrodes was 4×6 , 8×8 and 16×16 .

In addition, we computed the phase maps with ~ 900 interpolated points for the 8×8 basket, and as expected, the number of FIPs was lower than for the phase maps with 57600 interpolated points. This fact confirmed our hypothesis regarding the effect of increasing the resolution of the phase mapping through increasing the number of interpolated points, which yields a higher number of FIPs. This effect was also shown when comparing the 8×8 basket with the

16×16 basket: both had 57600 interpolated points but in case of the 8×8 basket the number of interpolated points doubled and the number of FIPs was higher.

To sum up, CT rotor detection accuracy improved slightly when increasing the number of electrodes above 8×8 for the SVC and CT positions. Improvement was significant for the CS position, in which the rotor coverage was poor. In addition, no FIPs appeared for the SVC and CS positions, whereas the percentage of FIPs decreased slightly for the CT position. However, accuracy worsened considerably and the percentage of FIPs increased greatly when decreasing the number of electrodes. Finally, the percentage of IMPs remained stable regardless of the electrode density.

5.4 Discussion

To date the accuracy of mapping AF to localize rotors using panoramic basket catheters has not been validated, in part because in clinical practice the fibrillatory activation patterns are not known. We have used computer simulations to analyse in detail factors affecting AF mapping and localization of rotors. For this purpose, we used a realistic 3D atrial model, in which we reproduced the experimentally reported atrial heterogeneity and the electrical remodelling in cAF. As a result we obtained complex atrial activation that included a rotor along the CT. The resultant propagation patterns were also realistic, since stable reentrant AF drivers have been observed in the RA, in the region where CT and PM converge due to the 90° angle formed by the fibers in that region¹⁹ (see fibers orientation in our realistic model in Figure 3.7). Then, we mapped the atrial electrical activity by using a 64-pole basket located in three different positions within the RA.

Our results showed that rotors may be identified by phase maps of electrical recordings directly from the endocardium-blood interface, but less reliable so by phase maps built from basket catheter recordings. Importantly, a potential inaccuracy of the basket maps included phantom rotors, which may confound targeting of ablation to terminate AF. Our analysis suggested that the appearance of the phantom rotors can be attributed to at least three factors: the distance between the basket electrodes and the endocardial wall (positioning); the distance between the atrial waves and the electrodes (far-field); and the inter-electrodes distance (interpolation) of data used to create the maps. Therefore, our results suggested that while phase maps based on basket catheters are a powerful tool to map AF and to localize real rotors and other ablative targets, they can also mislead physicians to ablate atrial regions that are in fact free of rotor sources of AF.

5.4.1 Effect of the Electrode-Endocardium Distance

The distance between the endocardial wall and the basket electrodes depends on the basket's position within the atria. At each electrode location distance changes non-uniformly, which clearly affects rotor detection. Our results reveal that in addition to the amount of RA area coverage with small distance ($d \leq 0.5$ cm), coverage of the rotor meandering area is important. In our simulations, the basket at the CS position was the farthest from the rotor meandering area and therefore it detected the rotor only 30% of the time, which was much lower than the SVC and CT positions at which the basket was closer to the rotor area and detection was over 90% of the simulation time. On the other hand, the false rotors (IMPSs and FIPSS) tend to appear in basket regions with $d > 0.5$ cm.

Thus, basket positioning with gaps between the electrodes and the endocardium may lead to poor rotor detection and probably low rates of AF termination.^{23,24,30,198} Our data agree with results by Narayan et al,²⁰ in which ablation of drivers slowed but did not terminate AF when the atrial coverage was poor because of the limited size of commercial baskets compared to the large size of the atrium. Narayan et al attributed the failure to the existence of residual sources in the unmapped regions. However, according to our results, unsuccessful AF termination may have been also due to ablation of phantom rotors appearing at electrodes near and distant from the true rotors locus. Unfortunately, according to our simulations, false detection of rotors cannot be excluded, because even short electrode-to-endocardial wall distances do not guarantee the elimination of false rotors. We found that the endocardium-blood interface maps could show false rotors as well, likely because of FF contribution of sources and the high sensitivity of the phase mapping to low amplitude signals (Figure 5.18). Interestingly, when the distance between the basket electrodes and the endocardium increases (after excluding part of the atrial tissue in the computations), IMPSs tend to disappear (Figure 5.18C), probably because scroll wave filaments originating at endocardial IMPSs do not reach deep into the cavity.¹⁶⁰

Our results also suggest that the generation of IMPSs depends on the distance from the electrodes to the endocardium together with a complex electrical activation in the atria (they were not present in the SR case exposed in Appendix B), regardless to the existence or lack of focal sources. False rotors have also been observed recently in a work from Vijayakumar et al.²¹⁶ However, since in their work the unipolar EGMs were reconstructed from the measured body surface potential and phase maps built in a patient-specific geometry, we cannot compare their methodology with ours. Anyway, in their study false rotors detection seems to be related to the hypersensitivity of the phase mapping, which enhances the propagation even if the amplitude of the EGMs is negligible, and the sequential activation of a region surrounding an

obstacle, similarly to our results on the endocardium-blood interface, in which our phase maps reveal as a rotor the rotational propagation around an anatomical obstacle (RWE).

5.4.2 Effect of Basket Catheter Electrode Density

The ideal full-contact mapping would be one with a high resolution mesh of electrodes at the endocardium-blood interface where all the events related to electrical propagation are detected on the phase maps. Such phase maps would resemble our endocardium-blood interface phase maps, where the spatial resolution is ~ 0.5 mm. This would approximate the high resolution optical mapping approaches employed in animal heart studies where the spatial resolution ranges between 0.4 and 0.8 mm.¹⁷ However, atrial mapping with a basket catheter is not a high resolution technique (inter-electrode distances might range from some millimeters to ~ 1 cm) and sometimes is far from full-contact.^{20,23,24,176} Basket catheters are also limited by their relatively small size (largest available diameter ~ 60 mm),¹⁷⁶ which is an even more important limitation for AF ablation than the low spatial resolution to map a whole atrium and the unpredictable inter-electrodes distance.

Our results confirm that an 8×8 -pole mapping basket catheter can yield sufficient spatial resolution for rotor detection when it is properly located in contact with the tissue and at the rotor meandering area (SVC and CT positions in our simulations). Increasing the electrode density did not significantly improve rotor detection. We however predict that decreasing the electrode density (e.g., 4×6) from an optimal level will reduce the ability to detect rotors, while increasing it (e.g., 16×16) will not substantially alter results if the basket is located close to the rotor area (a substantial improvement was observed only for the basket at the CS position, where the basket did not cover the meandering area of the rotor).

Other studies are consistent with our observations. Narayan et al¹² showed that irregular inter-electrodes distances do not alter the sequential activation across adjacent electrodes surrounding a rotor. In addition, the study by Rappel and Narayan²¹ suggested that the spatial resolution of a 64-pole mapping basket catheter is adequate to detect rotors, although noise in the EGMs and electrode position might affect accuracy. This is in accordance with our results showing that CT rotor detection was good for a 64-pole basket positioned in the SVC and CT, whereas it was poor for the CS position.

Recently Roney et al¹⁹⁴ found that basket catheters are prone to false detections and may incorrectly reveal rotors that are not present, and also that increasing the number of splines up to 16 reduces both the number of false PSs and the number of missing PSs. In general, our results are in accordance with their results. When we increased the number of splines up to 16, for the three

basket positions the false PSs due to the interpolation (FIPs) were strongly reduced and the sensitivity for detection of the real rotor increased (see Table 5.2). However, our study highlights the fact that rotor tracking is more effective if the basket catheter is placed appropriately inside the atrial cavity to ensure extensive coverage of the rotor meandering area. Indeed, false rotors appearing as a result of a larger than critical electrode-to-tissue distance (IMPSS) will persist even after improving the spatial resolution (Figure 5.21). Furthermore, for certain positions of the basket, the rotor would not be detected if it drifts to a poorly covered region, as seen for the SVC position when the rotor migrated toward the IVC and for the CT position when the rotor migrated toward the SVC (see Figure 5.8).

It should be noted that, in the clinic, if the basket is not large enough, it would not be possible to determine if it is properly located inside a cavity because one would not know a priori the rotors' location. Averaging all three positions analysed, detection of the CT rotor with the 8×8 basket occurred 73% of the time, whereas with the 16×16 basket it was detected 85% of the time, which suggests some improvement with the added electrodes. IMPSS also seem to be detected by the basket at all densities, mostly in electrodes separated from the endocardium by >0.5 cm. Averaging all three basket positions, IMPSS are detected 77% and 81% of the time with the 8×8 and 16×16 basket, respectively. On the other hand, false rotors due to interpolation (i.e., FIPs) appear only when inter-electrode distances are large (reducing the inter-electrode distance by increasing the density to 16×16 substantially decreased, or eliminated, the occurrence of FIPs). Averaging all three positions, FIPs are detected 37% and 4% of the time with the 8×8 and 16×16 basket, respectively. Overall, our simulations suggest that the probability of ablating an erroneous target would be higher than the probability of correctly ablating a target when using a small 8×8 basket to guide ablation. However, the probability of correctly ablating a target would increase substantially when using a small 16×16 basket.

CHAPTER 6

Limitations

We need to consider several potential limitations of our study. On the one hand, at cellular level, all the variations of the CRN model used in this PhD thesis have been carried out based on experimental observations (nine cellular models accounting for the atrial heterogeneity in control, pAF and cAF conditions). Resultant APs have been also validated by comparison with the experimental data available in the literature. However, these experimental data not always correspond to experimental studies on humans, but some of them correspond to experiments on animals due to the lack of studies on humans. This fact do not alter our results because although propagation patterns likely would change using other variations of the ionic models, our aim was to analyse the reliability of the multi-electrode systems to map atrial activity and detect rotors.

On the other hand, at tissue level, we have presented simulations of an homogeneous sheet of atrial tissue with stable reentries. We didn't considered heterogeneous sheets of tissue with more complex propagation patterns, containing wavebreaks and multiple reentries colliding and merging. Therefore, our ability to extrapolate the results to fibrillatory wave propagation scenarios is limited. At organ level, the 3D atrial model is anatomically and electrophysiologically realistic, but is simplistic regarding wall thickness and ionic heterogeneous details. Although it does not alter our main conclusion, the preferable distance to avoid false rotors (IMPSs; $d < 0.5$ cm in our simulations) could be dependent on the anatomy of the atrial model; for example, it is likely that if the atrial wall thickness would change, this distance would also change. Besides, we didn't introduce atrial fibrosis, which might provoke more complex propagation patterns. Moreover, we have presented simulations for a single scenario of a relatively large rotor area without additional wavebreaks. Such considerations, as for the tissue level simulations, limit our ability to extrapolate quantitatively the results to other fibrillatory wave propagation scenarios. At torso level, we didn't considered the fat and the muscular fibers, which could affect to the wavefront spreading from the atria to the rest of organs. However, their influence should be stronger in the ECG on the torso surface than in the intracavitary EGMs.

In addition, our study used a single signal processing protocol that included band-pass filtering and the HT, together with an automatic PS detection. We did not explore other EGM processing methods that could have affected the rotors detection, however the protocol used is considered generic to phase mapping and as such very clinically relevant. Another factor limiting the accuracy of phase maps is the quality of the signals used here compared to the actual clinical EGM signals, which are usually contaminated by far-field effects from the ventricles and noise. Patterns of real atrial waves and signals during AF are probably more complex and with a higher number of artefacts than those simulated here, which could decrease the reliability of the

computed phase maps.

Finally, we simulated the EGMs recorded by spherical mapping basket catheter located inside the RA and no deformations were applied. Although somewhat unrealistic, this geometrical configuration is well suited to highlight the clinically important effect of varying the distance between the electrodes and the endocardium^{20,23,24} as well as the difference between the basket phase maps and the endocardium-blood interface phase maps. Moreover, our characterization of the various effects of specific basket positions on detection of true and false rotors is based on solid theoretical principles that are commonly accepted in cardiac electrophysiology and provide insights into the drawbacks of using basket catheter-based phase mapping of AF rotor sources.

CHAPTER 7

Conclusions

The main objective of this PhD thesis was to study the accuracy of multi-electrode mapping systems when mapping the electrical activity of the human atria, specially during reentrant activity, using computational models and simulations. From our results, we can conclude that computational models and simulations are a powerful tool to study the accuracy of such systems, which is not always possible in the clinic. But the most important outcome from this work is that multi-electrode systems accuracy might be affected by factors like the inter-electrode distance, the electrode-to-tissue distance, the far field sources, and the interpolation of the EGMs carried out to improve maps visualization and rotor tracking, which might lead to false rotors detection.

We splitted the main objective in several specific objectives to cover the understanding about the multi-electrode systems accuracy from simplified geometrical arrays with constant inter-electrode and electrode-to-tissue distances to systems like the basket catheter, with non-constant inter-electrode and electrode-to-tissue distances. Our findings related to each specific objective are summarized below.

Development and validation of a realistic and multiscale 3D atria-torso model as a tool for computing intracavitary EGMs

Firstly, we conclude that the simulation of realistic intracavitary EGMs is possible as far as the adjustment of the atrial model is based on experimental observations regarding the atrial anatomy, electrophysiological heterogeneity and tissue anisotropy. This assures realistic simulations in relation to APs morphology and duration, as well as atrial activation times, which are comparable to experimental data. Therefore, the computed EGMs are also within the range of experimental observations.

Secondly, we conclude that the bidomain approximation proposed in this PhD thesis is a valid approach to compute intracavitary unipolar EGMs (in absence of external currents) only if the atria is immersed in a torso model, since the non-flux atria-air condition yields distorted EGMs if the torso is not considered in the computations. In case of bipolar EGMs computed with the atria-blood model, the distortion of the EGMs could be smoothed but we cannot assure their disappearance, since it would be completely dependent on the location of the electrodes.

Finally, we conclude that the torso has a strong influence in the computation of intracavitary unipolar EGMs and although we are not interested in simulating the P-waves, a torso model is needed to obtain realistic unipolar EGMs. Therefore, it is not recommendable to use an isolated atria model to compute them.

To sum up, our findings suggest that a realistic 3D atria-torso model is the best tool to compute intracavitary unipolar EGMs with the aim of mapping the electrical activity of the atria.

Analysis of factors affecting the accuracy of a multi-electrode system with equidistant inter-electrode distance when mapping reentries in a sheet of atrial tissue

On the one hand, our findings regarding the atrial tissue simulations demonstrate that although the torso has a strong influence in the computation of unipolar EGMs when considering a realistic atrial model, its influence is slight when the model is a sheet of atrial tissue instead of the whole atria. Unipolar EGMs are not distorted, they only suffer an increase in their amplitude (the strongest effect is seen at the epicardium while it is negligible at high distances from the tissue). Therefore, under this scenario there is no need to add a layer of torso in the model. Moreover, by increasing the electrode-to-tissue distance, the amplitude of the EGMs decreased; the contribution of the NF sources also decrease, while FF sources contribution increase, as expected. Thereby, at certain distances from the tissue, electrodes may mainly record remote electrical activity.

On the other hand, we conclude that localization of a rotor with high density multi-electrode arrays (short inter-electrode distances) placed in a cavity parallel to a flat endocardium can be accurate when the array is placed closest to the endocardium. For low density arrays (large inter-electrode distances), however, accuracy can be maintained by increasing the distance to the tissue. This effect is due to the fact that at higher distances, electrodes mainly record remote electrical activity while at short distances they record local activity. Therefore, for low density arrays the accuracy improves at higher distances, since at those distances the field of view of the electrodes is wider than in contact to the tissue and the tissue is better covered by the multi-electrode array.

Our results also demonstrate that phase maps per se do not allow the differentiation between functional and anatomical reentries (all of them registered as rotors) because they have a high sensitivity even for small amplitude EGMs. Then, signals of very low amplitude recorded over the orifices provoke a convergence of phases in the middle of the orifice, generating a PS (trajectories concentrated in the orifice). However, our results suggest that the multi-electrode arrays are very useful to detect reentries driving AF in an excitable sheet. Thus, the combination of phase and DF maps with PS detections is able to distinguish whether a reentry is anatomical or functional. For functional reentries the meandering area coincide with the highest DFs region, whereas for anatomical reentries the meandering area coincide with the lowest DFs region.

Finally, our outcomes suggest that cAF remodelling spatially stabilises rotors. Therefore, rotor meandering area is smaller for cAF than for pAF, while DFs are higher, as a consequence of the larger APD shortening due to the stronger remodelling in cAF compared to pAF conditions.

To sum up, we conclude that multi-electrode arrays are a powerful tool to detect reentrant activity, although the minimum spatial resolution to accurately track rotors depends on the electrode-to-tissue distance. High density multi-electrode arrays placed parallel and close to a flat endocardium are accurate, while for low densities it is needed to increase the distance to maintain the accuracy. In addition, multi-electrode arrays are able to differentiate functional and anatomical reentries by combining both, phase and DF maps.

Analysis of factors affecting the accuracy of multi-electrode systems with non-equidistant inter-electrodes (basket catheter) when mapping reentries in the atria

On the one hand, we conclude that atrial rotor detection can be achieved by a phase analysis of multi-electrode basket catheter positioned at any distance from the atrial tissue, but preferably placed closer than 0.5 cm to the atrial tissue, as basket electrodes far from the tissue tend to produce false rotors (IMPSs) in addition to real rotors due to the increased effect of distant activity when propagation patterns are complex. The increase of the distant activity contribution with the electrode-to-tissue distance, as well as the high sensitivity of phase analysis, observed for the atrial tissue simulations and the multi-electrode arrays, also influence rotors detection by generating false rotors when considering a realistic atrial anatomy mapped with a basket catheter (the larger distance, the stronger influence). However, results obtained with multi-electrode arrays (two-dimensional) placed parallel and close to a flat endocardium, in which for low densities it is needed to increase the distance to maintain the accuracy, cannot be extrapolated to basket catheters (three-dimensional) since the distance to the tissue might generate false rotors (IMPSs). Unlike multi-electrode arrays, not all the electrodes of the basket catheter are at the same distance from the tissue. If one side of the catheter is moved away from the tissue, then it approaches the tissue in the opposite area. Therefore, part of the basket mainly records local activation (electrodes close to the tissue) while the other part records remote activation (electrodes separated $d > 0.5$ cm from the tissue) and, as a consequence, we might observe false imaginary rotors (IMPSs).

On the other hand, our findings suggest that basket electrode grids of 8×8 or more are sensitive enough for detection of large area rotors, although accuracy will vary depending on the position of the basket inside the atrial cavity and the number of electrodes. For small size baskets, their location plays an important role in rotor detection. However, in an ablation procedure in the clinical practice, the location of rotors is a priori unknown and we cannot assure a proper location of the basket to obtain a high coverage of the rotor meandering area and, therefore, an accurate rotor detection. Then, electrodes with higher density than 8×8 might improve the outcomes: better real rotor detection and reduced number of false rotors due to the EGMs

interpolation (FIPs), as they tend to disappear by increasing electrodes density. Nevertheless, false rotors due to the electrode-to-tissue distance (IMPs) will still be detected regardless the electrodes density.

Finally summing up, we conclude that although basket catheters are currently used to guide patient-specific ablation of the AF drivers and seem to be a promising tool, spurious targets in the form of phantom rotors cannot be excluded and all detected rotors should be cautiously considered.

CHAPTER 8

Future Research Work

The main objective of this PhD thesis was to study the accuracy of multi-electrode mapping systems when mapping the electrical activity of the human atria through computational models and simulations. Our goal was achieved and we were able to successfully analyse such systems for accuracy. However, the limitations described in Chapter 6 point out the need to improve our 3D multiscale atria-torso model and the methodology in some aspects. For this purpose, the future work will be focused on the following issues:

1. Introduction of the heterogeneous thickness of the atrial wall in the 3D atrial model, in order to analyse its influence in the computation of the EGMs, the FF sources contribution and the detection of false rotors by the basket catheter.
2. Addition of fibrosis to the 3D atrial model when simulating AF, to generate more chaotic propagation patterns and analyse the accuracy of multi-electrode systems for such scenarios.
3. Consideration of simulations with multiple wavebreaks and rotors when mapping the atrial electrical activity with multi-electrode systems in order to be able to extrapolate our results to other fibrillatory wave propagation scenarios.
4. Addition of noise to our simulated EGMs in order to better approach the actual phase maps obtained in the clinic and prove the reliability of our study with computed phase maps.
5. Development of further studies with the aim of developing algorithms able to discriminate false from true rotors in the basket mapping.

CHAPTER 9

Contributions

As commonly occurs in the research field, this PhD thesis is not an isolated item. In fact, it has been developed within a multidisciplinary framework, in continuous and close collaboration with other research groups and institutions, as well as with other members in this research group itself. As a result, the highlights achieved in this work have been divulged in top level conferences, national and international, and journals with high impact factor indices.

9.1 Publications

Among the publications derived from this PhD thesis we find the following journal papers and conference papers and communications.

9.1.1 Journal Papers

Main Contributions:

1. **L. Martínez-Mateu**, L. Romero, A. Ferrer-Albero, R. Sebastian, JF. Rodríguez Matas, J. Jalife, O. Berenfeld and J. Saiz. Factors affecting basket catheter detection of real and phantom rotors in the atria: A Computational study. *PLoS Comput Biol*, 14(3):e1006017, 2018.
2. A. Ferrer-Albero, EJ. Godoy, M. Lozano, **L. Martínez-Mateu**, F. Atienza, J. Saiz and R. Sebastian. Non-invasive localization of atrial ectopic beats by using simulated body surface P-wave integral maps, *PLoS ONE*, 12(7):e0181263, 2017.

Related Contributions:

1. A. Ferrer, R. Sebastián, D. Sánchez-Quintana, JF. Rodríguez, EJ. Godoy, **L. Martínez** and J. Saiz. Detailed Anatomical and Electrophysiological Models of Human Atria and Torso for the Simulation of Atrial Activation. *PLoS ONE*, 10(11): e0141573, 2015
2. D. Calvo, F. Atienza, J. Saiz, **L. Martínez**, P. Ávila, J. Rubín, B. Herreros, A. Arenal, J. García-Fernández, A. Ferrer, R. Sebastián, P. Martínez-Cambor, J. Jalife and O. Berenfeld. Ventricular Tachycardia and Early Fibrillation in Patients with Brugada Syndrome and Ischemic Cardiomyopathy Show Predictable Frequency-Phase Properties on the Precordial ECG Consistent with the Respective Arrhythmogenic Substrate. *Circ Arrhythm Electrophysiol*, 8(5): 1133-1143, 2015

3. JF. Gomez, K. Cardona, **L. Martínez**, J. Saiz and B. Trenor. Electrophysiological and Structural Remodeling in Heart Failure Modulate Arrhythmogenesis. 2D Simulation Study. *PLoS ONE*, 9(7): e103273, 2014

9.1.2 Conference Papers and Communications

Main Contributions:

1. **L. Martínez**, L. Romero, O. Berenfeld, J. Jalife, J. Saiz. The high sensitivity of phase analysis might generate false rotors. *Atrial Fibrillation: from mechanisms to population science (CNIC)*, November 2017, Madrid, Spain.
2. **L. Martínez**, L. Romero, J. Jalife, O. Berenfeld and J. Saiz. Can false rotors be recorded by catheters when mapping complex atrial propagation? *European Medical and Biological Engineering Conference (EMBEC)*, June 2017, Tampere, Finland.
3. **L. Martínez**, L. Romero, A. Ferrer, J. Jalife, O. Berenfeld and J. Saiz. Effect of Multi-Electrode Configurations on Accuracy of Rotor Detection in the Atria. *Computing in Cardiology*, 43:1085-1088, September 2016, Vancouver, Canada.
4. **L. Martínez**, L. Romero, J. Jalife, O. Berenfeld and J. Saiz. Far field induces false rotors when mapping complex atrial arrhythmias. *CARDIOSTIM*, EP Europace; Volume 18 (Issue suppl1): Pages i141, June 2016, Nice, France.
5. **L. Martínez**, J. Jalife, O. Berenfeld and J. Saiz. Are Multi-electrode Arrays able to Differentiate Anatomical from Functional Reentries in an Excitable Sheet? *Computing in Cardiology*, 42:865-868, September 2015, Nice, France.
6. **L. Martínez**, O. Berenfeld, J. Jalife and J. Saiz. The sensitivity and specificity of localizing rotors during atrial fibrillation depends on the multi-electrode array properties. *Gordon Research Conference (GRC) on Cardiac Arrhythmia Mechanisms*, March 2015, Barga, Italy.
7. **L. Martínez Mateu**, L. Romero Pérez, O. Berenfeld, J. Jalife and J. Saiz Rodríguez. Caracterización de los parches multielectrodo para la detección de rotores durante fibrilación auricular. *XXXII Congreso*

Anual de la Sociedad Española de Ingeniería Biomédica (CASEIB), November 2014, Barcelona, Spain. The work presented at this conference was awarded: “**3er PREMIO CASEIB 2014 a las contribuciones científicas de los estudiantes**”.

8. **L. Martínez**, L. Romero, C. Tobón, JM. Ferrero, J. Jalife, O. Berenfeld and J. Saiz. Accurate Characterization of Rotor Activity during Atrial Fibrillation Depends on the Properties of the Multi-electrode Grid. *Computing in Cardiology*, 41:757-760, September 2014, Cambridge, Massachusetts (USA).

Related contributions:

1. S. Rocher, A. López, A. Ferrer, **L. Martínez**, D. Sánchez, FJ. Saiz. Desarrollo de un modelo 3D de la aurícula humana para el estudio de la propagación tisular durante la brilación auricular crónica. *XXXV Congreso Anual de la Sociedad Española de Ingeniería Biomédica (CASEIB)*, November 2017, Bilbao, Spain.
2. S. Rocher, A. López, A. Ferrer, **L. Martínez**, D. Sánchez-Quintana, J. Saiz. A true 3D model of the human atria for atrial fibrillation studies. *Atrial Fibrillation: from mechanisms to population science (CNIC)*, November 2017, Madrid, Spain.
3. A. Ferrer-Albero, EJ. Godoy, R. Sebastian, **L. Martínez** and J. Saiz. Analysis of in-silico Body Surface P-wave Integral Maps show Important Differences depending on the Connections between Coronary Sinus and Left Atrium. *Computing in Cardiology*, 43:745-748, September 2016, Vancouver, Canada.

9.2 Collaborations

This PhD thesis has been developed in close collaboration with the following institutions and research groups:

1. Center for Arrhythmia Research, University of Michigan, USA
Associate Professor Omer Berenfeld
Professor José Jalife
2. Computational Multiscale Simulation Lab, Department of Computer Science, Universitat de València, Spain

Associate Professor Rafael Sebastián

3. Dipartimento di Chimica, Materiali e Ingegneria Chimica Giulio Natta, Politecnico di Milano, Italy

Associate Professor José Félix Rodríguez Matas

9.3 Research projects

This work has been developed within the framework of the following research projects:

- Mejora en la prevención y tratamiento de patologías cardíacas a través de la modelización multi-escala y la simulación computacional (DIGITAL HEART). PROMETEO/2012/030, Generalitat Valenciana
- Tecnologías computacionales para la optimización de terapias personalizadas de patologías auriculares y ventriculares. DPI2016-75799-R (Plan Estatal de Investigación Científica y Técnica y de Innovación 2013-2016), Ministerio de Economía, Industria y Competitividad de España, Agencia Estatal de Investigación and European Commission (European Regional Development Funds-ERDF-FEDER).

APPENDIX **A**

CRN Model Formulation

The schematic representation of a cardiomyocyte modelled by the CRN model is shown in Figure A.1. All the equations describing the model are listed in this Appendix.

$$\frac{dV}{dt} = \frac{-(I_{ion} + I_{st})}{C_m}$$

$$I_{ion} = I_{Na} + I_{K1} + I_{to} + I_{Kur} + I_{Kr} + I_{Ks} + I_{CaL} + I_{pCa} + I_{NaK} + I_{NaCa} + I_{bNa} + I_{bCa}$$

$$\frac{dy}{dt} = \frac{y_{\infty} - y}{\tau_y} \text{ where } y \text{ is any gating variable}$$

$$\frac{d[Na^+]_i}{dt} = \frac{-3I_{NaK} - 3I_{NaCa} - I_{bNa} - I_{Na}}{FV_i}$$

$$\frac{d[K^+]_i}{dt} = \frac{2I_{NaK} - I_{K1} - I_{to} - I_{Kur} - I_{Kr} - I_{Ks} - I_{bK}}{FV_i}$$

$$\frac{d[Ca^{2+}]_i}{dt} = \frac{B1}{B2}$$

$$B1 = \frac{2I_{NaCa} - I_{pCa} - I_{CaL} - I_{bCa}}{2FV_i} + \frac{V_{up}(I_{up,leak} - I_{up}) + I_{rel}V_{rel}}{V_i}$$

$$B2 = 1 + \frac{[Trpn]_{max}K_{m,Trpn}}{([Ca^{2+}]_i + K_{m,Trpn})^2} + \frac{[Cmdn]_{max}K_{m,Cmdn}}{([Ca^{2+}]_i + K_{m,Cmdn})^2}$$

$$\frac{d[Ca^{2+}]_{up}}{dt} = I_{up} - I_{up,leak} - I_{tr} \frac{V_{rel}}{V_{up}}$$

$$\frac{d[Ca^{2+}]_{rel}}{dt} = (I_{tr} - I_{rel}) \left\{ 1 + \frac{[Csqn]_{max}K_{m,Csqn}}{([Ca^{2+}]_{rel} + K_{m,Csqn})^2} \right\}^{-1}$$

Equilibrium Potential:

$$E_x = \frac{RT}{zF} \log \frac{[X]_o}{[X]_i}, \text{ for } X = Na^+, K^+, Ca^{2+}$$

Fast Na⁺ Current:

$$I_{Na} = g_{Na} m^3 h j (V - E_{Na})$$

$$\alpha_m = \begin{cases} 0.32 \frac{V + 47.13}{1 - e^{[-0.1(V+47.13)]}} \\ 3.2, \end{cases} \quad \text{if } V = -47.13$$

$$\beta_m = 0.08 \cdot e^{\left(-\frac{V}{11}\right)}$$

$$\alpha_h = \begin{cases} 0.135e^{\left(-\frac{V+80}{6.8}\right)} \\ 0, \end{cases} \quad \text{if } V \geq -40$$

$$\beta_h = \begin{cases} \left\{ \left\{ 3.56e^{(0.079V)} + 3.1 \times 10^5 e^{(0.35V)} \right. \right. \\ \left. \left. \left[0.13 \left[1 + e^{\left(-\frac{V+10.66}{11.1}\right)} \right] \right] \right\}^{-1} \right\}, \quad \text{if } V \geq -40 \end{cases}$$

$$\alpha_j = \begin{cases} [-127.140e^{(0.2444V)} - 3.474 \times 10^{-5}e^{(-0.04391V)}] \frac{V + 37.78}{1 + e^{[0.311(V+79.23)]}} \\ 0, \end{cases} \quad \text{if } V \geq -40$$

$$\beta_j = \begin{cases} \left\{ \begin{array}{l} 0.1212 \frac{e^{(-0.01052V)}}{1 + e^{[-0.1378(V+40.14)]}} \\ 0.3 \frac{e^{[-2.535 \times 10^{-7}V]}}{1 + e^{[-0.1(V+32)]}}, \end{array} \right\} \quad \text{if } V \geq -40$$

$$\tau_\phi = (\alpha_\phi + \beta_\phi)^{-1}, \quad \phi_\infty = \alpha_\phi \tau_\phi, \quad \text{for } \phi = m, h, j$$

Time-Independent K^+ Current:

$$I_{K1} = \frac{g_{K1}(V - E_K)}{1 + e^{[0.07(V+80)]}}$$

Transient Outward K^+ Current:

$$I_{to} = g_{to} o_a^3 o_i (V - E_K)$$

$$\alpha_{o(a)} = 0.65 \left[e^{\left(-\frac{V+10}{8.5}\right)} + e^{\left(-\frac{V-30}{59.0}\right)} \right]^{-1}$$

$$\beta_{o(a)} = 0.65 \left[2.5 + e^{\left(\frac{V+82}{17.0} \right)} \right]^{-1}, \quad \tau_{o(a)} = [\alpha_{o(a)} + \beta_{o(a)}]^{-1} / K_{Q_{10}}$$

$$o_{a(\infty)} = \left[1 + e^{\left(-\frac{V+20.47}{17.54} \right)} \right]^{-1}, \quad \alpha_{o(i)} = \left[18.53 + e^{\left(\frac{V+113.7}{10.95} \right)} \right]^{-1}$$

$$\beta_{o(i)} = \left[35.56 + e^{\left(-\frac{V+1.26}{7.44} \right)} \right]^{-1}, \quad \tau_{o(i)} = [\alpha_{o(i)} + \beta_{o(i)}]^{-1} / K_{Q_{10}}$$

$$o_{i(\infty)} = \left[1 + e^{\left(\frac{V+43.1}{5.3} \right)} \right]^{-1}$$

Ultrarapid Delayed Rectifier K^+ Current:

$$I_{Kur} = g_{Kur} u_a^3 u_i (V - E_K), \quad g_{Kur} = 0.005 + \frac{0.05}{1 + e^{\left(-\frac{V-15}{13} \right)}}$$

$$\alpha_{u(a)} = 0.65 \left[e^{\left(-\frac{V+10}{8.5} \right)} + e^{\left(-\frac{V-30}{59.0} \right)} \right]^{-1}$$

$$\beta_{u(a)} = 0.65 \left[2.5 + e^{\left(\frac{V+82}{17.0} \right)} \right]^{-1}, \quad \tau_{u(a)} = [\alpha_{u(a)} + \beta_{u(a)}]^{-1} / K_{Q_{10}}$$

$$u_{a(\infty)} = \left[1 + e^{\left(-\frac{V+30.3}{9.6} \right)} \right]^{-1}, \quad \alpha_{u(i)} = \left[21 + e^{\left(-\frac{V-185}{28} \right)} \right]^{-1}$$

$$\beta_{u(i)} = e^{\left(\frac{V-185}{16} \right)}, \quad \tau_{u(i)} = [\alpha_{u(i)} + \beta_{u(i)}]^{-1} / K_{Q_{10}}$$

$$u_{i(\infty)} = \left[1 + e^{\left(\frac{V - 99.45}{27.48} \right)} \right]^{-1}$$

Rapid Delayed Outward Rectifier K⁺ Current:

$$I_{Kr} = \frac{g_{Kr} x_r (V - E_K)}{1 + e^{\left(\frac{V + 15}{22.4} \right)}}, \quad \alpha_{x(r)} = 0.0003 \frac{V + 14.1}{1 - e^{\left(-\frac{V + 14.1}{5} \right)}}$$

$$\beta_{x(r)} = 7.3898 \times 10^{-5} \frac{V - 3.3328}{e^{\left(\frac{V - 3.3328}{5.1237} \right)} - 1}, \quad \tau_{x(r)} = [\alpha_{x(r)} + \beta_{x(r)}]^{-1}$$

$$x_{r(\infty)} = \left[1 + e^{\left(-\frac{V + 14.1}{6.5} \right)} \right]^{-1}$$

Slow Delayed Outward Rectifier K⁺ Current:

$$I_{Ks} = g_{Ks} x_s^2 (V - E_K), \quad \alpha_{x(s)} = 4 \times 10^{-5} \frac{V - 19.9}{1 - e^{\left(-\frac{V - 19.9}{17} \right)}}$$

$$\beta_{x(s)} = 3.5 \times 10^{-5} \frac{V - 19.9}{e^{\left(\frac{V - 19.9}{9} \right)} - 1}, \quad \tau_{x(s)} = \frac{1}{2} [\alpha_{x(s)} + \beta_{x(s)}]^{-1}$$

$$x_{s(\infty)} = \left[1 + e^{\left(-\frac{V - 19.9}{12.7} \right)} \right]^{-1/2}$$

L-Type Ca₂₊ Current:

$$I_{CaL} = g_{CaL} df_{Ca}(V - 65)$$

$$\tau_d = \frac{1 - e\left(-\frac{V+10}{6.24}\right)}{0.035(V+10) \left[1 + e\left(-\frac{V+10}{6.24}\right)\right]}, \quad d_\infty = \left[1 + e\left(-\frac{V+10}{8}\right)\right]^{-1}$$

$$\tau_f = 9 \left[0.0197e^{-0.033^2(V+10)^2} + 0.02\right]^{-1}, \quad f_\infty = \left[1 + e\left(\frac{V+28}{6.9}\right)\right]^{-1}$$

$$\tau_{f(Ca)} = 2, \quad f_{Ca(\infty)} = \left(1 + \frac{[Ca^{2+}]_i}{0.00035}\right)^{-1}$$

Na⁺-K⁺ Pump Current:

$$I_{NaK} = I_{NaK(max)} f_{NaK} \frac{1}{1 + [K_{mNa(i)}/[Na^+]_i]^{1.5}} \frac{[K^+]_o}{[K^+]_o + K_{mK(o)}}$$

$$f_{NaK} = \left[1 + 0.1245e\left(-0.1\frac{FV}{RT}\right) + 0.0365\sigma e\left(-\frac{FV}{RT}\right)\right]^{-1}$$

$$\sigma = \frac{1}{7} \left[e\left(\frac{[Na^+]_o}{67.3}\right) - 1 \right]$$

Na⁺/Ca²⁺ Exchanger Current:

$$I_{NaCa} =$$

$$\frac{I_{NaCa(max)} \left\{ e^{[\gamma FV/(RT)][Na^+]_i^3[Ca^{2+}]_o} - e^{[(\gamma-1)FV/(RT)][Na^+]_o^3[Ca^{2+}]_i} \right\}}{(K_{mNa}^3 + [Na^+]_o^3)(K_{mCa} + [Ca^{2+}]_o) \cdot \{1 + e^{[(\gamma-1)FV/(RT)]}\}}$$

Background currents:

$$I_{bCa} = g_{bCa}(V - E_{Ca}), \quad I_{bNa} = g_{bNa}(V - E_{Na})$$

Ca²⁺ Pump Current:

$$I_{pCa} = I_{pCa(max)} \frac{[Ca^{2+}]_i}{0.0005 + [Ca^{2+}]_i}$$

Ca²⁺ Release Current From JSR:

$$I_{rel} = k_{rel}u^2vw([Ca^{2+}]_{rel} - [Ca^{2+}]_i), \quad \tau_u = 8.0$$

$$u_{\infty} = \left(1 + e^{\left[-\frac{F_n - 3.4175 \times 10^{-13}}{13.67 \times 10^{-16}} \right]} \right)^{-1}$$

$$\tau_v = 1.91 + 2.09 \left(1 + e^{\left[-\frac{F_n - 3.4175 \times 10^{-13}}{13.67 \times 10^{-16}} \right]} \right)^{-1}$$

$$v_{\infty} = 1 - \left(1 + e^{\left[-\frac{F_n - 6.835 \times 10^{-14}}{13.67 \times 10^{-16}} \right]} \right)^{-1}$$

$$\tau_w = 6.0 \frac{1 - e^{\left(-\frac{V - 7.9}{5} \right)}}{\left[1 + 0.3e^{\left(-\frac{V - 7.9}{5} \right)} \right] (V - 7.9)}$$

$$w_{\infty} = 1 - \left[1 + e^{\left(-\frac{V - 40}{17} \right)} \right]^{-1}$$

$$F_n = 10^{-12}V_{rel}I_{rel} - \frac{5 \times 10^{-13}}{F} \left(\frac{1}{2}I_{CaL} - \frac{1}{5}I_{NaCa} \right)$$

Transfer Current From NSR to JSR:

$$I_{tr} = \frac{[Ca^{2+}]_{up} - [Ca^{2+}]_{rel}}{\tau_{tr}}, \quad \tau_{tr} = 180$$

Ca²⁺ Uptake Current by the NSR:

$$I_{up} = \frac{I_{up(max)}}{1 + (K_{up}/[Ca^{2+}]_i)}$$

Ca²⁺ Leak Current by the NSR:

$$I_{up,leak} = \frac{[Ca^{2+}]_{up}}{[Ca^{2+}]_{up(max)}} I_{up(max)}$$

Ca²⁺ Buffers:

$$[Ca^{2+}]_{Cmndn} = [Cmndn]_{max} \frac{[Ca^{2+}]_i}{[Ca^{2+}]_i + K_m C_{mndn}}$$

$$[Ca^{2+}]_{Trpn} = [Trpn]_{max} \frac{[Ca^{2+}]_i}{[Ca^{2+}]_i + K_m Trpn}$$

$$[Ca^{2+}]_{Csqn} = [Csqn]_{max} \frac{[Ca^{2+}]_{rel}}{[Ca^{2+}]_{rel} + K_m C_{sqn}}$$

The CRN model formulation was implemented in Fortran in order to obtain the V_m by the *ELVIRA* software.

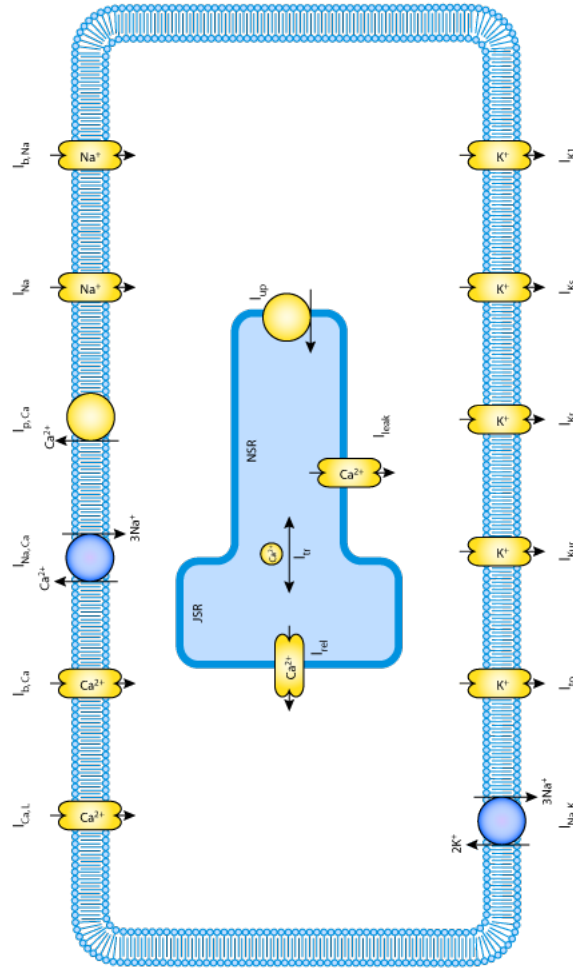


Figure A.1: Schematic representation of a cardiomyocyte modelled by the CRN model.

APPENDIX B

Propagation Patterns in the Basket Catheter for Sinus Rhythm

Propagation patterns in the basket catheter during atrial depolarization for the SVC, CT and CS positions are shown in Figure B.1, Figure B.2 and Figure B.3, respectively. As expected, no PSs are detected during SR.

For the SVC position (Figure B.1), in which the basket is located closer to the SAN region, depolarization spreads first from spline C to B-A-H-G (i.e. from SVC towards TV) and from electrode 1 to 8 (i.e. from SVC towards IVC), and then from C to D-E-F, also from the north pole to the south pole. Last electrodes recording the activation of the tissue are those located between splines D-G, at the south hemisphere of the basket.

For the CT position (Figure B.2), propagation patterns are similar to those obtained at the SVC position: from spline C to B-A-H-G and then from C to D-E-F (from SVC towards TV and IVC). But for this basket position, the direction of the propagation is not so marked from north pole to south pole.

Finally, for the CS position (Figure B.3), the propagation spreads from the equator, also from spline C to splines B-A-H-G (from SVC towards TV) and from spline C to D-E-F (from SVC towards IVC). Last electrodes recording the activation of the tissue are those located between splines D-G, close to the south pole.

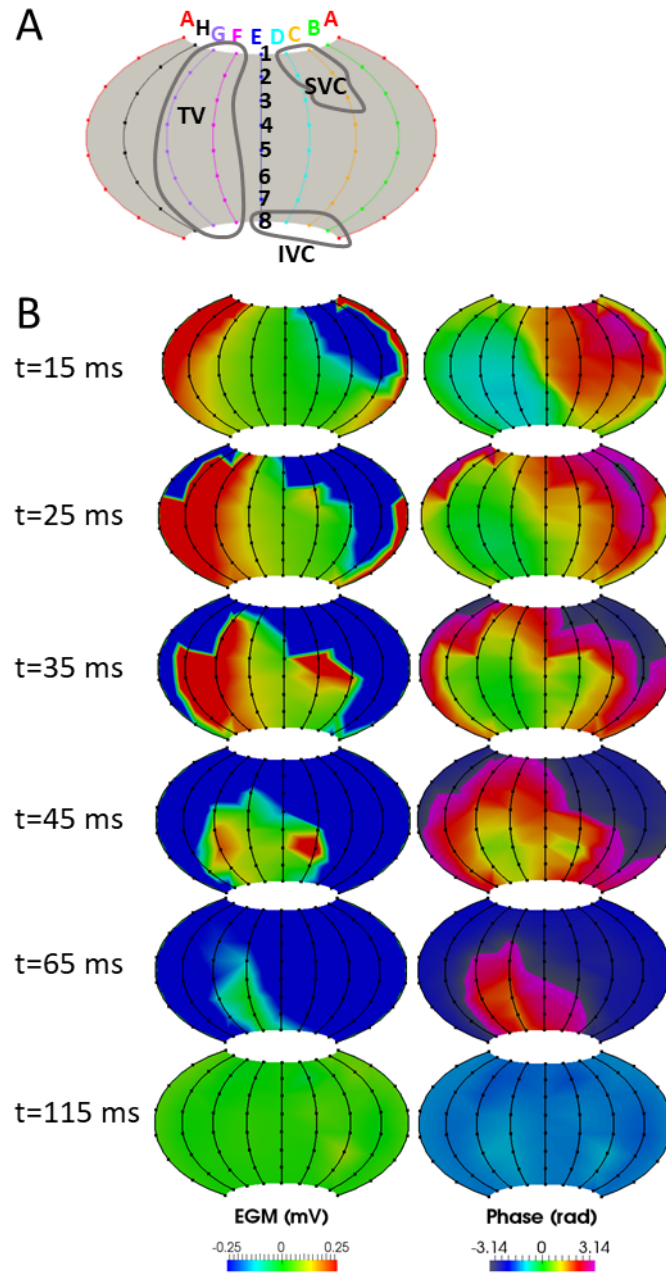


Figure B.1: Basket propagation pattern in SR for the SVC position. A) 2D projection of basket (TV, SVC and IVC orifices superimposed). B) Snapshots of the EGMs (left column) and phase maps (right column).

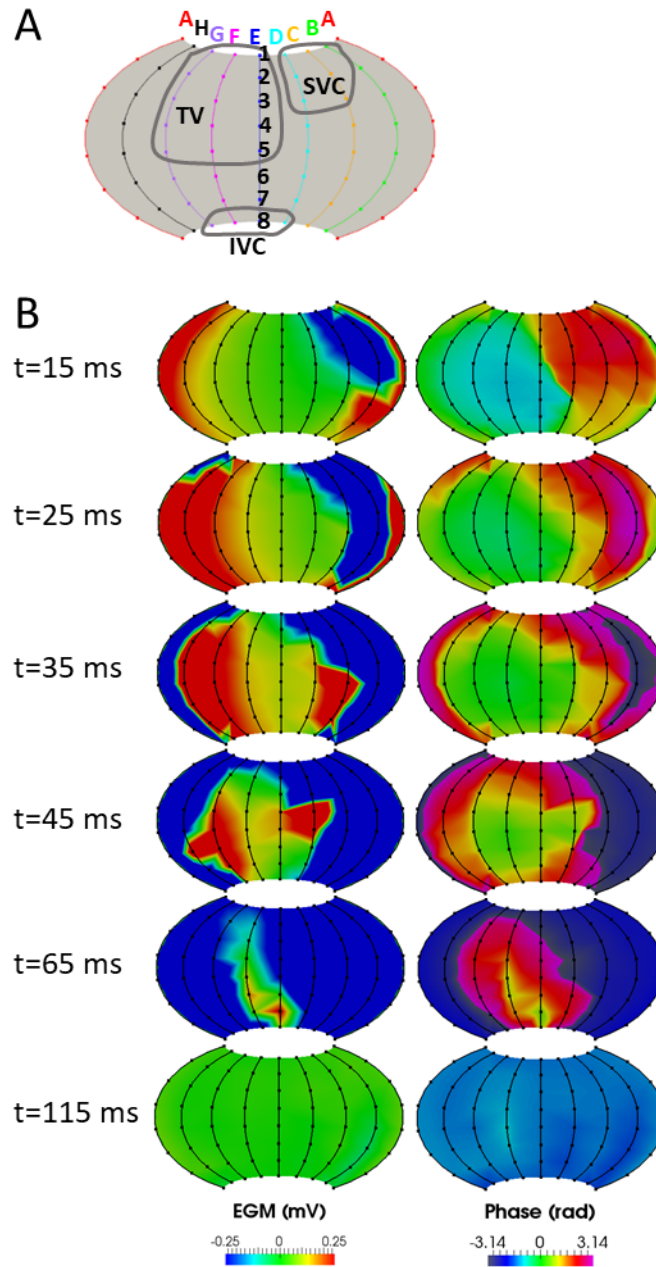


Figure B.2: Basket propagation pattern in SR for the CT position. A) 2D projection of basket (TV, SVC and IVC orifices superimposed). B) Snapshots of the EGMs (left column) and phase maps (right column).

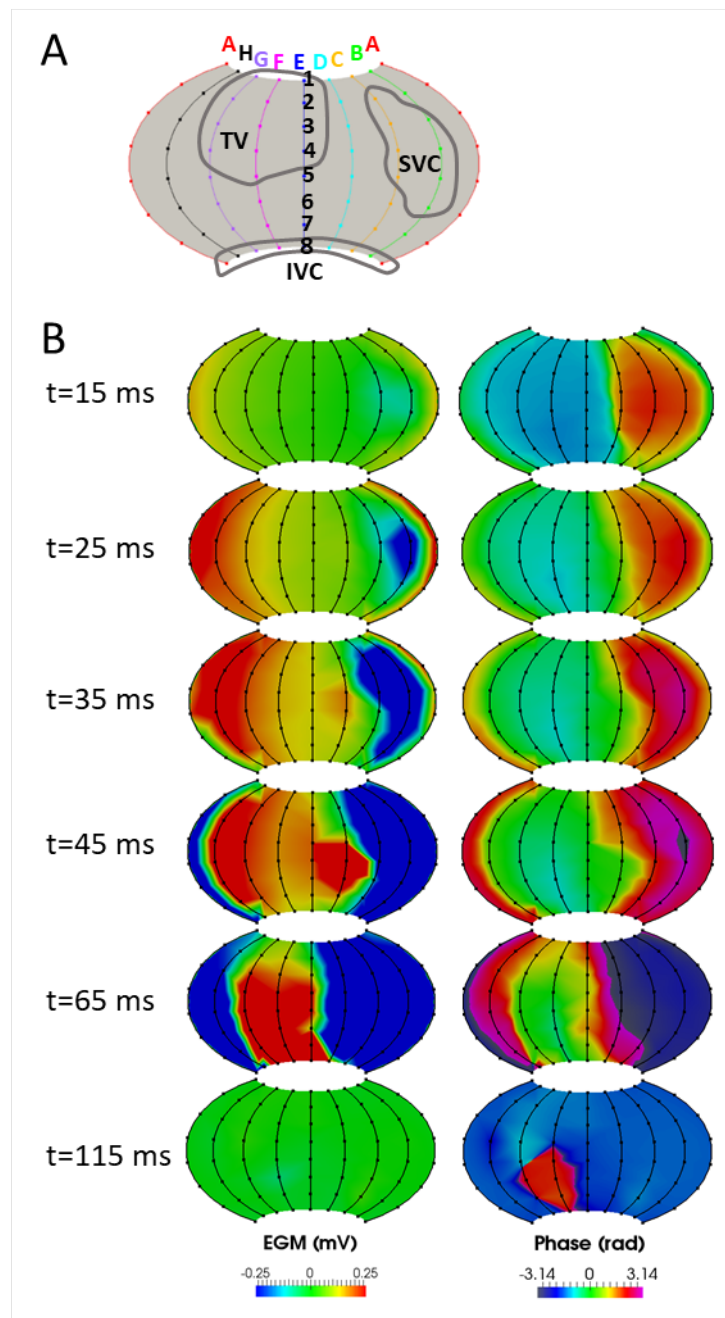


Figure B.3: Basket propagation pattern in SR for the CS position. A) 2D projection of basket (TV, SVC and IVC orifices superimposed). B) Snapshots of the EGMs (left column) and phase maps (right column).

Bibliography

- [1] S. Mendis, P. Puska, and B. Norrving. *Global Atlas on Cardiovascular Disease Prevention and Control*. World Health Organization, 2011.
- [2] H. Calkins, KH. Kuck, R. Cappato, J. Brugada, AJ. Camm, J. Edgerton, K. Ellenbogen, MD. Ezekowitz, and DE. Haines. 2012 HRS/EHRA/ECAS expert consensus statement on catheter and surgical ablation of atrial fibrillation: recommendations for patient selection, procedural techniques, patient management and follow-up, definitions, endpoints, and research trial design. *Journal of Interventional Cardiac Electrophysiology*, 33:171–257, 2012.
- [3] C.T. January, L.S. Wann, J.S. Alpert, H. Calkins, J.E. Cigarroa, J.C. Cleveland, J.B. Conti, P.T. Ellinor, M.D. Ezekowitz, M.E. Field, K.T. Murray, R.L. Sacco, W.G. Stevenson, P.J. Tchou, C.M. Tracy, C.W. Yancy, J.L. Anderson, J.L. Halperin, N.M. Albert, B. Bozkurt, R.G. Brindis, M.A. Creager, L.H. Curtis, D. Demets, R.A. Guyton, J.S. Hochman, R.J. Kovacs, E.M. Ohman, S.J. Pressler, F.W. Sellke, W. Shen, W.G. Stevenson, and C.W. Yancy. 2014 AHA / ACC / HRS Guideline for the Management of Patients With Atrial Fibrillation. A Report of the American College of Cardiology / American Heart Association Task Force on Practice Guidelines and the Heart Rhythm Society. *Circulation*, 130:e199–e267, 2014.
- [4] P. Kirchhof, S. Benussi, D. Kotecha, A. Ahlsson, D. Atar, B. Casadei, M. Castella, H.C. Diener, H. Heidbuchel, J. Hendriks, and G. Hindricks. 2016 ESC Guidelines for the management of atrial fibrillation developed in collaboration with EACTS. *European Heart Journal*, 2016.
- [5] L. Mont, F. Bisbal, A. Hernández-Madrid, N. Pérez-Castellano, X. Viñolas, A. Arenal, F. Arribas, I. Fernández-Lozano, A. Bodegas, J. Pérez-Villacastín, J.M. Guerra, P. Ávila, M. López-Gil, V. Castro, J.I. Arana, and J. Brugada. Catheter ablation vs. antiarrhythmic drug

- treatment of persistent atrial fibrillation: a multicentre, randomized, controlled trial (SARAsudy). *European Heart Journal*, 35:501–507, 2014.
- [6] L. Shi, R. Heng, S. Liu, and F. Leng. Effect of catheter ablation versus antiarrhythmic drugs on atrial fibrillation: A meta-analysis of randomized controlled trials. *Experimental and therapeutic medicine*, 10:816–822, 2015.
- [7] A. Hakalahti, F. Biancari, J.C. Nielsen, and M.J.P. Raatikainen. Radiofrequency ablation vs. antiarrhythmic drug therapy as first line treatment of symptomatic atrial fibrillation: systematic review and meta-analysis. *Europace*, 17:370–378, 2015.
- [8] M. Haïssaguerre, P. Jaïs, D.C. Shah, A. Takahashi, M. Hocini, G. Quiniou, S. Garrigue, A. Le Mouroux, P. Le Métayer, and J. Clémenty. Spontaneous initiation of atrial fibrillation by ectopic beats originating in the pulmonary veins. *The New England journal of medicine*, 339(10):659–666, 1998.
- [9] C. Pappone, G. Oreto, S. Rosanio, G. Vicedomini, M. Tocchi, F. Gugliotta, A. Salvati, C. Dicandia, M.P. Calabrò, P. Mazzone, E. Ficarra, C. Di Gioia, S. Gulletta, S. Nardi, V. Santinelli, S. Benussi, and O. Alfieri. Atrial Electroanatomic Remodeling After Circumferential Radiofrequency Pulmonary Vein Ablation. Efficacy of an Anatomic Approach in a Large Cohort of Patients with Atrial Fibrillation. *Circulation*, 104:2539–2544, 2001.
- [10] H. Oral, B.P. Knight, H. Tada, M. Özyaydn, A. Chugh, S. Hassan, C. Scharf, S.W.K. Lai, R. Greenstein, F.Jr. Pelosi, S.A. Strickberger, and F. Morady. Pulmonary Vein Isolation for Paroxysmal and Persistent Atrial Fibrillation. *Circulation*, 105:1077–1081, 2002.
- [11] D.M. Todd, A.C. Skanes, G. Guiraudon, C. Guiraudon, A.D. Krahn, R. Yee, and G.J. Klein. Role of the Posterior Left Atrium and Pulmonary Veins in Human Lone Atrial Fibrillation. *Circulation*, 108:3108–3114, 2003.
- [12] S.M. Narayan, D.E. Krummen, M.W. Enyeart, and W.J. Rappel. Computational Mapping Identifies Localized Mechanisms for Ablation of Atrial Fibrillation. *PLoS ONE*, 7(9):1–8, 2012.
- [13] S.M. Narayan, K. Shivkumar, D.E. Krummen, J.M. Miller, and W.J. Rappel. Panoramic Electrophysiological Mapping but not Electrogram Morphology Identifies Stable Sources for Human Atrial Fibrillation. Stable Atrial Fibrillation Rotors and Focal Sources Relate Poorly to Fractionated Electrograms. *Circulation Arrhythmia and Electrophysiology*, 6:58–67, 2013.

- [14] R. Mandapati, A. Skanes, J. Chen, O. Berenfeld, and J. Jalife. Stable microreentrant sources as a mechanism of atrial fibrillation in the isolated sheep heart. *Circulation*, 101(2):194–199, 2000.
- [15] M. Yamazaki, S. Mironov, C. Taravant, J. Brec, L.M. Vaquero, K. Bandaru, U.M.R. Avula, H. Honjo, I. Kodama, O. Berenfeld, and J. Kalifa. Heterogeneous atrial wall thickness and stretch promote scroll waves anchoring during atrial fibrillation. *Cardiovascular Research*, 94(1):48–57, 2012.
- [16] M. Mansour, R. Mandapati, O. Berenfeld, J. Chen, F.H. Samie, and J. Jalife. Left-to-right gradient of atrial frequencies during acute atrial fibrillation in the isolated sheep heart. *Circulation*, 103(21):2631–2636, 2001.
- [17] O. Berenfeld, A.V. Zaitsev, S.F. Mironov, A.M. Pertsov, and J. Jalife. Frequency-dependent breakdown of wave propagation into fibrillatory conduction across the pectinate muscle network in the isolated sheep right atrium. *Circulation Research*, 90(11):1173–1180, 2002.
- [18] B.J. Hansen, J. Zhao, T.A. Csepe, B.T. Moore, N. Li, L.A. Jayne, A. Kalyanasundaram, P. Lim, A. Bratasz, K.A. Powell, O.P. Simonetti, R.S.D. Higgins, A. Kilic, P.J. Mohler, P.M.L. Janssen, R. Weiss, J.D. Hummel, and V.V. Fedorov. Atrial fibrillation driven by micro-anatomic intramural re-entry revealed by simultaneous sub-epicardial and sub-endocardial optical mapping in explanted human hearts. *European Heart Journal*, 36(35):2390–2401, 2015.
- [19] J. Zhao, B.J. Hansen, Y. Wang, T.A. Csepe, L.V. Sul, A. Tang, Y. Yuan, N. Li, A. Bratasz, K.A. Powell, A. Kilic, P.J. Mohler, P.M. Janssen, R. Weiss, O.P. Simonetti, J.D. Hummel, and V.V. Fedorov. Three-dimensional Integrated Functional, Structural, and Computational Mapping to Define the Structural "Fingerprints" of Heart-Specific Atrial Fibrillation Drivers in Human Heart Ex Vivo. *Journal of the American Heart Association*, 6:e005922, 2017.
- [20] S.M. Narayan, D.E. Krummen, K. Shivkumar, P. Clopton, W.J. Rappel, and J.M. Miller. Treatment of atrial fibrillation by the ablation of localized sources: CONFIRM (Conventional Ablation for Atrial Fibrillation with or Without Focal Impulse and Rotor Modulation) trial. *Journal of the American College of Cardiology*, 60(7):628–636, 2012.
- [21] W.J. Rappel and S.M. Narayan. Theoretical considerations for mapping activation in human cardiac fibrillation. *Chaos*, 23(2), 2013.
- [22] T. Yamada. Pulmonary vein isolation with a multielectrode basket catheter. *Indian Pacing and Electrophysiology Journal*, 7(2):97–109, 2007.

- [23] P. Benharash, E. Buch, P. Frank, M. Share, R. Tung, K. Shivkumar, and R. Mandapati. Quantitative Analysis of Localized Sources Identified by Focal Impulse and Rotor Modulation Mapping in Atrial Fibrillation. *Circulation Arrhythmia and Electrophysiology*, 8(3):554–61, 2015.
- [24] N. Sasaki, Y. Okumura, I. Watanabe, K. Nagashima, K. Takahashi, and K. Iso. Localized rotors and focal impulse sources within the left atrium in human atrial fibrillation: A phase analysis of contact basket catheter electrograms. *Journal of Arrhythmia*, 32(2):141–144, 2016.
- [25] C.T. Tai and S.A. Chen. Noncontact Mapping of the Heart: How and When to Use. *Journal of cardiovascular electrophysiology*, 20:123–126, 2009.
- [26] J.L. Salinet, N. Masca, P.J. Stafford, G.A. Ng, and F.S. Schlindwein. Three dimensional dominant frequency mapping using autoregressive spectral analysis of atrial electrograms of patients in persistent atrial fibrillation. *BioMedical Engineering OnLine*, pages 1–15, 2016.
- [27] R. Weerasooriya, P. Khairy, J. Litalien, L. Macle, M. Hocini, F. Sacher, N. Lellouche, S. Knecht, M. Wright, I. Nault, S. Miyazaki, C. Scavee, J. Clementy, M. Haissaguerre, and P. Jais. Catheter Ablation for Atrial Fibrillation. Are Results Maintained at 5 Years of Follow-Up? *JACC*, 57(2):160–166, 2011.
- [28] E. Buch, M. Share, R. Tung, P. Sharma, J. Koneru, R. Mandapati, K.A. Ellenbogen, and K. Shivkumar. Long-term clinical outcomes of focal impulse and rotor modulation for treatment of atrial fibrillation: A multicenter experience. *Heart Rhythm*, 13(3):636–641, 2016.
- [29] R.F. Berntsen, T.F. Håland, R. Skårdal, and T. Holm. Focal impulse and rotor modulation as a stand-alone procedure for the treatment of paroxysmal atrial fibrillation: A within-patient controlled study with implanted cardiac monitoring. *Heart Rhythm*, 13(9):1768–1774, 2016.
- [30] J.M. Miller, R.C. Kowal, V. Swarup, J.P. Daubert, E.G. Daoud, J.D. Day, K.A. Ellenbogen, J.D. Hummel, T. Baykaner, D.E. Krummen, S.M. Narayan, V.Y. Reddy, K. Shivkumar, J.S. Steinberg, and K.R. Wheelan. Initial Independent Outcomes from Focal Impulse and Rotor Modulation Ablation for Atrial Fibrillation: Multicenter FIRM Registry. *Journal of Cardiovascular Electrophysiology*, 25(9):921–929, 2014.
- [31] K. Shivkumar, K.A. Ellenbogen, J.D. Hummel, J.M. Miller, and J.S. Steinberg. Acute termination of human atrial fibrillation by identification and catheter ablation of localized rotors and sources: First Multicenter Experience of Focal Impulse and Rotor Modulation (FIRM) Ablation. *Journal of cardiovascular electrophysiology*, 23(12):1277–1285, 2012.

- [32] K. Umapathy, K. Nair, S. Masse, S. Krishnan, J. Rogers, M.P. Nash, and K. Nanthakumar. Phase mapping of cardiac fibrillation. *Circulation: Arrhythmia and Electrophysiology*, 3(1):105–114, 2010.
- [33] A.C. Guyton and J.E. Hall. *Textbook of Medical Physiology*. Elsevier Saunders, 1600 John F. Kennedy Blvd, Suite 1800 Philadelphia, Pennsylvania 19103-2899, 11th edition, 2006.
- [34] A.J. Pullan, M.L. Buist, and L.K. Cheng. *Mathematically modelling the electrical activity of the heart: from cell to body surface and back again*. World Scientific, 5 Oh Tuck Link, Singapore 596224, 2005.
- [35] P.C. Franzone, L.F. Pavarino, and S. Scacchi. *Mathematical Cardiac Electrophysiology*. Springer, 2014.
- [36] K. Wang, S.Y. Ho, and R.H. Anderson. Architecture of atrial musculature in humans. *British Heart Journal*, 73:559–565, 1995.
- [37] S.Y. Ho, R.H. Anderson, and D. Sanchez-Quintana. Atrial structure and bres: morphologic bases of atrial conduction. *Cardiovascular Research*, 54:325–336, 2002.
- [38] R. Lemery, G. Guiraudon, and J.P. Veinot. Anatomic description of Bachmanns Bundle and its relation to the atrial septum. *The American Journal of Cardiology*, 91(12):1482–1485, 2003.
- [39] R.H. Anderson and A.C. Cook. The structure and components of the atrial chambers. *Europace*, 9:vi3–vi9, 2007.
- [40] J.A. Cabrera, S.Y. Ho, V. Climent, and D. Sanchez-Quintana. The architecture of the left lateral atrial wall: a particular anatomic region with implications for ablation of atrial brillation. *European Heart Journal*, 29:356–362, 2008.
- [41] D. Sanchez-Quintana, G. Pizarro, J.R. Lopez-Minguez, S.Y. Ho, and J.A. Cabrera. Standardized Review of Atrial Anatomy for Cardiac Electrophysiologists. *Journal of Cardiovascular Translational Research*, 6:124–144, 2013.
- [42] A. Goette, Kalman J.M., L. Aguinaga, Akar J., J.A. Cabrera, S.A. Chen, S.S. Chugh, D. Corradi, A. DAVila, D. Dobrev, M. Fenelon, G. amd Gonzalez, S.N. Hatem, R. Helm, G. Hindricks, S.Y. Ho, B. Hoit, J. Jalife, Y.H. Kim, G.Y. Lip, C.S. Ma, G.M. Marcus, K. Murray, A. Nogami, P. Sanders, W. Uribe, D.R. Van Wagoner, and S. Nattel. EHRA/HRS/APHRS/SOLAECE expert consensus on Atrial cardiomyopathies: Definition, characterisation, and clinical implication. *Journal of Arrhythmia*, 32(4):247–278, 2016.

- [43] G.A. Thibodeau, K.T. Patton, and S. Elsevier. *Anatomía y Fisiología*. University of Winsconsin, River Falls St. Charles Community College, 6th edition, 2007.
- [44] A. Ferrer-Albero. *Three-dimensional Multiscale Modelling and Simulation of atria and torso electrophysiology*. PhD thesis, Universitat Politècnica de València, 2017.
- [45] V.F. Cassola, F.M. Milian, R. Kramer, C.A.B. de Oliveira Lira, and H.J. Khoury. Standing adult human phantoms based on 10th, 50th and 90th mass and height percentiles of male and female Caucasian populations. *Physics in Medicine and Biology*, 56(13):3749–3772, 2011.
- [46] J.F. Bellemare, M.P. Cordeau, P. Leblanc, and F. Bellemare. Thoracic Dimensions at Maximum Lung Inflation in Normal Subjects and in Patients with Obstructive and Restrictive Lung Diseases. *CHEST*, 119(2):376–386, 2001.
- [47] G.H. Kramer, K. Capello, B. Bearrs, A. Lauzon, and L. Normandeau. Linear Dimensions and Volumes of Human Lungs Obtained From CT Images. *Health Physics*, 102(4):378–383, 2012.
- [48] I. Busscher, J.J.W. Ploegmakers, G.J. Verkerke, and A.G. Veldhuizen. Comparative anatomical dimensions of the complete human and porcine spine. *European Spine Journal*, 19(7):1104–1114, 2010.
- [49] R. Selthofer, V. Nikolić, T. Mrcela, R. Radić, I. Leksan, I. Rudez, and K. Selthofer. Morphometric analysis of the sternum. *Collegium antropologicum*, 30(1):43–47, 2006.
- [50] F. Bellemare, A. Jeanneret, and J. Couture. Sex differences in thoracic dimensions and configuration. *American Journal of Respiratory and Critical Care Medicine*, 168(3):305–312, 2003.
- [51] F.H. DeLand and W.A. North. Relationship Between Liver Size and Body Size. *Radiology*, 91(6):1195–1198, 1968.
- [52] W. Kratzer, V. Fritz, R.A. Mason, N.M. Haenle, V. Kaechele, and Roemerstein Study Group. Factors affecting liver size: a sonographic survey of 2080 subjects. *Journal of Ultrasound in Medicine*, 22(11):1155–1161, 2003.
- [53] J.M. Ferrero Corral, J.M. Ferrero y de Loma-Osorio, F.J. Saiz Rodríguez, and A. Arnau Vives. *Bioelectrónica: Seales bioeléctricas*. SPUPV, ISBN: 84-7721-250-3, 1994.
- [54] K.E. Barrett, S. Boitano, S.M. Barman, and H.L. Brooks. *Ganong’s Review of Medical Physiology*. McGraw-Hill, 23th edition, 2010.

- [55] N. Voigt, X.B. Zhou, and D. Dobrev. Isolation of Human Atrial Myocytes for Simultaneous Measurements of Ca^{2+} Transients and Membrane Currents. *Journal of Visualized Experiments*, 77:e50235, 2013.
- [56] ZG. Wang, LC. Pelletier, M. Talajic, and S. Nattel. Effects of flecainide and quinidine on human atrial action potentials. Role of rate-dependence and comparison with guinea pig, rabbit, and dog tissues. *Circulation*, 82(1):274–283, 1990.
- [57] R. Dumaine and J.M. Cordeiro. Comparison of K^{+} currents in cardiac Purkinje cells isolated from rabbit and dog. *J Mol Cell Cardiol*, 42:378–389, 2007.
- [58] M.A. McIntosh, S.M. Cobbe, and G.L. Smith. Heterogeneous changes in action potential and intracellular Ca^{2+} in left ventricular myocyte subtypes from rabbits with heart failure. *Cardiovascular Research*, 45:397–409, 2000.
- [59] A. Bénardeau, S.N. Hatem, C. Rücker-Martin, B. Le Grand, L. Macé, P. Dervanian, J.J. Mercadier, and E. Coraboeuf. Contribution of $\text{Na}^{+}/\text{Ca}^{2+}$ exchange to action potential of human atrial myocytes. *American Journal of Physiology*, 271:H1151–61, 1996.
- [60] J. Feng, L. Yue, Z. Wang, and S. Nattel. Ionic mechanisms of regional action potential heterogeneity in the canine right atrium. *Circulation research*, 83(5):541–551, 1998.
- [61] D. Li, L. Zhang, J. Kneller, and S. Nattel. Potential ionic mechanism for repolarization differences between canine right and left atrium. *Circulation research*, 88(11):1168–1175, 2001.
- [62] T.J. Cha, J.R. Ehrlich, L. Zhang, D. Chartier, T.K. Leung, and S. Nattel. Atrial tachycardia remodeling of pulmonary vein cardiomyocytes: Comparison with left atrium and potential relation to arrhythmogenesis. *Circulation*, 111(6):728–735, 2005.
- [63] Z. Wang, B. Fermini, and S. Nattel. Sustained depolarization-induced outward current in human atrial myocytes. Evidence for a novel delayed rectifier K^{+} current similar to $\text{Kv}1.5$ cloned channel currents. *Circulation research*, 73(6):1061–1076, 1993.
- [64] Z. Wang, B. Fermini, , and S. Nattel. Delayed rectifier outward current and repolarization in human atrial myocytes. *Circulation Research*, 73:276–285, 1993.
- [65] W. Einthoven, G. Fahr, and A. De Waart. On the direction and manifest size of the variations of potential in the human heart and on the influence of

- the position of the heart on the form of the electrocardiogram. *American Heart Journal*, 40:163–211, 1950.
- [66] F.N. Wilson, F.D. Johnston, A.G. Macleod, and P.S. Barker. Electrocardiograms that represent the potential variations of a single electrode. *American Heart Journal*, 9(4):447–458, 1934.
- [67] C. Schmitt, I. Deisenhofer, and B. Zrenner. *Catheter Ablation of Cardiac Arrhythmias: A Practical Approach*. Steinkopff Verlag, Darmstadt, 2006.
- [68] M.W. Keller. *Formation of Intracardiac Electrograms under Physiological and Pathological Conditions*. PhD thesis, Fakultät für Elektrotechnik und Informationstechnik des Karlsruher Instituts für Technologie (KIT), 2014.
- [69] J.M.T. Bakker and F.H.M. Wittkamp. The Pathophysiologic Basis of Fractionated and Complex Electrograms and the Impact of Recording Techniques on Their Detection and Interpretation. *Circulation: Arrhythmia and Electrophysiology*, 3:204–213, 2010.
- [70] J.J. Goldberger and J. Ng. *Practical Signal and Image Processing in Clinical Cardiology*. Springer-Verlag, London, 2010.
- [71] M.A. Allessie, N.M.S. DeGroot, R.P.M. Houben, U. Schotten, E. Boersma, J.L. Smeets, and H.J. Crijns. Electropathological Substrate of Long-Standing Persistent Atrial Fibrillation in Patients With Structural Heart Disease Longitudinal Dissociation. 2010.
- [72] W.T. O’Neal, H. Kamel, S.E. Judd, M.M. Safford, V. Vaccarino, V.J. Howard, G. Howard, and E.Z. Soliman. Usefulness of Atrial Premature Complexes on Routine Electrocardiogram to Determine the Risk of Atrial Fibrillation (from the REGARDS Study) . *American Journal of Cardiology*, 120:782–785, 2017.
- [73] R. Marinheiro, L. Parreira, P. Amador, C. Sá, T. Duarte, and R. Caria. Excessive atrial ectopic activity as an independent risk factor for ischemic stroke. *International Journal of Cardiology*, 249:226–230, 2017.
- [74] H. Coutio, J. Abugattas, M. Levinstein, G. Mugnai, D. Moran, V. De Regibus, E. Strker, K. Takarada, R. Choudhury, L. Marroqun, F. Salghetti, I. Lusoc, S. Iacopino, J. Sieira, C. De Asmundis, P. Brugada, and G. Chierchia. Role of the burden of premature atrial contractions during the blanking period following second-generation cryoballoon ablation in predicting late recurrences of atrial arrhythmias. *J Interv Card Electrophysiol*, 49:329–335, 2017.
- [75] B.S. Larsen, P. Kumarathurai, J. Falkenberg, O.W. Nielsen, and A. Sajadieh. Excessive Atrial Ectopy and Short Atrial Runs Increase

the Risk of Stroke Beyond Incident Atrial Fibrillation. *Journal of the American College of Cardiology*, 66:232–241, 2015.

- [76] N. Saoudi, F. Cosío, A. Waldo, S.A. Chen, Y. Iesaka, M. Lesh, S. Saksena, J. Salerno, and W. Schoels. A classification of atrial flutter and regular atrial tachycardia according to electrophysiological mechanisms and anatomical bases; a Statement from a Joint Expert Group from The Working Group of Arrhythmias of the European Society of Cardiology and the North American Society of Pacing and Electrophysiology. *Eur Heart J*, 22:1162–1182, 2001.
- [77] G. Steinbeck and E. Hoffmann. 'True' atrial tachycardia. *Eur Heart J*, 19 Suppl E:E10–2, E48–9, 1998.
- [78] R.L. Page, J.A. Joglar, M.A. Caldwell, H. Calkins, J.B. Conti, B.J. Deal, N.A.M. Estes, M.E. Field, Z.D. Goldberger, S.C. Hammill, J.H. Indik, B.D. Lindsay, B. Olshansky, A.M. Russo, W.K. Shen, C.M. Tracy, and S.M. Al-Khatib. 2015 ACC/AHA/HRS Guideline for the Management of Adult Patients With Supraventricular Tachycardia: A Report of the American College of Cardiology/American Heart Association Task Force on Clinical Practice Guidelines and the Heart Rhythm Society. *J Am Coll Cardiol*, 67:e27–e115, 2016.
- [79] K.I. Shine, J.A. Kastor, and P.M. Yurchak. Multifocal atrial tachycardia. Clinical and electrocardiographic features in 32 patients. *N Engl J Med*, 279:344–349, 1968.
- [80] J.M.S. Lee and S.P. Fynn. P Wave Morphology in Guiding the Ablation Strategy of Focal Atrial Tachycardias and Atrial Flutter. *Current Cardiology Reviews*, 11:103–110, 2015.
- [81] S.A. Kothari, S. Apiyasawat, N. Asad, and D.H. Spodick. Evidence supporting a new rate threshold for multifocal atrial tachycardia. *Clin Cardiol*, 28:561–563, 2005.
- [82] S. Bellet. *Clinical Disorders of the Heart Beat*. Lea & Febiger, Philadelphia, 1971.
- [83] J.E.P. Waktare. Atrial Fibrillation. *Circulation*, 106:14–16, 2002.
- [84] J.L. Merino. Mecanismos electrofisiológicos y diagnóstico de la fibrilación auricular. *Rev Esp Cardiol*, 16:12–19, 2016.
- [85] M.E. Silverman. From rebellious palpitations to the discovery of auricular fibrillation: contributions of Mackenzie, Lewis and Einthoven. *Am J Cardiol*, 73:384–389, 1994.

- [86] T. Lewis. Auricular fibrillation: a common clinical condition. *Br Med J*, 2:1528, 1909.
- [87] G.K. Moe. On the multiple wavelet hypothesis of atrial brillation. *Arch.Int.Pharmacodyn*, 140:183–188, 1962.
- [88] M.A. Allesie, W.J.E.P. Lammers, F.I.M. Bonke, and J. Hollen. *Experimental evaluation of Moe's multiple wavelet hypothesis of atrial fibrillation. In Cardiac Electrophysiology and Arrhythmias, eds. Zipes, D.P. and Jalife, J. Grune & Stratton, New York, 1985.*
- [89] J. Jalife, O. Berenfeld, A. Skanes, and R. Mandapati. Mechanisms of atrial fibrillation: mother rotors or multiple daughter wavelets, or both? *J Cardiovasc Electrophysiol*, 9:S2–12, 1998.
- [90] S. Nattel, B. Burstein, and D. Dobrev. Atrial Remodeling and Atrial Fibrillation Mechanisms and Implications. *Circ Arrhythmia Electrophysiol*, 1:62–73, 2008.
- [91] H. Calkins, G. Hindricks, R. Cappato, Y.H. Kim, E.B. Saad, L. Aguinaga, J.G. Akar, V. Badhwar, J. Brugada, J. Camm, P.S. Chen, S.A. Chen, and et al. 2017 HRS/EHRA/ECAS/APHRS/SOLAECE expert consensus statement on catheter and surgical ablation of atrial fibrillation. *Heart Rhythm*, 14:e275–e444, 2017.
- [92] R. Caballero, M. González de la Fuente, R. Gómez, A. Barana, I. Amorós, P. Dolz-Gaitón, L. Osuna, J. Almendral, F. Atienza, F. Fernández-Avilés, A. Pita, J. Rodríguez-Roda, Á. Pinto, J. Tamargo, and E. Delpón. In Humans, Chronic Atrial Fibrillation Decreases the Transient Outward Current and Ultrarapid Component of the Delayed Rectifier Current Differentially on Each Atria and Increases the Slow Component of the Delayed Rectifier Current in Both. *Journal of the American College of Cardiology*, 55(21):2346–2354, 2010.
- [93] A.J. Workman, K.A. Kane, and A.C. Rankin. The contribution of ionic currents to changes in refractoriness of human atrial myocytes associated with chronic atrial fibrillation. *Cardiovascular research*, 52(2):226–235, 2001.
- [94] R.F. Bosch, X. Zeng, J.B. Grammer, K. Popovic, C. Mewis, and V. Kühlkamp. Ionic mechanisms of electrical remodeling in human atrial fibrillation. *Cardiovascular research*, 44(1):121–131, 1999.
- [95] M.C.E.F. Wijffels, C.J.H.J. Kirchhof, R. Dorland, and M.A. Allesie. Atrial Fibrillation Begets Atrial Fibrillation. A Study in Awake Chronically Instrumented Goats. *Circulation*, 92:1954–1968, 1995.

- [96] A. Boldt, U. Wetzel, J. Lauschke, J. Weigl, J. Gummert, G. Hindricks, H. Kottkamp, and S. Dhein. Fibrosis in left atrial tissue of patients with atrial fibrillation with and without underlying mitral valve disease. *Heart*, 90:400–405, 2004.
- [97] N. Ellinwood, D. Dobrev, S. Morotti, and E. Grandi. In Silico Assessment of Efficacy and Safety of IKur Inhibitors in Chronic Atrial Fibrillation: Role of Kinetics and State-Dependence of Drug Binding. *Front Pharmacol*, 8:799, 2017.
- [98] N. Voigt, A. Trausch, M. Knaut, K. Matschke, A. Varró, D.R. Van Wagoner, S. Nattel, U. Ravens, and D. Dobrev. Left-to-right atrial inward rectifier potassium current gradients in patients with paroxysmal versus chronic atrial fibrillation. *Circulation: Arrhythmia and Electrophysiology*, 3(5):472–480, 2010.
- [99] F. Atienza, J. Almendral, J. Moreno, R. Vaidyanathan, A. Talkachou, J. Kalifa, A. Arenal, J.P. Villacastín, E.G. Torrecilla, A. Sánchez, R. Ploutz-Snyder, J. Jalife, and O. Berenfeld. Activation of Inward Rectifier Potassium Channels Accelerates Atrial Fibrillation in Humans: Evidence for a Reentrant Mechanism. *Circulation*, 114:2434–2442, 2006.
- [100] S. Lazar, S. Dixit, F.E. Marchlinski, D.J. Callans, and E.P. Gerstenfeld. Presence of Left-to-Right Atrial Frequency Gradient in Paroxysmal but Not Persistent Atrial Fibrillation in Humans. *Circulation*, 110:3181–3186, 2004.
- [101] F. Sarmast, A. Kolli, A. Zaitsev, K. Parisian, A.S. Dhamoon, P.K. Guha, M. Warren, J.M.B. Anumonwo, S.M. Taffet, O. Berenfeld, and J. Jalife. Cholinergic atrial fibrillation: IK,ACh gradients determine unequal left/right atrial frequencies and rotor dynamics. *Cardiovascular Research*, 59:863–873, 2003.
- [102] N. Voigt, J. Heijman, Q. Wang, D.Y. Chiang, N. Li, M. Karck, X.H.T. Wehrens, S. Nattel, and D. Dobrev. Cellular and Molecular Mechanisms of Atrial Arrhythmogenesis in Patients With Paroxysmal Atrial Fibrillation. *Circulation*, 129(2):145–156, 2014.
- [103] M.C. Brandt, L. Priebe, T. Böhle, M. Südkamp, and D.J. Beuckelmann. The Ultrarapid and the Transient Outward K⁺ Current in Human Atrial Fibrillation. Their Possible Role in Postoperative Atrial Fibrillation. *J Mol Cell Cardiol*, 32:1885–1896, 2000.
- [104] D.R. Van Wagoner, A.L. Pond, M. Lamorgese, S.S. Rossie, P.M. McCarthy, and J.M. Nerbonne. Atrial L-type Ca²⁺ currents and human atrial fibrillation. *Circulation research*, 85(5):428–436, 1999.

- [105] M. Skasa, E. Jüngling, E. Picht, F. Schöndube, and A. Lückhoff. L-type calcium currents in atrial myocytes from patients with persistent and non-persistent atrial fibrillation. *Basic Research in Cardiology*, 96:151–159, 2001.
- [106] D. Dobrev, E. Graf, E. Wettwer, H.M. Himmel, O. Hála, C. Doerfel, T. Christ, S. Schüler, and U. Ravens. Molecular basis of downregulation of G-protein-coupled inward rectifying K(+) current (I(K,ACh) in chronic human atrial fibrillation: decrease in GIRK4 mRNA correlates with reduced I(K,ACh) and muscarinic receptor-mediated shortening of action potentials. *Circulation*, 104(21):2551–2557, 2001.
- [107] D. Dobrev, E. Wettwer, A. Kortner, M. Knaut, S. Schuler, and U. Ravens. Human inward rectifier potassium channels in chronic and postoperative atrial fibrillation. *Cardiovascular Research*, 54:397–404, 2002.
- [108] D.R. Van Wagoner, A.L. Pond, P.M. McCarthy, J.S. Trimmer, and J.M. Nerbonne. Outward K⁺ Current Densities and Kv1.5 Expression Are Reduced in Chronic Human Atrial Fibrillation. *Circ Res*, 80:772–781, 1997.
- [109] J. Chrispin, E.G. Ipek, M. Habibi, E. Yang, D. Spragg, J.E. Marine, H. Ashikaga, J. Rickard, R.D. Berger, S.L. Zimmerman, H. Calkins, and S. Nazarian. Clinical predictors of cardiac magnetic resonance late gadolinium enhancement in patients with atrial fibrillation. *Europace*, 19:371–377, 2017.
- [110] N.F. Marrouche, D. Wilber, G. Hindricks, P. Jais, N. Akoum, F. Marchlinski, E. Kholmovski, N. Burgon, N. Hu, L. Mont, T. Deneke, M. Duytschaever, T. Neumann, M. Mansour, C. Mahnkopf, B. Herweg, E. Daoud, E. Wissner, P. Bansmann, and J. Brachmann. Association of atrial tissue fibrosis identified by delayed enhancement MRI and atrial fibrillation catheter ablation: the DECAAF study. *JAMA*, 311:498–506, 2014.
- [111] J. Saiz and C. Tobón. 35. Supraventricular Arrhythmias in a Realistic 3D Model of the Human Atria. In *Cardiac Electrophysiology: From Cell to Bedside (Sixth Edition)*, Editors D.P. Zipes and J. Jalife, pages 351 – 359. W.B. Saunders, Philadelphia, 2014.
- [112] P. Comtois, M. Sakabe, E.J. Vigmond, M. Munoz, A. Texier, A. Shiroshita-Takeshita, and S. Nattel. Mechanisms of atrial fibrillation termination by rapidly unbinding Na⁺ channel blockers: insights from mathematical models and experimental correlates. *Am J Physiol Heart Circ Physiol*, 295:H1489–H1504, 2008.

- [113] J. Jalife. Introduction to the Series on Computational Approaches to Cardiac Arrhythmias. Translation Into Diagnostics and Therapy. *Circ Res*, 112:831–833, 2013.
- [114] M.L. Buist and A.J. Pullan. The Effect of Torso Impedance on Epicardial and Body Surface Potentials: A Modeling Study. *IEEE Transactions on Biomedical Engineering*, 50:816–824, 2003.
- [115] B. Taccardi, B.B. Punske, R.L. Lux, R.S. MacLeod, P.R. Ershler, T.J. Dustman, and Y. Vyhmeister. Useful Lessons from Body Surface Mapping. *J Cardiovasc Electrophysiol*, 9:773–786, 1998.
- [116] A.L. Hodgkin and A.F. Huxley. A quantitative description of membrane current and its application to conduction and excitation in nerve. *J Physiol*, 117:500–544, 1952.
- [117] D. Noble. Cardiac Action and Pacemaker Potentials based on the Hodgkin-Huxley Equations. *Nature*, 188:495–497, 1960.
- [118] G. Giebisch and S. Weidmann. Membrane currents in mammalian ventricular heart muscle fibres using a "voltage-clamp" technique. *Helv Physiol Pharmacol Acta*, 25:CR189–90, 1967.
- [119] O.P. Hamill, A. Marty, E. Neher, B. Sakmann, and F.J. Sigworth. Improved patch-clamp techniques for high-resolution current recording from cells and cell-free membrane patches. *Pflugers Arch*, 391:85–100, 1981.
- [120] J. Heijman, P.E. Abdoust, N. Voigt, S. Nattel, and D. Dobrev. Computational models of atrial cellular electrophysiology and calcium handling, and their role in atrial fibrillation. *The Journal of Physiology*, 594(3):537–553, 2016.
- [121] D.W. Hilgemann and D. Noble. Excitation-contraction coupling and extracellular calcium transients in rabbit atrium: reconstruction of basic cellular mechanisms. *Proc R Soc Lond B Biol Sci*, 230:163–205, 1987.
- [122] D.S. Lindblad, C.R. Murphey, J.W. Clark, and W.R. Giles. A model for the action potential and underlying membrane currents in a rabbit atrial cell. *Am J Physiol Heart Circ Physiol*, 271:H1666–H1696, 1996.
- [123] R.L. Rasmusson, J.W. Clark, W.R. Giles, K. Robinson, R.B. Clark, E.F. Shibata, and D.L. Campbell. A mathematical model of electrophysiological activity in a bullfrog atrial cell. *Am J Physiol Heart Circ Physiol*, 259:H370–H389, 1990.
- [124] R.J. Ramirez, S. Nattel, and M. Courtemanche. Mathematical analysis of canine atrial action potentials: rate, regional factors and electrical remodeling. *Am J Physiol Heart Circ Physiol*, 279:H1767–H1785, 2000.

- [125] J. Kneller, H. Sun, N. Leblanc, and S. Nattel. Remodeling of Ca²⁺ handling by atrial tachycardia: evidence for a role in loss of rate-adaptation. *Cardiovasc Res*, 54:416–426, 2002.
- [126] L. Davies, J. Jin, W. Shen, H. Tsui, Y. Shi, Y. Wang, Y. Zhang, G. Hao, J. Wu, S. Chen, J.A. Fraser, N. Dong, V. Christoffels, U. Ravens, C.L. Huang, H. Zhang, E.J. Cartwright, X. Wang, and M. Lei. Mkk4 is a negative regulator of the transforming growth factor beta 1 signaling associated with atrial remodeling and arrhythmogenesis with age. *J Am Heart Assoc*, 3:e000340, 2014.
- [127] A. Nygren, C. Fiset, L. Firek, J.W. Clark, D.S. Lindblad, R.B. Clark, and W.R. Giles. Mathematical model of an adult human atrial cell: the role of K⁺ currents in repolarization. *Circ Res*, 82:63–81, 1998.
- [128] M. Courtemanche, R.J. Ramirez, and S. Nattel. Ionic mechanisms underlying human atrial action potential properties: insights from a mathematical model. *Am J Physiol Heart Circ Physiol*, 275:301–321, 1998.
- [129] C.H. Luo and Y. Rudy. A Dynamic Model of the Cardiac Ventricular Action Potential: I. Simulations of Ionic Currents and Concentration Changes. *Circ Res*, 74:1071–1096, 1994.
- [130] M. Wilhelms, H. Hettmann, M.M. Maleckar, J.T. Koivumäki, O. Dössel, and G. Seemann. Benchmarking electrophysiological models of human atrial myocytes. *Frontiers in Physiology*, 3:487(1–16), 2013.
- [131] E.M. Cherry and S.J. Evans. Properties of two human atrial cells models in tissue: Restitution, memory, propagation and reentry. *Journal of Theoretical Biology*, 254:674–690, 2008.
- [132] A. Nygren, L.J. Leon, and W.R. Giles. Simulations of the human atrial action potential. *Philos Trans A Math Phys Eng Sci*, 359:1111–1125, 2001.
- [133] M.M. Maleckar, J.L. Greenstein, W.R. Giles, and N.A. Trayanova. K⁺ current changes account for the rate dependence of the action potential in the human atrial myocyte. *Am J Physiol Heart Circ Physiol*, 297:H1398–H1410, 2009.
- [134] J.T. Koivumäki, T. Korhonen, and P. Tavi. Impact of Sarcoplasmic Reticulum Calcium Release on Calcium Dynamics and Action Potential Morphology in Human Atrial Myocytes: A Computational Study. *PLOS Comp Biol*, 7:e1001067:1–14, 2011.
- [135] E. Grandi, S.V. Pandit, N. Voigt, A.J. Workman, D. Dobrev, J. Jalife, and D.M. Bers. Human Atrial Action Potential and Ca²⁺ Model:

- Sinus Rhythm and Chronic Atrial Fibrillation. *Circulation Research*, 109(9):1055–1066, 2011.
- [136] O. Dössel, M.W. Krueger, F.M. Weber, M. Wilhelms, and G. Seemann. Computational modeling of the human atrial anatomy and electrophysiology. *Med Biol Eng Comput*, 50(8):773–799, 2012.
- [137] Y. Rudy and J.R. Silva. Computational biology in the study of cardiac ion channels and cell electrophysiology. *Q Rev Biophys*, 39:57–116, 2006.
- [138] M.W. Krueger, A. Dorn, D.U.J. Keller, F. Holmqvist, J. Carlson, P.G. Platonov, K.S. Rhode, R. Razavi, G. Seemann, and O. Dössel. In-silico modeling of atrial repolarization in normal and atrial fibrillation remodeled state. *Medical and Biological Engineering and Computing*, 51(10):1105–1119, 2013.
- [139] D. Deng, P. Jiao, X. Ye, and L. Xia. An Image-Based Model of the Whole Human Heart with Detailed Anatomical Structure and Fiber Orientation. *Computational and Mathematical Methods in Medicine*, 2012:891070:1–16, 2012.
- [140] L.K. Cheng, G.B. Sands, R.L. French, S.J. Withy, S.P. Wong, M.E. Legget, W.M. Smith, and A.J. Pullan. Rapid construction of a patient-specific torso model from 3D ultrasound for non-invasive imaging of cardiac electrophysiology. *Med Biol Eng Comput*, 43:325–330, 2005.
- [141] M.W. Krüger. *Personalized Multi-Scale Modeling of the Atria*. PhD thesis, KIT, 2012.
- [142] S.V. Pandit, O. Berenfeld, J.M.B. Anumonwo, R.M. Zaritski, J. Kneller, S. Nattel, and J. Jalife. Ionic Determinants of Functional Reentry in a 2-D Model of Human Atrial Cells During Simulated Chronic Atrial Fibrillation. *Biophysical Journal*, 88:3806–3821, 2005.
- [143] C. Sánchez, A. Corrias, A. Bueno-Orovio, M. Davies, J. Swinton, I. Jacobson, P. Laguna, E. Pueyo, and B. Rodríguez. The Na⁺/K⁺ pump is an important modulator of refractoriness and rotor dynamics in human atrial tissue. *Am J Physiol Heart Circ Physiol*, 302:H1146–H1159, 2012.
- [144] M. Aguilar, J. Feng, E. Vigmond, P. Comtois, and S. Nattel. Rate-Dependent Role of I_{Kur} in Human Atrial Repolarization and Atrial Fibrillation Maintenance. *Biophysical Journal*, 112:1997–2010, 2017.
- [145] M.W. Keller, S. Schuler, M. Wilhelms, G. Lenis, G. Seemann, C. Schmitt, O. Dössel, and A. Luik. Characterization of Radiofrequency Ablation Lesion Development Based on Simulated and Measured Intracardiac Electrograms. *IEEE Transactions on Biomedical Engineering*, 61:2467–2478, 2014.

- [146] D.M. Harrild and C.S. Henriquez. A Computer Model of Normal Conduction in the Human Atria. *Circ Res*, 87:e25–e36, 2000.
- [147] C. Ruiz-Villa. *Estudio de la vulnerabilidad a reentradas a través de modelos matemáticos y simulación de la aurícula humana*. PhD thesis, Universitat Politècnica de València, 2010.
- [148] A. Ferrer, R. Sebastián, D. Sánchez-Quintana, J.F. Rodríguez, E.J. Godoy, L. Martínez, and J. Saiz. Detailed Anatomical and Electrophysiological Models of Human Atria and Torso for the Simulation of Atrial Activation. *Plos One*, 10(11):e0141573, 2015.
- [149] M. Rodrigo, A.M. Climent, A. Liberos, F. Calvo, D. Fernández-Avilés, O. Berenfeld, F. Atienza, and M.S. Guillem. Identification of Dominant Excitation Patterns and Sources of Atrial Fibrillation by Causality Analysis. *Ann Biomed Eng*, 44:2364–2376, 2016.
- [150] C. Tobón. *Modelización y evaluación de factores que favorecen las arritmias auriculares y su tratamiento mediante técnicas quirúrgicas. Estudio de simulación*. PhD thesis, Universitat Politècnica de València, 2010.
- [151] C. Tobón, C.A. Ruiz-Villa, E. Heidenreich, L. Romero, F. Hornero, and J. Saiz. A Three-Dimensional Human Atrial Model with Fiber Orientation. Electrograms and Arrhythmic Activation Patterns Relationship. *PLoS ONE*, 8(2), 2013.
- [152] E.J. Vigmond, R. Ruckdeschel, and N. Trayanova. Reentry in a morphologically realistic atrial model. *J Cardiovasc Electrophysiol*, 12:1046–1054, 2001.
- [153] G. Seemann, C. Höper, F.B. Sachse, O. Dössel, A.V. Holden, and H. Zhang. Heterogeneous three-dimensional anatomical and electrophysiological model of human atria. *Philosophical transactions. Series A, Mathematical, physical, and engineering sciences*, 364(1843):1465–1481, 2006.
- [154] D. Deng, Y. Gong, G. Shou, P. Jiao, H. Zhang, X. Ye, and L. Xia. Simulation of biatrial conduction via different pathways during sinus rhythm with a detailed human atrial model. *J Zhejiang Univ-Sci B (Biomed Biotechnol)*, 13:676–694, 2012.
- [155] S. Zahid, H. Cochet, P.M. Boyle, E.L. Schwarz, K.N. Whyte, E.J. Vigmond, R. Dubois, M. Hocini, M. Haïssaguerre, P. Jaïs, and N.A. Trayanova. Patient-derived models link re-entrant driver localization in atrial fibrillation to fibrosis spatial pattern. *Cardiovasc Res*, 110:443–454, 2016.

- [156] D. Deng, M.J. Murphy, J.B. Hakim, W.H. Franceschi, S. Zahid, F. Pashakhanloo, N.A. Trayanova, and P.M. Boyle. Sensitivity of reentrant driver localization to electrophysiological parameter variability in image-based computational models of persistent atrial fibrillation sustained by a fibrotic substrate. *Chaos*, 27:181–196, 2017.
- [157] P.M. Boyle, M.J. Murphy, T.V. Karathanos, S. Zahid, R.C. Blake, and N.A. Trayanova. Termination of re-entrant atrial tachycardia via optogenetic stimulation with optimized spatial targeting: insights from computational models. *J Physiol*, 596:181–196, 2018.
- [158] D.U.J. Keller, F.M. Weber, G. Seemann, and O. Dössel. Ranking the influence of tissue conductivities on forward-calculated eegs. *IEEE Transactions on Biomedical Engineering*, 57(7):1568–1576, 2010.
- [159] Y. Rudy and R. Plonsey. A comparison of volume conductor and source geometry effects on body surface and epicardial potentials. *Circulation research*, 46:283–291, 1980.
- [160] M. Rodrigo, M.S. Guillem, A.M. Climent, J. Pedrón-Torrecilla, A. Liberos, J. Millet, F. Fernández-Avilés, F. Atienza, and O. Berenfeld. Body surface localization of left and right atrial high-frequency rotors in atrial fibrillation patients: A clinical-computational study. *Heart Rhythm*, 11(9):1584–1591, 2014.
- [161] R.S. MacLeod, C.R. Johnson, and P.R. Ershler. Construction of an inhomogeneous model of the human torso for use in computational electrocardiography. *Proceedings of the Annual Conference on Engineering in Medicine and Biology*, 13:688–689, 1991.
- [162] A. Ferrer-Albero, E.J. Godoy, M. Lozano, L. Martínez-Mateu, F. Atienza, J. Saiz, and R. Sebastian. Non-invasive localization of atrial ectopic beats by using simulated body surface P-wave integral maps. *PLOS ONE*, 12:e0181263:1–23, 2017.
- [163] D.B. Geselowitz and W.T. Miller. A bidomain model for anisotropic cardiac muscle. *Annals of Biomedical Engineering*, 11:315–334, 1983.
- [164] E.A. Heidenreich. *Algoritmos para ecuaciones de reacción difusión aplicados a electrofisiología*. PhD thesis, Universidad de Zaragoza, 2009.
- [165] L. Tung. *A bi-domain model for describing ischemic myocardial dc potentials*. PhD thesis, Massachusetts Institute of Technology, 1978.
- [166] M. Potse, B. Dubé, A. Vinet, and R. Cardinal. A comparison of monodomain and bidomain propagation models for the human heart. *Annual International Conference of the IEEE Engineering in Medicine and Biology - Proceedings*, (3):3895–3898, 2006.

- [167] A.T. Winfree. *When Time Breaks Down. The Three-Dimensional Dynamics of Electrochemical Waves and Cardiac Arrhythmias*. Princeton University Press, 1987.
- [168] R.A. Gray, A.M. Pertsov, and J. Jalife. Spatial and temporal organization during cardiac fibrillation. *Nature*, 392(5):75–78, 1998.
- [169] M.A. Bray, S. Lin, R.R. Aliev, B.J. Roth, and J.P. Wikswo. Experimental and Theoretical Analysis of Phase Singularity Dynamics in Cardiac Tissue. *J.Cardiovasc.Electrophysiol.*, 12:716–722, 2001.
- [170] R.H. Clayton, E.A. Zhuchkova, and A.V. Panlov. Phase singularities and filaments: Simplifying complexity in computational models of ventricular fibrillation. *Progress in Biophysics and Molecular Biology*, 90:378–398, 2006.
- [171] J.M. Rogers. Combined Phase Singularity and Wavefront Analysis for Optical Maps of Ventricular Fibrillation. *IEEE*, 51(1):56–65, Jan 2004.
- [172] M. Pachón-Iglesias and J. Jalife. Nuevos conceptos sobre los mecanismos de la brilacion ventricular. *Rev Esp Cardiol*, 54:373–382, 2001.
- [173] A.N. Iyer, R.E. Ideker, and R.A. Gray. Accurate localization of phase singularities during reentry. *IEEE*, 1999.
- [174] J. Chen, R. Mandapati, O. Berenfeld, A.C. Skanes, R.A. Gray, and J. Jalife. Dynamics of wavelets and their role in atrial fibrillation in the isolated sheep heart. *Cardiovascular Research*, 48:220–232, 2000.
- [175] M.A. Bray and J.P. Wikswo. Considerations in phase plane analysis for non-stationary reentrant cardiac behaviour. *Physical Review E*, 65:051902, 2002.
- [176] S.M. Narayan, D.E. Krummen, and W.J. Rappel. Clinical mapping approach to diagnose electrical rotors and focal impulse sources for human atrial fibrillation. *Journal of Cardiovascular Electrophysiology*, 23(5):447–454, 2012.
- [177] J. Kalifa, K. Tanaka, A.V. Zaitsev, M. Warren, R. Vaidyanathan, D. Auerbach, S. Pandit, K.L. Vikstrom, R. Ploutz-Snyder, A. Talkachou, F. Atienza, G. Guiraudon, J. Jalife, and O. Berenfeld. Mechanisms of Wave Fractionation at Boundaries of High-Frequency Excitation in the Posterior Left Atrium of the Isolated Sheep Heart During Atrial Fibrillation. *Circulation*, 113:626–633, 2006.
- [178] M. Yamazaki, U.M.R. Avula, O. Berenfeld, and J. Kalifa. Mechanistic Comparison of Nearly Missed Versus On-Target Rotor Ablation. *JACC:Clinical Electrophysiology*, 1(4):256–269, 2015.

- [179] M.A. Colman. *Mechanisms of Atrial Arrhythmias*, volume 9. 2014.
- [180] E.A. Heidenreich, J.M. Ferrero, M. Doblaré, and J.F. Rodríguez. Adaptive macro finite elements for the numerical solution of monodomain equations in cardiac electrophysiology. *Annals of Biomedical Engineering*, 38(7):2331–2345, 2010.
- [181] J.E. Saffitz, H.L. Kanter, K.G. Green, T.K. Tolley, and E.C. Beyer. Tissue-specific determinants of anisotropic conduction velocity in canine atrial and ventricular myocardium. *Circulation research*, 74:1065–1070, 1994.
- [182] M.S. Spach, P.C. Dolber, and J.F. Heidlage. Influence of the passive anisotropic properties on directional differences in propagation following modification of the sodium conductance in human atrial muscle. A model of reentry based on anisotropic discontinuous propagation. *Circulation research*, 62:811–832, 1988.
- [183] R. Lemery, D. Birnie, A.S.L. Tang, M. Green, M. Gollob, M. Hendry, and E. Lau. Normal atrial activation and voltage during sinus rhythm in the human heart: An endocardial and epicardial mapping study in patients with a history of atrial fibrillation. *Journal of Cardiovascular Electrophysiology*, 18(4):402–408, 2007.
- [184] T. Lin, A. Rillig, A. Metzner, S. Mathew, C. Heeger, P. Wohlmuth, R. Tilz, K. Kuck, and F. Ouyang. P-wave morphology and electrical activity of the isolated left atrial appendage on 12-lead ECG in patients with recurrent atrial tachyarrhythmias after pulmonary vein isolation. *J Interv Card Electrophysiol*, 50:169–178, 2017.
- [185] M.W. Krüger, S. Severi, K. Rhode, S. Genovesi, F.M. Weber, A. Vincenti, P. Fabbrini, G. Seemann, R. Razavi, and O. Dössel. Alterations of atrial electrophysiology related to hemodialysis session: insights from a multiscale computer model. *Journal of Electrocardiology*, 44:176–183, 2011.
- [186] S. Gabriel, R.W. Lau, and C. Gabriel. The dielectric properties of biological tissues: III. Parametric models for the dielectric spectrum of tissues. *Phys. Med. Biol.*, 41:2271–2293, 1996.
- [187] R.N. Klepfer, C.R. Johnson, and R.S. Macleod. The Effects of Inhomogeneities and Anisotropies on Electrocardiographic Fields: A 3-D Finite-Element Study. *IEEE Transactions on Biomedical Engineering*, 44:706–719, 1997.
- [188] C.P. Bradley, A.J. Pullan, and P.J. Hunter. Effects of Material Properties and Geometry on Electrocardiographic Forward Simulations. *Annals of Biomedical Engineering*, 28:721–741, 2000.

- [189] W. Kaufman and F.D. Johnston. The electrical conductivity of the tissues near the heart and its bearing on the distribution of the cardiac action currents. *Am Heart J*, 26:42–54, 1943.
- [190] S. Grimnes and O.G. Martinsen. *Bioimpedance and Bioelectricity Basics (2nd Edition)*. Academic Press, 2008.
- [191] C.F. Kay and H.P. Schwan. Specific resistance of body tissues. *Circ. Res.*, 4:664–670, 1956.
- [192] S. Rush, J.A. Abildskov, and R. McFee. Resistivity of body tissues at low frequencies. *Circ. Res.*, 12:40–50, 1963.
- [193] H.C. Burger and J.B. van Milaan. Measurements of the specific resistance of the human body to direct current. *Acta Med. Scand.*, 114:584–607, 1943.
- [194] C.H. Roney, C.D. Cantwell, J.D. Bayer, N.A. Qureshi, P.B. Lim, J.H. Tweedy, and et al. Spatial Resolution Requirements for Accurate Identification of Drivers of Atrial Fibrillation. *Circ Arrhythmia Electrophysiol*, pages 1–13, 2017.
- [195] J. Zhao, B.J. Hansen, T.A. Csepe, P. Lim, Y. Wang, M. Williams, P.J. Mohler, P.M.L. Janssen, R. Weiss, J.D. Hummel, and V.V. Fedorov. Integration of High Resolution Optical Mapping and 3D Micro-CT Imaging to Resolve the Structural Basis of Atrial Conduction in the Human Heart. *Circ Arrhythmia Electrophysiol*, 8:1514–1517, 2015.
- [196] M.W. Keller, S. Schuler, G. Seemann, and O. Dössel. Differences in Intracardiac Signals on a Realistic Catheter Geometry using Mono- and Bidomain Models. In *Computing in Cardiology 2012*, 39: 305–308.
- [197] M.W. Keller, S. Schuler, A. Luik, G. Seemann, C. Schilling, and O. Dössel. Comparison of Simulated and Clinical Intracardiac Electrograms. In *35th Annual International Conference of the IEEE, 2013*, 6858–6871.
- [198] S.M. Narayan, T. Baykaner, P. Clopton, A. Schricker, G.G. Lalani, D.E. Krummen, K. Shivkumar, and J.M. Miller. Ablation of rotor and focal sources reduces late recurrence of atrial fibrillation compared with trigger ablation alone: Extended follow-up of the CONFIRM trial (conventional ablation for atrial fibrillation with or without focal impulse and rotor modulat. *Journal of the American College of Cardiology*, 63(17):1761–1768, 2014.
- [199] S. Koumi, C.E. Arentzen, C.L. Backer, and J.A. Wasserstrom. Alterations in muscarinic K⁺ channel response to acetylcholine and to G protein-mediated activation in atrial myocytes isolated from failing human hearts. *Circulation*, 90(5):2213–2224, 1994.

- [200] M. Courtemanche, R.J. Ramirez, and S. Nattel. Ionic targets for drug therapy and atrial fibrillation-induced electrical remodeling: Insights from a mathematical model. *Cardiovascular Research*, 42(2):477–489, 1999.
- [201] M.A. Colman, O.V. Aslanidi, S. Kharche, M.R. Boyett, C. Garratt, J.C. Hancox, and H. Zhang. Pro-arrhythmogenic effects of atrial fibrillation-induced electrical remodelling: insights from the three-dimensional virtual human atria. *The Journal of physiology*, 591(Pt 17):4249–72, 2013.
- [202] G.I. Cohen, M. White, R.A. Sochowski, A.L. Klein, P.D. Bridge, W.J. Stewart, and K.L. Chan. Reference Values for Normal Adult Transesophageal Echocardiographic Measurements. *Journal of the American Society of Echocardiography*, 8:221–230, 1995.
- [203] M. Warren, P.K. Guha, O. Berenfeld, A. Zaitsev, J.M.B. Anumonwo, A.S. Dhamoon, S. Bagwe, S.M. Taffet, and J. Jalife. Blockade of the inward rectifying potassium current terminates ventricular fibrillation in the guinea pig heart. *Journal of Cardiovascular Electrophysiology*, 14(6):621–631, 2003.
- [204] M. Yamazaki, D. Filgueiras-Rama, O. Berenfeld, and J. Kalifa. Ectopic and reentrant activation patterns in the posterior left atrium during stretch-related atrial fibrillation. *Progress in Biophysics and Molecular Biology*, 110(2-3):269–277, 2012.
- [205] J. Chen, R. Mandapati, O. Berenfeld, and A.C. Skanes. High-Frequency Periodic Sources Underlie Ventricular Fibrillation in the Isolated Rabbit Heart. *Circulation Research*, 86:86–93, 2000.
- [206] N. D. Mermin. The topological theory of defects in ordered media. *Reviews of Modern Physics*, 51(3):591–648, 1979.
- [207] A. Goryachev and R. Kapral. Spiral waves in chaotic systems. *Physical review letters*, 76(10):1619–1622, 1996.
- [208] C. Schmidt, F. Wiedmann, N. Voigt, X. Zhou, J. Heijman, S. Lang, V. Albert, S. Kallenberger, A. Ruhparwar, G. Szab, K. Kallenbach, M. Karck, M. Borggreffe, P. Biliczki, J.R. Ehrlich, I. Baczk, P. Lugenbiel, P.A. Schweizer, B.C. Donner, H.A. Katus, D. Dobrev, and D. Thomas. Upregulation of K2P3.1 K+ Current Causes Action Potential Shortening in Patients With Chronic Atrial Fibrillation. *Circulation*, 132:82–92, 2015.
- [209] U. Schotten, S. Verheule, P. Kirchhof, and A. Goette. Pathophysiological mechanisms of atrial fibrillation: a translational appraisal. *Physiol Rev*, 91:265–325, 2011.
- [210] J. Jalife. Deja vu in the theories of atrial fibrillation dynamics. *Cardiovasc Res*, 89:766–775, 2011.

- [211] O. Berenfeld and H. Oral. The Quest for Rotors in Atrial fibrillation: Different Nets Catch Different Fishes. *Heart Rhythm*, 9:1440–1441, 2012.
- [212] J. Laughner, S. Shome, N. Child, A. Shuros, P. Neuzil, J. Gill, and M. Wright. Practical Considerations of Mapping Persistent Atrial Fibrillation With Whole-Chamber Basket Catheters. *JACC: Clinical Electrophysiology*, 2:55–65, 2016.
- [213] H.M.W. Van Der Velden, J. Ausma, M.B. Rook, A.J.C.G.M. Hellemons, T.A.A.B. Van Veen, M.A. Allessie, and H.J. Jongsma. Gap junctional remodeling in relation to stabilization of atrial fibrillation in the goat. *Cardiovascular Research*, 46(3):476–486, 2000.
- [214] M. Wilhelm, W. Kirste, S. Kuly, K. Amann, W. Neuhuber, M. Weyand, W.G. Daniel, and C. Garlichs. Atrial distribution of connexin 40 and 43 in patients with intermittent, persistent, and postoperative atrial fibrillation. *Heart Lung and Circulation*, 15(1):30–37, 2006.
- [215] G. Seemann, P. Bustamante, S. Ponto, M. Wilhelms, E.P. Scholz, and O. Dössel. Atrial fibrillation-based electrical remodeling in a computer model of the human atrium. *2010 Computers in Cardiology*, pages 417–420, 2010.
- [216] R. Vijayakumar, S.K. Vasireddi, P.S. Cuculich, M.N. Faddis, and Y. Rudy. Methodology Considerations in Phase Mapping of Human Cardiac Arrhythmias. *Circulation: Arrhythmia and Electrophysiology*, 9(11):e004409, 2016.